AD_____

AWARD NUMBER: DAMD17-03-1-0405

TITLE: Three Dimensional Reconstruction Algorithm for Imaging Pathophysiological Signals Within Breast Tissue Using Near Infrared Light

PRINCIPAL INVESTIGATOR: Hamid Dehghani, Ph.D.

CONTRACTING ORGANIZATION: Dartmouth College
Hanover, New Hampshire   03755-1404

REPORT DATE: July 2006

TYPE OF REPORT: Annual Summary

PREPARED FOR: U.S. Army Medical Research and Materiel Command
Fort Detrick, Maryland 21702-5012

DISTRIBUTION STATEMENT: Approved for Public Release;
Distribution Unlimited

The views, opinions and/or findings contained in this report are those of the author(s) and should not be construed as an official Department of the Army position, policy or decision unless so designated by other documentation.

REPORT DOCUMENTATION PAGE

Form Approved
OMB No. 0704-0188

Public reporting burden for this collection of information is estimated to average 1 hour per response, including the time for reviewing instructions, searching existing data sources, gathering and maintaining the data needed, and completing and reviewing this collection of information. Send comments regarding this burden estimate or any other aspect of this collection of information, including suggestions for reducing this burden to Department of Defense, Washington Headquarters Services, Directorate for Information Operations and Reports (0704-0188), 1215 Jefferson Davis Highway, Suite 1204, Arlington, VA 22202-4302. Respondents should be aware that notwithstanding any other provision of law, no person shall be subject to any penalty for failing to comply with a collection of information if it does not display a currently valid OMB control number. **PLEASE DO NOT RETURN YOUR FORM TO THE ABOVE ADDRESS.**

1. REPORT DATE *(DD-MM-YYYY)*	2. REPORT TYPE	3. DATES COVERED *(From - To)*
01-07-2006	Annual Summary	15 Jun 2003 – 14 Jun 2006

4. TITLE AND SUBTITLE

Three Dimensional Reconstruction Algorithm for Imaging Pathophysiological Signals Within Breast Tissue Using Near Infrared Light

5a. CONTRACT NUMBER

5b. GRANT NUMBER
DAMD17-03-1-0405

5c. PROGRAM ELEMENT NUMBER

6. AUTHOR(S)

Hamid Dehghani, Ph.D.

E-Mail: hamid.dehghani@dartmouth.edu

5d. PROJECT NUMBER

5e. TASK NUMBER

5f. WORK UNIT NUMBER

7. PERFORMING ORGANIZATION NAME(S) AND ADDRESS(ES)

Dartmouth College
Hanover, New Hampshire 03755-1404

8. PERFORMING ORGANIZATION REPORT NUMBER

9. SPONSORING / MONITORING AGENCY NAME(S) AND ADDRESS(ES)
U.S. Army Medical Research and Materiel Command
Fort Detrick, Maryland 21702-5012

10. SPONSOR/MONITOR'S ACRONYM(S)

11. SPONSOR/MONITOR'S REPORT NUMBER(S)

12. DISTRIBUTION / AVAILABILITY STATEMENT
Approved for Public Release; Distribution Unlimited

13. SUPPLEMENTARY NOTES

14. ABSTRACT

Near Infrared (NIR) tomography is an imaging technique that aims to image optical properties of biological tissue. This technique has been used to image and characterize breast tissue in healthy volunteers as well as detecting tumor in patients. Image reconstruction algorithms have been developed, which utilizes inherent wavelength dependant a-priori information (spectral) as well as concurrently measured MRI structural information (spatial) to show that the quantitative and qualitative accuracy isdramatically improved to provide clinically useful information. Three dimensional models have been developed that will allow the use of correct size and shape of the breast being imaged, reducing image artifacts by the use ofcorrect assumptions about the model of the breast. Novel models have also been developed that will account for otherwise ignored Refractive Index distribution of breast tissue, and the results indicate that providing the RI distribution of breast tissue is not extremely heterogeneous, the impact on reconstructed artifacts is minimal. Finally a modelthat demonstrates the use of exogenous fluorescent agents for imaging has also been developed.

15. SUBJECT TERMS
OPTICAL TOMOGRAPHY; NEAR INFRARED IMAGING; BREAST CANCER CHARACTERIZATION

16. SECURITY CLASSIFICATION OF:			17. LIMITATION OF ABSTRACT	18. NUMBER OF PAGES	19a. NAME OF RESPONSIBLE PERSON USAMRMC
a. REPORT	**b. ABSTRACT**	**c. THIS PAGE**			**19b. TELEPHONE NUMBER** *(include area code)*
U	U	U	UU	129	

Standard Form 298 (Rev. 8-98)
Prescribed by ANSI Std. Z39.18

Table of Contents

Introduction

In this work, a novel imaging technique is explored that uses non-harmful application of near infrared light to determine the pathophysiological properties of breast tissue. Using this technique, known as Near Infrared (NIR) tomography, an optical fiber placed on the surface of the region of interest, the breast, delivers an input signal while other optical fibers placed at different locations on the same surface detect the out-coming photons, which have propagated through the volume under investigation. The intensity and path-length distributions of the exiting light provide information about the optical properties of the transilluminated tissue using a model-based interpretation where photon propagation is simulated by the diffusion theory. Through iterative solution to match the theory to the real measurements, images of internal optical property distribution can be reconstructed, which have shown to be a function of their structure and more importantly, their physiological state. It is these qualities that provide an alternative method for the detection and characterization of tumor within breast tissue.

An important aspect for the success and accuracy of this method is the use of adequate modeling of light within breast tissue. In this work, we have used a Finite Element Model of the Diffusion Approximation, to calculate and predict light transport. Using such technique, we are able to determine the distribution of internal optical properties of the tissue under investigation. A major limitation in the development of near infrared imaging so far has been the lack of accurate and fast model-based reconstruction algorithm for this modality, which has been a direct aim of the project funded.

During the funding period, several advances and improvements to the modeling and image reconstruction algorithms have been implemented. The three dimensional image reconstruction algorithms have been further modified to improve computational speed and overhead allowing a more realistic time frame for image reconstruction. Additional improvements in the modeling capabilities have been incorporated, namely in terms of allowing for internal tissue Refractive Index (RI) distribution as well as tissue deformation, both of which are discussed below. The use of a-priori information within the image reconstruction algorithm have been investigates, namely through the use of structural (MRI) information and spectral (Wavelength dependant) information. Image analysis has been used utilizing the developed code to seek the pathophysiological properties of breast tissue and cancer. Finally the use of exogenous fluorescence agents have been investigated through the development of a modeling and image reconstruction algorithm, giving rise to information regarding the functional activity of the region under investigation.

Each of the area of research developed during this funded project will be addressed below together with the main findings and their implications of optical tomography of breast tissue in-vivo, specifically for the detection and characterization of breast cancer.

Body
Preliminary Clinical Results of Frequency Domain Diffuse Optical Tomography (DOT) System

Here, we present sample reconstructed images of internal absorption and scatter from 2 sets of exams where data was collected at multiple wavelengths, ranging from 761 nm to 826 nm on volunteers recruited at Dartmouth-Hitchcock Medical Center. The NIR imaging system hardware, developed by the research team at Dartmouth, is shown in Figure 1. The subject lies flat on the measurement bed Figure 1(a), which contains a single opening for the breast. The breast is suspended freely through this opening and the optical fibers, Figure 1(b), are brought into contact with the breast. The optical fiber arrangement consists of a total of 48 fibers, 16 fibers in 3 separate planes. Within each plane the fibers are arranged equidistantly (each separate plane is 10 mm apart from one another in the z direction). The fibers need to make full contact with the breast for high quality NIR measurements.
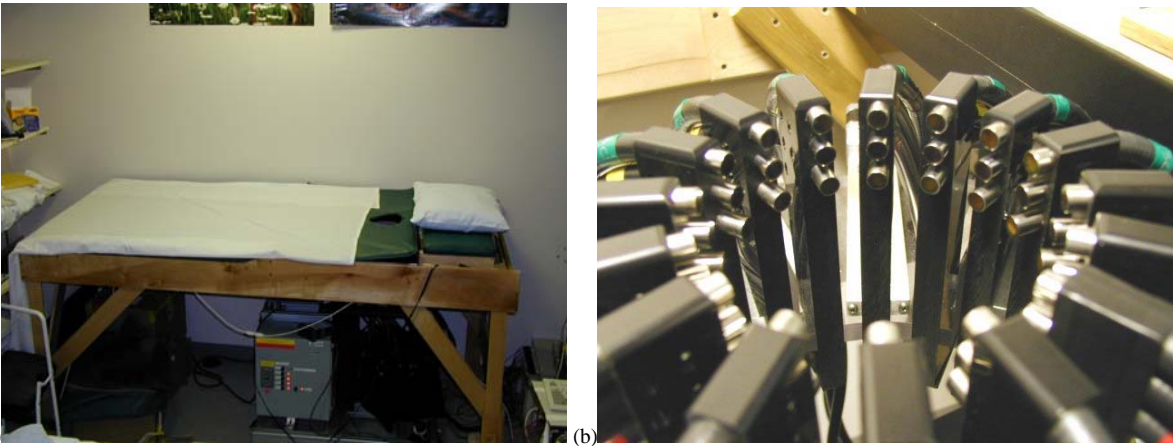

(a)   (b)

Figure 1. (a) The exam station with a single opening for the breast. (b) Optical fiber probe arrangement (16 equally spaced fibers at 3 separate levels, each level is separated by 10 mm) currently at use. The fibers can be opened or closed to suit each individual subject during setup. The breast is suspended through this opening, and optical fiber probes are brought into contact with the tissue surface.

For the NIR exams, an attendant translates the fiber optic probes into direct contact with the breast at the level of the clinical abnormality. We obtained three tomographic acquisitions centered on the region of interest, with contiguous slices above and below the primary plane of the abnormality. Measurements collected from a cylindrical phantom at each wavelength were also recorded for calibration purposes. From knowledge of the diameter of each measurement plane and of the separation between planes, we constructed a conical shaped mesh. For image reconstruction, each data set was calibrated for each wavelength according to procedures described elsewhere [1]. The reconstruction time after the initial calibration procedure was approximately 10 min per iteration on a 1.7-GHz PC with 2 Gigs of RAM.

Figure 2. Reconstructed images of absorption (top row) and reduced scattering (middle row) at each wavelength from measured volunteer data, (volunteer A), as well as calculated maps of blood content; each slice represents a plane through the mesh, from the bottom near the nipple to the top near the chest. The images are coronal views of the cross section through the breast at the tenth iteration at the wavelengths.

The first case, (patient A), presented for standard screening mammography, which revealed a subtle nodular density and associated architectural distortion in the lateral aspect of the right breast. Pathology showed an invasive carcinoma of 20 mm size. 3D images of internal absorption and reduced scattering were recovered simultaneously from NIR data collected at each wavelength. The mesh used for the calculation of the Jacobian contained 8334 nodes corresponding to 41623 linear tetrahedral elements. Images were reconstructed at four wavelengths of 761, 785, 808 and 826 nm, and they are shown in Figure 2. For image reconstruction the regularization parameter (λ) used was initially set to 10, and was allowed to decrease by a factor of $10^{1/4}$ if the projection error had decreased with respect to previous iteration. Images shown are those at the 10th iteration. Here the images are true 3D reconstructions and coronal slices at z = -60, -45, -30, -15 and 0 mm are shown. From the reconstructed images it can be seen that an anomaly is found within the mid-plane at approximately 9 o'clock position. The anomaly presents as an absorption variation with wavelength, whereas the reduced scatter is almost constant over all reconstructed wavelengths. The absorption images were used together with values of extinction coefficients for oxy and deoxy hemoglobin (HbO_2 and Hb respectively) for the calculation of Hb, HbO_2, total hemoglobin (HbT) and oxygen saturation (SO_2). The calculated 3D maps of Hb, HbO_2, total HbT and SO_2 are also shown in Figure 2.

From the calculated values of Hb it is seen that the anomaly shows a peak value of 47.7 μMole, compared to a background of 32.87 μM, whereas the HbO_2 image shows a peak value of 24.73 μM at a location on the periphery of the skin. The total hemoglobin value shows a peak at the location of the anomaly, with a value of 65.28 μM. SO_2 values, calculated by taking the ratio of oxygenated blood and total blood content, indicate a marked decrease at the location of the anomaly, with a value of 25.9%, as compared to a background value of 38.11%. These data are summarized in Table 1.
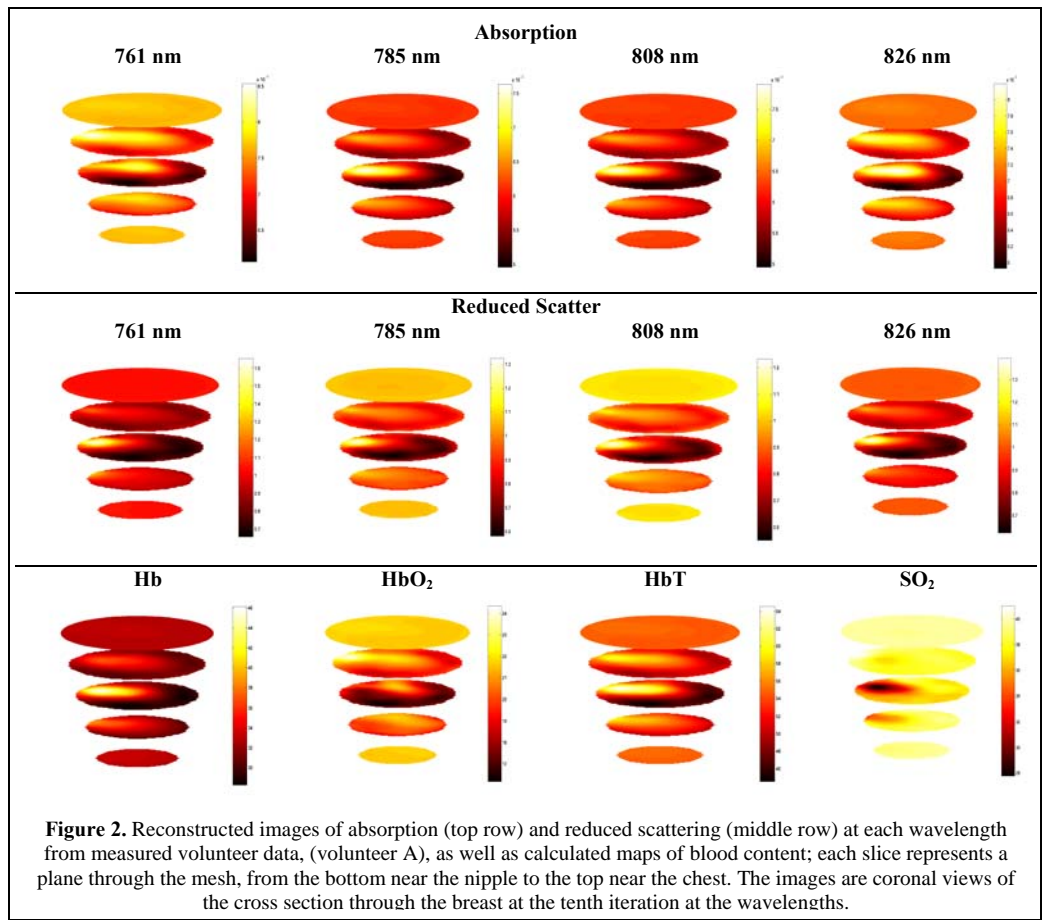
Volunteer B presented for standard

Table 1. Values of Hemoglobin and oxygen saturation maps shown in Figures 15 and 16. The arrows show the increase(↑) or decrease (↓) of values within the region of interest with respect to the background.

	Hb (μM)	HbO₂ (μM)	HbT (μM)	SO₂ (%)	Tumor Type
Volunteer A (anomaly)	47.7 ↑	24.73 ↑	65.28 ↑	25.9 ↓	Invasive ductal carcinoma
Volunteer A (background)	32.87	20.23	53.11	38.11	
Volunteer B (anomaly)	10.76 ↑	15.56 ↑	22.56 ↑	69.26 ↑	Benign ductal hyperplasia
Volunteer B (background)	7.71	8.40	16.11	51.52	

screening mammography, which after biopsy revealed a benign ductal hyperplasia region within the right breast. From the reconstructed NIR images shown in Figure 3 an anomaly is found within the mid-plane, off-center near the nine o'clock position. Here, the anomaly indicates the variation of absorption with wavelength, with a peak value of 0.0055 mm^{-1} at 761 nm, and the reduced scattering images show a peak value of 3.3 mm^{-1}, also at 761 nm. The calculated maps of Hb shows a value of 10.76 μMs at the

location of the anomaly, compared with a background of mean value of 7.7 μMs. The HbO_2 image shows a max value of 15.56 μMs, compared with a mean background value of 8.4 μMs. From the SO_2 images, the anomaly shows a marked increase to 69.26% in saturation, compared with a mean background saturation of 51.52% (Table 1).

For volunteer A, who had an invasive ductal carcinoma within the breast, the absorption and scattering increased within the region of interest. The calculated values of absorption were used together with extinction coefficients of Hb, HbO_2 to calculate deoxy, oxy and total hemoglobin maps, and from these data oxygen saturation images were generated. While the total hemoglobin level within the region of interest shows an increase with respect to background, the oxygen saturation shows a marked decrease within the same region. This trend is perhaps expected for malignant tissue, as one would

Figure 3 Reconstructed images of absorption (top row) and reduced scattering (middle row) at each wavelength from measured volunteer data, (volunteer B), as well as calculated maps of blood content; each slice represents a plane through the mesh, from the bottom near the nipple to the top near the chest. The images are coronal views of the cross section through the breast at the tenth iteration at the wavelengths.

expect a rise in blood content, due to an increase in blood vessel density, but since malignant tumors are more active, this would lead to a decrease in oxygen saturation.

For volunteer B, who had a benign ductal hyperplasia within the breast, the absorption and scattering also increased within the region of interest. For a benign condition, one might expect a rise in blood content due to an increase in blood vessel density, however benign tumors are not particularly more active, suggesting this would result in an increase in oxygen saturation as indicated.

It should be stressed that these results are preliminary, and further investigation is needed before one can claim tumor classification from tissue oxygenation maps. Further work is in progress with respect to building a larger database of such images, thereby allowing a proper and definite statistical analysis of the results.

Incorporation of anatomical data

An important advance has been the culmination of several years of effort towards refining an MRI compatible NIR tomography system which works comfortably with a breast imaging coil to sample light signals transmitted through breast tissue. The system is shown in the figure 4(a) below, with the ring of 16 bifurcated fibers appearing in the positioning array Figure 4(b), with brass loaded springs, which gently push the fibers against the breast. A series of tissue simulating phantoms were created with gelatin, and a three-layer phantom is shown in the figure below, where an interior layer is included to mimic glandular-tissue surrounded by adipose tissue. A spherical interior object is also included to mimic a large tumor. These images have been used in a series of basic studies, where we are determining the optimal way to integrate spatial a priori information into the NIR tomography reconstruction.
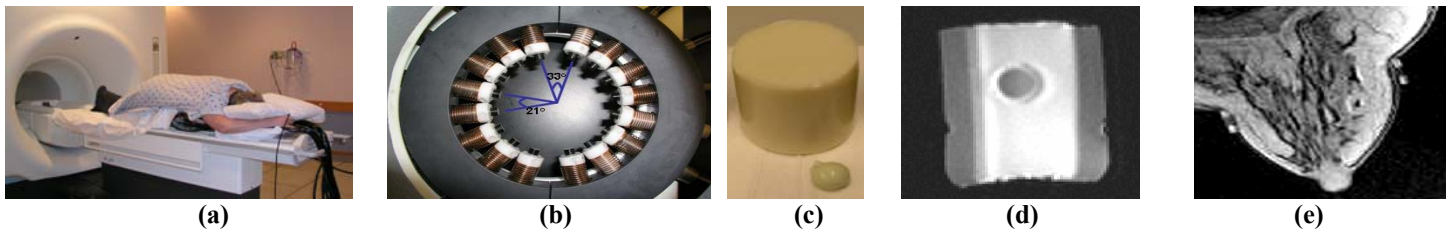

| (a) | (b) | (c) | (d) | (e) |

Figure 4. Image of the patient on the breast coil lying on the MRI bed is shown in (a). An image of the breast interface is shown in (b) with spring-loaded optical fibers arranged in a circle. A gelatin phantom is shown in (c) with varying concentrations of scatterer, absorber and copper sulphate solution, allowing simultaneous MRI and NIR phantom testing. MRI images of the phantom (d) and a breast (e) are shown where the presence of the array can be seen as indents in the phantom image, and as exterior fiducials in the breast image. On each fiber, a sponge ring fiducial is placed, allowing accurate imaging of the fiber tip on the breast tissue.

Reconstructed images of the phantoms used in this system are shown in Figure 5, with segmentation of the three layers in the phantom. Without using the MRI interior structural information, the image reconstruction of this phantom would appear as shown in
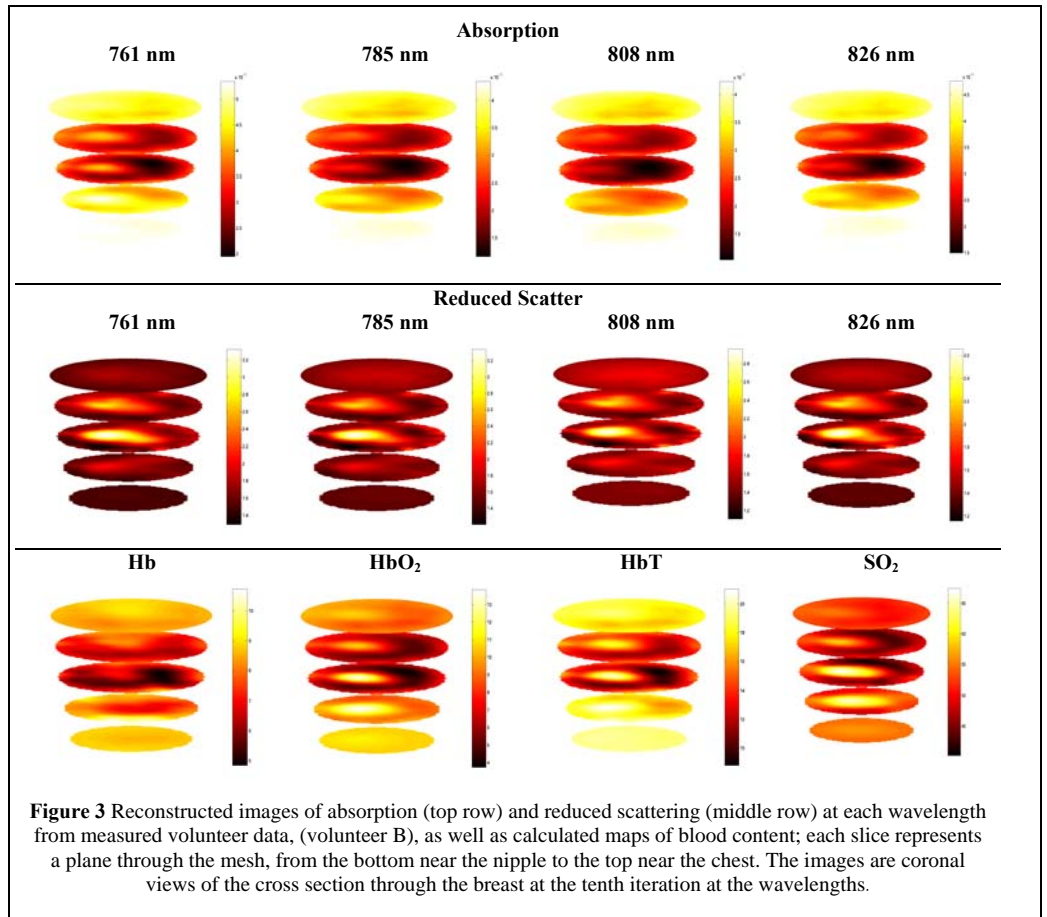
Figure 5(b). From the phantom data we note that it is possible to significantly improve the fitting of optical properties using a priori information. This latter approach is more accurate in estimating the peak value. Interestingly, if the regions were recovered as bulk values, reducing the number of estimators to only three, this approach leads to incorrect properties for the middle region. Thus, we have tentatively concluded that a priori information is better applied into the regularization parameter, than through segmentation and parameter reduction. Detailed analysis of the tradeoffs between parameter reduction (regionizing areas to be represented by a single pair of μ_a and $\mu_s^{/}$ values) versus full reconstruction with regionization of the regularization parameter has been completed on phantom data sets. The conclusions to date indicate that regularization-based constraints are much more stable in the presence of noise, and that the covariance between nodes in the same medium is a key factor to include in this recovery. Thus, our working plan has been to utilize interior information as carefully chosen variations in the regularization parameter.
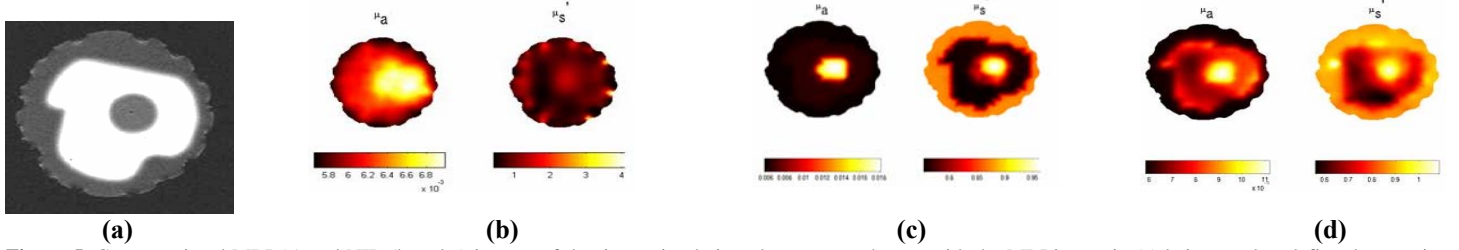

(a)   **(b)**   **(c)**   **(d)**

Figure 5. Cross sectional MRI (a) and NIR (b and c) images of the tissue simulating phantom are shown, with the MRI image in (a) being used to define the exterior and interior boundaries between regions. In (b) our standard NIR image reconstruction results are shown, where the peak absorption coefficient is found to reach only 0.007 mm^{-1}, where the true value was 0.02 mm^{-1}. If the phantom interior regions obtained from the MR image are used to vary the regularization parameter, the peak value increased to 0.011 mm^{-1} (c), however if covariance between nodes is also incorporated (d), the value peaks (0.018 mm^{-1}) nearer the true level.

In Figure 6, images of a fatty/scattered breast are shown in (a) and a heterogeneously dense breast in (b), where in the latter breast, it is possible to segment the two major tissue types. These tissues are adipose on the exterior and fibro-glandular structure on the interior. Without using these segmented regions, the typical NIR image of this breast would be as shown in (c), whereas with the segmentation of the regions, the two tissue types can be fit to average bulk values, which agree with the expected numbers for these tissues (see figure caption).
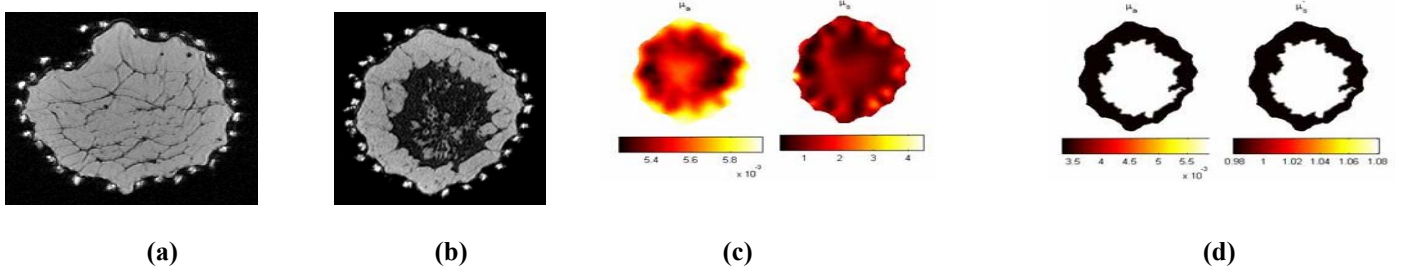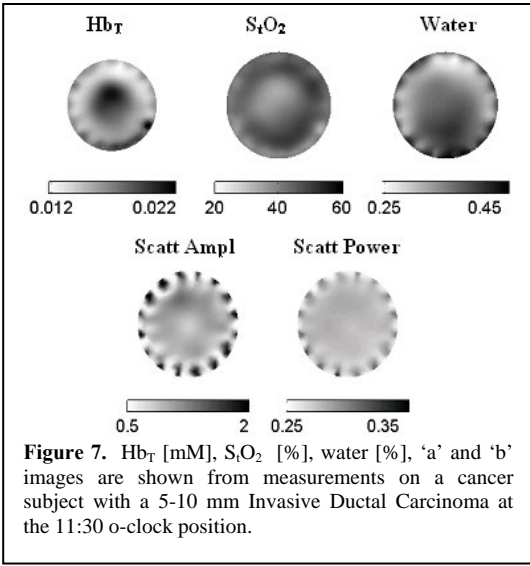

(a)   **(b)**   **(c)**   **(d)**

Figure 6. Coronal MRI images of a fatty/scattered breast are shown in (a), and a heterogeneously dense breast in (b) in the breast imaging array, with the fiber fiducial markers demarking the fiber locations. The reconstructed NIR images of the breast shown in (b) are presented in (c) without a priori interior information and (d) with interior spatial information applied. The values of the absorption coefficient for the breast tissue types in the fatty and glandular regions are 0.0035 mm^{-1} and 0.006 mm^{-1}.

Spectral imaging

Near Infra-Red (NIR) tomography is known for its ability to distinguish between malignant and normal tissue based on high-contrast arising from intrinsic processes such as angiogenesis and hypoxia in tumors. Absorption-based parameters can be recovered such as total hemoglobin, oxygen saturation and water fraction as well as scattering. These provide measures of physiology or pathophysiology related to the intra-vascular and extra-vascular spaces as well as composition of the tissue. Typically spectral tomography approaches must make use of only sparse data at discrete wavelengths instead of a complete spectrum, resulting in an insufficient measurement set for a unique solution. The reconstruction process is an ill-posed problem, which further amplifies this error leading to image artifacts and inaccuracy in quantifying the physiological parameters of the tissue. The current method illustrated here reduces the noise in recovery of chromophores, especially significant in water and scattering, by eliminating the need to reconstruct the absorption and scattering coefficients as intermediate endpoints. Instead, the chromophore concentrations and scatter parameters are reconstructed directly by incorporating the known linear spectral fit and scattering relationship with wavelength as constraints.

The method uses finite elements to model the diffusion equation and reconstructs images of five parameters: oxyhemoglobin (HbO), hemoglobin (Hb), water (H2O), scatter amplitude (a) and scatter power (b), with no assumptions on scatter amplitude (a) or scatter power (b). The results of the application of spectral constraints, in addition to showing a reduction in noise in the recovered chromophore concentrations, also provide evidence of reduced sensitivity to noise in measurements themselves.

The direct spectral reconstruction method has been tested using simulation and phantoms studies. As an illustration here, it has been applied to clinical tomography data obtained from measurements on a 66 year old subject with a 5-10 mm spiculated mass from mammography, later diagnosed as Invasive Ductal Carcinoma. The subject underwent the NIR exam in accordance with the Dartmouth protocol, and written consent was obtained from the subject. The position of the anomaly was provided by mammography and found to be at 11:30 o'clock in the cranocaudal view. The tumor was known to be located about 1cm from surface; data was collected in three planes. Reconstructed images are shown in Figure 7, for the plane in line with the tumor. The localized increase in Hb_T was observable and the contrast available was 1.7:1.0 in tumor versus background. The S_tO_2 image showed a decrease at the location of the tumor, with a contrast of 0.7:1. The corresponding S_tO_2 image with the conventional technique (not shown here) was noisier, and a similar decrease was not observed. The water image showed heterogeneity in the range 25 to 50%, which is considerably smaller than the range of 0 to 100% observed with the old method. Tighter data ranges are similarly observed in the scatter images, and artifacts in the separate wavelength technique have been completely suppressed in the spectral approach.

Figure 7. Hb_T [mM], S_tO_2 [%], water [%], 'a' and 'b' images are shown from measurements on a cancer subject with a 5-10 mm Invasive Ductal Carcinoma at the 11:30 o-clock position.

In summary, the new direct spectral reconstruction technique has been applied to homogeneous and heterogeneous data and the results have consistently shown reduced artifacts as well as improved quantitative accuracy in recovered parameters. With this new technique, higher hemoglobin content at site of tumor is observed in the clinical case, as well as lower oxygen saturation. The water and scattering images most significantly show improvement in all cases by reduction in the errors due to decreased artifacts.

Spectral and spatial a-priori information
The use of spatial a priori information was investigated during the first year of funding under this program. Namely, realistic breast phantoms were used to investigate the use of spatial information to constrain and penalize the reconstruction algorithm and have been shown to improve both the qualitative and quantitative accuracy of the reconstructed images.

The concept underpinning parametric or spectrally constrained imaging is the generation of a derived response from multi-spectral data [2-4]. Typically, images are formed serially, wavelength-by-wavelength, and do not impose connectivity between the image estimate at one wavelength with that of at another. By using a spectral model composed of certain wavelength-independent parameters, as in Figure 8, it becomes possible to combine multi-spectral data in a new way. Concepts of multi-spectral and spatially constrained image reconstruction have recently been extended to NIR which has reached the point of application

Figure 8. Absorption coefficients of various chromophores as a function of NIR wavelengths.

to experimental and clinical data. Specifically, multiple wavelengths NIR data have been used simultaneously to reconstruct absolute values of chromophore concentration (deoxy and oxygenated blood concentration and water) as well as scattering properties (scattering power (b) and amplitude (A)). Thus, instead of estimating the absorption and reduced scatter properties at each wavelength, independently and then using these values to derive specific chromophore concentrations and scattering parameters, the aim is to encode directly the linear map between wavelength-dependent optical properties and chromophore concentrations through their known spectral signatures. This leads to a single reconstruction to estimate all of the final images simultaneously and has shown to offer the advantage of reducing image sensitivity to noise at specific (individual) wavelengths, especially in the water and oxygen saturation distributions [5, 6].
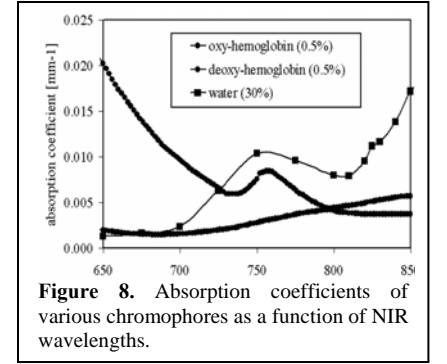
Image reconstruction using spectral and spatial a-priori information
The inverse problem being ill-posed, as often is the approach, we seek to minimize the least squares functional

$$\chi^2 = \sum_{j=1}^{M} \left(\phi_j^m - \phi_j^c\right)^2 \tag{1}$$

where M is the total number of measurements at each wavelength, and ϕ_j^m and ϕ_j^c are the measured and calculated fluence at the boundary for each measurement point j. The minimization in Equation (1) is carried out by applying a Newton-Raphson iterative method where the boundary data is calculated at a sufficiently close set of initial optical properties, along with the Levenberg Marquardt regularization for stabilizing the inversion. The inversion is given by the matrix equation

$$\partial\mu = \left(J^T J + \alpha I\right)^{-1} J^T \partial\phi \tag{2}$$

where J is the Jacobian containing the derivatives of ϕ with respect to the optical properties μ given by (μ_a, κ), where μ_a is the absorption coefficient in mm^{-1} and κ is the diffusion coefficient ($\kappa=1/3(\mu_a+\mu_s')$ in mm), and μ_s' is the reduced scattering coefficient in mm^{-1}. α governs the regularization or smoothness applied to the problem which balances data errors due to noise. Solving Equation

(2) using $\partial\phi = \left(\phi^m - \phi_k^{\ c}\right)$, we obtain a new search direction for the solution for the kth iteration μ_k from $\delta\mu$, our measure of convergence being χ^2 less than 2% of that of the previous iteration.

Solving the inverse problem in this manner, absorption and reduced scattering coefficient images at six wavelengths are obtained and this is followed by a least squares fit to Beer's law, $\mu_a = [\varepsilon]c$, where ε is the molar absorption spectra of the absorbing tissue chromophores, in our case, oxy-hemoglobin (HbO$_2$), deoxy-hemoglobin (Hb), and water, and c is their concentrations (dimensions of $3 \times N$, where N = number of unknowns within the model, i.e. nodes). Similarly, for scattering the approximation to Mie theory $\mu_s^{\ /} = A\lambda^{-b}$ is used to derive images of scatter amplitude (A) and scatter power (b), where λ is the wavelength in microns. Both variables A and b are vectors of length $N \times 1$.

In order to implement these spectral relationships into the reconstruction directly, the least squares functional is modified to be

$$\chi^2 = \sum_{j=1}^{Mn} \left(\phi_j^m - \phi_j^c\right)^2 \tag{3}$$

so that j now includes all wavelength measurements (Mn), where n is the number of wavelengths available (6 in our case). The Newton method then gives a different relationship, which for each wavelength is represented by

$$\partial\phi_\lambda = J_{c,\lambda}\delta c + J_{A,\lambda}\delta A + J_{b,\lambda}\delta b \tag{4}$$

where $J_{c,\lambda}$, $J_{A,\lambda}$ and $J_{b,\lambda}$ represent the Jacobians for each of the chromophore and scattering parameters. The relationships between these Jacobians and $J_{\mu_a} = \dfrac{\partial\phi}{\partial\mu_a}$ and $J_\kappa = \dfrac{\partial\phi}{\partial\kappa}$ calculated before have been derived in [6] and Equation (2) is suitably modified so that the update in chromophores ∂c occurs directly:

$$\partial c = \left(\tilde{J}^T\tilde{J} + \alpha I\right)^{-1}\tilde{J}^T\partial\phi \tag{5}$$

where

$$\partial\phi = \left(\phi^{m,\lambda} - \phi_k^{c,\lambda}\right)_{\lambda=1:n} \tag{6}$$

and

$$\tilde{J} = \left[J_{c,\lambda}, J_{A,\lambda}, J_{b,\lambda}\right]_{\lambda=1:n} \tag{7}$$

In order to add the spatial constraint to this further, the minimization functional is modified to include a penalty term for *a priori* information of tissue structure, given by:
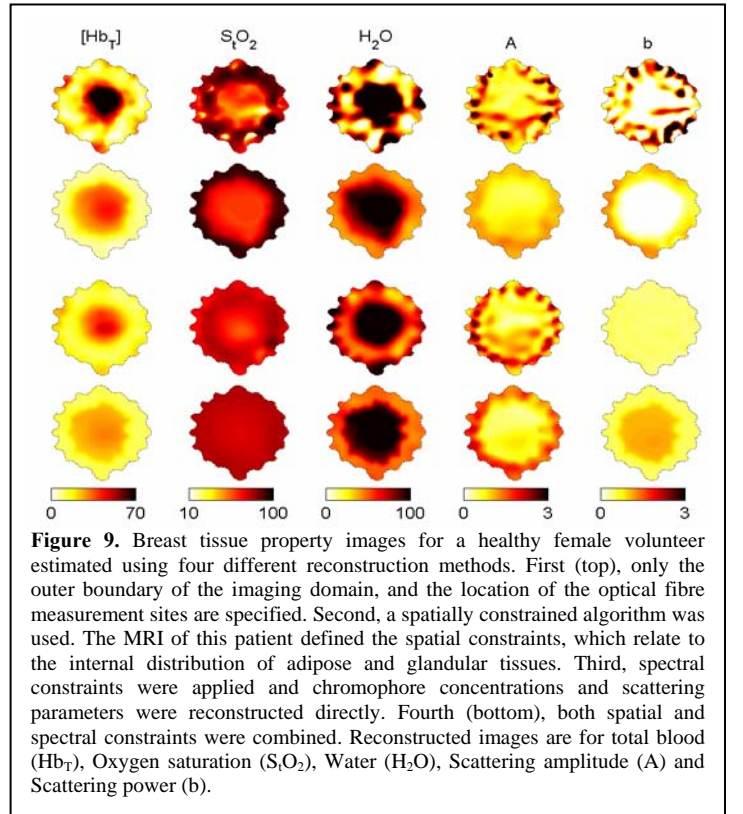
$$\chi^2 = \sum_{j=1}^{Mn}\left(\phi_j^m - \phi_j^c\right)^2 + \beta\sum_{j=1}^{Mn}L(\mu_j - \mu_{o,j})^2 \tag{8}$$

where β is the regularizing term for spatial prior and L is a matrix generated using MRI-derived spatial information, acting on the solution μ. This matrix links all the nodes in a particular type tissue (glandular or fatty) so that a second differential operator is approximated within each region. This is similar to total variation minimization approach allowing sharp boundaries to exist, while providing flexibility to encode these boundaries from MRI information. Each node in the FEM mesh is labeled according to the region, or tissue type, with which it is associated (in the MR image). For the ith node in region R, $L_{i,i}=1$. When nodes i and j are in the same region, $L_{i,j}= -1/n$, where n is the total number nodes within region R, otherwise $L_{i,j}=0$. Applied with the spectral prior, the final matrix equation is

$$\partial c = \left(\tilde{J}^T\tilde{J} + \alpha I + \beta L^T L\right)^{-1}\tilde{J}^T\partial\phi \tag{9}$$

The values for α, β have been chosen empirically to be 10 through simulations and experiments.

A combined NIR-MRI imaging system has been used [3, 4] in a case study to estimate the properties of healthy breast tissue, Figure 9. The images obtained for the NIR parameters using an unconstrained reconstruction shows noisy images with boundary artifacts. The spatial priors act on these images, making them

Figure 9. Breast tissue property images for a healthy female volunteer estimated using four different reconstruction methods. First (top), only the outer boundary of the imaging domain, and the location of the optical fibre measurement sites are specified. Second, a spatially constrained algorithm was used. The MRI of this patient defined the spatial constraints, which relate to the internal distribution of adipose and glandular tissues. Third, spectral constraints were applied and chromophore concentrations and scattering parameters were reconstructed directly. Fourth (bottom), both spatial and spectral constraints were combined. Reconstructed images are for total blood (Hb$_T$), Oxygen saturation (S$_t$O$_2$), Water (H$_2$O), Scattering amplitude (A) and Scattering power (b).

smoother, but preserving the trend for the quantification. For example, the scatter power shows a reduction in the glandular tissue (row 2) similar to the values obtained in the no-priors reconstruction (row 1). However, previous studies have indicated that, glandular tissue having higher number density of scatterers, may actually have higher values for scatter power, than fatty tissue. Hence, the results from spatially constrained reconstruction, while appearing smoother, may be misleading. The scatter power image obtained by application of the spectrally constrained method is more quantitatively acceptable and the spatial priors acting on this spectral method gives the most intuitively acceptable image for this parameter, showing the layered structure of the breast tissue. We observed elevated [Hb$_T$] (25:13 μM), water (91:49 %), and scattering power (1.0:0.5) in glandular tissue relative to adipose tissue using the combined priors, which matches the higher vascularization in the glandular tissue.

The results so far show that, while anatomical information improves the image quality resulting in reduced artifacts, it may not significantly improve quantification. The spectral prior obtained using the intrinsic behavior of tissue chromophores and scattering in the near infrared wavelength regime plays a more important role in addressing this problem, and finally, a synergy between these two priors yields the most accurate characterization of breast tissue properties currently possible.

Effect of Refractive Index variation

Previous studies [7] reported results in modeling the effect of Refractive Index (RI) on the forward model. In the results obtained during this funding period, the initiative was advanced to investigating the effect of RI variation on NIR image reconstruction, by assuming either correct knowledge of the RI of each tissue or applying a homogenous value throughout the model. The study showed that providing the RI of the glandular tissue is not far from the value of adipose tissue, it has little effect on the qualitative and quantitative accuracy of the results, as demonstrated in Figure 10. Assuming the RI of the whole breast is similar, for example, the RI is 1.455 for adipose and 1.4 for glandular tissue, reconstructed images of absorption and scatter can be obtained which ignore the effect of RI with modest degradation in the recovery of information about an abnormality. However, it is also important to note that this analysis was completed under the assumption that the abnormality (i.e. tumor) has the same RI as its background tissue and is most typically located in the fibroglandular tissue. Further studies are required to establish the RI variation for different types of tumors and to investigate how such variations might alter NIR tomography. The absolute values of RI for breast tissue types are still a subject under investigation. Estimates are difficult to obtain accurately in-vivo, but some data has been reported for various tissue types [8, 9]. Although adipose tissue (fatty layer) has been measured to be 1.455, no results exist for fibro-glandular tissue. Nonetheless the RI of glandular tissue is believed to be lower than that of adipose (e.g. values of 1.4 have been assumed in [8, 10]). The rationale for a lower value is sound in that estimates of the composition of fibroglandular tissue place its water (typically over 60%) and blood content (over 1%) to be high, indicating that its bulk refractive index is likely close to that of water [11, 12].
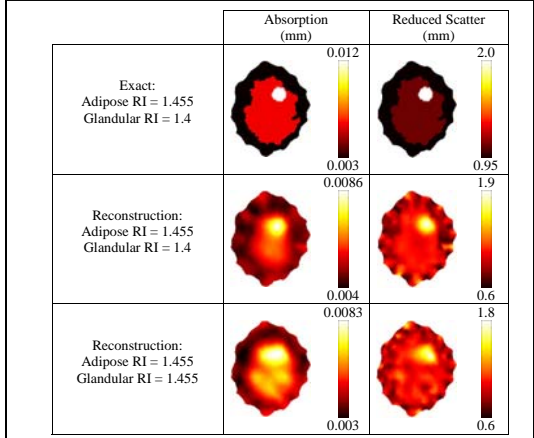
Figure 10. Images reconstructed using a model with refractive index variation. Top row shows the exact optical properties where adipose and glandular tissue have different optical properties and different refractive index (RI) of 1.455 and 1.4, respectively. Middle row shows reconstructed images assuming the correct RI distribution. Bottom row shows reconstructed images assuming a homogenous RI of 1.455.

Breast deformation modeling

In order to obtain good NIR data measurements it is essential to have good contact between the optical fibers and the breast which in-turn results in the deformation of the breast, Figure 11, due to the soft plasticity of the tissue. A tissue deformation model of the female breast has been developed that will account for the altered shape of the breast during clinical NIR measurements, Figure 12. Using a deformed model of a breast, NIR data was used to reconstruct
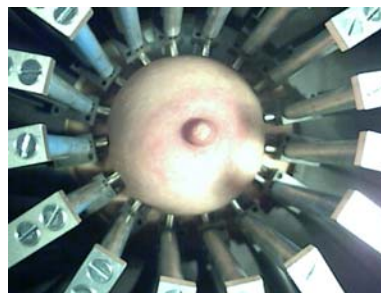
Figure 11. Photo of the breast being compressed by the optical fibers to ensure good contact for data collection.
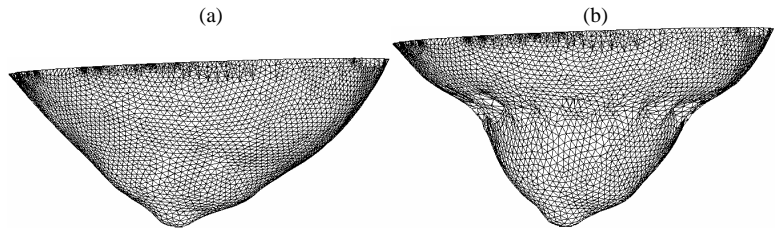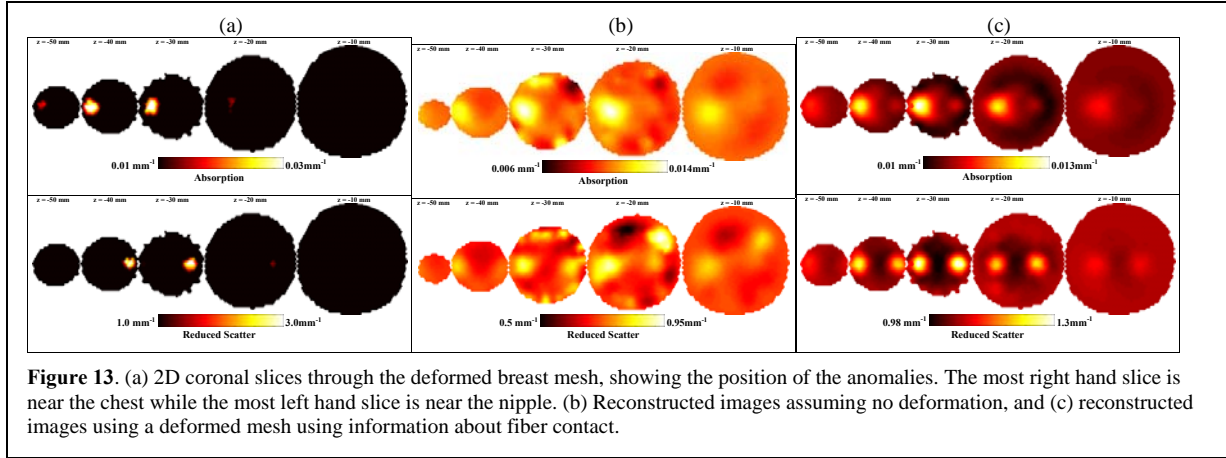
Figure 12. Volume mesh of (a) the normal suspended breast and (b) the deformed mesh after the application of the optical fiber array.

images of tissue absorption and reduced scatter using assumptions about the imaging domain, Figure 13 [13].

Assuming a non-deformed breast shape for image reconstruction has shown to lead to poor quality images since the geometry of the breast is greatly altered, whereas using the correct deformed geometry produces the best images. The goal of this work was to incorporate this new model of breast deformation with more accurate information regarding the mechanical properties of the breast to improve the NIR image reconstruction. The mechanical property information is readily available from other imaging modalities, and

the synthesis of this information may provide fundamentally new information about breast physiologic response to pressure, and/or breast pathology response to pressure. An accurate model of breast deformation should in principle allow us to create patient specific models and meshes, which would in-turn provide more clinically useful data.

Figure 13. (a) 2D coronal slices through the deformed breast mesh, showing the position of the anomalies. The most right hand slice is near the chest while the most left hand slice is near the nipple. (b) Reconstructed images assuming no deformation, and (c) reconstructed images using a deformed mesh using information about fiber contact.

Fluorescence Tomography: Numerical Modeling and Image reconstruction

As part of this project we have also developed a Finite Element Model of simulating of light propagation and image reconstruction in Fluorescence optical diffuse tomography. In Fluorescence tomography the use of exogenous fluorescence agents has the potential to improve the contrast as well as providing preferential accumulation of the agent in diseased tissue. Furthermore the agent may have different decay properties in diseased tissue which maybe useful to localize tumors independently of fluorophore concentration. Another advantage of using such agents is that diagnostic agents can be tuned so that they selectively target receptors specific to cancer cells. In this technique, after the introduction of agents into the imaging domain, light is launched into the tissue at the excitation wavelength of the fluorophore (in a tomographic manner, same as NIR tomography), and the exiting photons at both the excitation and emission (those emitted by the fluorophore) wavelength are measured. The reconstruction algorithm is then used for the reconstruction of fluorescence yield and lifetime, as well as the absorption and reduced scatter coefficient in turbid media. The forward problem in a tissue like medium (highly scattering), i.e. that of prediction photon propagation in the medium can be described using two coupled diffusion equations:

$$-\nabla \cdot D_x(r)\nabla\Phi_x(r,\omega) + (\mu_{ax} + \frac{i\omega}{c})\Phi_x(r,\omega) = q_0(r,\omega) \tag{10}$$

$$-\nabla \cdot D_m(r)\nabla\Phi_m(r,\omega) + (\mu_{am} + \frac{i\omega}{c})\Phi_m(r,\omega) = \Phi_x(r,\omega)\eta\mu_{af}(r)\frac{1 - j\omega\tau(r)}{1 + [\omega\tau(r)]^2} \tag{11}$$

where subscript x and m defined either the excitation or emission field respectively, μ_a and μ_s` are the absorption and reduced scatter coefficients, μ_{af} is the fluorophore absorption coefficient (dependant on its concentration) and η and τ are the fluorophore quantum efficiency and lifetime, respectively. For image reconstruction, most commonly, one uses the excitation wavelength tomographic data together with equation (10) to reconstruct the absorption and scattering coefficient. Using this reconstructed data, it is often valid to assume that the emission absorption and scattering values are the same as those at the excitation wavelength. The fluorophore properties then can be reconstructed using these data and equation (11). As an example, consider a complex multi-layered model shown in Figure 14(a). Here forward data was generated using equations (10) and (11) for the emission and excitation wavelength. After adding 1% noise to the data, to more realistically simulate experimental measurements, images of absorption and reduced scatter, as well as lifetime and fluorescence yield ($\eta\mu_{af}$) were reconstructed. These results, although preliminary, indicate the feasibilities of fluorescence imaging and will provide a good basis for implementation of Bioluminescence Tomography.
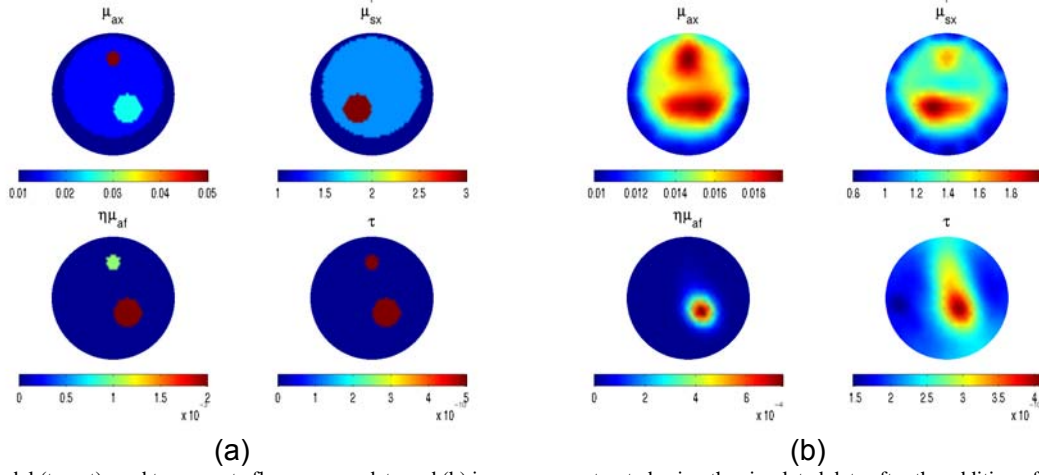
Figure 14. (a) The model (target) used to generate fluorescence data and (b) images reconstructed using the simulated data after the addition of 1% noise. In (a) both absorber and scattering objects are shown, with the scattering object not co-located, but with the absorbing objects co-located with fluorescent objects, as might typically be encountered in tumors. The reconstructed images of absorption and scattering illustrate the typically good accuracy and resolution that can be achieved, despite this being a highly ill-posed problem. The fluorescence images recovered in (b) are not perfect, but have excellent spatial resolution and are well-representative of the dominant fluorophore distributions in (a).

Contrast-detail analysis in fluorescence tomography image reconstruction

Contrast-detail analysis were used to evaluate the imaging performance of diffuse optical fluorescence tomography (DOFT), characterizing spatial resolution limits, signal-to-noise limits, and the trade-off between object contrast and size. Reconstructed images of fluorescence yield from simulated noisy data were used to determine the contrast-to-noise ratio (CNR). The results provide a best-case analysis for imaging tissue containing fluorophore in vivo with this algorithm.
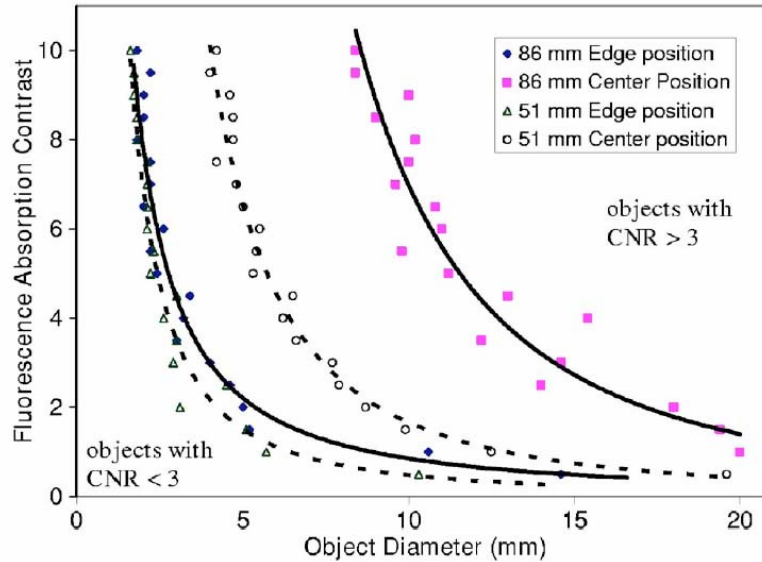

Figure 15 Contrast-detail curve showing the CNR of 3 to approximate limits of detectable contrast and diameter for two anomaly positions in 51-mm (dashed lines) and 86-mm (solid lines) diameter test fields. In this analysis, objects above and to the right of each line are in the region where CNR>3 and "detection" is considered possible.

Simulated data was generated by solving the model system using typical tissue optical property parameters of μ_a=0.01 mm^{-1} and μ_s'=1.0 mm^{-1}, and extracting the boundary data at each simulated detector position. To compare the influence of domain size on contrast-detail characteristics, two circular test fields were used; one 51 mm in diameter and the other 86 mm in diameter. The smaller test field approximates a domain expected to be encountered in small animal imaging and the 86-mm test field mimics larger imaging fields such as a human breast. Each test field was simulated as a 10,000-node circular mesh circumscribed by 16 source/detector fiber positions and used to generate 240 data points, matching our experimental fluorescence tomography design. The system is similar to our automated tomography system currently in clinical trials. Random noise was added to each transmission data point with 1% mean error.

The contrast-detail results for a threshold limit of CNR =3 are plotted in Figure 15 for two test fields and object positions. Objects that are recovered with greater than CNR =3 have contrast-detail characteristics that are above and to the right of the line shown in Figure 15, while those below and to he left are too small or have too little contrast to be recovered with CNR>3 in the image. Accordingly, the limiting diameter for an object near the edge of the field is approximately 1.7 mm for both test field diameters. There seems to be

12

little influence of test field diameter on CNR limits for high contrast objects near the edge. Above an object contrast of about 8, the continued decrease in the minimum size for CNR=3 is very small with increasing contrast, indicating that this size is a fundamental limit of the imaging algorithm for this geometry. It does not appear that the fundamental limits have been reached for objects near the center of either test field for the contrast range studied and expected to be encountered experimentally. Furthermore, CNR value of objects near the center is strongly influenced by the test field size. For a 51-mm test object, the limiting diameter is approximately 4 mm, for the maximum object contrast (10). This increases to approximately 8.5 mm for the larger test field. These results indicate the dramatic decrease in sensitivity for objects deeper in the test field.

A number of factors will increase the contrast and size required to detect an anomaly in an experimental or clinical setting, thus shifting the contrast-detail curves up and to the right, including: (1) reconstruction of unknown intrinsic optical properties; (2) heterogeneity of optical properties and fluorophore distribution; (3) excitation cross-talk in the fluorescence signal;

Measured normal breast tissue properties

The MRI-guided spectral NIR reconstruction technique discussed above has been applied to 11 clinical cases and the cumulative results are shown in Table 2 for all subjects imaged along with the standard deviation and total range. All parameters lie within, or overlap the ranges of bulk average breast properties measured in previous studies, [11, 12, 14, 15] which uniformly report large inter-subject variations in estimated NIR parameters. Based upon the reported standard deviations between subjects, scattering power shows the highest relative variability (61% in glandular tissue), and hemoglobin oxygen saturation shows the lowest (8% in adipose tissue). Glandular tissue NIR parameters are thought to vary with the menstrual cycle more than those for adipose tissue. Chromophore concentration inter-subject variations were not significantly different between glandular and adipose tissue (Table 2). This could be attributed to the small population of subjects imaged.

The differences between the optically relevant parameters of the two different tissue types in the images were analyzed. Table 3 shows that hemoglobin oxygen saturation, S_tO_2, is the only parameter not significantly different in adipose versus glandular tissue for these 11 exams. Glandular tissue shows elevated values of all other parameters relative to adipose tissue. These trends match several expectations based upon physiology, as glandular tissue is know to contain more blood vessels than adipose tissue, and to have a greater blood supply and water content[16]. The connection between physiology and NIR scattering parameters A and Scatter Power (SP) less obvious to interpret. However an ex vivo validation of this is provided by Peters et al [17] who measured the scattering spectrum of excised glandular and adipose tissue in the near infrared wavelength range and observed a higher scattering power in glandular tissues. It is likely that scattering amplitude and power are surrogate measures of particle density and size, respectively, but this is an area of ongoing research.

Property	Adipose tissue		Glandular tissue	
	Mean ± SD	Total range	Mean ± SD	Total range
Hb_T concentration	17.1 ± 3.2 μM	11.7-22.9 μM	22.4 ± 7.3 μM	9.8-35.6 μM
S_tO_2	70.7 ± 8.6 %	51.8-77.4 %	69.7 ± 10.4 %	38.8-80.2 %
Water fraction	46.8 ± 18.5 %	23.0-78.5 %	60.3 ± 23.6 %	17.5-93.5 %
A	1.34 ± 0.54	0.86-2.77	0.94 ± 0.38	0.32-1.79
SP	0.56 ± 0.32	0.00-0.94	0.79 ± 0.48	0.00-1.36

Table 2. The average values, standard deviations, and total ranges observed for total hemoglobin concentration, hemoglobin oxygen saturation, water fraction, scattering amplitude, and scattering power of adipose and glandular tissue.

	Adipose vs Glandular (n=11)	Scattered (n= 6) vs Dense (n= 5)	
		Adipose	Glandular
	Mean Diff. (p-value)	Mean Diff. (p-value)	Mean Diff. (p-value)
$[Hb_T]$	0.022*	0.902	0.009*
StO_2	0.798	0.166	0.170
Water	0.040*	0.769	0.068
A	0.005*	0.673	0.579
SP	0.045*	0.324	0.892

Table 3. Paired t-test p-values indicating differences between NIR derived properties associated with (left) different tissue types, (center) adipose tissue in women with different radiographic densities, and (right) glandular tissue in women with different densities.

Characterization of Breast Tumors In Vivo

Multi-wavelength Near-Infrared (NIR) Tomography was utilized to non-invasively quantify physiological parameters of breast tumors using direct spectral reconstruction. Images of total hemoglobin, oxygen saturation, water, and scatter parameters were obtained with higher accuracy than previously reported. Using this spectral approach, in vivo NIR images were used and interpreted through a series of case studies (n=6 subjects) having differing abnormalities. The corresponding mammograms and ultrasound images were also evaluated. Three of six cases were malignant (infiltrating ductal carcinomas) and showed higher hemoglobin (34-86% increase), a reduction in oxygen saturation, an increase in water content as well as scatter changes relative to surrounding normal tissue. Three of

six cases were benign, two of which were diagnosed with fibrocystic disease and showed a dominant contrast in water, consistent with fluid filled cysts. Scatter amplitude was the main source of contrast in the volunteer with the benign condition fibrosis, which typically contains denser collagen tissue. The changes monitored correspond to physiological changes associated with angiogenesis, hypoxia and cell proliferation anticipated in cancers. These changes represent potential diagnostic indicators, which can be assessed to characterize breast tumors.

Key research accomplishments

1. Assuming that the effect of the refractive index (RI) variation in breast tissue is small, such that if ignored, the errors obtained within reconstructed images are minimal. This in reality is acceptable, given that the variation in RI of tissue within the breast is small, ranging from 1.4 to 1.455.
2. The effect of breast deformation tissue to optical fiber contact has been investigated. It is shown that if the deformation is large, adequate priori knowledge about the shape of the breast is essential for useful clinical images. Such information can either be obtained using mechanical models (as demonstrated) or using a-priori structural images from for example MRI.
3. Spectral and spatial priori constrains have been developed and implemented to show improved accuracy in clinical information about reconstructed images. It is shown that incorporation of both such information significantly improves both qualitative and quantitative accuracy of images.
4. To date, spectral constraints have been used to analyze clinical data. It has been demonstrated that addition of such constraints can significantly improve the clinical accuracy of physiological data obtained from clinical cases.
5. A set of normal subjects have been imaged using a dual modality multi-spectral imaging technique that has enabled the definition of a set of normal values for breast tissue.
6. A small set of patients presenting varying abnormalities were imaged and pathophysiology of the imaged abnormalities were quantified.
7. A modeling and image reconstruction algorithm has been developed that allows the reconstruction of fluorescent markers within tissue, giving rise to a-priori information regarding tumor location as well as physiological function of the tissue.

Reportable outcomes

The funding of this project has led to a number of peer reviews publications as well as oral presentation at international conferences. Links and collaborations have been established with Washington University at St. Louis who are now routinely using the developed code. Further collaboration has been established with University of Pennsylvania through the development of alternative image reconstruction algorithms allowing the use of large datasets. Reportable outcomes include:
1. Oral presentation at the Optical Society of America (OSA) international meeting in 2004
2. Oral presentation at the International Society for Optical Engineering international meeting in 2005
3. Applied for funding from NCI through R01 mechanism (PI Hamid Dehghani, "Breast Deformation Modeling for Near Infrared Tomography" 3 year project)
4. Applied for funding from DoD through the IDEA award mechanism (PI Hamid Dehghani, "Neoadjuvant Therapy Treatment monitoring using CT Guided Optical Tomography" 3 year project)
5. Filed patent for spectral Near Infrared optical imaging (Title: TOMOGRAPHY SYSTEMS AND METHODS USING SPECTRAL DERIVATIVE IMAGE RECONSTRUCTION)

Conclusions

In conclusion, throughout the progress and the funded period of this project, much has been achieved that has progressed the field of NIR optical tomography, specifically in the area of detection and characterization of breast cancer. For each of specific aims, goals have been met, and these can be finalized as:
1. <u>Validate, improve and accelerate a three-dimensional finite element model of light propagation within the breast tissue as well as the image reconstruction algorithm for simultaneously calculating the internal absorption and scattering coefficients.</u>
   This aim has been thoroughly investigated throughout numerous phantom experiments and image reconstruction development. Furthermore, we have achieved the utilization of spectral imaging techniques and this has surpassed much of the original aims. Specifically, it has allowed a fast, more computationally efficient method of calculating tissue properties, reducing image noise artifacts and overall increasing the quantitative and qualitative accuracy of the imaging method.

2. <u>Investigate the benefits and limits of using a-priori information from dual modality images, for example, MRI and Near Infrared data.</u>
   The use of spatial structural information has been a topic of much investigation within this program. With the development of a dual modality MRI-NIR system, it has been possible to validate the modeling techniques once again. The use of novel NIR phantoms allowed a careful investigation of different image reconstruction algorithms and a robust method based on a differential operator was implemented. Through this method, optical images of healthy volunteers has enabled the measurement of normal healthy optical properties of tissue.

3. Explore the benefits and limits of using Fluorescent contrast-agents, which will target specific molecular markers of the tumor, giving rise to a-priori information regarding tumor location as well as physiological function of the tissue.

Later during the funded period, an image reconstruction algorithm based upon the idea of fluorescence imaging has been developed and tested using measured from collaborators. This method was then used to calculate the Contract Noise Ratio of the imaging technique to allow a better understanding of the advantages of this imaging method for detection and characterization of breast cancer.

4. Test the developed algorithm on patient data and compare results with available mammograms and biopsy results to evaluate algorithm accuracy.

Finally, images of both healthy and diseased breast were used to understand breast tissue physiology and also enable the understanding of cancer pathology. These techniques are now firmly in place and are routinely used with Dartmouth's NIR optical imaging facilities.

References

1. Dehghani, H., et al., *Multiwavelength Three-Dimensional Near-Infrared Tomography of the Breast: Initial Simulation, Phantom, and Clinical Results.* Applied Optics, 2003. **42**(1): p. 135-145.
2. Xu, H., Springett, R., Dehghani, H., Pogue, B.W., Paulsen, K.D., and Dunn, J.F., *MRI coupled Broadband Near Infrared Tomography System for Small Animal Brain Studies.* Appl. Opt., 2005. **44**(11): p. 2177-2188.
3. Brooksby, B., Jiang, S., Dehghani, H., Pogue, B. W., Paulsen, K. D., Weaver, J., Kogel, C., and Poplack, S. P., *Combining near infrared tomography and magnetic resonance imaging to study in vivo breast tissue: implementation of a Laplacian-type regularization to incorporate magentic reasonance structure.* JBO, 2005. **10**(5).
4. Brooksby, B., Jiang, S., Kogel, C., Doyley, M., Dehghani, H., Weaver, J. B., Poplack, S. P., Pogue, B. W., Paulsen, K. D., *Magnetic Resonance-Guided Near-Infrared Tomography of the Breast.* Rev. Sci. Instrum., 2004. **75**(12).
5. Brooksby, B., Srinivasan, S., Jiang, S., Dehghani, H., Pogue, B.W., Paulsen, K.D., Weaver, J., Kogel, C., and Poplack, S.P., *Spectral-prior information improves Near-Infrared diffuse tomography more than spatial-prior.* Optics letters, 2005. **30**(15): p. 1968-1970.
6. Srinivasan, S., Pogue, B. W., Jiang, S., Dehghani, H., and Paulsen, K. D., *Spectrally Constrained Chromophore and Scattering NIR Tomography Provides Quantitative and Robust Reconstruction.* Appl. Opt., 2005. **44**(10): p. 1858-1869.
7. Dehghani, H., Brooksby, B., Vishwanath, K., Pogue, B. W., Paulsen K. D., *The effects of internal refractive index variation in near infrared optical tomography: A finite element modeling approach.* Phys. Med. Biol., 2003. **48**: p. 2713-2727.
8. Bolin, F.P., Preuss, L. E., Taylor, R. C., Ference, R. J, *Refractive index of some mammalian tissue using a fiber optic cladding method.* Applied Optics, 1989. **28**(12): p. 2297-2303.
9. Brooksby, B., Dehghani, H., Vishwanath, K., Pogue, B. W., Paulsen, K. D., *Internal refractive index changes affect light transport in tissue.* proceedings of spie, 2003. **4955**: p. 296-304.
10. Tromberg, B.J., Coquoz, O., Fishkin, J. B., Pham, T., Anderson, E. R., Butler, J., Cahn, M., Gross, J. D., Venugopalan, V., Pham, D., *Non-invasive measurements of breast tissue optical properties using frequency-domain photon migration.* Phil. Trans. R. Soc. Lond. B, 1997. **352**: p. 661-668.
11. Srinivasan, S., Pogue, B. W., Jiang, S., Dehghani, H., Kogel, C., Soho, S., Gibson, J. J., Tosteson, T. D., Poplack, S. P., Paulsen, K. D., *Interpreting Hemoglobin and Water Concentration, Oxygen Saturation and Scattering Measured In Vivo by Near-Infrared Breast Tomography.* PNAS, 2003. **100**(21): p. 12349-12354.
12. Pogue, B.W., Jiang, S., Dehghani, H., Kogel, C., Soho, S., Srinivasan, S., Song, X., Poplack, S. P., Paulsen, K. D., *Characterization of Hemoglobin, Water and NIR Scattering in Breast Tissue: Analysis of inter-subject variability and menstrual cycle changes relative to lesions.* JBO, 2004. **9**(3): p. 541-552.
13. Dehghani, H., Doyley, M. M., Pogue, B. W., Jiang, S., Geng, J., and Paulsen, K. D., *Breast deformation modeling for image reconstruction in near infrared optical tomography.* phys. med. biol, 2004. **49**(7): p. 1131-1146.
14. Cerussi, A.E., et al., *Sources of absorption and scattering contrast for near-infrared optical mammography.* Academic Radiology, 2001. **8**(3): p. 211-8.
15. Shah, N., et al., *Noninvasive functional optical spectroscopy of human breast tissue.* Proceedings of the National Academy of Sciences of the United States of America, 2001. **98**(8): p. 4420-5.
16. Thomsen, S.T., D., *Physiological and Pathological Factors of Human Breast Disease That Can Influence Optical Diagnosis.* Annals of the New York Academy of Sciences, 1998. **838**: p. 171-193.
17. Peters, V.G., Wyman, D. R., Patterson, M. S., Frank G. L., *Optical properties of normal and diseased breast tissue in the visible and near infrared.* Phys. Med. Biol., 1990. **35**: p. 1317-1334.

Publications List

S. Srinivasan, B. W. Pogue, S. Jiang, **H. Dehghani**, C. Kogel, S. Soho, J. J. Gibson, T. D. Tosteson, S. P. Poplack, K. D. Paulsen, "*Interpreting Hemoglobin and Water Concentration, Oxygen Saturation and Scattering Measured In Vivo by Near-Infrared Breast Tomography*" PNAS vol 100 no 21 pp 12349-12354 2003

X. Song, B. W. Pogue, s. Jiang, M. M. Doyley, **H. Dehghani**, T. D. Tosteson, K. D. Paulsen, "*Automated Region Detection Based Upon Contrast To Noise Ratio in Near-Infrared Tomography,*" Applied Optics 43(5) 1053-1062, 2004

H. Dehghani, M. M. Doyley, B. W. Pogue, S. Jiang, J. Geng and K. D. Paulsen, "*Breast deformation modeling for image reconstruction in near infrared optical tomography*" Phys. Med. Biol. Volume 49, Number 7, pp 1131-1146 2004.

S. Srinivasan, B. W. Pogue, **H. Dehghani**, S. Jiang, X. Song and K. D. Paulsen, "*Improved Quantification of Small Objects in Near-Infrared Diffuse Optical Tomography* JBO 9(6) 1161-1171 2004

B. W. Pogue, S. Jiang, **H. Dehghani**, C. Kogel, S. Soho, S. Srinivasan, X. Song, S. P. Poplack, and K. D. Paulsen, "*Characterization of Hemoglobin, Water and NIR Scattering in Breast Tissue: Analysis of inter-subject variability and menstrual cycle changes relative to lesions*" JBO, 9(3) 541-552, 2004.

Ben Brooksby, Shudong Jiang, Christine Kogel, Marvin Doyley, **Hamid Dehghani**, John B Weaver, Steven P Poplack, Brian W Pogue and Keith D Paulsen, "*Magnetic Resonance Guided Near Infrared Tomography of the Breast*", Rev. Sci. Inst. 75 5262-5270 2004

Heng Xu, Brian W. Pogue, **Hamid Dehghani**, Keith D. Paulsen, Roger Springett and Jeff F. Dunn, "*Absorption and scattering imaging of tissue with steady-state second-differential spectral-analysis tomography*" Optics letters 29(17) 2043-2045 2004

Hamid Dehghani, Nirmal Soni, Ryan Halter, Alex Hartov and Keith D Paulsen, "*Excitation patterns in three-dimensional electrical impedance tomography*" Physiol. Meas. 26 S185-S197 2005

Heng Xu, Roger Springett, **Hamid Dehghani**, Brian W Pogue, Keith D Paulsen and Jeff F Dunn, "*MRI coupled Broadband Near Infrared Tomography System for Small Animal Brain Studies*", Applied Optics 44(11) 2177-2188 2005

Hamid Dehghani, Ben Brooksby, Brian W Pogue and Keith D Paulsen, "*Effect of Refractive Index on Near Infrared Tomography of the Breast*" Applied Optics 44(10) 1870-1878, 2005

Subhadra Srinivasan, Brian W Pogue, Shudong Jiang, **Hamid Dehghani** and Keith D Paulsen, "*Spectrally Constrained Chromophore and Scattering NIR Tomography Improved Quantification and Robustness of Reconstruction*", Applied Optics 44(10) 1858-1869, 2005

Ben Brooksby, Shudong Jiang, **Hamid Dehghani**, Brian W. Pogue, Keith D. Paulsen, "*Combining near infrared tomography and magnetic resonance imaging to study in vivo breast tissue: implementation of a Laplacian-type regularization to incorporate MR structure*" JBO 2005 Accepted

Ben Brooksby, Subhadra Srinivasan, Shudong Jiang, **Hamid Dehghani**, Brian W. Pogue, Keith D. Paulsen, John Weaver, Christine Kogel and Steven P. Poplack, "*Spectral-prior information improves Near-Infrared diffuse tomography more than spatial-prior*" Optic Letters 2005 Accepted

Subhadra Srinivasan, Brian W. Pogue, **Hamid Dehghani**, Shudong Jiang, Xiaomei Song, Keith D. Paulsen, "*Effect of image reconstruction bias upon spectroscopy-based quantification of chromophores in nearinfrared tomography*" In Biomedical Topical Meetings on CD-ROM (The Optical Society of America, Washington, DC) 2004.

Ben A. Brooksby, Shudong Jiang, Gordon Ehret, **Hamid Dehghani**, Brian W. Pogue, Keith D. Paulsen, "*Development of a system for simultaneous MRI and Near-infrared diffuse tomography to diagnose breast cancer* In Biomedical Topical Meetings on CD-ROM (The Optical Society of America, Washington, DC) 2004.

Heng Xu, **Hamid Dehghani**, Brian W. Pogue, Keith D. Paulsen, Roger Springett, Jeff F. Dunn, "*Optical tomography system based on second-differential spectroscopy for small animal brain study* In Biomedical Topical Meetings on CD-ROM (The Optical Society of America, Washington, DC) 2004.

Brian Pogue, Shudong Jiang, Subhadra Srinivasan, Xiaomei Song, **Hamid Dehghani**, Keith Paulsen, Tor Tosteson, Christine Kogel, Sandra Soho, Steven P. Poplack, "*Near-infrared scattering spectrum differences between benign and malignant breast tumors measured in vivo with diffuse tomography* In Biomedical Topical Meetings on CD-ROM (The Optical Society of America, Washington, DC) 2004.

Hamid Dehghani, Brian W. Pogue, Marvin M. Doyley, Jason Geng, Keith D. Paulsen, "*Breast deformation in near infrared optical tomography* In Biomedical Topical Meetings on CD-ROM (The Optical Society of America, Washington, DC) 2004

Ben Brooksby, Subhadra Srinivasan, Brian W Pogue, Shudong Jiang, **Hamid Dehghani**, Christine Kogel, John Weaver, Steven Poplack, Justin D Pearlman and Keith D Paulsen, "*Quantifying adipose and fibroglandular breast tissue properties using MRI-guided NIR tomography*", Proceedings of SPIE 5693, 2005

Phaneendra K Yalavarthy, **Hamid Dehghani**, Brian W Pogue and Keith D Paulsen, "*Measurement optimization for Near-Infrared optical tomography*", Proceedings of SPIE 5693, 2005

Subhadra Srinivasan, Brian W Pogue, Shudong Jiang, **Hamid Dehghani** and Keith D Paulsen, "*Spectrally Constrained NIR tomography for breast Imaging: Simulations and Clinical Results*", Proceedings of SPIE 5693, 2005

Hamid Dehghani, Ben Brooksby, Brian W Pogue and Keith D Paulsen, "*Effect of Refractive Index on Near Infrared Tomography of the Breast*" Applied Optics 44(10) 1870-1878, 2005

Subhadra Srinivasan, Brian W Pogue, Shudong Jiang, **Hamid Dehghani** and Keith D Paulsen, "*Spectrally Constrained Chromophore and Scattering NIR Tomography Improved Quantification and Robustness of Reconstruction*" Applied Optics 44(10) 1858-1869, 2005

Ben Brooksby, Shudong Jiang, **Hamid Dehghani**, Brian W. Pogue, Keith D. Paulsen, "*Combining near infrared tomography and magnetic resonance imaging to study in vivo breast tissue: implementation of a Laplacian-type regularization to incorporate MR structure*" JBO 10(5), 0515041-10 (2005).

Subhadra Srinivasan, Brian W. Pogue, Ben Brooksby, Shudong Jiang, **Hamid Dehghani**, Christine Kogel, Steven P. Poplack and Keith D. Paulsen, "*Near-Infrared Characterization of Breast Tumors In Vivo using Spectrally-Constrained Reconstruction*" Technology in Cancer Research & Treatment, 4(5), 513-526 (2005)

Scott C. Davis, Brian W. Pogue, **Hamid Dehghani** and Keith D. Paulsen, "*Contrast-detail analysis characterizing diffuse optical fluorescence tomography image reconstruction*" JBO letters 10(5), 050501-3 (2005)

Phaneendra K. Yalavarthy, Colin Carpenter, Shudong Jiang, **Hamid Dehghani**, Brian W. Pogue and Keith D. Paulsen, "*Incorproration of MR structural information in diffuse optical tomography using Helmholtz type regularization*" Biomedical Optics Topical Meeting on CD-ROM (The Optical Society of America, Washington, DC), March 19-22, (2006)

<u>Appendices</u>
Papers are included as appendices, which are as a direct result of the project funding:

Breast deformation modelling for image reconstruction in near infrared optical tomography

Hamid Dehghani[1]**, Marvin M Doyley**[2]**, Brian W Pogue**[1]**, Shudong Jiang**[1]**, Jason Geng**[3] **and Keith D Paulsen**[1]

[1] Thayer School of Engineering, Dartmouth College, Hanover, NH 03755, USA
[2] Department of Radiology, Dartmouth Medical School, Hanover, NH 03755, USA
[3] Genex Technologies Inc., 10605 Concord Street, Suite 500 Kensington, MD 20895-2504, USA

Abstract

Near infrared tomography (NIR) is a novel imaging technique that can be used to reconstruct tissue optical properties from measurements of light propagation through tissue. More specifically NIR measurements over a range of wavelengths can be used to obtain internal images of physiologic parameters and these images can be used to detect and characterize breast tumour. To obtain good NIR measurements, it is essential to have good contact between the optical fibres and the breast which in-turn results in the deformation of the breast due to the soft plasticity of the tissue. In this work, a tissue deformation model of the female breast is presented that will account for the altered shape of the breast during clinical NIR measurements. Using a deformed model of a breast, simulated NIR data were generated and used to reconstruct images of tissue absorption and reduced scatter using several assumptions about the imaging domain. Using either a circular or irregular 2D geometry for image reconstruction produces good localization of the absorbing anomaly, but it leads to degradation of the image quality. By modifying the assumptions about the imaging domain to a 3D conical model, with the correct diameter at the plane of NIR measurement, significantly improves the quality of reconstructed images and helps reduce image artefacts. Finally, assuming a non-deformed breast shape for image reconstruction is shown to lead to poor quality images since the geometry of the breast is greatly altered, whereas using the correct deformed geometry produces the best images.

(Some figures in this article are in colour only in the electronic version)

1. Introduction

Near infrared (NIR) tomography is an emerging alternative imaging method used to image physiologic parameters of biological tissue *in vivo* such as water and haemoglobin.

Measurements of light propagation (600–900 nm) within tissue can be used to map internal chromophore concentrations within tissue. Light is transmitted through tissue using multiple input and output locations on the surface of the region to be imaged, similar to a fan-beam x-ray computed tomography geometry, but using optical fibres for delivery and pick up of the light signals. The intensity and path-length distributions of the exiting photons provide information about the optical properties of the transilluminated tissue using a model-based interpretation where photon propagation is simulated by diffusion theory. Using these techniques implemented in hardware and software, NIR optical tomography becomes an inherently three-dimensional imaging method and is used to reconstruct physiologically relevant chromophore distributions from the region under investigation (Eda *et al* 1999, Fantini *et al* 1999, Boas *et al* 2001, Hebden *et al* 2001, Pogue *et al* 2001, McBride *et al* 2002, Dehghani *et al* 2003a, 2003b, 2003c). The main interest in this study lies in the ability to detect and characterize tumours within the female breast (Pogue *et al* 2001, Brooksby *et al* 2003). Since the absorption and scattering of light in tissue is a function of its optical properties, and hence its physiological state, the aim is to obtain images of internal optical absorption coefficient μ_a, reduced scattering coefficient μ_s' and ultimately images of total haemoglobin and oxygen saturation distributions. These images should in principle provide information about the physiological state of the tissue under investigation and help identify and characterize tumours within the breast. However, in recent years it has become apparent that the external shape of the tissue can dramatically impact the quality of the reconstruction, and this is largely due to mismatch between the model prediction and the actual shape of the tissue boundary. In this study, a focused effort has been put forward to examine the extent to which external boundary changes will degrade image quality and, more importantly, how this could be corrected with appropriate model-based analysis.

To obtain clinical measurements with a sufficient signal-to-noise ratio, it is key to ensure that good contact exists between the optical fibres and the tissue. More specifically to our studies, the patient lies prone on the measurement bed, which contains a single opening for the breast. The breast is suspended freely through this opening, below which the optical fibres are brought into contact with the breast. Normally, the optical fibre arrangement consists of a total of 48 fibres, 16 fibres in three separate planes. However, for the purpose of this work only one plane of 16 fibres is considered. The fibres need to make full contact with the breast for a good and adequate NIR measurement.

The breast is a soft tissue, which will deform and alter its shape on the application of external pressure. The amount of deformation is a function of the tissue mechanical properties and the amount of displacement and the external pressure applied by the optical fibre array. In most image reconstruction algorithms, the general assumption is made that the region under investigation is a uniform circular (2D) or conical or cylindrical (3D) domain. Little work has been done to evaluate the effect of any incorrect geometry in image reconstruction. For simple symmetric geometries, for example a 3D cylinder, work has been described to accurately calibrate the data to account for 2D/3D mismatch (Hillman *et al* 2000). More recently, work has been done with regard to neonatal head imaging that a slight change to the geometry model, both in terms of geometry and mesh, will result into large change in modelled data (Gibson *et al* 2003a).

In this work, the effect of such assumptions is investigated by creating a deformation of the breast model in 3D to generate simulated clinical data. Images are then reconstructed using various assumptions regarding the imaging domain including a circular or irregular 2D models as well as a 3D conical shaped model and the non-deformed breast model to evaluate image quality. An important part of this modelling effort is the recent advances which have been made in modelling soft tissue deformation (Paulsen *et al* 1999, Doyley *et al* 2000, Van Houten *et al*

2000). Beyond this, it is also becoming established that soft tissue elastic properties can be directly measured with elastography imaging *in vivo*, thereby providing the key information needed for predicting the deformation of tissue under force or displacement conditions. In this study, this displacement modelling was used along with the NIR tomography modelling to create a comprehensive three-dimensional prediction of how to approach appropriate modelling of deformed tissue that is being imaged with NIR tomography.

2. Theory

2.1. Breast deformation model

Soft tissues exhibit nonlinear elastic behaviour (Fung 1993). Nevertheless, it can be considered a linear elastic material in situations where the deforming forces produce infinitesimal deformations (i.e. $\leqslant 5\%$) (Timoshenko and Goodier 1970). For the purpose of this study, the breast was modelled as linear isotropic pseudo-incompressible (i.e. Poisson's ratio (ν) = 0.495 (Fung 1993)). Under these assumptions and ignoring internal body force, the governing elasticity equations for quasi-static deformation are given by Timoshenko and Goodier (1970) and Fung (1993)

$$(\lambda + \mu)\nabla(\nabla \cdot u) + \mu\nabla^2 u = 0 \tag{1}$$

for internal nodes in domain Ω, and

$$((\lambda + \mu)\nabla(\nabla \cdot u) + \mu\nabla^2 u) \cdot \hat{n} = h \tag{2}$$

for nodes on the boundary $\delta\Omega$.

Here $\hat{n}$ represents a unit vector directed outwards from Ω, and h represents the traction on the surface or boundary of the breast. Note that u represents the displacement components in all coordinate directions, and μ and γ are Lame's elastic constants. For an isotropic medium these constants are related to the more familiar Young's modulus (E) and the Poisson's ratio (ν) by

$$\mu = \frac{E}{2(1+\nu)} \qquad \lambda = \frac{\nu E}{(1+\nu)(1-2\nu)}. \tag{3}$$

The first Lame's elastic constant (i.e. μ) is generally known as shear modulus.

It should be stated that in this study, the breast was assumed to be traction free (i.e. no other forces are associated) and internal body forces were neglected, thus the problem is solved by imposing a prescribed displacement (i.e. induced when the optical fibres are coupled to the breast) as described in Doyley *et al* (1999).

2.2. Light propagation model

Under the assumption that scattering dominates absorption for NIR light in tissue, the Boltzmann transport equation can be simplified to the diffusion approximation, which in the frequency domain is given by

$$-\nabla \cdot D\nabla\Phi(r, \omega) + \left(\mu_a + \frac{i\omega}{c}\right)\Phi(r, \omega) = q_0(r, \omega) \tag{4}$$

where $q_0(r, \omega)$ is an isotropic source, $\Phi(r, \omega)$ is the photon fluence rate at position r and $D = \frac{1}{3(\mu_a + \mu'_s)}$ is the diffusion coefficient. We use the Robin (Type III) boundary condition:

$$\Phi(\gamma) + \frac{D}{\alpha}\hat{n} \cdot \nabla\Phi(\gamma) = 0 \tag{5}$$

where α is a term which incorporates reflection as a result of refractive index mismatch (Schweiger *et al* 1995, Dehghani *et al* 2003c) at the boundary, and $\hat{n}$ is the outward pointing normal to the boundary ($\delta\Omega$) at γ.

We assume that the data are represented by a nonlinear operator $y^* = F[\mu_a, D]$, where our data y^* are a complex vector having a real and imaginary components, which are mapped to log amplitude and phase shift in measurement. Then the image reconstruction method is posed as a solution to the following expression:

$$(\hat{\mu}_a, \hat{D}) = \arg\min_{\mu_a, \kappa} \|(y^* - F(\mu_a, D))\| \tag{6}$$

where $\|\cdot\|$ is the weighted L2-norm, representing the square root of the sum of the squared elements, $\hat{\mu}_a$ is a vector of the absorption coefficients and $\hat{D}$ is a vector of the diffusion coefficients. The magnitude of this is sometimes referred to as the projection error and provides a value for determining the convergence of the iterative reconstruction algorithm.

In this study, a finite-element method (FEM) is used as a general and flexible method for solving the forward problem in arbitrary geometries (Arridge *et al* 1993, Jiang *et al* 1996). In the inverse problem, where the goal is to recover internal optical property distributions from boundary measurements, it is assumed that $\mu_a(\mathbf{r})$ and $D(\mathbf{r})$ are expressed in a basis with a limited number of dimensions (less than the dimension of the finite element system matrices). A number of different strategies for defining reconstruction bases are possible; in this paper a linear pixel basis (Schweiger and Arridge 1999) is used. To find $(\hat{\mu}_a, \hat{D})$ in equation (6) we have used a Levenberg–Marquardt algorithm, where we repeatedly solve:

$$\hat{a} = J^T(JJ^T + \rho I)^{-1}\hat{b} \tag{7}$$

where $\hat{b}$ is the data vector, $\hat{b} = [y^* - F[\mu_a, D]]^T$, $\hat{a}$ is the solution update vector, $\hat{a} = [\delta\hat{D}; \delta\hat{\mu}_a]$. Here, ρ is the regularization factor and J is the Jacobian matrix for our model which is calculated using the Adjoint method (Arridge and Schweiger 1995, Dehghani *et al* 2003b, 2003c).

3. Methods

3.1. Breast deformation

A volume mesh of a female breast of a volunteer was created from surface image data that was acquired using a 3D surface camera (Rainbow 3D Camera, Genex Technologies, Kensington MD). The 3D camera projects structural illumination patterns onto the object and calculates 3D surface profile described by over 300 000 data points (Geng 1996, Galdino *et al* 2002). A volume mesh is then generated using the Delaunay algorithm. The mesh has a geometry of $130 \times 136 \times 60$ mm, figure 1(a), and contained 15 501 nodes corresponding to 61 171 linear tetrahedral elements. The diameter of the breast at its mid-plane where optical fibre array will be applied is approximately 88 mm. To calculate the deformation due to 16 equally spaced optical fibres being applied at the mid-plane of the breast, i.e. $z = -30$ mm, it is assumed that each optical fibre pushed the breast so that the final breast diameter at $z = -30$ mm is 70 mm, and that the diameter of each optical fibre is 6 mm. The modelled elastic properties of tissue, equation (3), were assumed as isotropic and homogenous with Young's modulus of 20 kPa (Krouskop *et al* 1998) and Poisson's ratio of 0.495 (Fung 1993). Further, it was assumed that the topmost part of the mesh, i.e. $z = 0$ mm was not allowed to move since it is connected to the chest. Using this applied displacement as a boundary condition, the displacement at all nodes due to the application of the optical fibres was calculated and a deformed mesh was created, figure 1(b).
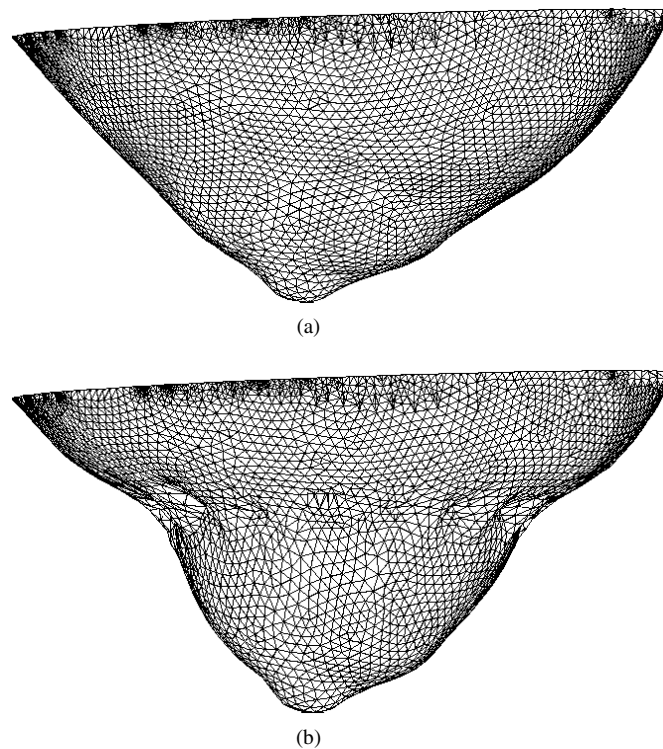
(a)

(b)

Figure 1. Volume mesh of the (a) normal suspended breast and (b) the deformed mesh after the application of the optical fibre array.

3.2. Simulation of data from deformed breast

In order to accurately simulate the clinical settings, two localized anomaly regions were placed within the mid-plane of the normal breast, both at $z = -30$ mm, figure 2(a). First was an absorbing anomaly, 19 mm from the surface and a radius 10 mm with a coefficient value of 0.03 mm^{-1}. Second was a reduced scattering anomaly, also 19 mm from the surface but with a radius of 7.5 mm and a value of 3 mm^{-1}. These anomalies were chosen as they represent the size and contrast we aim to image and so that absorption and scatter separation can also be investigated. The background optical properties were modelled with an absorption coefficient of 0.01 mm^{-1} and a reduced scatter coefficient of 1.0 mm^{-1}. For the deformed breast model the same optical properties of the normal breast were assumed (the anomalies were also assumed to have the same elastic properties of the background). Once the deformation of the model was calculated, it was assumed that the anomalies were free to move, depending on the elastic properties of the breast, figure 2(b). It is interesting to note that the displacement of the anomalies is not so much dependent on the mesh density of the breast, but more dependent on the mechanical properties, applied pressure and non-symmetric nature of the breast.

Using the deformed mesh, together with the displaced anomalies, data were simulated for 16 equally circularly spaced optical fibres placed at $z = -30$ mm. Amplitude and phase data were simulated at 100 MHz, and 1% noise was added. These data were then used as simulated patient data in the following sections. In addition, to allow data calibration as done using clinical data, and discussed elsewhere (Dehghani *et al* 2003c, McBride *et al* 2003), the data were simulated for 16 equally spaced optical fibres placed in a circle around the mid-plane of a
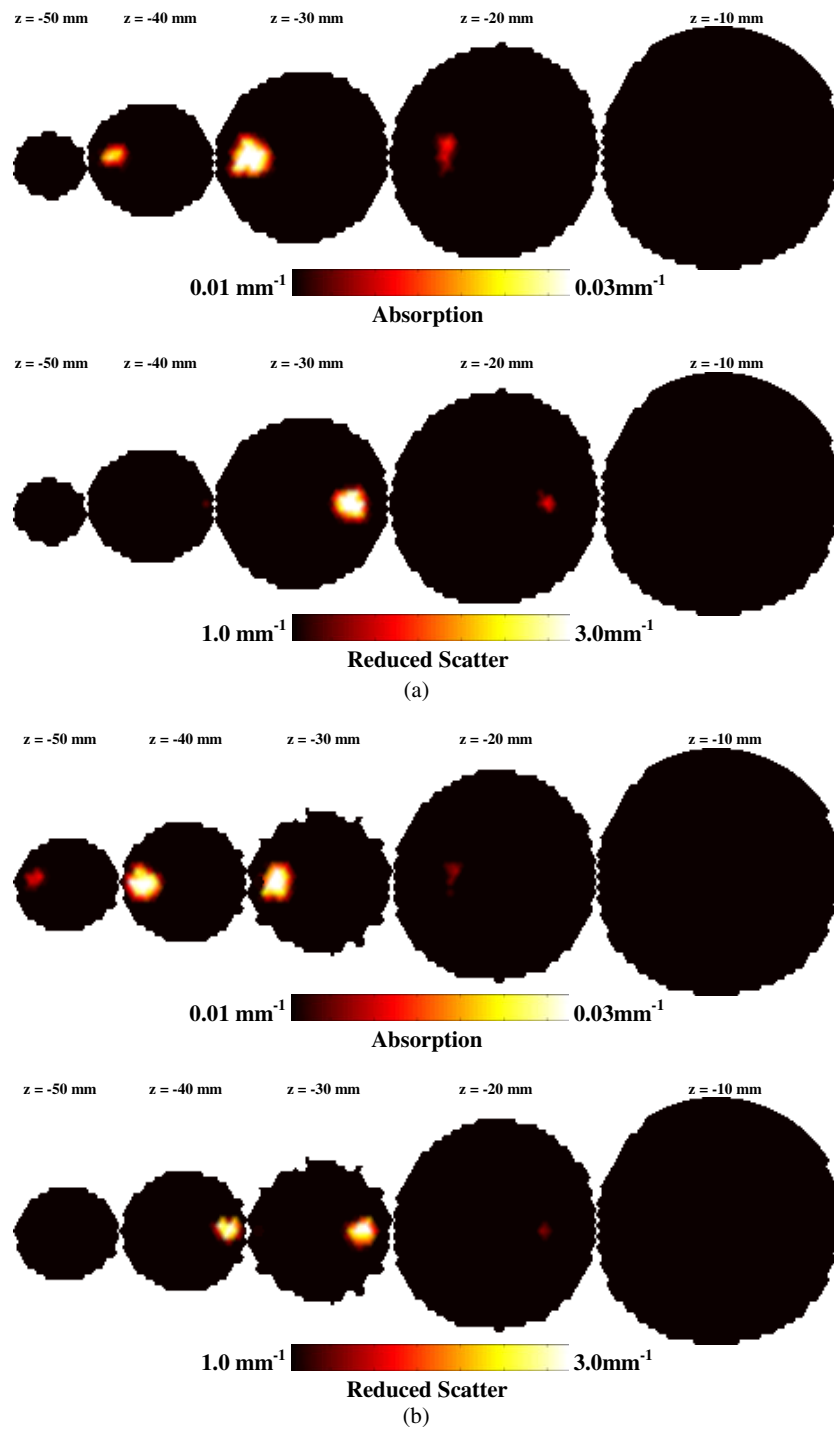
Figure 2. 2D coronal slices through (a) the normal breast mesh and (b) the deformed breast mesh, showing the position of the anomalies. The most right-hand slice is near the chest while the most left-hand slice is near the nipple.
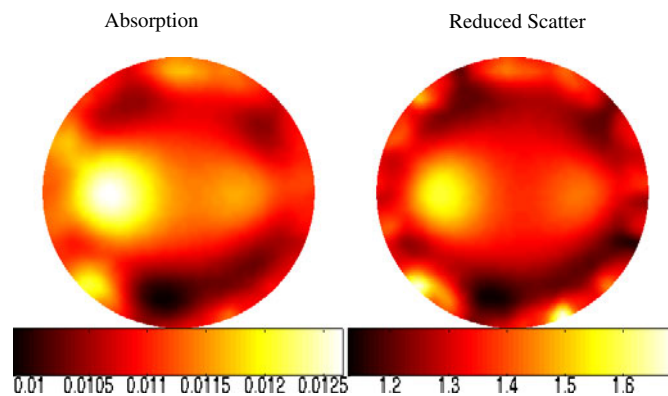
Absorption   Reduced Scatter

0.01 0.0105 0.011 0.0115 0.012 0.0125   1.2   1.3   1.4   1.5   1.6

Figure 3. 2D simultaneous reconstruction of absorption and reduced scatter from deformed breast model simulated data. The mesh used for the reconstruction is a circular mesh whose diameter is the same as the optical fibre array diameter used to deform and simulate data NIR from the breast model.

non-deformable cylindrical model with a known homogenous background optical properties. The same calibration data file has been used for all presented reconstructions.

3.3. Image reconstruction using 2D meshes

Using the computed data for the deformed mesh and the reference phantom, as simulated measurements with 1% random noise added, the data were calibrated (Dehghani *et al* 2003c, McBride *et al* 2003) and images were reconstructed using two different 2D meshes. Assuming that the imaging domain was a circular domain with a radius equal to the radius of the optical fibre array, i.e. 35 mm, images were reconstructed and the results are shown in figure 3. The circular mesh used contained 1785 nodes corresponding to 3418 linear triangular elements. For the reconstruction basis (basis used for the update of the optical parameters), a 20×20 regular grid (piecewise linear) was used and the initial regularization parameter was set to 100. Images shown here, and all following sections are at iteration level where the projection error was within 5% of the previous iteration. In the 2D reconstruction cases, this projection error was reached typically in the 7th iteration.

It is evident from figure 1(b) that the breast at the plane of measurement, i.e. $z = -30$ mm, was no longer circular. In order to evaluate if a more correct *a priori* information regarding the 2D boundary at the plane of measurement would be useful, a 2D irregular mesh, with a boundary whose profile is the same as the boundary at $z = -30$ mm for the deformed mesh, was created and used for image reconstruction. The resulting images reconstructed on this mesh are shown in figure 4. The irregular mesh used contained 2405 nodes corresponding to 4619 linear triangular elements. For the reconstruction basis, a 20×20 regular grid was used and the initial regularization parameter was set to 100. Thus in this case, the irregular boundary was matched, but still the image reconstruction was approximated by a 2D forward solution.

3.4. Image reconstruction using 3D conical mesh

In the next section, we examined the improvement if a true 3D forward calculation was assumed, but with a regular geometry. In a previous work, it was hypothesized that given a set of 3D patient data, those images could be reconstructed with reasonable accuracy if
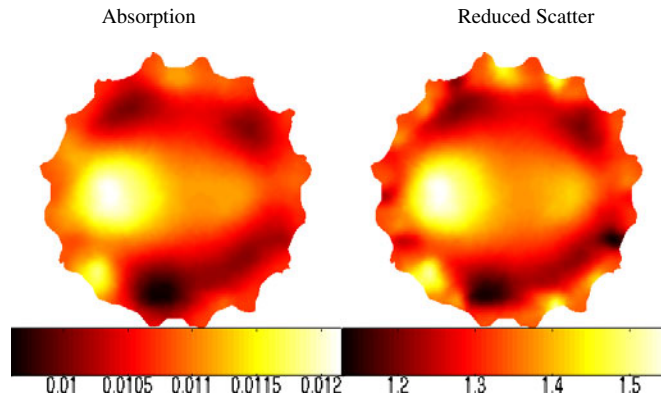
Absorption   Reduced Scatter

Figure 4. 2D simultaneous reconstruction of absorption and reduced scatter from deformed breast model simulated data. The mesh used for the reconstruction is an irregular whose boundary is the same as the boundary of the deformed breast mesh at $z = 30$ mm.
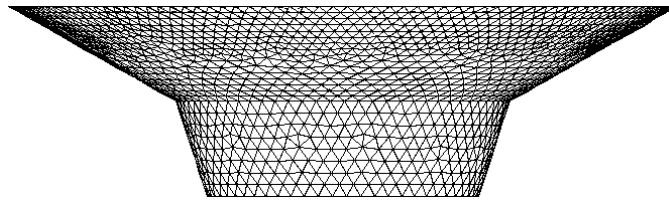

Figure 5. The conical shaped volume mesh. The geometry of the mesh is such that the diameter at the mid-plane corresponds to the diameter of the optical fibre array used to deform and simulate NIR data of the breast model. The diameter at 20 mm above and 20 mm below the NIR measurement plane of the deformed breast were also used to set the upper and lower bound of the cone model.

the breast was assumed to be a conical shaped model (Dehghani *et al* 2003c). To create a conical mesh, the information about the diameter of the measurement fibre array as well as the diameter of the breast at 20 mm above and 20 mm below the measurement plane was used, which would include all boundary information other than effects due to tissue bulging. Following this procedure, a conical shaped volume mesh was created, as shown in figure 5, which shows the upper chest wall and the confined partial-conical breast shape as a regular geometry approximation to the circularly compressed breast shape. The mesh contained 9332 nodes corresponding to 42 281 linear tetrahedral elements and was created using NETGEN (Schoberl). Using this mesh and the simulated data for the deformed breast mesh, images were reconstructed and the results are shown in figure 6.

For the reconstruction basis, a $20 \times 20 \times 10$ regular grid was used and the initial regularization parameter was set to 100. The images shown here and all through the following section are at iteration level where the projection error was within 5% of the previous iteration. These presented from the 3D cases are from the 14th iteration.

3.5. Image reconstruction using the normal and deformed breast mesh

Assuming that correct information regarding the breast is available, before the application of the optical fibre array, the normal, non-deformed mesh was used as shown in figure 1(a),
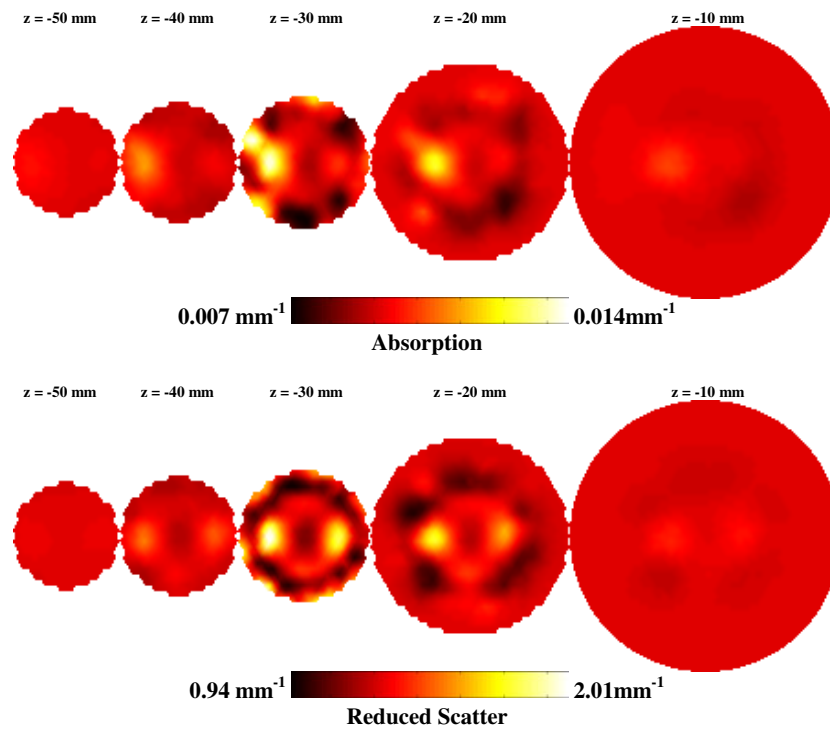
Figure 6. 3D simultaneous reconstruction of absorption and reduced scatter from deformed breast model simulated data. The mesh used for the reconstruction is the mesh shown in figure 5. The most right-hand slice is near the chest while the most left-hand slice is near the nipple.

as the reconstruction mesh for the images shown in figure 7. The reconstruction basis and parameters used were the same as for the conical model already described. Finally, to show the best possible reconstruction, the deformed mesh, figure 1(b) was used for reconstruction of images and these are shown in figure 8.

4. Results

The deformed breast mesh, as a result of applying a circular optical fibre array at $z = 30$ mm, is shown in figure 1(b). It is evident that the mesh has been compressed at the plane of applied displacement with slight bulging in-between each optical fibre. The breast mesh has also extended in the z direction near the nipple to maintain a constant volume as the nodes on the chest wall are assumed fixed. Although the mechanical properties of the tissue are assumed constant, it is interesting to note that the modelled anomalies have also been displaced due to the deformation, figures 2(a) and (b). Both the anomalies have been reduced in diameter, but have extended in the z direction as a result of the applied deformation.

Two-dimensional images reconstructed using the simulated deformed breast data are shown in figures 3 and 4. In both cases where a circular or an irregular boundary was used, good images were recovered in terms of localization of the absorption anomaly (within 1.2 mm for the circular model, and 2.0 mm for the irregular model). The recovery of the
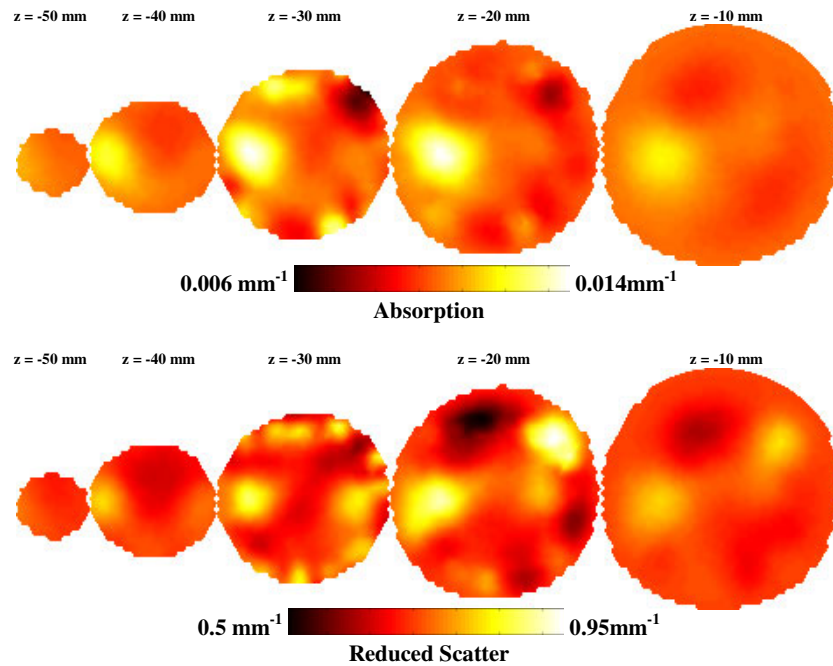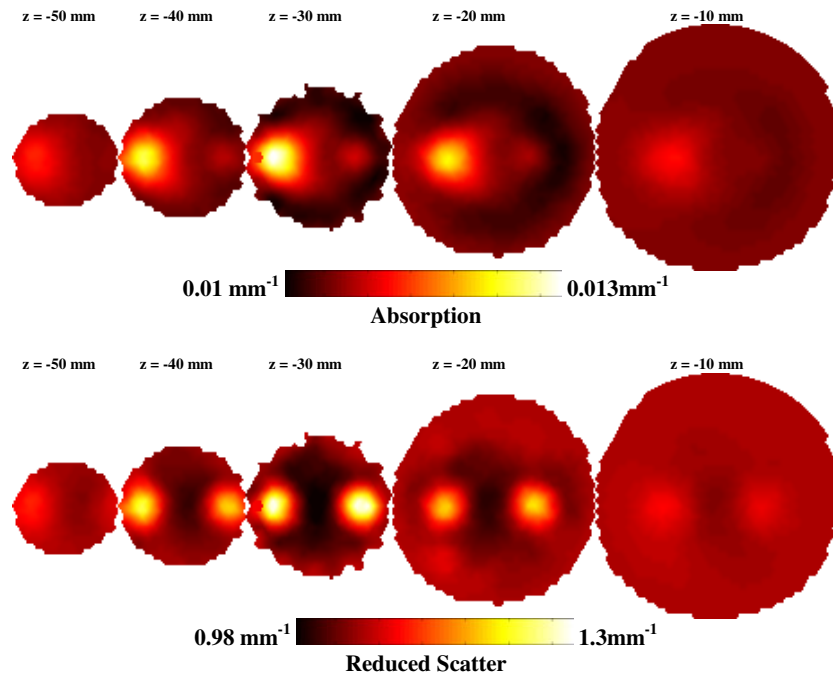
Figure 7. 3D simultaneous reconstruction of absorption and reduced scatter from deformed breast model simulated data. The mesh used for the reconstruction is the mesh shown in figure 1(a). The most right-hand slice is near the chest while the most left-hand slice is near the nipple.

reduced scattering anomaly was not as good as the absorption, and both sets of images contain large boundary artefacts. The background values of both the absorption and reduced scatter were close to the expected value, however, the target absorption value is less than 50% than expected.

Three-dimensional images reconstructed assuming a conical shaped breast are shown in figure 6. In that case, both the absorption and the scattering anomalies were recovered with good localization (within 2.00 mm for both the absorption and scattering objects) and with little boundary artefacts. Since the measured data were about the mid-plane of the breast, and the modelled cone geometry also had the optical fibres around its mid-plane, the objects recovered are centred at $z = -30$ mm. Here the background values of absorption and scatter were a little lower than expected values, however, the absorption anomaly had a maximum value of 0.014 mm^{-1} and the scattering object had a maximum value of 2 mm^{-1}.

Images reconstructed using the assumption of correct non-deformed breast geometry are shown in figure 7. In this case, although the absorbing anomaly has been reconstructed, the reduced scattering images contain large artefacts. The background absorption and scatter values are about 0.006 mm^{-1} and 0.5 mm^{-1}, respectively, while the maximum absorption for the anomaly is 0.014 mm^{-1}. Finally, images reconstructed assuming correct 3D deformed boundary are shown in figure 8. Here, both the absorbing and scattering regions have been recovered within less than 1.00 mm of expected location, giving great localization accuracy. There exists some cross talk between the absorbing and scattering anomalies. The background absorption and scatter values are about 0.01 mm^{-1} and 0.98 mm^{-1}, respectively, while the maximum absorption and scatter values for the anomaly is 0.013 mm^{-1} and 1.3 mm^{-1}, respectively.

Figure 8. 3D simultaneous reconstruction of absorption and reduced scatter from deformed breast model simulated data. The mesh used for the reconstruction is the mesh shown in figure 1(b). The most right-hand slice is near the chest while the most left-hand slice is near the nipple.

5. Discussions

The deformation of the breast due to the application of 16 circular equally spaced optical fibres has been modelled using a computational mechanic model. Using this deformed model which also contains a single absorbing and a single scattering perturbations, data were simulated and 1% noise was added to more adequately represent clinical measurements. Using these simulated data, reconstructed images of absorption and reduced scatter were generated simultaneously using various different geometries of the mesh upon which the reconstruction would take place. In the first case, it was assumed that the model used for reconstruction was circular with a radius equal to the radius of the optical fibre array after breast compression, which was 35 mm. The reconstructed images have shown good accuracy in the localization of the absorbing object with a maximum absorption value of 0.014 mm^{-1}. The recovery of the scattering objects is much poorer than the absorbing anomaly, which can be attributed, perhaps, to its small size (15 mm diameter). There exist boundary artefacts in both the absorbing and scattering images. It is possible to improve the quality of the reconstructed 2D images by using several methods, including the use of various regularization parameters and/or use of *a priori* information. A good method to improve the reconstructed images in this case would be to segment the reconstructed images shown in figure 3, and use these as *a priori* information to more accurately obtain quantitative results. The application of such algorithm is discussed elsewhere, and has been found to provide superior results (Srinivasan *et al* 2004). In the case of knowing and using correct 2D boundary information in image reconstruction, figure 4, no useful improvement was seen. Although correct information was added to the reconstruction

with regard to the boundary, the image reconstruction algorithm was still constrained to be 2D. While it has been shown many times that the 2D geometry can be used to recover accurate image data from NIR tomography with a circular boundary (Pogue and McBride 1999), it is not surprising, perhaps, to find that this simplification does not continue to work as the exterior boundary becomes more complex in shape. The reconstruction mesh is no longer symmetric and contains many irregular edges, which gives rise to high frequency noise at the boundary, and those changes occur symmetrically around each optical fibre making the calculation even more dependent upon the 3D geometry out of the plane of imaging.

Next for the case where the imaging domain was assumed to be conical in shape, the reconstructed images were shown in figure 6. Here it was assumed that the mid-plane of the cone had a radius equal to the radius of the optical fibre array after breast compression. Further, it was assumed that the measurements of the diameter of the breast 20 mm above and 20 mm below the measurement plane were known. Using these data, a conical shaped mesh could be created for any patient exam as shown in figure 5. The reconstructed images had recovered both the absorbing and scattering anomalies with reasonable success. The calculated background values for absorption and scatter were 0.007 mm^{-1} and 0.94 mm^{-1}, respectively. There exists a small cross talk between the absorption and reduced scatter images, plus artefacts at the boundary of the images. The qualitative and quantitative accuracy of the conical shaped model reconstruction are better than the 2D circular case, simply because a more accurate 3D model, rather than a 2D model is used.

In the case where it is assumed that the exact breast geometry was known, but have ignored information regarding the compression due to the optical fibres, the resulting images are shown in figure 7. Here, although the absorption anomaly was recovered with relatively good accuracy, the reduced scattering image contains a large artefact. Furthermore, the calculated background values for absorption and scatter are 0.006 mm^{-1} and 0.5 mm^{-1}, respectively, which are much lower than expected. These images are, perhaps, not as accurate and useful as the conical geometry case, since, although there is a more accurate 3D model, the diameter of the breast was not correct, particularly within the measurement plane, i.e. $z = -30$ mm. Finally, for the case of using a geometrically correct deformed mesh to reconstruct, the images are shown in figure 8. Here, the reconstructed images of absorption and scatter were found with superior localization accuracy. The scattering object has also been recovered in this case. However, the quantitative accuracy of the recovered anomalies is not as good with maximum values for absorption and scattering objects of 0.013 mm^{-1} and 1.3 mm^{-1}, respectively. This low quantitative accuracy has been reported elsewhere and is a common problem in 3D NIR imaging algorithms (Dehghani *et al* 2003b, Gibson *et al* 2003b), which may be solved using of multistage reconstruction algorithms (Srinivasan *et al* 2004) or with inclusion of *a priori* data (Brooksby *et al* 2003). Finally, using the correct model with correct information regarding the deformed boundary has produced images with very little or no artefacts.

6. Conclusions

In this work, we have presented a breast deformation model that would account for the change in shape and geometry of the breast due to the application of a circular array of optical fibres for NIR measurements. The proposed model, at present, assumes that the breast has homogenous mechanical properties, which, although not accurate, provide a good initial estimate for modelling of any deformation. Future studies may focus on using spatially

distributed mechanical properties, as these can be imaged with good spatial resolution with MR elastography (Paulsen *et al* 1999, Van Houten *et al* 2000, Weaver *et al* 2001, Doyley *et al* 2003). Also, in this work, we have deformed the breast more than adequately needed by 19 mm, whereas in a real clinical setting, the deformation will be of lower magnitude, typically about 5–10 mm. In practice for our imaging exams, we currently attempt to deform the breast as minimally as possible, however, there are strategic benefits to compressing in that the signal transmitted can be higher, and there can be pressure-induced changes which might provide meaningful contrast about what the tissue is composed of (Jiang *et al* 2003). Nevertheless we have chosen such a large deformation to provide us with a worst-case scenario for NIR image reconstruction, and to examine if it is feasible to exploit larger magnitude deformations in clinical studies while not compromising the integrity of the data collected from the breast.

Using simulated data from the deformed breast that also contains optical anomalies, we have reconstructed images assuming various reconstruction geometries. In the first case of assuming that the reconstruction mesh is either a circular or irregular 2D mesh, the reconstructed images have shown good accuracy in recovering the location of the absorbing anomaly. The 2D reconstructed scattering images are not as good as expected, which is perhaps due to the fact that the scattering object had a small diameter of 15 mm and a contrast which was three times the background, and thus the image being dominated by boundary artefacts. Also it is evident from the reconstructed images that there exist large boundary artefacts which are due to the incorrect model. However, both the quality and quantitative accuracy of 2D image reconstruction will be improved by the incorporation of *a priori* information as well as a multi-step image reconstruction where regions of interest can be identified and isolated for regional reconstruction.

In the case of 3D image reconstruction, assumptions regarding the breast not being deformed might be used and the reconstructed images provide relatively good absorption distributions, but the images contain large artefacts which will likely confound their interpretation. The reason for this can be explained by considering the overall shape of the breast before and after deformation. The non-deformed mesh at the plane of measurement has radius that is 19 mm larger than the deformed mesh. Additionally, as evident from figures 1(a) and 1(b), it is found that the breast expands above, below and between each optical fibre once compressed. This large change in shape of the breast contributes to the large artefacts seen within the reconstruction. However, if one assumes that the diameter of the breast is known within the measurement plane, as well as an approximate diameter above and below it, it is possible to create a pseudo-3D conical shaped mesh for image reconstruction. Images reconstructed using this 3D conical mesh have shown a better accuracy in recovering both the absorbing and scattering anomalies. Finally, if accurate knowledge regarding the breast deformation is available, images of optical properties can be reconstructed which localize both anomalies with great accuracy, and also contain little or no artefact which otherwise would arise from model mismatch.

The goal of this work is to incorporate this new model of breast deformation with more accurate information regarding the mechanical properties of the breast to improve the NIR image reconstruction. The mechanical property information is readily available from other imaging modalities, and the synthesis of this information may provide fundamentally new information about breast physiologic response to pressure, and/or breast pathology response to pressure. An accurate model of breast deformation should in principle allow us to create patient specific models and meshes, which would in-turn provide more clinically useful data. Work is in progress to validate and further improve the deformation model with application to the female breast imaging.

Acknowledgments

References

Arridge S R and Schweiger M 1995 Photon-measurement density functions. Part2: finite-element-method calculations *Appl. Opt.* **34** 8026–37

Arridge S R, Schweiger M, Hiraoka M and Delpy D T 1993 A finite element approach for modelling photon transport in tissue *Med. Phys.* **20** 299–309

Boas D A, Brooks D H, Miller E L, DiMarzio C A, Kilmer M, Gaudette R J and Zhang Q 2001 Imaging the body with diffuse optical tomography *IEEE Signal Process. Mag.* **18** 57–75

Brooksby B, Dehghani H, Pogue B W and Paulsen K D 2003 Infrared (NIR) tomography breast image reconstruction with *a priori* structural information from MRI: algorithm development for reconstructing heterogeneities *IEEE J. Sel. Top. Quantum Electron.* **9** 199–209

Dehghani H, Brooksby B, Vishwanath K, Pogue B W and Paulsen K D 2003a The effects of internal refractive index variation in near infrared optical tomography: a finite element modelling approach *Phys. Med. Biol.* **48** 2713–27

Dehghani H, Pogue B W, Jiang S, Brooksby B and Paulsen K D 2003b Three dimensional optical tomography: resolution in small object imaging *Appl. Opt.* **42** 3117–28

Dehghani H, Pogue B W, Poplack S P and Paulsen K D 2003c Multiwavelength three-dimensional near-infrared tomography of the breast: initial simulation, phantom, and clinical results *Appl. Opt.* **42** 135–45

Doyley M M, Meaney P M and Bamber J C 2000 Evaluation of an iterative reconstruction method for quantitative elastography *Phys. Med. Biol.* **45** 1521–40

Doyley M M, Weaver J B, Van Houten E E, Kennedy F E and Paulsen K D 2003 Thresholds for detecting and characterizing focal lesions using steady-state MR elastography *Med. Phys.* **30** 495–504

Eda H, Oda I, Ito Y, Wada Y, Oikawa Y, Tsunazawa Y, Tsuchiya Y, Yamashita Y, Oda M, Sassaroli A, Yamada Y and Tamaru M 1999 Multichannel time-resolved optical tomographic imaging system *Rev. Sci. Instrum.* **70** 3595–602

Fantini S, Franceschini M A, Gratton E, Hueber D, Rosenfeld W, Maulik D, Stubblefield P G and Stankovic M R 1999 Non-invasive optical mapping of the piglet in real time *Opt. Exp.* **4** 308–14

Fung Y C 1993 *Mechanical Properties of Living Tissue* (Berlin: Springer)

Galdino G M, Manson P N, Nahabedian M, Chang B, Zhuang P, Geng J Z and Vander Kolk C A 2002 Three dimensional photography in plastic surgery: clinical applications for breast surgery *Plastic Reconstr. Surg.* **110** 1–13

Geng Z 1996 Rainbow 3D camera—a new concept for high speed and low-cost 3D vision *J. Opt. Eng.* **35** 376

Gibson A, Riley J, Schweiger M, Hebden J c, Arridge S R and Delpy D T 2003a A method for generating patient specific finite element meshes for head modelling *Phys. Med. Biol.* **48** 481–95

Gibson A, Yusof R M, Hillman E M C, Dehghani H, Riley J, Everdale N, Richards R, Hebden J C, Schweiger M, Arridge S R and Delpy D T 2003b Optical tomography of a realistic neonatal head phantom *Appl. Opt.* **42** 1–8

Hebden J C, Veenstra H, Dehghani H H, Hillman E M C, Schweiger M, Arridge S R and Delpy D T 2001 Three dimensional time-resolved optical tomography of a conical breast phantom *Appl. Opt.* **40** 3278–87

Hillman E, Hebden J C, Schmidt F E W, Arridge S R, Schweiger M, Dehghani H and Delpy D T 2000 Calibration techniques and datatype extraction for time-resolved optical tomography *Rev. Sci. Instrum.* **71** 3415–27

Jiang H, Paulsen K D, Osterberg U L, Pogue B W and Patterson M S 1996 Optical image reconstruction using frequency-domain data: simulations and experiments *J. Opt. Soc. Am.* A **13** 253–66

Jiang S, Pogue B W, Paulsen K D, Kogel C and Poplack S P 2003 *In vivo* near-infrared spectral detection of pressure-induced changes in breast tissue *Opt. Lett.* **28** 1212–4

Krouskop T A, Wheeler T M, Kallel F, Garra B S and Hall T 1998 Elastic moduli of breast and prostate tissues under compression *Ultrason. Imaging* **20** 260–74

McBride T O, Pogue B W, Jiang S, Osterberg U L, Paulsen K D and Poplack S P 2002 Multi-spectral near-infrared tomography: a case study in compensating for water and lipid content in haemoglobin imaging of the breast *J. Biomed. Opt.* **7** 72–9

McBride T O, Pogue B W, Osterberg U L and Paulsen K D 2003 Strategies for absolute calibration of near infrared tomographic tissue imaging *Oxygen Transport Tissue XXIV* (Dordrecht: Kluwer) pp 85–99

Paulsen K D, Miga M I, Kennedy F E, Hoopes P J, Hartov A and Roberts D W 1999 A computational model for tracking subsurface tissue deformation during stereotactic neurosurgery *IEEE Trans. Biomed. Eng.* **46** 213–25

Pogue B W, Geimer S, McBride T O, Jiang S, Österberg U L and Paulsen K D 2001 Three-dimentional simulation of near-infrared diffusion in tissue: boundary condition and geometry analysis for finite element image reconstruction *Appl. Opt.* **40** 588–600

Pogue B W and McBride T *et al* 1999 Comparison of imaging geometries for diffuse optical tomography of tissue *Opt. Exp.* **4** 270–86

Schoberl J *NETGEN—An Automatic 3D Tetrahedral Mesh Generator* http://www.sfb013.uni-linz.ac.at/~joachim/netgen/

Schweiger M and Arridge S R 1999 Optical tomographic reconstruction in a complex head model using *a priori* region boundary information *Phys. Med. Biol.* **44** 2703–22

Schweiger M, Arridge S R, Hiroaka M and Delpy D T 1995 The finite element model for the propagation of light in scattering media: boundary and source conditions *Med. Phys.* **22** 1779–92

Srinivasan S, Pogue B W, Dehghani H, Jiang S, Song X and Paulsen K D 2004 Improved quantification of small objects in near-infrared diffuse optical tomography *J. Biomed. Opt.* at press

Timoshenko S P and Goodier J N 1970 *Theory of Elasticity* (Singapore: McGraw-Hill)

Van Houten E E, Weaver J B, Miga M I, Kennedy F E and Paulsen K D 2000 Elasticity reconstruction from experimental MR displacement data: initial experience with an overlapping subzone finite element inversion process *Med. Phys.* **27** 101–7

Weaver J B, Van Houten E E, Miga M I, Kennedy F E and Paulsen K D 2001 MR elastography using 3D gradient echo measurements of steady state motion *Med. Phys.* **28** 1620

Breast Deformation in Near Infrared Optical Tomography

Hamid Dehghani[1], Brian W. Pogue[1], Marvin M. Doyley[2], Jason Geng[3] and Keith D. Paulsen[1]
[1]Thayer School of Engineering, Dartmouth College, Hanover, NH 03755
[2]Department of Radiology, Dartmouth Medical School, Hanover, NH 03755
[3]Genex Technologies, Inc. 10605 Concord Street, Suite 500, Kensington, MD 20895-2504
email:dehghani@dartmouth.edu, Tel:(603) 646-9193, Fax:(603) 646-3856

Abstract: In NIR tomography of the breast, good contact is needed by the fibers, resulting in breast deformation. We present a deformation model to account for the change of shape and discuss implications in image reconstruction.
©2004 Optical Society of America
OCIS codes: (170.3830) Mammography; (170.6960) Tomography; (100.3010) Image reconstruction techniques; (100.3190) Inverse problems

1. Introduction

Near Infrared (NIR) tomography is an emerging alternative imaging method used to image physiologic parameters of biological tissue in-vivo such as water and hemoglobin [1]. Measurements of light propagation (600 – 900 nm) within tissue can be used to map internal chromophore concentrations within tissue. Light is transmitted through tissue using multiple input and output locations on the surface of the region to be imaged using optical fibers for delivery and pickup of the light signals. To obtain clinical measurements with a sufficient signal to noise ratio, it is key to ensure good contact exists between the optical fibers and the tissue. The breast is a soft tissue, which will deform and alter its shape on the application of external pressure. The amount of deformation is a function of the tissue mechanical properties and the amount of displacement and the external pressure applied by the optical fiber array. In most image reconstruction algorithms, the general assumption is made that the region under investigation is a uniform circular (2D) or conical or cylindrical (3D) domain [2]. Little work has been done to evaluate the effect of any incorrect geometry in image reconstruction. In this work, the effect of such assumptions is investigated by creating a deformation of the breast model in 3D to generate stimulated clinical data. Images are then reconstructed using various assumptions regarding the imaging domain such as 3D conical shaped models and the non-deformed breast model to evaluate image quality.

2. Methods

Soft tissues exhibit nonlinear elastic behavior. Nevertheless, they can be considered a linear elastic material in situations where the deforming forces produce infinitesimal deformations (i.e. ≤ 5 %). For the purpose of this study, the breast was modeled as linear isotropic pseudo-incompressible medium (i.e. Poisson's ratio $(\nu)= 0.495$). Under these assumptions and ignoring internal body force, the governing elasticity equations for quasi-static deformation is given by:

$$(\lambda + \mu)\nabla(\nabla \cdot \vec{u}) + \mu\nabla^2\vec{u} = 0 \qquad \text{for internal nodes in domain } \mathbf{\Omega} \qquad (1)$$

$$\left((\lambda + \mu)\nabla(\nabla \cdot \vec{u}) + \mu\nabla^2\vec{u}\right)\hat{n} = h \qquad \text{for nodes on the boundary } \delta\Omega. \qquad (2)$$

Here $\hat{n}$ represents a unit vector directed outwards from Ω, and h represents the traction on the surface or boundary of the breast. Note that $\vec{u}$ represents the displacement components in all coordinate directions, and μ and λ are Lame's elastic constants. For an isotropic medium these constants are related to the more familiar Young's modulus (E) and the Poisson's ratio (ν) by $\mu = \dfrac{E}{2(1+\nu)}$ and $\lambda = \dfrac{\nu E}{(1+\nu)(1-2\nu)}$.

It should be stated that in this study the breast was assumed to be traction free and internal body forces were neglected, thus the problem was solved by imposing a prescribed displacement [3]. A volume mesh of a female breast of a volunteer was created from surface image data that was acquired using a 3D surface camera [Rainbow 3D Camera, Genex Technologies, Kensington MD]. The 3D camera projects structural illumination patterns onto the object and calculates 3D surface profile described by over 300,000 data points [4]. A volume mesh was then generated using the Delaunay algorithm**.** The mesh has a geometry of 130 x 136 x 60 mm, Figure 1(a) and contained 15501 nodes corresponding to 61171 linear tetrahedral elements. The diameter of the breast at its mid-plane where

optical fiber array would be applied is approximately 88 mm. To calculate the deformation due to 16 equally spaced optical fibers being applied at the mid-plane of the breast, i.e. z = -30 mm, it is assumed that each optical fiber pushed the breast so that the final breast diameter at z = -30 mm is 70 mm, and that the diameter of each optical fiber is 6 mm. The modeled elastic properties of tissue, were assumed as isotropic and homogenous with Young's Modulus of 20 kPa and Poisson's ratio of 0.495. Further, it was assumed that the top most part of the mesh, i.e. z = 0 mm was not allowed to move since it is connected to the chest. Using this applied displacement as a boundary condition, the displacement at all nodes due to the application of the optical fibers was calculated and a deformed mesh was created, Figure 1(b).
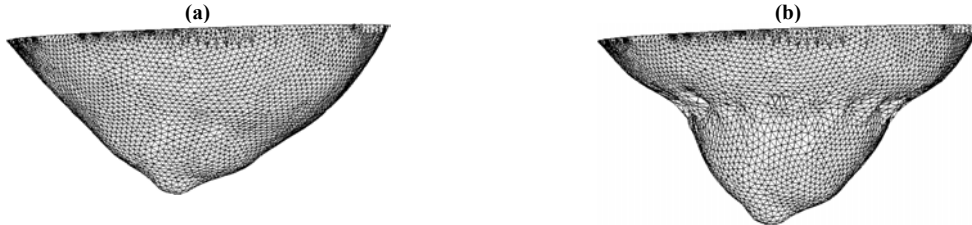
Figure 1. Volume mesh is shown of the (a) normal suspended breast and (b) the deformed mesh after the application of the optical fiber array.

In order to accurately simulate the clinical settings, two localized anomaly regions were placed within the mid-plane of the normal breast, both at z = -30 mm, Figure 2(a). First was an absorbing anomaly, 19 mm from the surface and a radius 10 mm with a coefficient value of 0.03 mm^{-1}. Second was a reduced scattering anomaly, also 19 mm from the surface but with a radius of 7.5 mm and a value of 3 mm^{-1}. The background optical properties were modeled with an absorption coefficient of 0.01 mm^{-1} and a reduced scatter coefficient of 1.0 mm^{-1}. For the deformed breast model the same optical properties of the normal breast, including the anomalies were assumed. Once the deformation of the model was calculated, it was assumed that the anomalies were free to move, depending on the elastic properties of the breast, Figure 2(b).
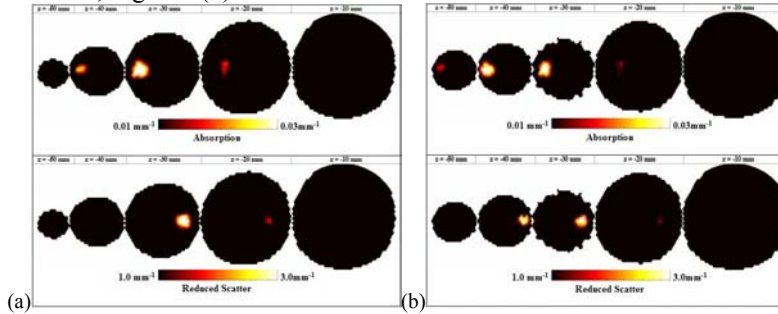

Figure 2. 2D coronal slices through (a) the normal breast mesh and (b) the deformed breast mesh, showing the position of the anomalies. The right hand slice is near the chest while the most left hand slice is near the nipple.

Using the deformed mesh, together with the displaced anomalies, NIR data were simulated for 16 equally circularly spaced optical fibers placed at z = -30 mm. Amplitude and phase data were simulated at 100 MHz, and 1% noise were added. This data was then used as simulated patient data in the following sections. In addition, to allow data calibration as done using clinical data, and discussed elsewhere [2], the data was simulated for 16 equally spaced optical fibers placed in a circle around the mid-plane of a cylindrical model with homogenous background optical properties.

3. Results

Assuming that correct anatomical information regarding the breast is available, before application of the optical fiber array, the normal, non-deformed mesh was used, Figure 1(a), during reconstruction to produce the images shown in Figure 3(a). Also, images reconstructed assuming a conical shaped breast (diameter at z = -30 set to equal the diameter of the optical fiber array) are shown in Figure 3(b). Finally, to show the best possible reconstruction, the deformed mesh was used for reconstruction of images and these results are shown in Figure 3(c).

From images reconstructed using the correct but non-deformed breast, although the absorbing anomaly has been recovered, the reduced scattering images contain large artifacts. The background absorption and scatter values are about 0.006 mm^{-1} and 0.5 mm^{-1} respectively, while the maximum absorption for the anomaly is 0.014 mm^{-1}. In images assuming a conical model the background absorption and scatter values are about 0.007 mm^{-1} and 0.94 mm^{-1}

respectively, while the maximum absorption for the anomaly is 0.014 mm^{-1}. Here, although the target values are better quantitatively, the images contain artifacts, are much smaller, and the absorption scatter cross-talk is more than expected. In images reconstructed assuming correct 3D deformed boundary, both the absorbing and scattering regions have been recovered with improved localization accuracy. Some cross talk exists between the absorbing and scattering anomalies. The background absorption and scatter values are about 0.01 mm^{-1} and 0.98 mm^{-1} respectively, while the maximum absorption and scatter values for the anomalies are 0.013 mm^{-1} and 1.3 mm^{-1} respectively. It is important to note that although the images in Figure 3(a) show a better quantitative accuracy for the recovered absorbing anomalies, the background values are much lower than expected and the images contain far more artifacts.
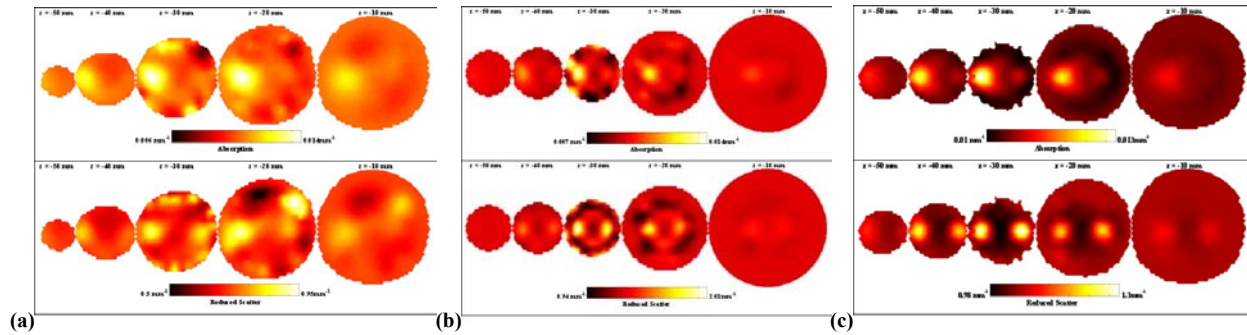
Figure 3. 3D simultaneous reconstruction of absorption and reduced scatter from deformed breast model simulated data are shown. The mesh used for the reconstruction was (a) the normal un-deformed breast; (b) conical mesh and (c) the correct deformed breast. The most right hand slice is near the chest while the most left hand slice is near the nipple in each set of images.

4. Discussion

In the case where it is assumed that the exact breast geometry is known, but the details of the fibers compression have been ignored, although the absorption anomaly was recovered with relatively good accuracy, the reduced scattering image contains a large artifact. Furthermore, the calculated background values for absorption and scatter are 0.006mm^{-1} and 0.5 mm^{-1} respectively, which are much lower than expected. These images are, perhaps, not as accurate and useful as the conical geometry case, since, although there is a more accurate 3D model, the diameter of the breast was not correct, particularly within the measurement plane, i.e. z = -30 mm. When using the geometrically correct deformed mesh to reconstruct images of absorption and scatter, superior localization accuracy resulted. The scattering object has also been recovered in this case. However, the quantitative accuracy of the recovered anomalies is not as good with maximum values for absorption and scatter of 0.013mm^{-1} and 1.3 mm^{-1}, respectively. This modest degradation in quantitative accuracy has been reported elsewhere and is a common problem in 3D imaging algorithms, which may be solved through the use of multi-stage algorithms [5] or with inclusion of a priori data. Nonetheless using the correct model with correct information regarding the deformed boundary has produced images with very little to no artifacts.

5. Acknowledgements

6. References

1. McBride, T.O., Pogue B W , S. Jiang, U. L. Osterberg, K. D. Paulsen, and S. P. Poplack, *Multi-spectral near-infrared tomography: a case study in compensating for water and lipid content in hemoglobin imaging of the breast.* J. Biomed. Opt., 2002. **7**.
2. Dehghani, H., Pogue, B. W., Poplack, S. P., Paulsen, K. D., *Multiwavelength Three-Dimensional Near-Infrared Tomography of the Breast: Initial Simulation, Phantom, and Clinical Results.* Applied Optics, 2003. **42**(1): p. 135-145.
3. Doyley, M.M., Meaney, P. M., and Bamber, J. C., *Evaluation of an iterative reconstruction method for quantitative elastography.* Phys. Med. Biol., 2000. **45**(6): p. 1521-1540.
4. Geng, Z., *Rainbow 3D Camera - A New Concept for High Speed and Low-Cost 3D Vision.* Journal Optical Engineering, 1996. **35**(2): p. 376.
5. Srinivasan, S., Pogue, B. W., Dehghani, H., Jiang, S., Song, X., and Paulsen, K. D., *Improved Quantification of Small Objects in Near-Infrared Diffuse Optical Tomography.* J. Biomed. Opt., 2003. **Submitted**.

Magnetic resonance-guided near-infrared tomography of the breast

Ben Brooksby, Shudong Jiang, Hamid Dehghani, Brian W. Pogue, and Keith D. Paulsen
Thayer School of Engineering, Dartmouth College, Hanover, New Hampshire 03755

Christine Kogel, Marvin Doyley, John B. Weaver, and Steven P. Poplack
Department of Diagnostic Radiology, Dartmouth Medical School, Hanover, New Hampshire 03755

The design and implementation of a multispectral, frequency-domain near infrared tomography system is outlined, which operates in a MRI magnet for utilization of MR-guided image reconstruction of tissue optical properties. Using long silica optical fiber bundles, measurements of light transmission through up to 12 cm of female breast tissue can be acquired simultaneously with MRI scans. The NIR system utilizes six optical wavelengths from 660 to 850 nm using intensity modulated diode lasers nominally working at 100 MHz. Photomultiplier tube detector gain levels are electronically controlled on a time scale of 200 ms, thereby allowing rapid switching of the source to locations around the tissue. There are no moving parts in the detection channels and for each source position, 15 PMTs operating in parallel allow sensitivity down to 0.5 pW/cm^2 at the tissue surface. Images of breast tissue optical absorption and reduced scattering coefficients are obtained using a Newton-type reconstruction algorithm to solve for an optimal solution using the measurement data. In medical imaging, it is beneficial to compare the same tissue volume as seen by a variety of modalities, and perhaps more importantly, there is the hypothesis that one imaging system which has high spatial resolution can be used to enhance the reconstruction of another system which has good contrast resolution. In this study we explore the synergistic benefits of a combined NIR-MRI data set, specifically the ways in which MRI (i.e., high spatial resolution) enhances NIR (i.e., high contrast resolution) image reconstruction. The design, calibration, and performance of the imaging system are described in the context of preliminary phantom tests and initial *in vivo* patient imaging. Co-registered MRI validates and improves optical property estimation in 2D tomographic image reconstructions when specialized algorithms are used. © *2004 American Institute of Physics.* [DOI: 10.1063/1.1819634]

I. INTRODUCTION

Diffuse optical tomography (DOT) with near infrared (NIR) light can be used to produce spatially resolved images of tissue optical properties. These optical property maps can be acquired at different wavelengths and combined to reveal hemoglobin concentration, oxygen saturation, water and fat content, as well as a description of scattering structures.[1–5] These latter parameters are important indicators of metabolic activity, functional processes, or presence and staging of disease. NIR diffuse tomography generally suffers from comparatively low spatial resolution due to the multiple scattering events that occur along each photon path.[6–8] However, the promise of this imaging modality lies in the fact that it affords new physical bases for contrast in tissue. For example, hemoglobin-based contrast in tumors relative to normal tissue is exceptionally high (i.e, between 100%–300%).[9] However, improving the limitations associated with its low spatial resolution is fundamental to implementing this technology clinically. *A priori* knowledge of tissue structure can be used to constrain/guide the iterative NIR image reconstruction process, and improve the spatial resolution and quantitative accuracy of recovered physiological parameters. Consequently, NIR techniques have been combined with several high spatial-resolution, structure-bearing imaging mo-

dalities including x-ray tomosynthesis,[10] ultrasound (US),[11] and magnetic resonance imaging (MRI),[12–14] to study human tissues and small animals. In this report, we present a combined NIR-MRI system for imaging female breast tissue, and explore the benefits of the combined data set in a planar tomographic geometry where the breast is imaged pendent in a standard MR breast coil.

In recent years, several important technological factors have contributed to the advancement of NIR spectral imaging applied to breast cancer characterization, including an increased understanding of light and tissue interaction, and new software-based developments in image-reconstruction algorithms for DOT.[5] NIR radiation (700–900 nm) is nonionizing, light delivery and detection instrumentation is relatively inexpensive, and uncomfortable tissue compression is not required (as in mammographic level compression). Detection systems with high signal-to-noise ratios can routinely measure NIR light transmission through 10 cm of breast tissue. This distance may increase to 12 cm for breasts with fatty composition (i.e., lower radiographic density and NIR attenuation). Photon propagation within the breast is well described by diffusion theory since the probability of photon scattering is much greater than absorption. Light transmission measurements can be combined with diffusion theory to provide robust image reconstruction of tissue optical coeffi-

cients. We use a Newton-type algorithm to solve for the optimal solution that provides a minimum error between the measured data and predicted response from a model of the frequency-domain diffusion equation.[15] In theory, the approach allows separation of the absorption and reduced scattering coefficients (μ_a and $\mu_s^{/}$). Frequency-domain measurements of optical flux provide both amplitude and time-based (i.e., phase shift) information—a unique data set to solve the estimation problem associated with recovering both coefficients simultaneously.

A variety of imaging methods have achieved high-spatial-resolution imaging with acceptable to excellent soft tissue contrast, including x-ray computed tomography (CT), US, and MRI. These techniques primarily provide images of tissue structure and have a limited ability to monitor parameters related to tissue function other than through the introduction of exogeneous contrast agents. Alternatively, nuclear medicine approaches are routinely used to image tissue functions, such as metabolic fluorodeoxyglucose uptake,[16] and many commercial systems exist to co-register these images with the structural data derived from CT, US, and MRI. The combination of high resolution structural imaging with lower resolution functional information is a major emphasis in contemporary medical imaging, and customized hybrid imaging systems are being developed to avoid the complications associated with tissue movement between imaging exams, which compromises the accuracy of postprocedure co-registration.

The application of NIR tomography to provide spatially-resolved functional information, such as hemoglobin levels, oxygen saturation, water, lipid and scatterer content will likely be important, yet customized imaging systems which couple to MRI, US or CT need to be developed to evaluate and exploit this potential. The pioneering work of Ntziachristos *et al.*[13] was the first to demonstrate feasibility of the hybrid NIR-MR approach for clinical breast imaging. Their approach consisted of a co-planar array of optical source/sensors detecting time-resolved illuminations when applied to the surface of the breast. Data was presented as maps of localized optical response at each detector site but was otherwise not processed into depth-resolved images of optical property distributions. Zhu *et al.*[11] have demonstrated clinical application of a combined NIR-US system. With a handheld probe, they simultaneously measure reflection of ultrasound and modulated NIR excitations at the breast tissue surface, and construct co-registered images of structure and optical absorption and hemoglobin concentration.

One of the most challenging issues in hybrid system development is the incorporation of anatomical information as prior constraints into NIR image reconstruction. This has been explored theoretically in several successful reports.[17–22] Structural information can be used to guide functional image reconstruction through knowledge of tissue composition and location by: (i) alteration of the objective functions used in image reconstruction,[10,23] (ii) reduction of the number of unknown parameters by treating regions of the same tissue type as single zones,[13,24] or (iii) introduction of special regularization schemes that can stabilize the inverse problem and emphasize image contrasts.[10,25,26] Optimizing spatial resolution

more likely will depend on the application of all three techniques, while also being strongly influenced by the signal to noise ratio of the measurements, the optical contrast available, and the number of projections used. Some investigators have successfully combined different approaches with multi-stage image reconstruction algorithms.[20,21] However, there is still no clear consensus on how best to utilize the structural information to enhance or improve the recovery of functional NIR information.

This work describes the first system to combine multi-spectral frequency-domain NIR in a planar tomographic geometry with MRI for imaging breast tissue. NIR tomography has shown the ability to localize changes in functional tissue parameters *in vivo*, and MRI has the advantage of offering a particularly rich amount of anatomical information, specifically about the layered adipose and glandular tissue structure of the breast. This system is designed to combine the benefits of both modalities into the construction of a single quantitative image. In particular, since NIR tomography has significant difficulty with the recovery of properties in layered structures, the initial information from MRI can significantly improve the estimation of breast properties, including in localized regions such as tumors.

The design and operation of the NIR-MRI system elements are described in Sec. II. The NIR component is similar to an imaging system described previously,[27] which is currently being evaluated clinically, yet has the unique design feature of having no moving parts in the detection channels, allowing significant reduction in the NIR data acquisition time. In Sec. III we outline the theoretical basis, and the practical application and utilization of image reconstruction in NIR tomography. After applying several approaches to optimizing this hybrid reconstruction, an algorithm is examined that takes advantage of the composite data set. In Sec. IV we discuss system performance and present images of phantom and breast optical properties which are both high resolution and quantitatively accurate.

II. SYSTEM DESIGN

This section describes the four elements that comprise the NIR-MRI system: (A) light delivery, (B) detector array, (C) fiberoptic patient interface, and (D) computer control and electronics. Element (C) extends from (A) and (B) into a MRI scanner for clinical studies, as shown schematically in Fig. 1. Photographs of the rack-mounted system and patient interface are presented in Fig. 2. Section (E) briefly describes phantom fabrication, and its importance in imaging system development and validation.

A. Light delivery

The system deploys six laser diodes: 661 nm (40 mW), 752 nm (50 mW), 785 nm (50 mW), 805 nm (50 mW), 829 nm (50 mW), and 849 nm (50 mW). Each wavelength is amplitude modulated at 100 MHz by mixing a dc current source (LDX-3220, ILX Lightwave, Bozeman, MT) and an ac current from a frequency generator (IFR-2023A, IFR Systems, Wilmington, MA), through a bias T (#5545, Picosecond Pulse Labs, Boulder, CO). Each diode is held in a laser
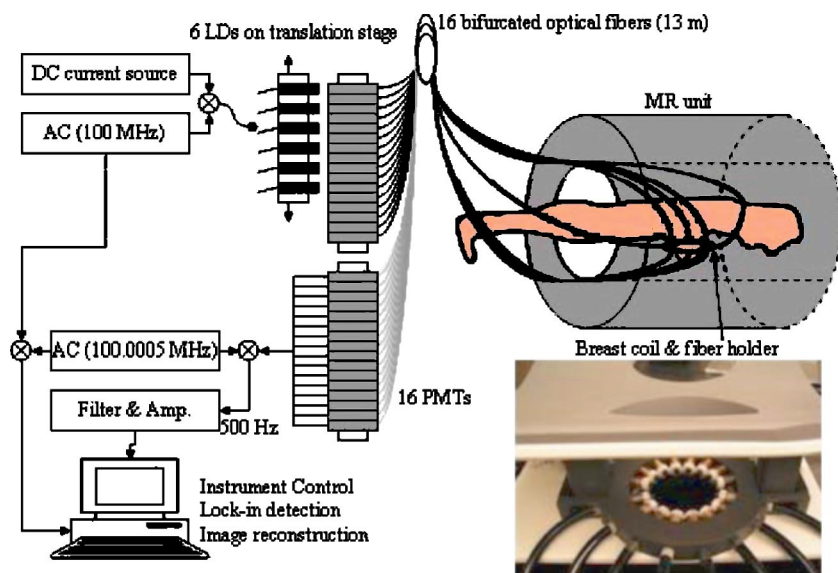
FIG. 1. (Color online) Schematic design of a dual modality NIR-MRI system (left). Frequency-domain NIR tomography is performed inside the MRI unit (upper right). Six laser diodes (660–850 nm) are amplitude modulated, and sixteen projections yield 240 measurements of amplitude and phase of transmitted light. The fiberoptic array is positioned inside the open breast coil, to allow positioning along the length of the pendant breast (bottom right).

tube (Thorlabs, Newton, NJ), and mounted on a linear translation stage (MA2515P5-S2.5 Velmex, Bloomfield, NY). This stage directs a specified wavelength into one of sixteen bifurcated optical fiber bundles which were custom designed for this application (Ceramoptec, East Longmeadow, MA). The 248-piece bundles (0.37 N.A., 0.68 packing fraction) are pure silica core (210 μm), silicone clad (230 μm) fibers suitable for transmission wavelengths from 400 nm to 2400 nm. The source light is delivered through the central seven fibers in each bundle, and the remaining fibers surrounding these are delivered to the detectors. The common end, which makes contact with the tissue, has a diameter of 4 mm. Each fiber bundle is 13 m in length and extends from the instrument cart, located outside of the MR suite, into the bore of the scanner (1.5T whole body imager, GE Medical Systems, Milwaukee, WI) to the patient interface. The efficiency of the optical switching is approximately 50%, yielding an average source power of 15 mW at the tissue surface.

B. Light detection

For each source excitation, light transmission is recorded from 15 surface locations. This signal is measured by 15

photomultiplier tubes (PMT R6357, Hamamatsu, Japan) operating in parallel. The gain of the PMTs is varied to account for the large variation in light level between detectors depending on their distance from the source. The gains are set with PMT modules (HC120, Hamamatsu) by applying computer generated voltages between 0.4 and 1.2 V to their control lines, which sets the anode to cathode voltage between approximately 350 V to 1000 V, respectively. Using the higher gain settings, a PMT can reliably measure optical signals in the pW range. The optimal gain levels are determined prior to each imaging series. Each PMT is fixed to a particular fiber, so it is necessary to switch gains electronically during the course of data collection. A 100 MΩ resistor was used in the dynode chain of each PMT to achieve fast settling times after gain adjustment (200 ms for large gain changes). Electrical heterodyning through rf mixers (Minicircuits, Brooklyn, NY) is used to down convert the 100 MHz PMT signal to a lower frequency (500 kHz). This offset frequency is achieved with a second frequency-synthesizer which is synchronized to the one driving the laser current, and is set to 100.0005 MHz. The resulting offset frequency is filtered and amplified by a 16 channel circuit designed for
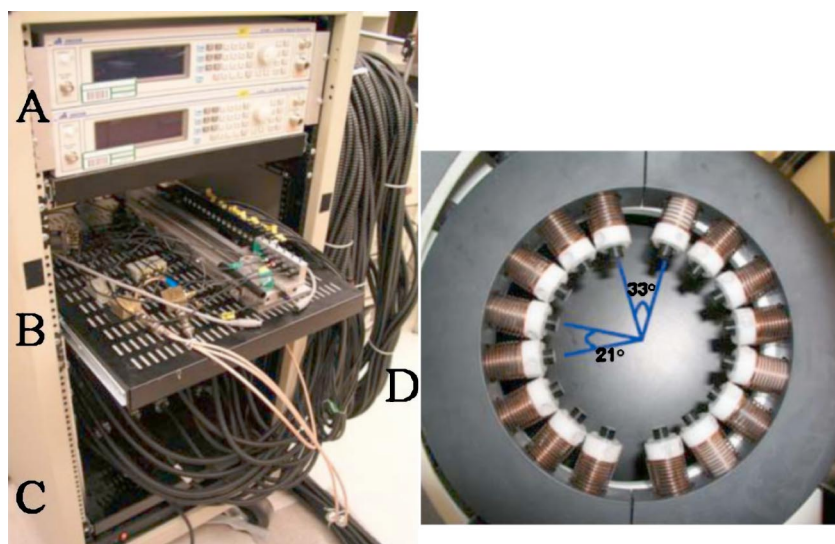

FIG. 2. (Color online) Photograph of the rack mounted, portable system (left). System components are marked, including (A) frequency generators, (B) optical switching stage, (C) PMT detection plate, and (D) optical fibers and patient interface. The fiber-patient interface (at right) can accommodate breasts 6–12 cm in diameter. A close up of the tissue coupling system shows that the fibers are spring-loaded and make light contact with the full circumference of a pendant breast.

this application (Audon Electronics, Nottingham, UK), then read by the computer. Lock-in detection is executed in software to extract amplitude and phase data for each of the detectors in parallel.

C. Fiberoptic patient interface

The MR exam is performed using a breast array coil (MRI Devices, Waukesha, WI) that offers high-resolution imaging. The coil also provides an open architecture, which allows for the integration of the NIR-breast interface shown in Fig. 1. A circular ring machined from polyvinyl chloride (PVC) positions the common ends of the sixteen fibers around the full circumference of the pendant breast. Phosphor bronze compression springs ($k=0.09$ lbs/in., Ace Wire Spring and Form, McKees Rocks, PA) guide each fiber through holes in the ring, into light contact with the tissue surface. The ring separates into equal halves so that it can easily be moved from one breast to the other. The angular separation between each fiber is 21°, except between fibers adjacent to the line of ring devision, where the separation is 33°. The ring can be positioned vertically, such that the plane of measurements intersects the region of interest in tissue. This design allows each fiber to move independently, therefore their radial positions may vary by several millimeters. In order to avoid serious artifacts in reconstructed images, the position of each fiber must be accurately known during data acquisition. Annular fiducial markers (MM 3005, IZI Medical Products, Baltimore, MD) are fixed to each fiber and can be located with submillimeter accuracy in the MRI.

D. Computer system

A PC running Labview software (National Instruments, Austin, TX) is used to control all light delivery and detection equipment. The laser current source and frequency generator parameters are set by a general purpose interface bus (GPIB, NI). The linear translation stage is addressed through the serial port. An analog output board (NI) is used for PMT gain control. A multipurpose data acquisition (DAQ) board acquires the 16 analog input channels and the single reference channel. This board also provides six digital output lines to the high power radio-frequency switch for the laser sources. For each source position, 15 signals from the detector system are amplified by a gain of 1000 and low pass filtered to prevent aliasing prior to the DAQ board using a 16 channel amplifier and filter network mounted in a BNC coupled box (Audon Electronics, Nottingham, UK). Data are acquired for 500 ms, and phase and amplitude of each signal are calculated and written to file. Including the time required to determine optimal gain values, measurement with 6 wavelengths takes approximately 4 min. The MR exam is controlled separately, operated in parallel, and a full volume breast MRI is of similar duration. A FORTRAN, or MATLAB based reconstruction program reads and processes the NIR data.[28–30] MR images are processed off-line with an addition to the MATLAB software package, and incorporated into a modified iterative optical property reconstruction (see Sec. III).

E. Phantom design

Tissue-simulating phantoms with known property distributions, geometries, and imaging orientations are commonly used to validate imaging systems. We have developed a recipe for producing gelatin materials with desired optical properties, and a shelf life of several months.[31] A heated mixture of water, gelatin (G2625, Sigma Inc.), India ink (for absorption), and titanium dioxide powder (for scatter) (TiO_2, Sigma Inc.) is poured into a mold of a desired shape, and solidified by cooling to room temperature. Variation in the water concentration provides MR contrast, and variable gel stiffness. The phantom imaged here (Sec. IV B) combines three gels with different optical properties in an irregular structure.

III. DATA PROCESSING AND IMAGE RECONSTRUCTION

Quantitative NIR imaging with model-based methods requires (A) important instrument calibration procedures, and (B) a reconstruction algorithm that incorporates an accurate model of light propagation in tissue.

A. System calibration

Calibration issues and other practical considerations associated with our NIR imaging approach have been discussed in detail elsewhere.[29] Two important procedures are briefly noted here: (1) detector calibration, and (2) homogeneous phantom calibration. First, the amplitude and phase response of each detection channel must be characterized in order to remove systematic noise in the data acquisition hardware. Each detector is exposed to the same optical signal, and the differences in log amplitude and phase are used as correction factors. The log amplitude response of the PMT is plotted against the log of the input power for each gain setting. A log–log regression is performed and the coefficients are used to calibrate detected PMT amplitude in terms of optical power. The phase does not fluctuate significantly with changing light level for a single gain setting (i.e., minimal phase-amplitude cross-talk), but is altered dramatically with changing gain. Relative phase differences between detectors are stored for calibration. These calibration curves are very similar to those created by McBride et al.[27] This characterization needs to be performed only once as long as the system is not modified.

The second important practical procedure is the correction for inter fiber variations and coupling issues, which is accomplished through a homogeneous phantom calibration process.[29,32] This accounts for offsets due to optical fiber differences in transmission and alignment, as well as any errors in discretization or data-model mismatch. A homogeneous phantom is generally measured each day, and after system changes. The differences between data measured from the phantom, and data calculated from the model are stored and subtracted from measurements of the heterogeneous phantom or tissue under investigation. A homogeneous fitting algorithm is used to determine the μ_a and $\mu_s^/$ values supplied to the model calculation. This algorithm can also be used to calculate the initial optical properties specified in

iterative reconstruction of heterogeneous media. When dealing with tissues having arbitrary shape, the effectiveness of this fitting algorithm and homogeneous phantom calibration hinges on the accurate specification of source and detector locations. The ability to extract accurate fiber positions from MRI scans preserves the integrity of this method for nonuniform boundary data.

B. FEM analysis

Data acquired from the detection system is processed by a FEM based reconstruction algorithm to generate tomographic images of absorption and reduced scattering coefficients simultaneously. The algorithm exploits the frequency-domain diffusion equation approximation to light behavior in a highly scattering medium,[28]

$$ -\nabla \cdot D(\mathbf{r}) \nabla \Phi(\mathbf{r}, \omega) + \left(\mu_a(r) + \frac{i\omega}{c} \right) \Phi(\mathbf{r}, \omega) = S(r, \omega), $$

$$(1)$$

where $S(r, \omega)$ is an isotropic light source at position r, $\Phi(r, \omega)$ is photon density at r, c is the speed of light in tissue, ω is the frequency of light modulation, μ_a is the absorption coefficient, and $D = 1/[3(\mu_a + \mu_s')]$ is the diffusion coefficient. The reduced (transport) scattering coefficient is given by $\mu_s' = \mu_s(1-g)$, where g is the mean cosine of the single scatter function (the anisotropy factor), and μ_s is the scattering coefficient.

For a given μ_a and μ_s' distribution, the diffusion equation is used to predict the optical flux at the detector sites for each source excitation. In the inverse problem (image reconstruction), the goal is the estimation of optical properties at each FEM node, based on measurements of optical flux at the detector sites on the tissue surface. This is achieved numerically by minimizing the difference between the calculated data Φ^C, and measured data, Φ^M, for all source/detector combinations (NM). Typically,

$$ \chi^2 = \sum_{i=1}^{NM} (\Phi_i^C - \Phi_i^M)^2 $$

$$(2)$$

is minimized in a least squares sense by setting the first derivative equal to zero, and using a Newton–Raphson approach to find the set of optical property values which approximate the point of stationarity. We use a Levenberg Marquardt algorithm, and repeatedly solve the equation

$$ a = (J^T J + \lambda I)^{-1} J^T b, $$

$$(3)$$

where $b = (\Phi^C - \Phi^M)^T$ is our data vector, and a is the solution update vector, $a = \lfloor \delta D_j; \delta \mu_{aj} \rfloor$, defining the difference between the true and estimated optical properties at each reconstructed node j. Here, λ is a regularization factor to stabilize matrix inversion and J is the Jacobian matrix for our model, which is calculated using the Adjoint method.[33]

Improving NIR reconstructions by incorporating MRI data has been explored in previous work,[22,23] and by other authors.[13,21,24] Techniques used to produce the images shown in Sec. IV include: (i) accurately defining the imaging volume, (ii) tailoring a regularization scheme which optimizes the reconstructed contrast of a suspicious area in the image,
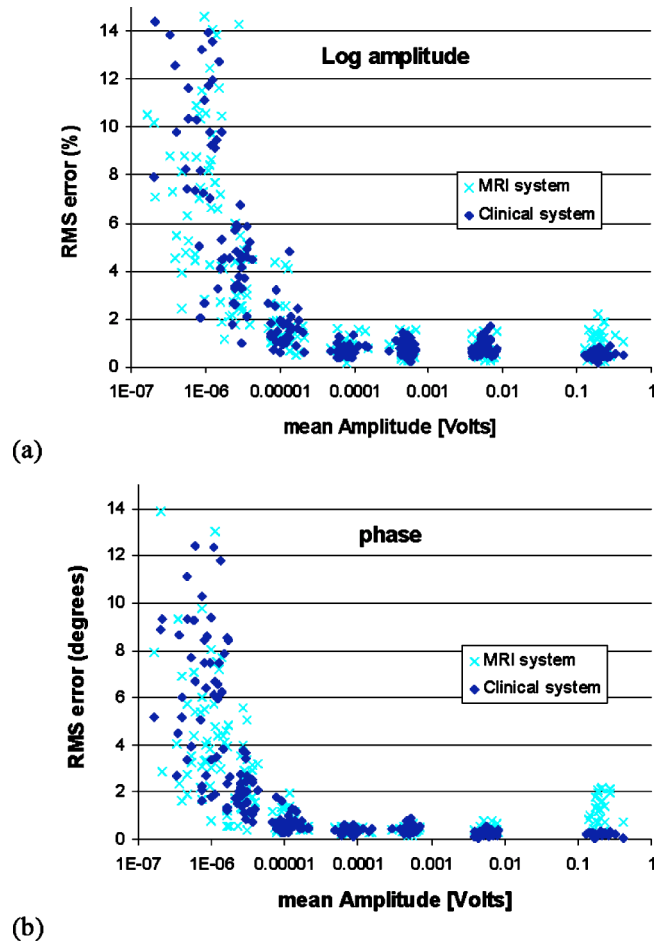

(a)

(b)

FIG. 3. (Color online) Repeatability assessment for (a) log amplitude and (b) phase of NIR component of combined NIR-MRI system and stand-alone NIR tomography system at Dartmouth. The performance of the two systems is comparable. In routine operation, PMT voltage signals are above 1.0×10^{-5} V.

and (iii) reducing the number of unknown parameters by segmenting tissue types visible in the MRI. Defining the imaging volume, (i), is relatively straight forward and can be accomplished by creating a structured finite element mesh from the MRI. This mesh will often contain regional differences depending on tissue types present, and an irregular outer boundary due to impressions caused by fiber-tissue contact. In simulation studies, not presented here, it has been found that image reconstruction accuracy is easily degraded if the mesh (2D or 3D) does not represent the true outer tissue boundary. Step (ii) can be accomplished by changing λI in Eq. (3) to λA, where A is a regularization matrix, or filter matrix. Regularization can be thought of as a smoothing operator, where one can apply selective smoothing by linking together the property updates for all nodes associated with the same region or tissue type. Modifications to the Jacobian matrix size in a parameter reduction technique are used to implement step (iii).[23]

IV. PERFORMANCE AND EXPERIMENTAL RESULTS

In this section we (A) compare measurements from this system to those from a similar NIR tomography instrument

TABLE I. Optical properties at 785 nm for 15 tissue simulating phantoms, and % differences from values determined using another NIR tomography system.

	$\mu_a(mm^{-1})$ (NIR-MRI)	% difference	$\mu'_s(mm^{-1})$ (NIR-MRI)	% difference
Mean	0.0055	−6.2	1.34	9.1
Max	0.0102	−23.4	1.91	29.6
Std. Dev.	0.0024	8.7	0.41	7.9

TABLE II. Approximate optical properties of gelatin phantom.

	Outer layer	Inner layer	Inclusion
$\mu_a(mm^{-1})$	0.0044	0.0062	0.02
$\mu'_s(mm^{-1})$	0.51	0.68	0.9

the two systems, consistent throughout the range of phantom properties. The absorption and scattering coefficients show correlation coefficients of $R^2=0.984$ and $R^2=0.980$, respectively.

described previously[27] for a number of tissue simulating phantoms. NIR-MRI phantom studies are described in (B), and *in vivo* images are shown in (C). For all results presented here, we used a single laser diode (785 nm) for convenience, and 2D modeling and image reconstruction. System performance and image quality at the other five wavelengths are comparable, and 3D imaging is readily achievable.

A. System performance

Measurement repeatability in terms of phase and log amplitude error was assessed by serially imaging a phantom with optical properties similar to those of average breast tissue ($\mu_a=0.004$, $\mu'_s=1.35$). The average rms error at each detector site was determined to be 0.26% in ac intensity and 1.04° in phase. These values compare with those obtained from the system described by McBride *et al.* (0.32% in ac intensity and 0.48° in phase).[27] rms error for each of the 240 source-detector combinations for both systems is plotted versus the PMT signal in Fig. 3. For both phase and amplitude, error sharply increases when incident light falls below approximately 0.5 pW. These points are excluded in the calculation of average rms error. As an additional comparison, we used both devices to measure a collection of homogeneous phantoms ($N=15$) of varying diameters (73–91 mm) and optical properties ($\mu_a=0.0023–0.0102$ mm^{-1}, $\mu'_s=0.33–1.91$ mm^{-1}). After processing the measurements with the calibration procedure described in Sec. III, we used the homogeneous fitting algorithm to determine a single μ_a and μ'_s for each material. Table I shows the optical coefficients obtained with the NIR-MRI system, along with a measure of their discrepancy with those obtained with our stand-alone DOT instrumentation. We observed good agreement between

B. Phantom imaging

Due to the limited spatial resolution of DOT, layered media, small objects, and low contrast heterogeneity pose key challenges in image reconstruction. The capability of the presented system to address these challenges was investigated by imaging a phantom comprised of three gels with different optical properties. The phantom is cylindrical and the boundary between the outer layer and inner layer is irregular. A two centimeter spherical inclusion is embedded within the inner layer. The optical coefficients of each gel are known (Table II), as each material was created using a practiced recipe to give desired values. Furthermore, the true value of each layer was validated by creating a separate homogenous phantom for each layer (at the same time as creating layered phantom) and measuring bulk properties with a homogeneous fitting algorithm. To increase MRI contrast between layers, Omniscan™ (gadodiamide) was added to the inner layer (0.005 g/ml).

A photograph of the phantom, alongside another spherical inclusion is shown in Fig. 4(a). Figure 4(b) shows a T1-weighted, gradient echo MRI (25 ms TR, 3 ms TE, 45° flip angle) crosssection of the phantom in the plane of the optical fibers. This was used to create a 2D structured finite element mesh and to locate the positions of the 16 fibers [Fig. 4(c)]. Fiber fiducials were not used in this experiment, but the 16 impressions caused by each optical fiber are clearly visible around the perimeter of the gel. Each of the three regions are also visible, corresponding to each of the three types of optically variant gel. 3D meshing and imaging is also possible, given that a stack of MR slices represent the full volume
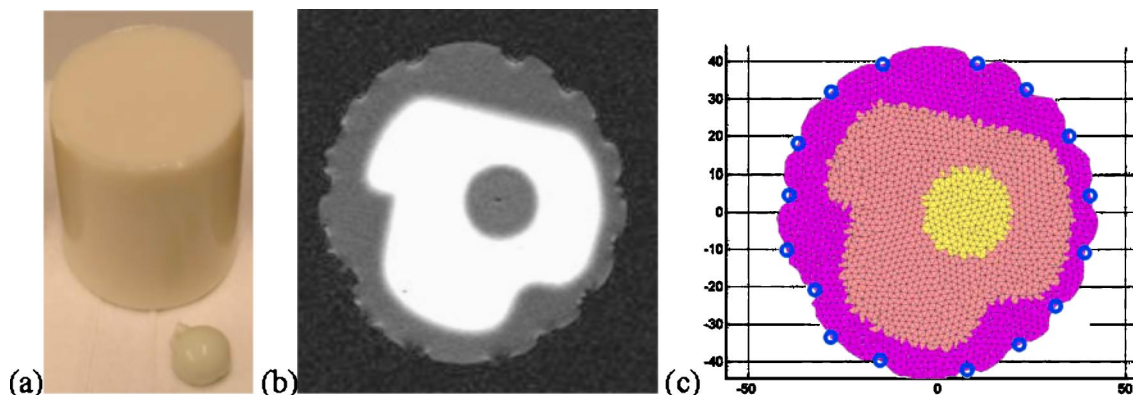

FIG. 4. (Color online) (a) The gelatin phantom. (b) T1-weighted MRI image of the structure of the phantom cross section. The inner layer (light region) contains gadodiamide for MR contrast (0.005 g/ml). The inner inclusion is a 2 cm diameter sphere. (c) Finite element mesh derived from the three-layered structure image in (b). The circles on the outer boundary indicate the fiber locations. Axes are in millimeters.
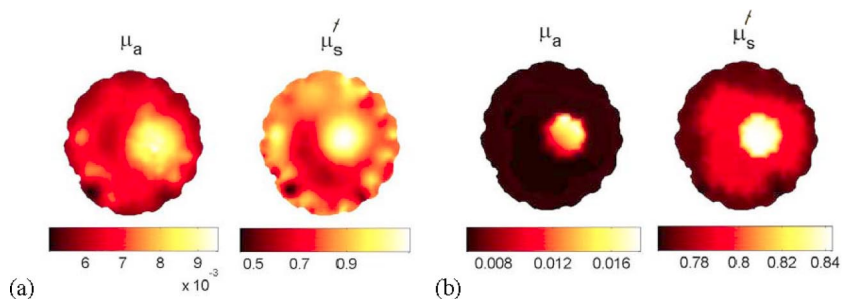
FIG. 5. (Color online) Images in (a) show absorption coefficient (left) and reduced scattering coefficient (right) reconstructions without MRI guidance. In (b), reconstructions improve when the interior structural information of the MRI is incorporated. Comparing these two images, the latter has a reduction in artifacts in the reduced scattering coefficient image, and both the spatial resolution and contrast have improved. The recovered values compare favorably with the approximate true values shown in Table II.

structure of the phantom. The system design allows for NIR data acquisition in multiple planes if desired.

Using log amplitude and phase data, images of optical properties were reconstructed with two different algorithms. The first algorithm solves Eq. (3) without *a priori* guidance, except for the use of the mesh and source locations from Fig. 4(c). The corresponding reconstructed images are presented in Fig. 5(a). The second algorithm uses the layered structure from the MRI to constrain Eq. (3). The regularization parameter associated with each reconstructed node is adjusted based upon its location and area of influence. Lower values are used for small regions close to the center of the reconstructed volume, whereas peripheral regions (which are prone to large artifacts) have larger regularization. A regularization matrix (A), or filter matrix, based upon the *a priori* structural information from the MRI was also used to further improve the algorithm. The optimal values for λ and A were determined in simulation studies of this geometry, using similar contrast and noise levels. These can also be chosen automatically once an empirical knowledge of their effect is established. The images reconstructed from this modified constrained algorithm are shown in Fig. 5(b).

Qualitatively, the algorithm that uses MRI information to guide the iterative process performs much better. The optical property images in Fig. 5(a) are blurry and "edge artifacts" are clearly visible, especially for μ_s'. The absorbing sphere near the center of the phantom is recovered with poor spatial resolution, and its contrast is underestimated. The property maps in Fig. 5(b) have improved resolution. Spatial resolution and contrast of the spherical inclusion are better. As a quantitative measure of the accuracy of image reconstruction, we compute the rms error between the target image and the reconstructions, node by node. This measure indicates a dramatic improvement for the second method [rms(μ_a) $=0.0024$, rms(μ_s')$=0.19$] relative to the first [rms(μ_a) $=0.0034$, rms(μ_s')$=0.25$].

C. *In vivo* imaging

The Institutional Review Board (IRB) at the Dartmouth Hitchcock Medical Center approved this clinical examination protocol, and written informed consent was obtained from all volunteering women. Figures 6(a) and 6(b) show a photograph of a subject lying on the examination platform, and an anatomical axial MR image through the breast. NIR measurements (4 wavelengths in this case) and a full volume MRI (50 coronal slices, 25 ms TR, 6 ms TE, 45° flip angle, 2 mm slice thickness) were obtained in less than 10 min. Fig. 7(a) shows an anatomically coronal MRI with 16 fiducial-marked fibers (appearing as bright white spots outside the breast). The radiographic density of this participant is heterogeneously dense (HD), and a large interior region of glandular tissue is easily defined in the FEM mesh shown in Fig. 7(b).

As with the phantom study, we present images of μ_a and μ_s' at 785 nm reconstructed with two different algorithms. The first result, obtained by solving Eq. (3), without *a priori* guidance, is shown in Fig. 7(c). As expected, we see higher absorption and scatter in the glandular region (central) relative to the adipose tissue (peripheral). However, the region of increase does not span the full area expected, and heterogeneity is visible (especially around the perimeter of the image). The second algorithm assumes homogeneous optical properties for each tissue type, and utilizes parameter reduction,[23] which leads to a "fitting" for four values: $\mu_{a\ \text{adipose}}=0.003$, $\mu_{s\ \text{adipose}}'=0.93$, $\mu_{a\ \text{glandular}}=0.006$, $\mu_{s\ \text{glandular}}'=1.12$ [Fig. 7(d)]. This algorithm is robust to noise and converges after a few iterations. The result is quantita-
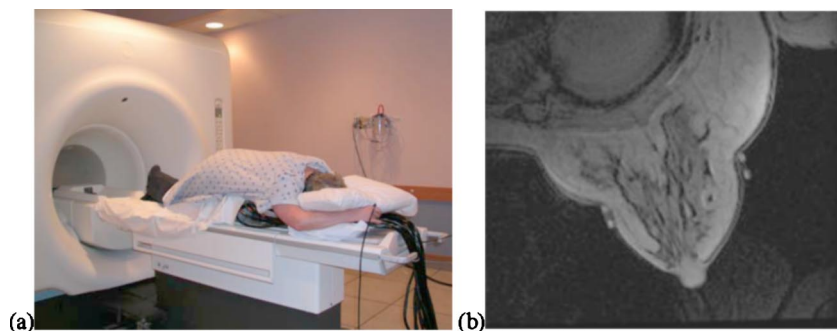

FIG. 6. (Color online) Photograph in (a) shows a female volunteer prepared for the simultaneous MRI-NIR exam. In an anatomically axial T1-weighted MRI slice from the right breast, (b), fiducial markers (outside the breast) indicate the location of the fiber plane.
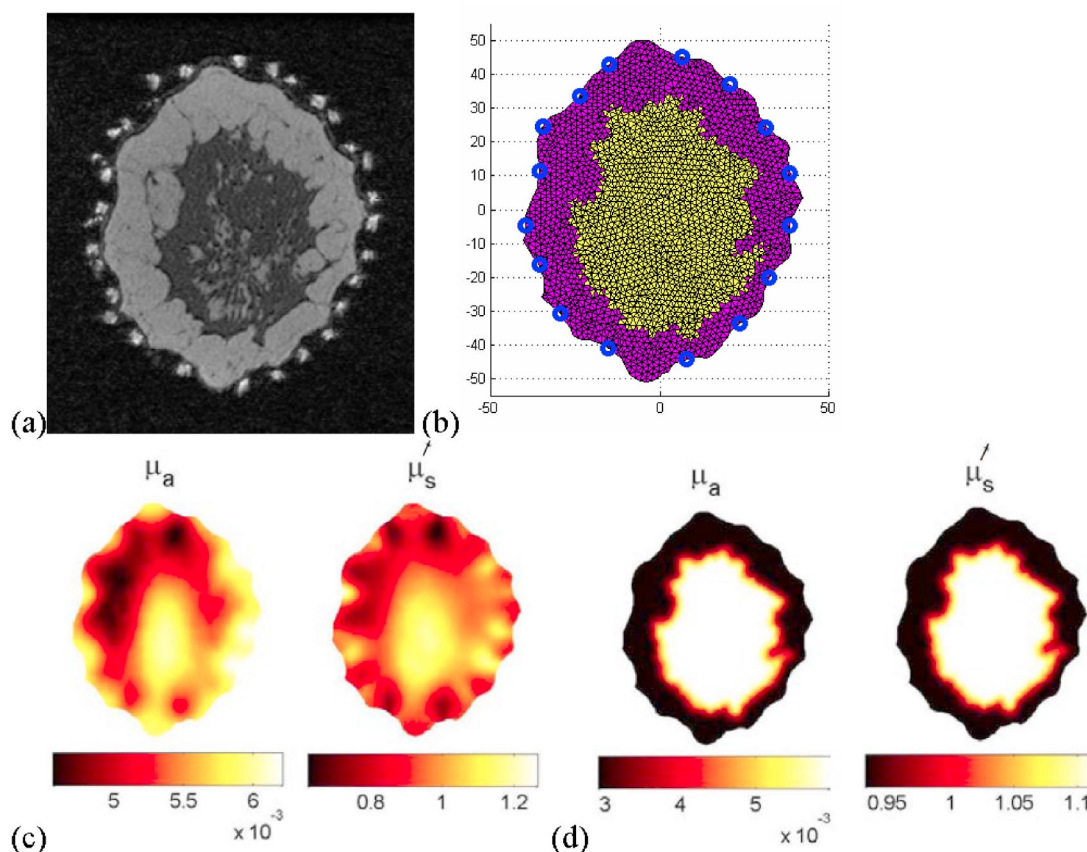
FIG. 7. (Color online) In (a), an anatomically coronal T1-weighted MRI displays adipose (outer) and glandular (inner) tissue types. A two layer structured FEM mesh and source locations, created from (a), is shown in (b). Absorption and reduced scattering coefficient (mm^{-1}) reconstructions in (c) are obtained without utilizing the internal structure of (b). In (d), MRI data guides a two-region parameter fitting algorithm. Relative to (c), resolution has improved and contrast has increased—showing higher absorption and scatter in glandular relative to adipose tissue.

tively logical, and similar values are recovered using spatially varying regularization (as described in the phantom reconstruction).

V. DISCUSSION

This article describes a novel *in vivo* breast imaging system that synergistically combines NIR tomography with MRI. Tissue structures visible with high resolution in MRI can be applied *a priori* to optical property reconstructions from frequency-domain NIR measurements. Thus, the reconstruction process can be optimized to produce high resolution, quantitatively accurate maps of absorption and reduced scattering coefficients, and ultimately physiologically relevant parameters. Various physiological tissue types exhibit significant contrast in the NIR, primarily though, the combined system could be very effective at locating and diagnosing breast tumors.

The NIR component provides multispectral (6 wavelengths) frequency-domain (log amplitude and phase) data from 16 fiber-tissue contact positions around the breast's circumference. Data acquisition is fully automated, and a complete set of measurements (240 source-detector pairs) for one wavelength requires approximately 40 s. Light detection is highly sensitive (subpicowatt limit) with low noise (rms $<0.26\%$, $<1.04°$ in phase). All optical elements and controls are mounted in a portable cart, and operation inside strong magnetic fields is facilitated with long optical fibers and an easy-to-use positioning system/patient interface.

The deployment of dual modality NIR imaging systems in clinical applications has been limited to date, mainly because of the complexity of the image reconstruction problem. Here, a representative phantom and *in vivo* study using one wavelength (785 nm) are presented. We have shown that co-registered MRI validates and improves optical property estimation in 2D tomographic image reconstructions when specialized algorithms are used. Future work will involve 3D modeling and reconstruction, which could further improve both qualitative and quantitative aspects of the recovered coefficient values.

Preliminary results are encouraging, and have allowed us to optimize reconstruction techniques, and automate constraint selection. We have performed several phantom studies, and demonstrated the feasibility of imaging volunteers with healthy breasts. Through the study of more healthy subjects, with different radiographic densities, we aim to compare functional parameters of adipose versus glandular tissue. To test the system's ability at diagnosing tumors, cancer patients will be recruited, and the simultaneous exam will likely involve MR contrast enhancement.

ACKNOWLEDGMENTS

[1] V. Ntziachristos, A. H. Hielscher, A. G. Yodh, and B. Chance, IEEE Trans. Med. Imaging **20**, 470 (2001).

[2] B. W. Pogue, S. P. Poplack, T. O. McBride, W. A. Wells, O. K. S. Osterman, U. L. Osterberg, and K. D. Paulsen, Radiology **218**, 261 (2001).

[3] S. Srinivasan, B. W. Pogue, S. Jiang, H. Dehghani, C. Kogel, S. Soho, J. J. Gibson, T. D. Tosteson, S. P. Poplack, and K. D. Paulsen, Proc. Natl. Acad. Sci. U.S.A. **100**, 12349 (2003).

[4] B. J. Tromberg, N. Shah, R. Lanning, A. Cerussi, J. Espinoza, T. Pham, L. Svaasand, and J. Butler, Neoplasia **2**, 26 (2000).

[5] S. R. Arridge, Inverse Probl. **15**, R41 (1999).

[6] H. Dehghani, B. W. Pogue, S. Jiang, B. A. Brooksby, and K. D. Paulsen, Appl. Opt. **42**, 3117 (2003).

[7] V. Chernomordik, A. H. Gandjbakhche, M. Lepore, R. Esposito, and I. Delfino, J. Biomed. Opt. **6**, 441 (2001).

[8] D. A. Boas, K. Chen, D. Grebert, and M. A. Francheschini, Opt. Lett. **29**, 1506 (2004).

[9] B. W. Pogue, S. Jiang, H. Dehghani, C. Kogel, S. Soho, S. Srinivasan, X. Song, T. D. Tosteson, S. P. Poplack, and K. D. Paulsen, J. Biomed. Opt. **9**, 541 (2004).

[10] A. Li, E. L. Miller, M. E. Kilmer, T. J. Brukilaccio, T. Chaves, J. Stott, Q. Zhang, T. Wu, M. Choriton, R. H. Moore, D. B. Kopans, and D. A. Boas, Appl. Opt. **42**, 5181 (2003).

[11] Q. Zhu, N. G. Chen, and S. H. Kurtzman, Opt. Lett. **28**, 337 (2003).

[12] B. W. Pogue, H. Zhu, C. Nwaigwe, T. O. McBride, U. L. Osterberg, K. D. Paulsen, and J. F. Dunn, Oxygen Transport to Tissue, Vol. XXIV, p. 215 (2002).

[13] V. Ntziachristos, A. G. Yodh, M. D. Schnall, and B. Chance, Neoplasia **4**, 347 (2002).

[14] G. Gulsen, H. Yu, J. Wang, O. Nalcioglu, S. Merritt, F. Bevilacqua, A. J. Durkin, D. J. Cuccia, R. Lanning, and B. J. Tromberg, Technol. Cancer Res. Treat. **1**, 1 (2002).

[15] K. D. Paulsen and H. Jiang, Med. Phys. **22**, 691 (1995).

[16] M. Tatsumi, C. Cohade, Y. Nakamoto, and R. L. Wahl, Radiology **229**, 831 (2003).

[17] R. L. Barbour, H. L. Graber, J. Chang, S. S. Barbour, P. C. Koo, and R. Aronson, IEEE Comput. Sci. Eng. **2**, 63 (1995).

[18] A. H. Barnett, J. P. Culver, A. G. Sorensen, A. Dale, and D. A. Boas, Appl. Opt. **42**, 3095 (2003).

[19] V. Ntziachristos, X. H. Ma, and B. Chance, Rev. Sci. Instrum. **69**, 4221 (1998).

[20] M. Torregrossa, C. V. Zint, and P. Poulet, Opt. Tomography and Spectroscopy of Tissue V (2003).

[21] M. Schweiger and S. R. Arridge, Phys. Med. Biol. **44**, 2703 (1999).

[22] B. W. Pogue, T. O. McBride, C. Nwaigwe, U. L. Osterberg, J. F. Dunn, and K. D. Paulsen, Proc. SPIE **3597**, 484 (1999).

[23] B. A. Brooksby, H. Dehghani, B. W. Pogue, and K. D. Paulsen, IEEE J. Sel. Top. Quantum Electron. **9**, 199 (2003).

[24] N. G. Chen, P. Guo, S. Yan, D. Piao, and Q. Zhu, Appl. Opt. **40**, 6367 (2001).

[25] B. W. Pogue, T. O. McBride, J. Prewitt, U. L. Osterberg, and K. D. Paulsen, Appl. Opt. **38**, 2950 (1999).

[26] M. Belge, M. E. Kilmer, and E. L. Miller, Inverse Probl. **18**, 1161 (2002).

[27] T. O. McBride, B. W. Pogue, S. Jiang, U. L. Osterberg, and K. D. Paulsen, Rev. Sci. Instrum. **72**, 1817 (2001).

[28] H. Dehghani, B. W. Pogue, S. P. Poplack, and K. D. Paulsen, Appl. Opt. **42**, 135 (2003).

[29] T. O. McBride, B. W. Pogue, U. L. Osterberg, and K. D. Paulsen, Oxygen Transport to Tissue Vol. XXIV, p. 85 (2002).

[30] B. W. Pogue, S. Geimer, T. O. McBride, S. Jiang, U. L. Osterberg, and K. D. Paulsen, Appl. Opt. **40**, 588 (2001).

[31] D. Li, P. M. Meany, T. D. Tosteson, S. Jiang, T. Kerner, T. O. McBride, B. W. Pogue, A. Hartov, and K. D. Paulsen, Med. Phys. **30**, 2194 (2003).

[32] S. Jiang, B. W. Pogue, T. O. McBride, M. M. Doyley, S. P. Poplack, and K. D. Paulsen, J. Electron. Imaging **12**, 613 (2003).

[33] S. R. Arridge and M. Schweiger, Appl. Opt. **34**, 8026 (1995).

Measurement optimization for Near-Infrared optical tomography

Yalavarthy Phaneendra Kumar, Hamid Dehghani, Brian W. Pogue, and Keith D. Paulsen

Thayer School of Engineering, Dartmouth College, Hanover, NH 03755

ABSTRACT

The image resolution and contrast in Near-Infrared (NIR) tomographic image reconstruction is in part affected by the number of available boundary measurements. In the presented study, singular-value decomposition (SVD) of the Jacobian has been used to find the benefit of the total number of measurements that can be obtained in a two-dimensional (2D) and three-dimensional (3D) problem. Reconstructed images show an increase in improvement in the reconstructed images when the number of measurements are increased, with a central anomaly showing more improvement as compared to a more superficial one. It is also shown that given a 2D model of the domain, the increase in amount of useful data drops exponentially with an increase in total number of measurements. For 3D NIR tomography use of three fundamentally different data collection strategies are discussed and compared. It is shown that given a 3D NIR problem, using three planes of data gives more independent information compared to the single plane of data. Given a three planes of data collection fibers, it is shown that although more data can be collected in the out-of-plane data collection strategy as compared to the only in-plane case, the addition of new data does not increase image accuracy dramatically where as it increases the data collection and computation time.

Keywords: Near infrared optical tomography, optimization, singular-value analysis.

1. INTRODUCTION

Near infrared (NIR) optical tomography uses measurements taken from the boundary of the domain for reconstructing the distributions of optical absorption (μ_a) and reduced scattering coefficient ($\mu_s^/$) of the given domain. Major applications of NIR optical imaging includes breast and brain imaging[1-4]. NIR light is non-invasive and non-ionizing and the optical properties of tissue can give clinically useful information regarding tissue physiology and state, such as chromophore concentration and oxygen saturation[1-3]. Typically a source fiber/fiber-bundle carrying NIR light (wavelengths 650-900 nm) illuminates the domain to be imaged and light is collected on the boundary using a set of fiber-bundles.

Light scattering being the dominant mechanism in the tissue, makes the reconstruction of optical parameters a difficult problem. In general practice, a model-based iterative algorithm is used for reconstructing these optical parameters (μ_a & $\mu_s^/$). Inherently NIR optical tomography being a non-linear, ill-posed and ill-conditioned problem, more number of boundary measurements can improve the image resolution[5, 6]. However, due to instrumentational constrains, such as light-collection/delivery fiber size and the image geometry makes the maximum number of measurements limited. In a clinical set-up, there are additional constraints such as data acquisition and image computation time. It is also worth noting that in a model-based iterative algorithm, more number of measurements corresponds to a longer computation time.

Optimizing the fiber positions for NIR tomography has been investigated previously by various groups[7-11]. Singular-value decomposition (SVD) analysis of the Jacobian (also known as Weight or Sensitivity matrix) has been employed by Culver et al[11] in the optimization of the detector placement in the reflectance and direct transmittance geometries of a homogeneous medium (slab geometry), and indicated that this could be extended to arbitrary geometries with heterogeneous tissue volumes. Still there are many unknowns regarding the appropriate number of measurements required to get the best reconstructed image. Even though light propagation in tissue is three-dimensional (3D) [12-18], conventional methods use only two-dimensional (2D) models[1, 2, 19-23]. This is mainly due to the complexity and computation effort involved in reconstructing 3D images. 3D NIR imaging problem being more ill-determined compared to the 2D one, as increase in the number of measurements should lead to a better image resolution. There exits lot of ambiguity in quantifying the exact number of measurements for getting the best reconstructed image for a given domain, a problem addressed in this work.

---

* Phaneendra.K.Yalavarthy@Dartmouth.edu, Tel: (603) 646-2685, Fax: (603) 646-3856

The presented work addresses the issues such as number of useful measurements in 2D and 3D NIR optical tomography for a given domain. For 2D case, a circular domain is considered and similarly for 3D case a cylinder of same diameter considered. In 2D the impact of increasing total number measurements on the sensitivity and over all reconstructed image space is shown. In 3D case, three entirely different imaging strategies are considered (details are given in Sec. 2), where a comparison and contrast of all these strategies is presented. To illustrate the effectiveness of three-dimensional imaging, a comparison with the two-dimensional imaging problem is also presented.

2. METHODS

Conventional numerical methods for the forward calculations in NIR imaging use the Finite Element Method (FEM), which is considered as a flexible and accurate approach to modeling heterogeneous domains with arbitrary boundaries. Light transport in tissue can be described by the Diffusion Approximation (DA) to the Radiative Transfer Equation (RTE) [20]:

$$- \nabla . \kappa(r) \nabla \Phi(r, \omega) + \left(\mu_a(r) + \frac{i\omega}{c} \right) \Phi(r, \omega) = q_0(r, \omega) \tag{1}$$

where $\Phi(r, \omega)$ is the photon density at position r and modulation frequency ω (typically 100 MHz, as used throughout this work), and $\kappa = 1/[3(\mu_a + \mu_s^{/})]$, the diffusion coefficient, where μ_a and $\mu_s^{/}$ are the probabilities per unit length of absorption and transport scattering, respectively, and q_0 is an isotropic source term. In this work, we used a Robin (Type III) boundary condition is used which best describes the light interaction from a scattering medium to the external air boundary[24]. The calculated boundary data values with a frequency domain system are the amplitude and phase of the signal, from which the diffusion and absorption coefficients are reconstructed.

The Jacobian is calculated using the Adjoint method[25], which has dimension of (2xSxD) by (2xN), where S & D are the number of sources and detectors corresponding to each source respectively. N represents the number of nodes in the mesh used for the reconstruction. Here the Jacobian maps the changes in log amplitude and phase (2xSxD) to both absorption and diffusion changes at each node of the FEM model (2xN). The Jacobian which maps the change in detected signal to image space, consists of four parts:

$$\mathbf{J1} \equiv \frac{\partial \ln I}{\partial \kappa} \; ; \; \mathbf{J2} \equiv \frac{\partial \ln I}{\partial \mu_a} \; ; \; \mathbf{J3} \equiv \frac{\partial \theta}{\partial \kappa} \; ; \; \mathbf{J4} \equiv \frac{\partial \theta}{\partial \mu_a} \tag{2}$$

In this analysis, only $\mathbf{J2}$ is considered (with a dimension of (SxD) by N), which maps a small change in the absorption coefficient to a small change in measured log intensity of the signal. Since all parts of the complete Jacobian show similar results, the discussion is limited to the results only of $\mathbf{J2}$, and shall henceforth referred as $\mathbf{J}$.

In the reconstruction procedure presented here, a Levenberg-Marquadt algorithm is used[10] for calculating the estimates of μ_a only, which is an iterative procedure solving:

$$[\Delta\mu_a] = [J^T J + \lambda I]^{-1}. J^T b \tag{3}$$

Here, $[\Delta\mu_a]$ is an update vector for the absorption coefficient, I is an identity matrix and λ is a regularization parameter[14]. Also, b = [y - F(μ_a)], where y is the measured (or simulated) heterogeneous boundary data (log amplitude) and F(μ_a) is the forward data for the current estimate of μ_a. In all of the presented work using simulated data, 1% randomly distributed noise is added to the amplitude, which is a typical noise observed in experimental data[2].

In this work, for two-dimensional case a circular object with a diameter of 86 mm centered at (x=0, y=0) and with homogeneous optical properties of $\mu_a = 0.01$ mm^{-1} and $\mu_s^{/} = 1$ mm^{-1} is considered. The light collection/delivery fibers are arranged in a circular equally spaced fashion, where one fiber is used as the source while all other fibers are used as detectors, to give 'P' number of measurements (where P= M(M-1), where M is number of fibers). In all the simulations, the source is a Gaussian source of Full Width Half Maximum (FWHM) 3mm, and it is placed one transport scattering distance within the external boundary. For 3D case a cylindrical medium with a diameter of 86 mm having height of 100 mm centered at (x=0, y=0, z=0), with homogeneous optical properties of $\mu_a = 0.01$ mm^{-1} and $\mu_s^{/} = 1$ mm^{-1}. The light collection/delivery fibers are arranged in a circular and equally spaced fashion and are in either a single plane of 16 fibers (z = 0mm) or 3-palnes of 16 fibers per plane (z = 0, -10, 10mm), totaling 48 fibers, (Fig. 1). FEM mesh of 20160 nodes corresponding to 103680 linear tetrahedral elements is used in the 3D case. Specifically for the 3D model three different strategies for data collection are considered:

a) Single layer: The 16 fibers are arranged in a circular and equally spaced fashion in a single Layer-I (Fig. 1), where one fiber is used at a time as the source while all other fibers are used as detectors, to give 240 (16x15) amplitude measurements.

b) Three layers of in-plane: The 48 fibers are arranged in a circular equally spaced fashion in all three layers (Layers-I, II & III of Fig. 1), giving 16 fibers per plane, where one fiber is used at a time as the source while only those fibers in the same "source fiber layer" are used as detectors, to give 720 (3x16x15) amplitude measurements.

c) Three layers of -out-of-plane: Same as above, except when one fiber is used at a time as the source, all other fibers in all three planes are used as detectors. This leads to 2256 (48x47) amplitude measurements.
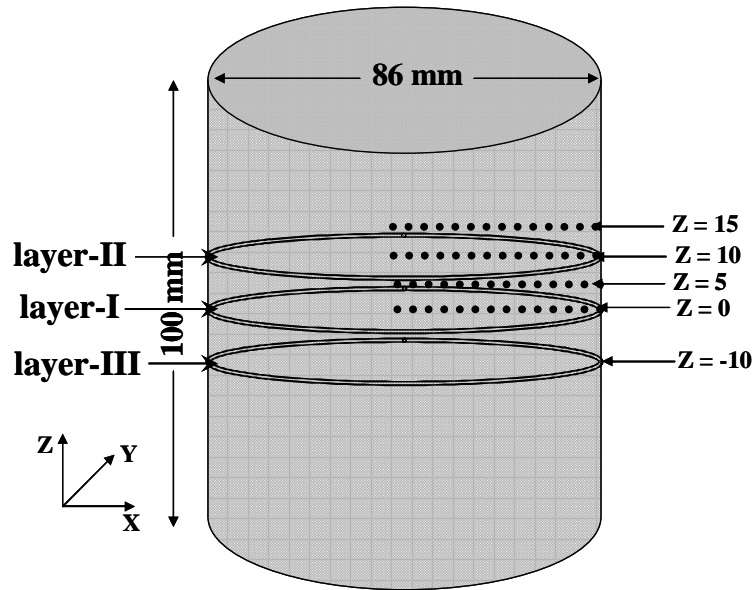
Figure 1. Schematic diagram of data collection geometry used in three-dimensional (3D) simulation studies.

2.1. Singular-Value analysis

Singular-Value (SV) analysis for the Jacobian matrix is explained in detail elsewhere[10]. Using SV-analysis, the Jacobian is decomposed into:

$$\mathbf{J = USV}^{\text{T}} \tag{4}$$

where, U & V are orthonormal matrices containing the eigenvectors of J and S is a diagonal matrix containing the singular values of J. Vectors of U and V correspond to the modes in the detection space and image space, respectively, while the magnitude of the singular values in S represents the importance of the corresponding eigenvectors in U and V. More nonzero singular values indicate more modes are effective in between the two spaces, which bring more detail and improve the resolution in the space. There are normally P nonzero singular values in the diagonal matrix and these values are sorted in decreasing order. Typically only those singular values are used which are above the expected noise level (in this case, 1 % noise in amplitude) as containing useful information. Thus, it is possible to determine whether increasing the number of measurements gives rise to an increase in the number of useful singular values, which indicates improvement in image resolution.

Percentage of useful measurements with respect to total number of measurements are

$$\text{Useful measurements (in \%)} = \left[\frac{\text{Useful no. of singular values}}{\text{Total no. of singular values}} \right] \text{X100} \tag{5}$$

The condition number of the Jacobian is also calculated, which indicates the stability of the inverse problem in each of the models. Condition number (C) of matrix A is defined as

$$C = \| A \| \| A^{-1} \| \tag{6}$$

Where, $\| . \|$ indicates the matrix norm. C is a measure of the sensitivity of the solution of $J\Delta\mu_a = \Delta b$ to perturbations of $\Delta\mu_a$ or Δb. A well-posed problem will have a condition number of 1, and a larger condition number indicates high instability in the inverse problem. Magnitude of the largest singular value is also calculated, which gives the importance of the contribution of that first and most dominant mode in the reconstruction image space.

2.2 Reconstruction examples

As only **J2** is used for the reconstruction in this study, only the absorption coefficient profiles are reconstructed for 2D case. For the 2D circular domain, the circular anomaly of diameter of 10 mm having an absorption contrast of 2:1 compared to its background is considered. For the forward calculations a mesh of 1785 nodes corresponding to 3418 linear triangular elements is used and the pixel basis of 30x30 is utilized for the reconstruction[6]. A total of 4 separate positions of absorption inhomogeneity are considered with its center x, y at (0, 0), (12,0), (24,0), (30, 0) for various number of measurements (P) starting from 56 to 4032 corresponding to 8 to 64 source/detector fibers. The natural logarithm of rms error of the horizontal cross-section between the reconstructed and original absorption profile was calculated for each case.

3. RESULTS

Useful number of singular values of Jacobian (part of the Jacobian-**J2**) which are above the noise level (1%) are calculated, which indicates the effective number of measurements which will have a useful contribution to the reconstructed image space, and the reconstructed image quality.

3.1 Two-dimensional (2D) case

A mesh with 1785 nodes corresponding to 3418 linear triangular elements is used for the calculation of Jacobian and the expected noise level in the measurements was assumed to be at 1%. The number of useful singular values that are above the noise level are given in Table-1. Useful measurements in percentage (given by Eq. 5) for each set of measurements is also presented in Table-1.

Table-1. Results of Singular-value analysis of two-dimensional circular geometry.

Number of source/detector fibers (M)	8	16	24	32	40	48	56	64
Number of measurements (P)	56	240	552	992	1560	2256	3080	4032
Useful Singular values	38	91	111	121	123	133	137	139
Useful measurements (in %)	67.86	37.92	20.12	12.2	7.89	5.9	4.45	3.45

The reconstruction of a circular object with a centralized absorption anomaly of diameter of 10mm using different number of measurements, along with original μ_a distribution, is shown in Fig. 2. The contrast of the inhomogeneity to background is 2:1. For these reconstructions a pixel basis of 30x30 elements was used. A comparison with the same kind of effort as above for an circular absorption inhomogeneity having a diameter of 10mm and centered at (30,0) is also shown in Fig. 2.

In order to better investigate the improvements in the reconstructed images, the rms error was calculated in the horizontal cross-section (as depicted by horizontal lines on original μ_a distribution of Fig. 2) through the center of domain between the original and reconstructed object profiles for each set of measurements. These results are presented in Table-2. Other rows in this Table-2 are the results from similar cases where the absorption inhomogeneity is placed at different distances from the center. In all these reconstructions, only the absorption coefficient was reconstructed using log amplitude data. The initial regularization parameter for all these cases were kept at 10, and the iteration number is such that the projection error (residual) did not improve more than 1%.
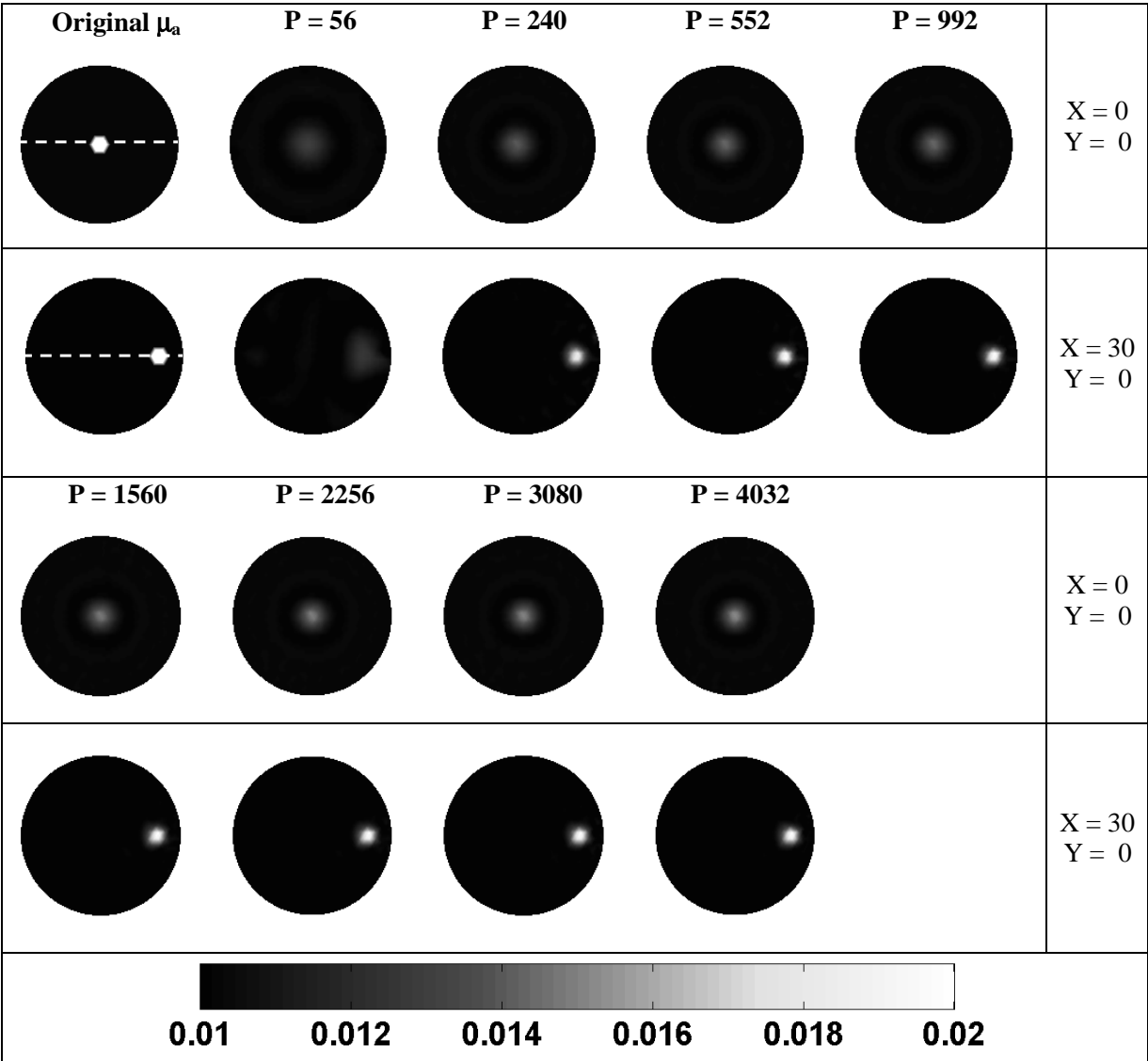
Figure 2. Comparison of the reconstructions of μ_a distribution (in 2D) using log amplitude for an object with an absorbing inhomogeneity at center and 30mm from the center, using various number of measurements. The original μ_a distribution is shown as the first image. The remaining images are the reconstruction results (using 1% noise added to simulated data), where the number of measurements used in the reconstruction are shown at the top of each image.

3.2 Three-dimensional (3-D) case

Table-3 summarizes the results of the methods discussed in Sec. 2.1. The number of useful singular values are higher for the three layer out-of plane strategy. Useful percentage of measurements is higher for the 3D single pane of data, where as the condition number is very high for the 3D three-layer out of plane case. Data is also included for comparison purposes of the two-dimensional case discussed above for 16 source and detector fibers (240 measurements).

Table-2. rms error in the horizontal cross-section of μ_a at y = 0 (as shown in original μ_a distribution of Fig. 2) versus number of measurements for various positions of an absorption inhomogeneity.

Number of measurements (P)	56	240	552	992	1560	2256	3080	4032
rms error (inhomogeneity – X = 0; Y = 0)	0.002487	0.002208	0.002116	0.002117	0.002005	0.00197	0.00194	0.001913
rms error (inhomogeneity – X = 12; Y = 0)	0.002624	0.001984	0.00189	0.001952	0.001904	0.001867	0.001833	0.001805
rms error (inhomogeneity – X = 24; Y = 0)	0.002543	0.001571	0.001218	0.001219	0.001238	0.001173	0.001185	0.001214
rms error (inhomogeneity – X = 30; Y = 0)	0.002568	0.00132	0.001143	0.001147	0.001145	0.001137	0.001141	0.001139

Table-3. Comparison of different data acquisition strategies (in 3D) on a cylindrical geometry (Fig. 1).

	Number of Unknowns	Number of Measurements	Number of Useful Singular values	Useful measurements (in %)	Magnitude of largest singular value	Condition No
2D	1785	240	91	37.9167	796.418	30706140
3D 1layer	20163	240	107	44.5833	117.125	39150
3D 3layer-inplane	20163	720	269	37.3611	163.99	262980
3D 3layer-out of plane	20163	2256	328	14.5390	304.562	58799540

.

4. DISCUSSION

In the 2D case, the number of useful singular values, which are above noise level (1% in amplitude) increased with increasing number of measurements, as evident from Table-1. The increase is not in proportion to the measurements increase. Further, the percentage of useful measurements (useful singular values) drops exponentially as the number of measurements is increased. In this analysis, only one component of the full Jacobian matrix, **J2** (in Eq. 2) is used, so reconstruction of only μ_a using log amplitude data is done using a forward mesh of 1785 nodes and a reconstruction basis 30 by 30-pixel. Noise added data were simulated for various radial positions of absorption inhomogeneity with a contrast of 2 with respect to the background and having a diameter of 10 mm. The rms error was calculated and presented in Table-2 as the difference in the original and the reconstructed horizontal cross-sections of each image, as a function of number of measurements. The results show that although there is a decrease in rms error as the number of measurements is increased, the improvement in the reconstructed images is not significant for measurements greater than 552 (corresponding to 24 fibers). This is in good agreement with the singular-value analysis.

In order to better understand the effect of increasing the number of measurements on total sensitivity for a given model the magnitude of the Jacobian was examined as a function of number of measurements for the mesh. To achieve this, the horizontal cross-section of the whole Jacobian is plotted (Fig. 3), which is summed up over all number of measurements, from center (x = 0, y = 0) to boundary (x = 43, y = 0), and examined as the number of measurements increased. As the Jacobian provides relative sensitivity, the cross-section plot is normalized in each case, with respect to its magnitude at the center of the model. This is plotted as a function of number of measurements (56 to 4032). Fig. 3 shows that the sensitivity of the domain becomes more uniform by increasing the sensitivity deep within the model, while suppressing the hypersensitivity near the external boundaries. This is also evident from Table-2, that for a central

anomaly, the rms error continues to decrease with increasing number of measurements, whereas for an anomaly near the boundary the rms error does not improve more that 0.5% with respect to 552 measurements.
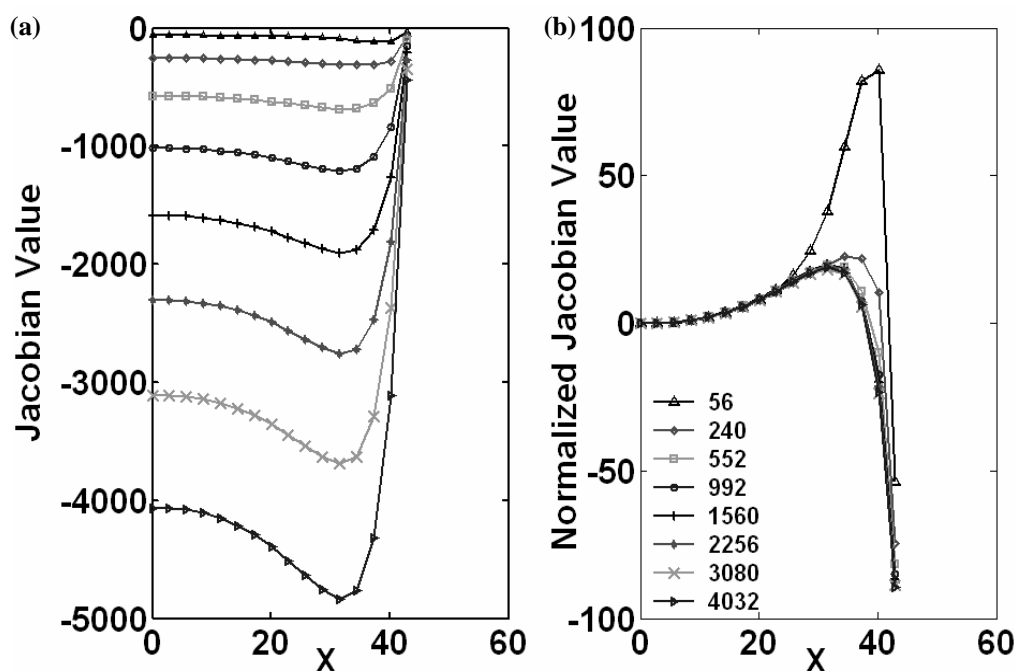

Figure 3. (a). The horizontal cross-sectional plot of the sum of Jacobian for the 2D model is shown, from center (x = 0) to the boundary (x = 43) at y = 0. These are plotted for various numbers of measurements, as listed in the legend, shown in (b). In (b) the normalized Jacobian is plotted as normalized to its central value (at x = 0, y = 0) for each of its corresponding number of measurements.

From Table-3 (3D case) it can be seen that three layers of out-of-plane measurements yields more number of useful singular values, but the useful percentage of the total measurements is below 15%. More measurements corresponds to more data acquisition and computation time. Non-linear iterative image reconstruction procedures in NIR imaging use repeated calculation of the forward data. Therefore increasing the number of sources and measurements dramatically increases the computation time. In comparing the three layer in-plane and three layer out-of-plane strategies, having more than three times the measurements in the latter case does not improve the useful singular values in the same proportion dramatically. The improvement in the number of useful singular values is not significant if the data acquisition time is considered as well as the computation time. The magnitude of the singular values indicates the importance of that eigenvector in the image space, which is directly related to image quality. To compare the magnitude of the largest singular value, even though it is at its highest for the three layer out-of-plane strategy, it should be noted that only 3 of the singular values are above 163.99 (magnitude of largest singular value of 3D 3layer-inplane), indicating that there would not be dramatic differences in the image resolution in both these cases. If we compare magnitude of largest singular value in 2D & 3D, in 2D the magnitude is higher, whereas the number of useful singular values are lower than 3D, indicating that the modes that contribute to image space are fewer and the quality of the reconstructed image in 2D is going to be lower than 3D. From Table-3, it can also be seen that the useful number of measurements is less than 15% for three layer out-of-plane strategy. It should be noted that there is always a trade-off between image quality and computation time. Therefore having out-of-plane data increases the image resolution, but taking into consideration the overall computation time, this improvement is perhaps not so significant.

The plots of the 3D Jacobian magnitude as normalized (using the same methods discussed above for the 2D case) to the value at the center of the model in the X-Y plane is shown in Fig. 4. Fig. 4 shows that, all the three strategies of data collection in 3D are hypersensitive (in X & Y direction) at the boundary and it is even more for the 3D single-plane case. By increasing the number of measurements, the hyper sensitivity near the boundary is decreased. Still the sensitivity is high at the boundary compare to the center but it is less in comparison to the single layer case. Figs. 4(b-d) also indicate

that if the anomaly does not lie in the imaging plane, the single-layer data collection strategy sensitivity is poor and this strategy will fail to reconstruct the anomaly. However, if the location of the anomaly is known, using a single plane of data is sufficient to reconstruct the image. These figures also show that although the sensitivity is still higher at the boundary, there is no significant difference in the sensitivity behavior between three layer in-plane or out-of-plane strategy. Overall, having out-of-plane data increases the image resolution, but taking into consideration the overall computation time, this improvement is perhaps not so significant.
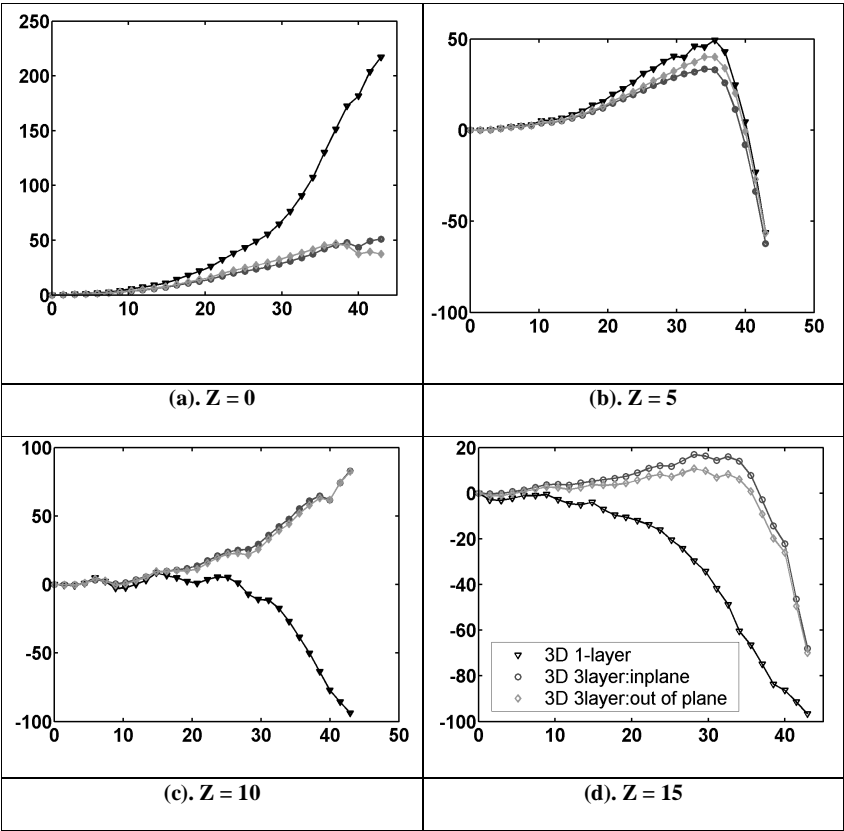
Figure 4. Normalized cross-section for the 3D model in X-Y plane of total sensitivity across dotted line in Fig. 1 from x= 0 to x = 43 (center to boundary) at y = 0 normalized with sensitivity at the origin.

5. CONCLUSIONS

Increasing the number of measurements increases the amount of information available, which is biased to the central region in the 2D case. Reconstructed images quality may not improve after a certain maximum number of measurements, as the most of the modes contributing to the reconstructed image space will be below noise level. Note that all this analysis is domain specific. This work in 3D case has shown the benefits and drawbacks of multi-plane data collection as well as the use of in-plane versus out-of-plane data measurements. It has been shown that the use of three-planes of data yields more number of useful information compared to the single-plane of data. The use of in-plane and out-of-plane data (in three-panes of data collection case) has been addressed and is shown that although the use of out-of-plane data provides more independent and useful information for image reconstruction, the magnitude of this additional information does not provide enough advantages to perhaps warrant the additional data acquisition and image computation time. Finally, it should be noted that the results presented here can be modified for complex and non-symmetrical models to allow the best possible data collection strategy for any imaging problem, and that the reconstructed images can be improved dramatically by use of more sophisticated algorithms.

6. ACKNOWLEDGEMENTS

7. REFERENCES

1. Boas, D.A., D. H. Brooks, E. L. Miller, C. A. DiMarzio, M. Kilmer, R. J. Gaudette, and Q. Zhang, *Imaging the body with diffuse optical tomography.* IEEE Signal Processing Magazine, 2001. **18**(6): p. 57-75.
2. Pogue, B.W., et al., *Instrumentation and design of a frequency-domain diffuse optical tomography imager for breast cancer detection.* Opt. Express, 1997. **1**(13): p. 391-403.
3. Srinivasan, S., Pogue, B. W., Jiang, S., Dehghani, H., Kogel, C., Soho, S., Gibson, J. J., Tosteson, T. D., Poplack, S. P., and Paulsen, K. D., *Interpreting Hemoglobin and Water Concentration, Oxygen Saturation and Scattering Measured In Vivo by Near-Infrared Breast Tomography.* PNAS, 2003. **100**(21): p. 12349-12354.
4. Chance, B., *Near-infrared images using continuous, phase-modulated, and pulsed light with quantitation of blood and blood oxygenation.* Annals of the New York Academy of Sciences, 1998. **838**: p. 29-45.
5. Arridge, S.R., *Optical tomography in medical imaging.* Inverse Problems, 1999. **15**(2): p. R41-R93.
6. Kumar, Y.P., Dehghani, H., Pogue, B. W., Paulsen, K. D., *Image Reconstruction in Near Infrared Optical Tomography: Effect of Mesh Resolution, Measurement Number and Reconstruction Basis.* Phys. Med. Biol., 2005. **(submitted)**.
7. Polydorides, N., and McCann, H., *Electrode configurations for improved spatial resolution in electrical impedance tomography.* Meas. Sci. Technol., 2002. **13**: p. 1862-1870.
8. Graves, E.E., Culver, J. P., Ripoll, J., Weissleder, R., Ntziachristos, V., *Singular-value analysis and optimization of experimental parameters in fluorescence molecular tomography.* JOSA A, 2004. **21**(2): p. 231-241.
9. Graves, E.E., Ripoll, J., Weissleder, R., Ntziachristos, V., *A sub-millimeter resolution fluorescence molecular imaging system for small animal imaging.* Med. Phys., 2003. **30**(5): p. 901-911.
10. Xu, H., et al., *Near-infrared imaging in the small animal brain: optimization of fiber positions.* Journal of Biomedical Optics, 2003. **8**(1): p. 102-110.
11. Culver, J.P., Ntziachristos, V., Holboke, M. J., Yodh, A. G, *Optimization of optode arrangements for diffuse optical tomography: A singular-value analysis.* Applied Optics, 2001. **26**(10): p. 701-703.
12. Dehghani, H., Pogue, B. W., Poplack, S. P., Paulsen, K. D., *Multiwavelength Three-Dimensional Near-Infrared Tomography of the Breast: Initial Simulation, Phantom, and Clinical Results.* Applied Optics, 2003. **42**(1): p. 135-145.
13. Dehghani, H., Pogue B W, Jiang, S., Brooksby, B., and Paulsen K D, *Three Dimensional Optical Tomography: Resolution in Small Object Imaging.* Applied Optics, 2003. **42**(18): p. 3117-3128.
14. Dehghani, H., . Pogue, B. W., Jiang, S., Poplack, S., and Paulsen, K. D., *Optical images from Pathophysiological signals within breast tissue using three-dimensional near-infrared light.* Presented at proceedings of spie 4955, 2003.
15. Pogue, B.W., Geimer, S., McBride, T. O., Jiang, S., Österberg, U. L., Paulsen, K. D., *Three-dimentionsal Simulation of Near-Infrared Diffusion in Tissue: Boundary Condition and Geometry Analysis For Finite Element Image Reconstruction.* Appl. Opt., 2001. **40**(4).
16. Hebden, J.C., H. Veenstra, H, H. Dehghani, E. M. C. Hillman, M. Schweiger, S. R. Arridge, and D. T. Delpy, *Three dimensional time-resolved optical tomography of a conical breast phantom.* Applied Optics, 2001. **40**: p. 3278-3287.
17. Hebden, J.C., Gibson, A., Yusof, R. M., Everdell. N., Hillman, E. M. C., Delpy. D. T., Arridge. S. R., Austin. T., Meek. J. H., and Wyatt, J. S., *Three-dimensional optical tomography of the premature infant brain.* Phys. Med. Biol., 2002. **42**: p. 4155-4166.
18. Gibson, A., R. M. Yusof, E. M. C. Hillman, H. Dehghani, J. Riley, N. Everdale, R. Richards, J. C. Hebden, M. Schweiger, S. R. Arridge, and D. T. Delpy, *Optical tomography of a realistic neonatal head phantom.* Applied Optics, 2003. **42**(1).
19. Barbour, R.L., Graber, H. L., Wang, Y., Chang, J. H., Aronson, R., *A perturbation approach for optical diffusion tomography using continuous-wave and time resolved data*, in *Medical Optical Tomography: Functional Imaging and Monitoring*, G. Muller, Editor. 1993, SPIE Publ.: Bellingham, WA. p. 87-120.

20.   Jiang, H., Paulsen K. D., Osterberg, U. L., Pogue, B. W., Patterson, M. S., *Optical image reconstruction using frequency-domain data: simulations and experiments.* J. Opt. Soc. Am. A, 1996. **13**(2): p. 253-266.

21.   Hielscher, A.H., A.D. Klose, and K.M. Hanson, *Gradient-based iterative image reconstruction scheme for time-resolved optical tomography.* Ieee Transactions On Medical Imaging, 1999. **18**(3): p. 262-271.

22.   Holboke, M.J., Tromberg, B. J., Li, X. , Shah, N., Fishkin, J., Kidney, D., Butler, J., Chance, B., Yodh, A. G., *Three-dimensional diffuse optical mammography with ultrasound localization in a human subject.* Journal of Biomedical Optics, 2000. **5**: p. 237-247.

23.   Culver, J.P., Choe, R., Holboke, M. J., Zubkov, L., Durduran, T. , Slemp, A., Ntziachristos, V., Chance, B., Yodh, A. G, *Three-dimensional diffuse optical tomography in the parallel plane transmission geometry: Evaluation of a hybrid frequency domain/continuous wave clinical system for breast imaging.* Med. Phys., 2003. **30**(2): p. 235-247.

24.   Schweiger, M., S R Arridge, M Hiroaka and D T Delpy, *The Finite Element Model for the Propagation of Light in Scattering Media: Boundary and Source Conditions.* Med. Phys., 1995. **22**: p. 1779-1792.

25.   Arridge, S.R., and Schweiger, M., *Photon-measurement density functions. Part2: Finite-element-method calculations.* Applied Optics, 1995. **34**: p. 8026-8037.

Spectrally Constrained NIR tomography for Breast Imaging: Simulations and Clinical Results

Subhadra Srinivasan[*], Brian W. Pogue, Shudong Jiang,
Hamid Dehghani, Keith D. Paulsen
Thayer School of Engineering, Dartmouth College, Hanover NH 03755

ABSTRACT

A multi-spectral direct chromophore and scattering reconstruction for frequency domain NIR tomography has been implemented using constraints of the known molar spectra of the chromophores and a Mie theory approximation for scattering. This was tested in a tumor-simulating phantom containing an inclusion with higher hemoglobin, lower oxygenation and contrast in scatter. The recovered images were quantitatively accurate and showed substantial improvement over existing methods; and in addition, showed robust results tested for up to 5% noise in amplitude and phase measurements. When applied to a clinical subject with fibrocystic disease, the tumor was visible in hemoglobin and water, but no decrease in oxygenation was observed, making oxygen saturation, a potential diagnostic indicator.

INTRODUCTION

Near Infra-red (NIR) tomography is a growing area of research in medical imaging, principally due to the functional nature of the information this modality provides. Light is absorbed by the hemoglobin and water in tissue, and in the NIR wavelength region (600-1000nm) this absorption is low enough to allow penetration through a few centimeters of tissue[1]. Though scattering dominates, making it difficult to separate the two, measurement techniques and model-based reconstruction schemes have allowed the field to overcome this limitation and obtain concentrations of tissue chromophores and scatter-based parameters.

In breast imaging, this is of potential diagnostic value since tumors, show increased absorption[2], due to the localized increase in total hemoglobin. Additional factors such as dense fibrosis and cell proliferation show contrast in scatter[3]; and water may give a measure of the extravascular space[4]. Oxygen saturation obtained using concentrations of de-oxy and oxyhemoglobin, relate to the pO_2 of oxygen in tissue, and this helps assess the hypoxia in tumors, critical in separating malignancies from benign tumors[5, 6]. The current clinical modality of choice is mammography and suffers from high-false positive rates and the cumulative risk of a false positive result is 49.1% after 10 mammograms[7]. Overall, NIR has a niche in the evaluation of cancers, due to its ability to complement information from other modalities such as mammography and MRI, which are structure-based.

NIR tomography has emerged possible due to two principal areas of technological development, including NIR instrumentation and capabilities for diffuse image reconstruction. Advances in instrumentation have enabled multi-wavelength measurements from time-domain based[8] or frequency-domain based[9] systems to be obtained with percent noise established around 1%. In addition continuous-wave measurements[10] exist, which allow broadband interrogation with intensity measurements, but no phase information, making the separation of absorption and scatter difficult. The current system built at Dartmouth and documented in McBride et al[9] is a multi-wavelength frequency domain instrument allowing amplitude and phase measurement along the periphery of the breast. Having obtained this data, the second area of focus, which is pursued in this paper, is image reconstruction. This takes several forms[11] such as analytical solutions for homogeneous geometries, statistical methods such as Monte Carlo and numerical approaches such as finite element and finite difference models. Initially images of absorption and scatter at single wavelengths were used to establish contrasts[12], using some of these methods, and this was followed by multi-wavelength fitting at sufficient wavelengths to yield images of total hemoglobin, oxygen saturation, water[13], and scatter-based parameters[14].

[*] E-mail: Subha@dartmouth.edu; Tel: (603) 646-2859; Fax (603) 646-3856

Next were quantification improvement schemes using techniques relating to regularization[15], contrast-to-noise measures[16] and second derivative[17] to establish accuracy. The most recent technique[18-20] which has been a breakthrough in terms of quantitative accuracy is the reconstruction for direct images of chromophore concentrations and scatter without intermediate recovery of optical properties, by usage of all available wavelengths of data simultaneously. This is achieved by incorporating the spectral behavior of these chromophores and scattering into the image-formation process as apriori information. Applied to continuous-wave data[18, 19], with suitable assumptions on scatter, results have shown optimized images with lower noise and reduced cross-talk between the parameters.

We have implemented this type of spectrally constrained approach to frequency domain measurements, and preliminary results shown in Srinivasan et al[20], applied in homogeneous experiments have shown substantial quantitative and qualitative improvements. Our goal in the current paper is to validate this method in tumor-simulating phantom measurements with suitable heterogeneities in different parameters. We show further the robust nature of the algorithm to increasingly noisy data, compared to the conventional technique, and apply it to measurements made on a clinical subject with fibrocystic disease (FCD). Our studies show that contrast in hemoglobin and water is observed in FCD and scatter and oxygenation may be key to studying the differences between such a case and cancer.

MATERIALS AND METHODS

Data Acquisition

The frequency domain data acquisition system is designed for cross sectional imaging of the pendant breast in three planes spaced 1cm apart. A 16 source-detector fiber system for each plane is set up in a radial configuration, and is automated so that both the height and the diameter of the ring can be changed. Light signals at six wavelengths between 660 and 850nm are intensity modulated at 100MHz and multiplexing of the source into each of the fibers is achieved by a circular translation stage. Light detection is done using high gain photo-multiplier tubes (PMTs) and heterodyning using mixers is carried out to obtain a low frequency signal (500Hz) which is read by the computer. Complete details of the instrumentation can be found elsewhere [9, 21, 22].

Image Reconstruction

Breast tissue being a highly scattering media, the diffusion approximation to the Radiative transfer equation has been used for modeling light propagation, ignoring anisotropic effects [23]:

$$-\nabla . \kappa(r) \nabla \Phi(r, \omega) + \left(\mu_a(r) + \frac{i\omega}{c} \right) \Phi(r, \omega) = q_0(r, \omega) \qquad (1)$$

where $\Phi(r,\omega)$ is the isotropic fluence at modulation frequency ω and position r, $\kappa(r)$ is the diffusion coefficient, $\mu_a(r)$ is the absorption coefficient, c is the speed of light in the medium and $q_0(r,\omega)$ is an isotropic source. The diffusion coefficient can be written as

$$\kappa(r) = \frac{1}{3[\mu_a(r) + \mu_s'(r)]}$$

(2)

where μ_s' is the reduced scattering coefficient. The finite element method has been used to model this equation for its versatility in dealing with inhomogeneous and complicated geometries. The forward solver obtains the fluence for a given distribution of optical properties by applying suitable boundary conditions, type III (Robin-type) in our case[24]. In NIR tomography, the inverse problem has to be solved to obtain images of the optical properties from the measured amplitude and phase. This inverse problem is ill-posed and in order to prevent the solution from being overwhelmed by noise in the measurements, regularization techniques have been applied. An initial guess sufficiently close to the optical properties is obtained using a homogeneous pre-fitting algorithm[22] and we use the Newton Raphson iterative procedure to minimize the least squares functional:

$$\chi^2 = \sum_{j=1}^{M} \left(\phi_j^m - \phi_j^c \right)^2, \qquad (3)$$

where M is the total number of measurements at each wavelength, and ϕ_j^m and ϕ_j^c are the measured and calculated fluence at the boundary for each measurement point j. The corresponding matrix equation[24] is:

$$\left(\mathfrak{J}^T\mathfrak{J}+\lambda I\right)\partial\mu = \mathfrak{J}^T\partial\phi, \tag{4}$$

where $\mathfrak{J}$ is the Jacobian containing the derivatives of ϕ with respect to the optical properties μ given by (μ_a, κ) and α is the Levenberg Marquardt regularization[25] parameter which is a smoothing function and keeps the solution within reasonable limits. In this manner, we obtain new search direction for update in (μ_a, κ) iteratively, the convergence criteria being χ^2 less than 2% of that of the previous iteration, and obtain images for these optical properties.

Using the relationship from Beer's law for chromophore concentrations (*c*) relating to absorption, $\mu_a = [\varepsilon]c$, where ε is the molar absorption spectra of the absorbing chromophores, the concentrations are obtained using a constrained least squares fit. The primary absorbers are oxy-hemoglobin (HbO$_2$), de-oxyhemoglobin (Hb) and water, the effect of lipids being negligible since the wavelengths of use are below 850nm. Further, total hemoglobin is calculated as Hb$_T$ = HbO$_2$ + Hb (in µM), and oxygen saturation as S$_t$O$_2$ = HbO$_2$/ Hb$_T$ x100 (in %).

Similarly, for scattering the approximation to Mie theory[26, 27] $\mu_s' = a\lambda^{-b}$ is used to derive images of scatter amplitude (*a*)and scatter power (*b*), where λ is the wavelength in microns. Both the scattering power and amplitude depend on the scattering center size and number density and may reflect variations in breast structural composition due to different cellular, organelle and structural sizes/densities for fatty and glandular tissue.

Spectral Constraints
The spectral shapes from Beer's law and Mie theory can directly be incorporated into the reconstruction as constraints and details of this implementation are given elsewhere[20]. Briefly, all the wavelengths of data available are coupled together and used simultaneously in a new relationship which now minimizes the functional:

$\chi^2 = \sum_{j=1}^{Mn}\left(\phi_j^m - \phi_j^c\right)^2$, so that *j* now includes all wavelength measurements (*Mn*), where n is the number of wavelengths

available (6 in our case). The corresponding matrix equation for direct update in chromophores ∂c is:

$$\left(\mathfrak{J}^T\mathfrak{J}+\alpha I\right)\partial c = \mathfrak{J}^T\partial\phi, \tag{5}$$

where
$$\partial\phi = \begin{pmatrix}\partial\phi_{\lambda 1}\\ \partial\phi_{\lambda 2}\\ ..\\ \partial\phi_{\lambda n}\end{pmatrix},\ \mathfrak{J} = \begin{bmatrix}\mathfrak{J}_{c1,\lambda 1}\mathfrak{J}_{c2,\lambda 1}\mathfrak{J}_{c3,\lambda 1}\mathfrak{J}_{a,\lambda 1}\mathfrak{J}_{b,\lambda 1}\\ \mathfrak{J}_{c1,\lambda 2}\mathfrak{J}_{c2,\lambda 2}\mathfrak{J}_{c3,\lambda 2}\mathfrak{J}_{a,\lambda 2}\mathfrak{J}_{b,\lambda 2}\\ .....\\ \mathfrak{J}_{c1,\lambda n}\mathfrak{J}_{c2,\lambda n}\mathfrak{J}_{c3,\lambda n}\mathfrak{J}_{a,\lambda n}\mathfrak{J}_{b,\lambda n}\end{bmatrix}\ and\ \partial c = \begin{pmatrix}\partial c_1\\ \partial c_2\\ \partial c_3\\ \partial a\\ \partial b\end{pmatrix}$$

and the relations between $\left[\mathfrak{J}_{c,\lambda},\mathfrak{J}_{a,\lambda},\mathfrak{J}_{b,\lambda}\right]_{\lambda=1:n}$ and $\mathfrak{J}_{\mu_a} = \dfrac{\partial\phi}{\partial\mu_a}$ and $\mathfrak{J}_\kappa = \dfrac{\partial\phi}{\partial\kappa}$ have been derived in Srinivasan et al[20], *c1*, *c2*, *c3* being the concentrations of oxy, de-oxyhemoglobin and water. Similar Levenberg-Marquardt regularization was applied as before and the computation time was approximately 25minutes for typically 5-7 iterations, the measure of convergence being when the projection error was less than 2% of previous iteration value. The approach can easily be extended to additional wavelengths without any computational expense in the inversion process since the size of the matrix to be inverted in equation 5 depends on number of nodes (which is fixed) and not on the number of measurements, though the number of wavelengths will influence the calculation of individual Jacobian matrices.

RESULTS

Tumor-simulating Phantom results

Amplitude and phase measurements were generated for a heterogeneous phantom using the finite element forward solver and 1% random Gaussian noise was added to mimic experimental noise[9]. This phantom was of diameter 86mm, and contained an inclusion of size 20mm, with total hemoglobin contrast of 3:1, with respect to the background. The anomaly also had lower oxygen saturation of 30% compared to the background at 60%, and contrast in scatter amplitude, with value 1.5, compared to 1.2 in background. Water and scatter power were maintained homogeneous at 60% and 0.6 respectively. The spectrally constrained direct chromophore and scattering reconstruction was applied to this data. In addition, the conventional method of reconstructing at each wavelength separately and then applying least squares fit to Beer's law and Mie theory, was also applied , and Figure 1 shows the corresponding images obtained, compared to the true images in the top row. The figure shows much smoother images for all the parameters in the spectral reconstruction compared to the conventional technique. Quantitative accuracy is improved in addition to the reduced standard deviation, with spectrally constrained method giving results accurate with less than 15% error overall, and this error limit being at 43% for the conventional technique. There is also a reduction in cross-talk observed between hemoglobin and water, from 30% in conventional method to 7% in spectral; and a similar trend is seen between scatter amplitude and power as well.
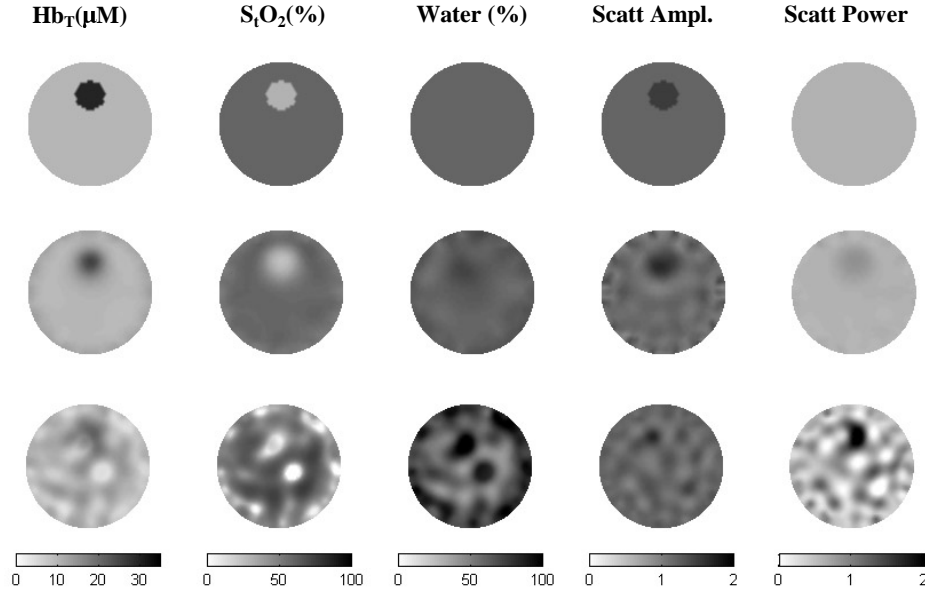
Figure 1: Recovered NIR parameter images are shown for a heterogeneous phantom with true values in the top row, as reconstructed with 1% random Gaussian noise added. The middle row shows images obtained using the spectrally-constrained reconstruction and the bottom row shows the same set of images using the conventional method of applying least squares fitting to images of absorption and reduced scattering coefficients, and then sequentially fitting for chromophore images.

Further to test the robust aspect of this algorithm, increasing amounts of random Gaussian noise from 0 to 5% in steps of 0.5% was added to this test phantom, and the mean and standard deviation in the NIR parameters as recovered from both conventional and direct spectral reconstruction have been plotted (see figure 2) alongside the true values. At 1% noise, which is the level found in our tomography system[9], the reduction in standard deviations in oxygen saturation, water and scatter power are most striking. The trend is continued at 5% noise in the amplitude and phase data (5% is possibly the limit of noisy data found typically in such measurement systems). The spectrally constrained technique still gives quantification accurate within 15% of true values overall, but this is not the case in the conventional method, where the high standard deviations in the images make it impossible to obtain useful NIR information.
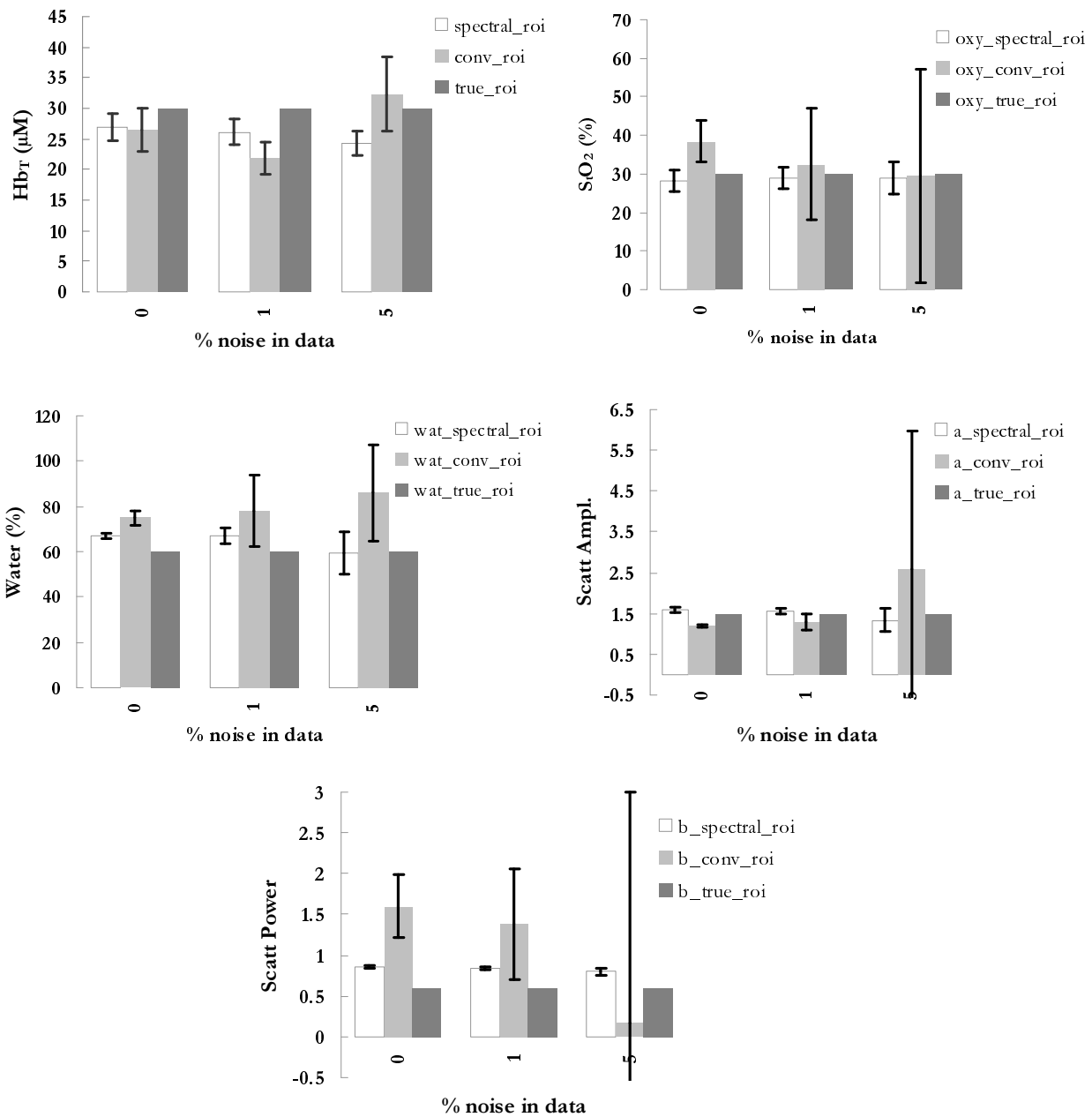
Figure 2: Mean and standard deviations from the images recovered are shown, using both spectrally constrained reconstruction and the conventional method, for the test phantom used in Figure 1, with increasing amounts of random Gaussian noise as the abscissa. The results are average values taken from the region of the heterogeneity, for (a) Hb_T in μM, (b) S_tO_2 in %, (c) water in %, (d) scatter amplitude and (e) scatter power. The background values were observed to stay constant for both methods.

Clinical Case: Fibrocystic Disease (FCD)

Frequency domain measurements were obtained from a subject with an 8mm tumor, diagnosed as FCD, in the left breast. The total breast diameter was measured to be 102mm in the plane 1, where the location of cyst was marked, and given by the Radiologist as upper inner quadrant, 11.00-12.00 clock position. Results from the previous section and as

documented[20] suggest that the spectrally constrained technique is significantly superior to the conventional method in both quantitative and qualitative aspects, and hence only the NIR parameter images obtained using this reconstruction have been shown here (see figure 3). The tumor is visible in the 12.00 position in the total hemoglobin and water images. There is a contrast of 1.25:1 in the Hb_T image, between the maximum in the tumor and background mean, which is much lower than that typically found in malignancies. In addition, no decrease in oxygenation is observed, with this parameter remaining almost homogeneous. Water shows an increase of up to a maximum value of 85% at the site of the tumor, which corresponds well with theory that FCDs may contain fluid filled cysts. Since the physiology of this disease is complex, and may vary from distinct masses to diffuse masses and/or palpable lesions[28], the additional increases in hemoglobin and water found close to the tumor may very well be physiologically true. The radiodensity category of the breast of this subject was given to be fatty/scattered type with less of glandular tissue, and the recovered background hemoglobin (~ 10μM) agrees well with the expected lower vascularity in such tissue. In addition, the low values of scatter power correspond well with a previous hypothesis that scattering may be a non-invasive indicator of radio-density[4].
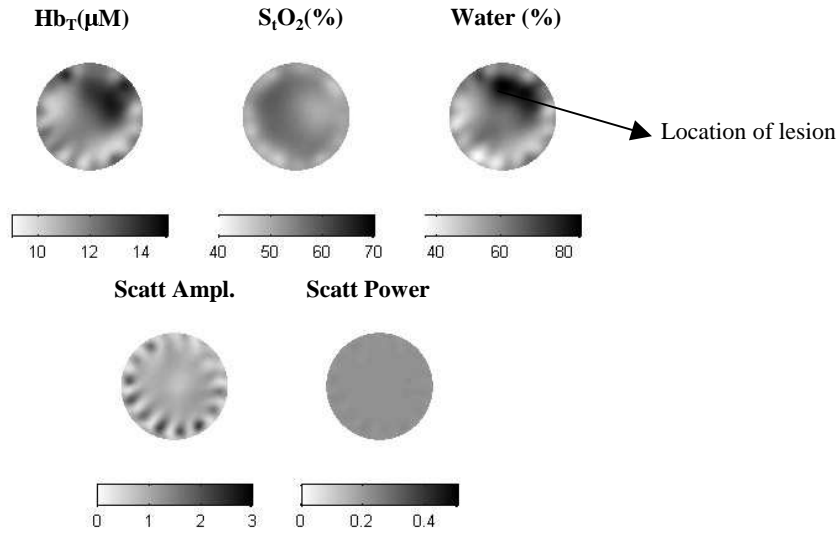
Figure 3: Recovered images for the NIR parameters are shown as reconstructed with the spectrally-constrained reconstruction, using data collected from a subject with a localized area of fibrocystic disease of size 8mm, at the 12:00 o'clock position of this circular cranocaudal view. Contrast is observed at location of the lesion, in total hemoglobin and water, and no decrease in oxygen saturation is observed.

DISCUSSION

The approach of using spectrally-constrained direct chromophore and scatter tomography using frequency domain measurements has been validated here, for a heterogeneous phantom simulation with 1% random Gaussian noise. The inclusion of size 20mm contained contrast in total hemoglobin and scatter and lower oxygen saturation corresponding to malignancies[28]. Reconstruction was carried out by both the spectral technique, and the conventional method involving single wavelength optical properties recovery, and the images recovered were compared to the true images in figure 1. Results showed substantial improvement in the image quality with suppression of noise and image artifacts, using the new technique. Quantification was also improved with the recovered mean values for the NIR parameters in the anomaly accurate within 85% of true values.

The significant reduction in the crosstalk between oxyhemoglobin and water can be explained by the nature of the chromophore and scattering spectra. Water and oxy-hemoglobin show similar behavior in the 600-800nm range[3], and the water characteristics which help separate the two appear only at longer wavelengths, in our case 849nm. In the spectrally-constrained reconstruction, this being apriori information, the cross-talk between the two, and hence the noise in water images is significantly suppressed. In the conventional technique, this cross-talk over-rides the reconstruction, affecting the accuracy and quality of water images. Similarly, both the de-oxyhemoglobin and Mie scattering follow a

decreasing trend, making it difficult to separate the two in the conventional technique. However, since the specific trends of these are applied as constraints in the new method, significantly more robust scatter images result. These constraints are also responsible for the robust nature of the algorithm to higher levels of noise as compared to before, and this has been tested out for up to 5% random Gaussian noise in the measurements of amplitude and phase. Figure 2 shows that the mean values for this level of noise are quantitatively accurate and show significant reduction in the standard deviations in the region of the heterogeneity.

Finally, the method has been used to characterize fibrocystic disease using clinical data from a subject with an 8mm tumor. FCDs cover a broad range of alterations from diffuse masses to distinct tumors and frequently, many of these tumors with ductal proliferation mimic cancers making diagnosis difficult[28]. By understanding the NIR parameter images for this disease, it may be possible to overcome this limitation. In the images we have recovered here using the spectrally constrained technique, contrast in total hemoglobin and water at the location of the tumor was observed. The increase in hemoglobin (13.8µM maximum in region of tumor, compared to 11µM in background) is lower than typical of cancers, and the contrast in water agrees well with theoretical predictions of the physiology of this benign disease[28]. No decrease in oxygenation is observed and this is the distinguishing parameter between FCDs and cancers. We are currently following this trend in further clinical cases, and the results shown here and in progress hold promise in understanding the nature of NIR information.

REFERENCES
1. F.F. Jobsis, "Non-invasive, infra-red monitoring of cerebral and myochardial oxygen sufficiency and circulatory parameters." *Science*, vol. 198 pp. 1264-1267.1977.
2. B.W. Pogue, S.P. Poplack, T.O. McBride, W.A. Wells, O.K. S., U.L. Osterberg, and K.D. Paulsen, "Quantitative Hemoglobin Tomography with Diffuse Near-Infrared Spectroscopy: Pilot Results in the Breast." *Radiology*, vol. 218(1) pp. 261-6.2001.
3. B.J. Tromberg, N. Shah, R. Lanning, A. Cerussi, J. Espinoza, T. Pham, L. Svaasand, and J. Butler, "Non-invasive in vivo characterization of breast tumors using photon migration spectroscopy." *Neoplasia (New York)*, vol. 2(1-2) pp. 26-40.2000.
4. S. Srinivasan, B.W. Pogue, S. Jiang, H. Dehghani, C. Kogel, S. Soho, J.J. Gibson, T.D. Tosteson, S.P. Poplack, and K.D. Paulsen, "Interpreting hemoglobin and water concentration, oxygen saturation and scattering measured in vivo by near-infrared breast tomography." *PNAS*, vol. 100(21) pp. 12349-12354.2003.
5. M. Hockel, P.Vaupel, "Tumor Hypoxia : Definitions and Current Clinical, Biologic, and Molecular Aspects." *J. Natl. Cancer Inst.*, vol. 93(4) pp. 266-276.2001.
6. D. Grosenick, H. Wabnitz, K.T. Moesta, J. Mucke, M. Moller, C. Stroszczynski, J. Stossel, B. Wassermann, P.M. Schlag, and H. Rinneberg, "Concentration and oxygen saturation of haemoglobin of 50 breast tumours determined by time-domain optical mammography." *Phys Med Biol*, vol. 49(7) pp. 1165-81.2004.
7. J.G. Elmore, M. B. Barton, V. M. Moceri, S. Polk, P. J. Arena and S. W. Fletcher, "Ten-Year Risk of False Positive Screening Mammograms and Clinical Breast Examinations." *The New England Journal of Medicine*, vol. 338(16) pp. 1089-1096.1998.
8. M.S. Patterson, C. B., and B.C. Wilson, "Time resolved reflectance and transmittance for the non-invasive measurement of tissue optical properties." *Appl. Opt.*, vol. 28 pp. 2331-2336.1989.
9. T.O. Mcbride, B.W. Pogue, S. Jiang, U.L. Osterberg, and K.D. Paulsen, "A parallel-detection frequency-domain near-infrared tomography system for hemoglobin imaging of the breast in vivo." *Review of Scientific Instruments*, vol. 72(3) pp. 1817-1824.2001.
10. M.G. Nichols, Hull, E. L. and Foster, T. H., "Design and testing of a white-light, steady-state diffuse reflectance spectrometer for determination of optical properties of highly scattering systems." *Applied Optics*, vol. 36(1) pp. 93-104.1997.
11. S.R. Arridge and M. Schweiger, "Image reconstruction in optical tomography." *Phil. Trans. R. Soc. Lond. B*, vol. 352 pp. 717-726.1997.

12. B.J. Tromberg, Coquoz, O., Fishkin, J. B., Pham, T., Anderson, E. R., Butler, J., Cahn, M., Gross, J. D., Venugopalan, V., Pham, D., "Non-invasive measurements of breast tissue optical properties using frequency-domain photon migration." *Phil. Trans. R. Soc. Lond. B*, vol. 352 pp. 661-668.1997.

13. T.O. McBride, B.W. Pogue, S. Jiang, U.L. Osterberg, K.D. Paulsen, and S.P. Poplack, "Multi-spectral near-infrared tomography: a case study in compensating for water and lipid content in hemoglobin imaging of the breast." *J. Biomed. Opt.*, vol. 7 pp. 72-79.2002.

14. T. Durduran, R.Choe, J.P.Culver, L.Zubkov, M.J.Holboke, J.Giammarco, B.Chance and A.G.Yodh, "Bulk optical properties of healthy female breast tissue." *Phys. Med. Biol.*, vol. 47 pp. 2847-2861.2002.

15. S. Srinivasan, Pogue, B. W., Dehghani, H., Jiang, S., Song, X. and Paulsen, K. D., "Improved quantification of small objects in near-infrared diffuse optical tomography." *Journal of Biomed Opt.*, vol. 9(6) pp. 1161-71.2004.

16. X. Song, B.W. Pogue, S. Jiang, M.M. Doyley, H. Dehghani, T.D. Tosteson, and K.D. Paulsen, "Automated region detection based on the contrast-to-noise ratio in near-infrared tomography." *Appl Opt*, vol. 43(5) pp. 1053-62.2004.

17. E. Heffer, V. Pera, O. Schutz, H. Siebold, and S. Fantini, "Near-infrared imaging of the human breast: complementing hemoglobin concentration maps with oxygenation images." *Journal of Biomed Opt.*, vol. 9(6) pp. 1152-60.2004.

18. A. Corlu, T. Durduran, R. Choe, M. Schweiger, E.M. Hillman, S.R. Arridge, and A.G. Yodh, "Uniqueness and wavelength optimization in continuous-wave multispectral diffuse optical tomography." *Opt Lett*, vol. 28(23) pp. 2339-41.2003.

19. A. Li, Q. Zhang, J.P. Culver, E.L. Miller, and D.A. Boas, "Reconstructing chromosphere concentration images directly by continuous-wave diffuse optical tomography." *Opt Lett*, vol. 29(3) pp. 256-8.2004.

20. S. Srinivasan, B.W. Pogue, S. Jiang, H. Dehghani, and K.D. Paulsen, "Spectrally Constrained Chromophore and Scattering NIR Tomography Provides Quantitative and Robust Reconstruction." *Applied Optics*.2005-in press.

21. B.W. Pogue, M. Testorf, T. McBride, U. Osterberg, and K. Paulsen, "Instrumentation and design of a frequency-domain diffuse optical tomography imager for breast cancer detection." *Opt. Express*, vol. 1(13) pp. 391-403.1997.

22. T.O. McBride, B.W. Pogue, U.L. Österberg, and K.D. Paulsen, "Strategies for Absolute Calibration of Near Infrared Tomographic Tissue Imaging", in *Oxygen Transport to Tissue XXI*, J.F. Dunn, Swartz, H. M., Editor. 2001, Lengerich: Pabst.

23. A. Ishimaru, *Wave propagation and scattering in random media*. Vol. 1. 1978: Academic Press, Inc., New York.

24. K.D. Paulsen, and Jiang, H., "Spatially varying optical property reconstruction using a finite element diffusion equation approximation." *Med. Phys.*, vol. 22(6) pp. 691-701.1995.

25. D.W. Marquardt, "An algorithm for least squares estimation of nonlinear parameters." *J. Soc. Ind. Appl. Math.*, vol. 11 pp. 431-441.1963.

26. H.J. van Staveren, C.J.M. Moes, J. van Marle, S.A. Prahl, and M.J.C. van Gemert, "Light scattering in intralipid-10% in the wavelength range of 400-1100 nm." *Applied Optics*, vol. 30(31) pp. 4507.1991.

27. J.R. Mourant, T. Fuselier, J. Boyer, T.M. Johnson, and I.J. Bigio, "Predictions and measurements of scattering and absorption over broad wavelength ranges in tissue phantoms." *Applied Optics*, vol. 36(4) pp. 949.1997.

28. S. Thomsen, and D. Tatman, "Physiological and Pathological Factors of Human Breast Disease That can Influence Optical Diagnosis." *Ann. N. Y. Acad. Sci.*, vol. 838 pp. 171-193.1998.

Excitation patterns in three-dimensional electrical impedance tomography

**Hamid Dehghani, Nirmal Soni, Ryan Halter, Alex Hartov
and Keith D Paulsen**

Thayer School of Engineering, Dartmouth College, Hanover, NH 03755, USA

Abstract
Electrical impedance tomography (EIT) is a non-invasive technique that aims
to reconstruct images of internal electrical properties of a domain, based on
electrical measurements on the periphery. Improvements in instrumentation
and numerical modeling have led to three-dimensional (3D) imaging. The
availability of 3D modeling and imaging raises the question of identifying the
best possible excitation patterns that will yield to data, which can be used to
produce the best image reconstruction of internal properties. In this work,
we describe our 3D finite element model of EIT. Through singular value
decomposition as well as examples of reconstructed images, we show that
for a homogenous female breast model with four layers of electrodes, a driving
pattern where each excitation plane is a sinusoidal pattern out-of-phase with
its neighboring plane produces better qualitative images. However, in terms
of quantitative imaging an excitation pattern where all electrode layers are in
phase produces better results.

Keywords: impedance tomography, finite element modeling, image
reconstruction

(Some figures in this article are in colour only in the electronic version)

1. Introduction

Electrical impedance tomography (EIT) is a method that aims to reconstruct images
of internal electrical property (conductivity, permittivity and permeability in some high-
frequency non-medical applications) distributions from electrical measurements obtained
on the periphery. In recent years EIT has been the subject of study for a variety of
clinical problems such as lung ventilation (Adler *et al* 1997, Brown *et al* 1994, Frerichs 2000,
Metherall *et al* 1996, Noble *et al* 1999, Woo *et al* 1992, Valente Barbas 2003, Newell *et al*
1993, van Genderingen *et al* 2004, 2003), cardiac volume changes (Hoetink *et al* 2001,

Brown *et al* 1992, Vonk Noordegraaf *et al* 1997), gastric emptying (Erol *et al* 1996), head imaging (Holder 1992, Bagshaw *et al* 2003) and breast cancer detection (Cherepenin *et al* 2003, Kerner *et al* 2002, Wang *et al* 2001, Zou and Guo 2003).

In EIT, measurements over a region of interest are acquired from a set of electrodes by applying currents and measuring resulting voltages or vice versa. Depending on the application, various driving schemes have been used for electrode excitation, including stimulation of adjacent and opposite pairs or trigonometric spatial patterns (Boone *et al* 1997, Lionheart 2004, Brown 2003). Once boundary measurements are acquired, estimates of the electrical property distributions in tissue can be determined through the appropriate model-based matching of the data.

The majority of modeling and image reconstruction studies have involved two-dimensional (2D) assumptions; yet, a three-dimensional (3D) treatment of electrical transmission in tissue provides a more accurate prediction of the field distribution in the medium. Recently, there has been significant progress in developing 3D modeling and image reconstruction which is computationally more complex but also more accurate (Metherall *et al* 1996, Goble 1990, Molinari *et al* 2002, Polydorides and Lionheart 2002, Vauhkonen *et al* 1999). As 3D image reconstruction becomes more fully developed it is crucial to define the appropriate excitation (drive) patterns that will provide the maximum information on the internal properties of the domain being imaged. This is particularly true when using experimental patient data, since theoretical simulations will typically not represent the level of noise and systematic error present in actual data sets and simple symmetrical geometries no longer apply. Some results have appeared in this regard, notably the work by Goble (1990), who extended the original distinguishability of Isaacson (1986). This work showed that the eigenfunctions for a finite 3D cylinder constitute an optimal drive pattern set on discrete electrodes.

In the presented paper, we describe our implementation of a 3D finite element model (FEM) for EIT. In section 2, we describe our implementation of the FEM for EIT in some detail to accurately describe the software used for the presented study. We use simulation studies coupled to singular value decomposition (SVD) of the data to evaluate the performance of various excitation patterns for a homogenous female breast model that contains 64 electrodes distributed over 4 planes of 16 electrodes each. We validate these findings by reconstructing images from simulated data. We show that for a homogenous female breast model with four layers of electrodes, a driving pattern where each excitation plane is a sinusoidal pattern, which is out-of-phase with its neighboring planes, produces better qualitative images. However, in terms of quantitative imaging an excitation pattern where all electrode layers are in phase produces the best results.

2. Theory

Under certain low-frequency assumptions, it is well established that the full Maxwell equations can be simplified to the complex-valued Laplace equation

$$\nabla \cdot \sigma^* \nabla \Phi^* = 0 \tag{1}$$

where Φ^* is the complex-valued electric potential and σ^* is the complex conductivity of the medium ($\sigma^* = \sigma - i\omega\varepsilon_o\varepsilon_r$, for ω is the frequency, ε_o and ε_r are the absolute and relative permittivities). In order to obtain a reasonable model for EIT, appropriate boundary conditions need to be enforced (Vauhkonen 1997). In this work we use the complete electrode model, which takes into account both the shunting effect of the electrodes and the contact impedance

between the electrodes and tissue. Using this boundary condition the EIT model includes (Vauhkonen 1997)

$$\Phi^* + z_l \sigma^* \frac{\partial \Phi^*}{\mathrm{d}n} = V_l^*, \qquad x \in e_l, \quad l = 1, 2, \ldots, L \tag{2}$$

$$\int_{e_l} \sigma^* \frac{\partial \Phi^*}{\mathrm{d}n} \, \mathrm{d}S = I_l^*, \qquad x \in e_l, \quad l = 1, 2, \ldots, L \tag{3}$$

$$\sigma^* \frac{\partial \Phi^*}{\mathrm{d}n} = 0, \qquad x \in \partial\Omega \big/ \cup_l^L e_l \tag{4}$$

where z_l is the effective contact impedance between the lth electrode and the tissue, n is the outward normal, V^* is the complex-valued voltage, I^* is the complex-valued current and e_l denotes the electrode l. $x \in \partial\Omega \big/ \cup_l^L e_l$ indicates a point on the boundary not under the electrodes.

2.1. Finite element implementation

The finite element discretization of a domain Ω can be obtained by subdividing it into D elements joined at V vertex nodes. In finite element formalism, $\Phi(\mathbf{r})$ at spatial point r is approximated by a piecewise continuous polynomial function $\Phi^h(r, w) = \sum_i^V \Phi_i(w) u_i(r) \in \Omega^h$, where Ω^h is a finite-dimensional subspace spanned by basis functions $\{u_i(r); i = 1, \ldots, V\}$ chosen to have limited support. The problem of solving for Φ^h becomes one of sparse matrix inversion: in this work, we use a bi-conjugate gradient stabilized solver. Equation (1) in the FEM framework can be expressed as a system of linear algebraic equations:

$$(K(\sigma^*) + z^{-1}F)\Phi^* = 0 \tag{5}$$

where the matrices $K(\sigma^*)$ and F have entries given by:

$$K_{ij} = \int_\Omega \sigma^*(r) \nabla u_i(r) \cdot \nabla u_j(r) \, \mathrm{d}^n r \tag{6}$$

$$F_{ij} = \oint_{\partial\Omega \in l} u_i(r) u_j(r) \, \mathrm{d}^{n-1} r \tag{7}$$

where $\delta\Omega \in l$ is the boundary under each electrode.

2.2. Image reconstruction

In the inverse (imaging) problem, the goal is the recovery of σ^* at each FEM node based on measurements at the object surface. Here, we aim to recover internal electrical property distributions from the boundary measurements. We assume that σ and ε_r are expressed in a piecewise linear basis with a limited number of dimensions (less than the dimension of the finite element system matrices). A number of different strategies for defining the reconstruction basis are possible; in this paper we use a linear pixel basis of dimensions $30 \times 30 \times 10$ (x, y and z), which spans the whole domain.

Image reconstruction is achieved numerically by minimizing an objective function, which depends on the difference between measured data, Φ^{M^*}, and calculated data, Φ^{C^*}, from the FEM solution to equation (1) under the assumptions of the present iteration property estimate. Typically this is written as the minimization of χ^2:

$$\chi^2 = \sum_{i=1}^{NM} \left| \Phi_i^{M^*} - \Phi_i^{C^*} \right|^2 \tag{8}$$

where NM is the number of measurements and $||$ indicates the magnitude of the difference vector of a complex number which in the complex plane is formed by multiplying the difference vector by its complex conjugate transpose to produce a real-valued scalar. χ^2 can be minimized in a least-squares sense by setting its derivatives with respect to the electrical distribution parameter equal to zero, and solving the resultant nonlinear system using a Newton–Raphson approach. We use a Levenberg–Marquardt algorithm, to repeatedly solve

$$a = J^T (JJ^T + \lambda I)^{-1} b \tag{9}$$

where b is the data vector, $b = (\Phi^{M^*} - \Phi^{C^*})^T$; a is the solution update vector, $a = \delta[\sigma + i\omega\varepsilon_o\varepsilon_r]$, defining the difference between the true and estimated electrical properties at each reconstructed basis. λ is the regularization factor to stabilize matrix inversion; J is the Jacobian matrix for our model, which is calculated using the so-called adjoint method (Polydorides and Lionheart 2002). It has the form

$$J = \begin{bmatrix} \frac{\delta\Phi_1^*}{\delta\sigma_1^*} & \frac{\delta\Phi_1^*}{\delta\sigma_2^*} & \cdots & \frac{\delta\Phi_1^*}{\delta\sigma_j^*} \\ \frac{\delta\Phi_2^*}{\delta\sigma_1^*} & \frac{\delta\Phi_2^*}{\delta\sigma_2^*} & \cdots & \frac{\delta\Phi_2^*}{\delta\sigma_j^*} \\ \vdots & \vdots & \ddots & \vdots \\ \frac{\delta\Phi_n^*}{\delta\sigma_1^*} & \frac{\delta\Phi_n^*}{\delta\sigma_2^*} & \cdots & \frac{\delta\Phi_n^*}{\delta\sigma_j^*} \end{bmatrix} \tag{10}$$

where $\frac{\delta\Phi_n^*}{\delta\sigma_j^*}$ are the sub-matrices that define the derivative relation between the nth measurement with respect to σ^* at the jth reconstructed node. It may be worth noting that equation (9) is the under-determined equivalent of the more generally used over-determined problem, i.e. $a = (J^T J + \lambda I)^{-1} J^T b$, where the size of the Hessian matrix (second derivative) JJ^T is n^2 as compared to $J^T J$ which has a size of j^2 (where j is the total number of nodes). Since, in most cases when $n \ll j$, it is computationally significant to use this scheme.

3. Methods

In order to evaluate the best excitation pattern options to use in a 3D imaging system, a realistic female breast model of dimensions 63.2 mm $\times$ 58.9 mm $\times$ 94.5 mm (x, y, z) was simulated (figure 1). The mesh consisted of 16 303 nodes corresponding to 66 151 linear tetrahedral elements. The resolution of the mesh was chosen such that the model is numerically accurate, as compared to a higher node density or higher order elements. Four planes of electrodes were modeled (at $z = -20$ mm, -40 mm, -60 mm and -80 mm) with each plane consisting of 16 circular electrodes of diameter 5 mm, and spaced vertically 20 mm apart. The model assumed homogenous electrical properties of $\sigma = 2$ Sm^{-1} and $\varepsilon_r = 80$. All of the data presented in this work were confined to an excitation frequency of 125 kHz.

In the first analysis, the 'voltage' drive mode was considered. Here, one applies a set of voltage patterns at each electrode simultaneously and measures the resulting currents at the same electrodes. Three voltage driving patterns were considered: (1) 15 sinusoidal voltage patterns distributed circumferentially in the plane and in-phase between all four planes, (2) 15 sinusoidal voltage patterns distributed circumferentially within each plane but 45° out-of-phase with respect to neighboring planes, and (3) 15 sinusoidal voltage patterns distributed circumferentially within each plane but 90° out-of-phase with respect to neighboring planes. In each case, the Jacobian was calculated and used to evaluate the amount of information available for each set of current patterns. Singular value decomposition of the Jacobian matrix
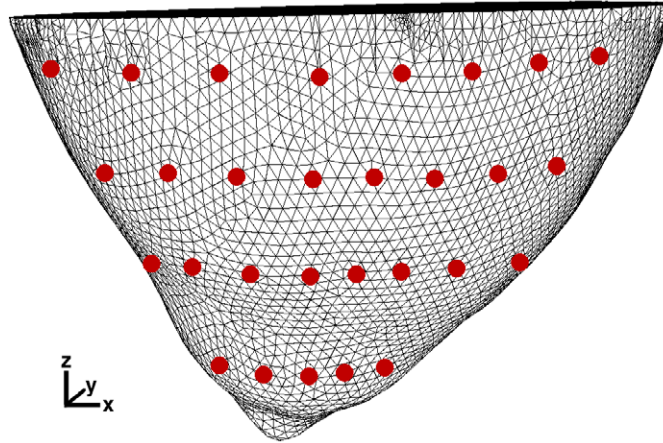
Figure 1. Finite element model used for the generation of the Jacobian and simulated forward data. The mesh is a realistic female breast model of dimensions 63.2 mm × 58.9 mm × 94.5 mm (x, y, z). Four planes of electrodes (represented by shaded circles) are also modeled. Each plane contains 16 equally spaced circular electrodes of radius 5 mm, at $z = -20, -40, -60$ and -80 mm.

yields a triplet of matrices:

$$J = USV^{T} \tag{11}$$

where U and V are orthonormal matrices containing the singular vectors of J and S is a diagonal matrix containing the singular values of J. Since J serves to map measurements onto electrical properties, it can be viewed as an interface between the detection space and the image space. Furthermore, the vectors of U and V correspond to the modes in detection space and image space, respectively, while the magnitude of the singular values in S represents the importance of the corresponding singular vectors in U and V. Specifically, more nonzero singular values mean more modes are active in the two spaces which brings more detail and improves the resolution in the resultant image. In a practical setup, noise must be considered because only the singular values larger than the noise level provide useful information. The singular values of the sensitivity maps for the whole domain are calculated. There are normally M nonzero singular values in the diagonal matrix when N (number of nodes) is larger than M (number of measurements) and those values are sorted in descending order. Thus, it is possible to determine whether a given set of excitation patterns provides more information about the domain under investigation relative to other pattern options.

In order to evaluate further the suitability of one excitation pattern over another, boundary data were calculated for each set of excitation patterns in the presence of two anomalies: a single spherical conductor (5 times the background value, radius 10 mm, located at mid-plane, 20 mm from center) and a single spherical permittivity anomaly (10 times the background value, radius 10 mm, located at mid-plane, 20 mm from center) (figure 2). Using these data sets, images were reconstructed using a linear pixel scheme. For image reconstruction, the initial value of regularization was chosen to be 1×10^{-5}. At each iteration, if the projection error, χ^2, was found to have decreased as compared to the previous iteration, regularization was decreased by a factor of $10^{1/8}$. All images shown are those chosen when the projection error χ^2 did not decrease by more than 1% as compared to the previous iteration.
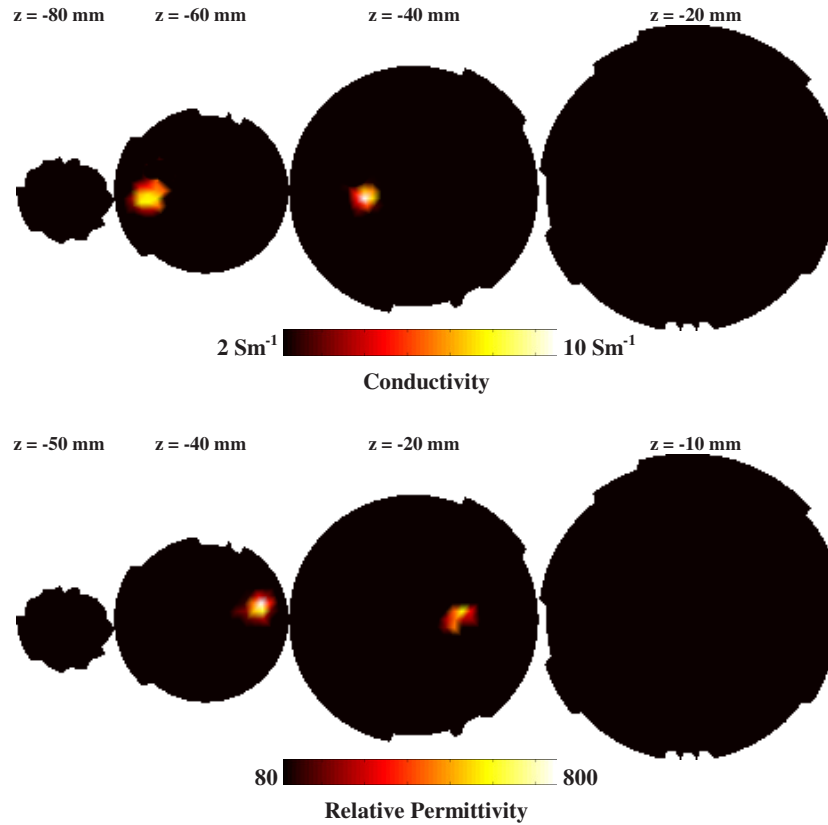
Figure 2. 2D coronal slices through the breast mesh showing the position of the anomalies. The most right-hand slice is near the chest while the most left-hand slice is near the nipple.

4. Results

Singular values of each Jacobian were calculated for each excitation pattern and the normalized values (normalized to the first and largest singular value) are plotted in figure 3. It is evident from this plot that the second and third excitation patterns, where the applied voltage at each plane is out-of-phase with the other planes, provide more information than the first pattern. The total number of singular values is 960 (15 excitation patterns times 64 measurements), and if one takes into account the expected noise in the measurement system it is possible to calculate the total number of useful singular values (proportional to the amount of useful information) for each pattern. Assuming that the noise in the measured data from a clinical instrument is about 0.1%, the total number of useful singular values is: 269 for the first pattern, 329 for the second pattern and 330 for the third pattern. This suggests that using out-of-phase patterns at each level produces better reconstructed images of the domains internal electrical properties from the measured data.

Reconstructed images from the simulated data in the presence of anomalies within the domain (figure 2) are shown in figures 4–6, using the first, second and third patterns, respectively. Both the conductivity and permitivity anomalies have been recovered for all excitation patterns, at approximately the correct location and with good separation. These are the images at the fifth iteration, which were obtained with a computation time of approximately
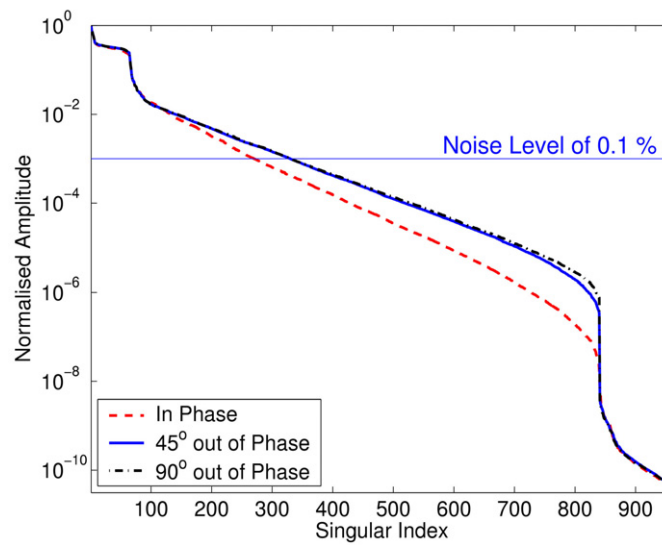
Figure 3. Singular values of each Jacobian calculated using the three different applied patterns. Each set of singular values is normalized with respect to the first and largest singular value. The solid horizontal line represents the cut-off level when 0.1% noise is expected in the data.

Table 1. The target and the calculated volume of each reconstructed anomaly.

	Target	Pattern 1	Pattern 2	Pattern 3
Conductivity volume (mm^3)	4.2×10^3	23×10^3	15×10^3	13×10^3
Permittivity volume (mm^3)	4×10^3	11×10^3	7.8×10^3	7.7×10^3

10 min per iteration on a 1.7 GHz PC with 2 GB of RAM. It is evident that the recovered target values are much lower than expected, a problem that is commonly reported in 3D imaging with related modalities (Dehghani *et al* 2003, Gibson *et al* 2003). No doubt these quantitative values can be dramatically improved using different and more sophisticated regularization schemes as well as addition of appropriate penalty function (Borsic 2002).

In order to more clearly analyse the results, the total volume of each reconstructed anomaly has been calculated and displayed in table 1. The volumes were computed as the total volume of mesh elements with nodes having a reconstructed value of greater than the full width half maximum (FWHM) of the anomaly. It should be noted here that since the mesh is not regular the actual anomaly does not have a perfect spherical shape, which gives rise to the different volume estimated for the conductivity and permittivity objects.

Finally, in order to investigate the application of *a priori* information in image reconstruction, images were reconstructed using the known location of each anomaly in a parameter reduction (region basis) algorithm as outlined by Dehghani *et al* (2003). Briefly, images are reconstructed assuming correct knowledge of the location and size of the anomalies (potentially obtainable from other modalities). This information is then used to reduce the number of unknowns to three (background, and two anomalies) for image reconstruction. Reconstructed images using this algorithm and the first excitation pattern are shown in figure 7. All three excitation patterns produced the same reconstruction, but the first pattern
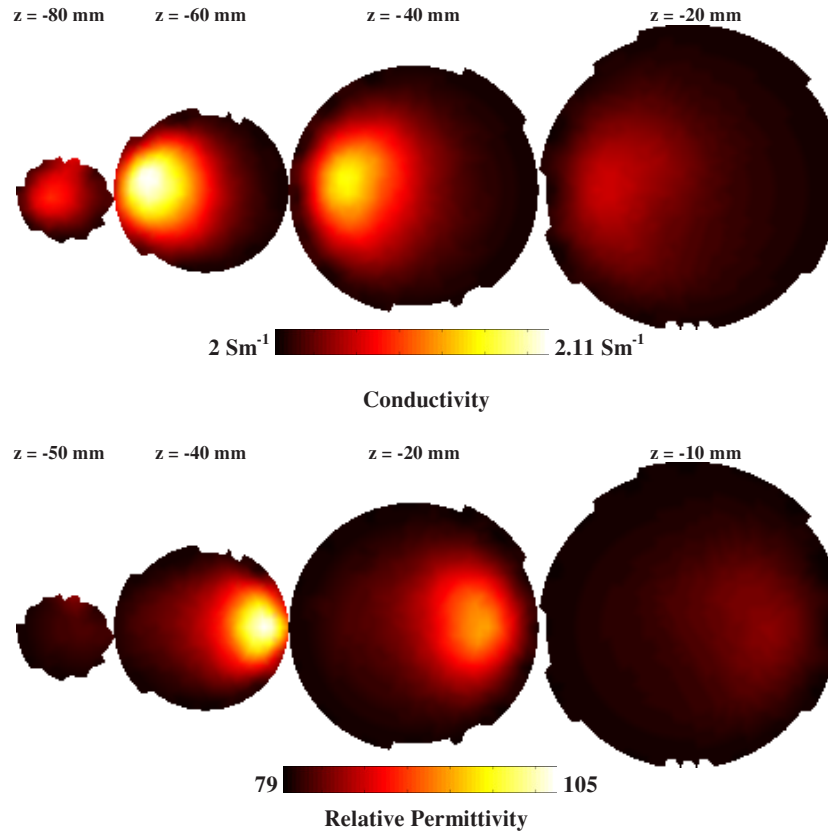
z = -80 mm   z = -60 mm   z = -40 mm   z = -20 mm

2 Sm^{-1} ▮▮▮▮▮▮ 2.11 Sm^{-1}

Conductivity

z = -50 mm   z = -40 mm   z = -20 mm   z = -10 mm

79 ▮▮▮▮▮▮ 105

Relative Permittivity

Figure 4. 2D coronal slices of the 3D reconstruction of internal conductivity and permittivity distributions using the first excitation pattern. The most right-hand slice is near the chest while the most left-hand slice is near the nipple.

iterated to a stable solution at iteration 13, whereas the second and third patterns stabilized by iteration 8.

5. Discussion

In this work, we have presented our implementation of a three-dimensional finite element model for electrical impedance imaging. We have used this model to investigate three-dimensional excitation patterns for a female breast model consisting of 4 levels of 16 electrodes. Specifically we have calculated the Jacobian (sensitivity map) for the whole model using each in-phase and out-of-phase drive pattern and performed singular value decomposition to examine the amount of information available from each drive pattern, which is above the noise floor of a typical measurement system. It has been shown that using an excitation pattern where each level of electrodes is excited with a sinusoidal pattern in the plane that is in-phase with all of the other planes contained the least amount of information about the imaging domain. By comparison, when the driving patterns for each plane of electrodes were out-of-phase with one another, there is a significant increase in the total number of singular values (figure 3), which occur above the noise threshold with the third pattern (each plane
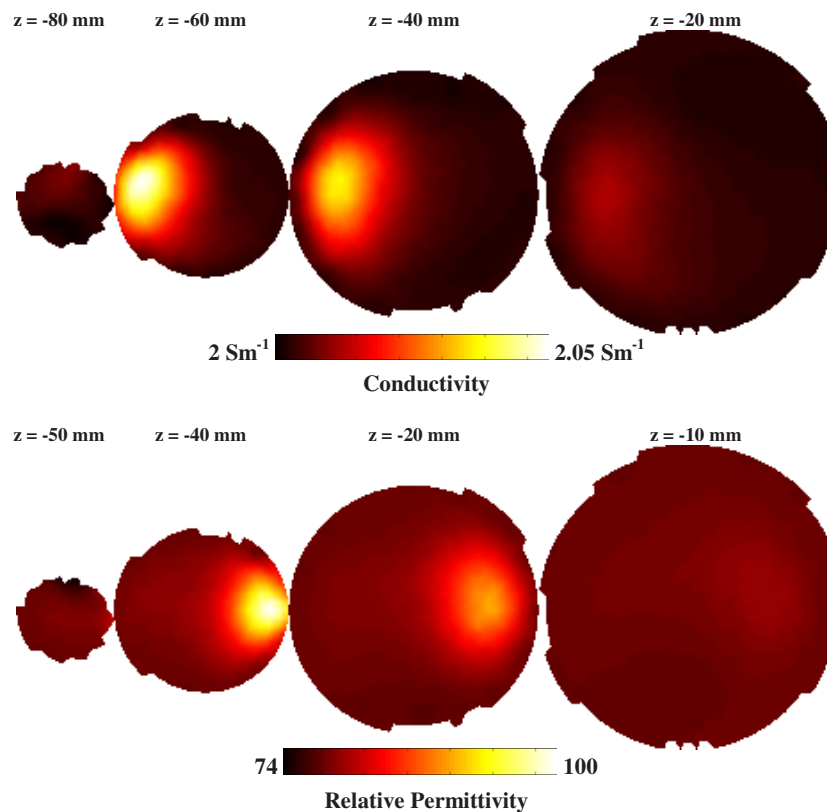
Figure 5. As in figure 4, but using the second drive pattern (45° out of phase).

being 90° out phase) producing the best results. The second and third patterns are such that they dictate a sinusoidal driving pattern, not only in the plane of the electrodes, but also in the z-direction. Other similar studies (Polydorides and McCann 2002) have used the SVD analysis as well as Picard plots to show how different electrode configuration can increase resolution in a 2D EIT problem. In their work they have shown that in an ill-posed problem where the measurements are contaminated with some noise, a stable solution exists if the Picard criterion is satisfied. According to these criteria, the Picard coefficients $\{U^T_i b\}$ should decay to zero faster than the (generalized) singular values, where U is the left orthogonal factor of J and b the measurements vector. The work presented, particularly the results shown in figure 3 where the number of useful singular values above the expected noise limits can also be expanded to show relevant Picard plots, but it is expected that identical results will be achieved; namely that more information regarding the domain being imaged can be obtained with a driving pattern where each plane is out-of-phase with another.

The increase in the total useful number of singular values for the out-of-phase driving pattern can be explained by considering the flow of current within the medium. For a driving pattern where all planes of excitation are of the same phase, the current will flow through the medium without being forced to sample the areas directly underneath and between the planes of each electrode. Whereas for the out-of-phase driving patterns, due to the potential difference between each electrode of different phase, the current is forced to sample the volume underneath and between each electrode plane as well as sampling deep within the medium,
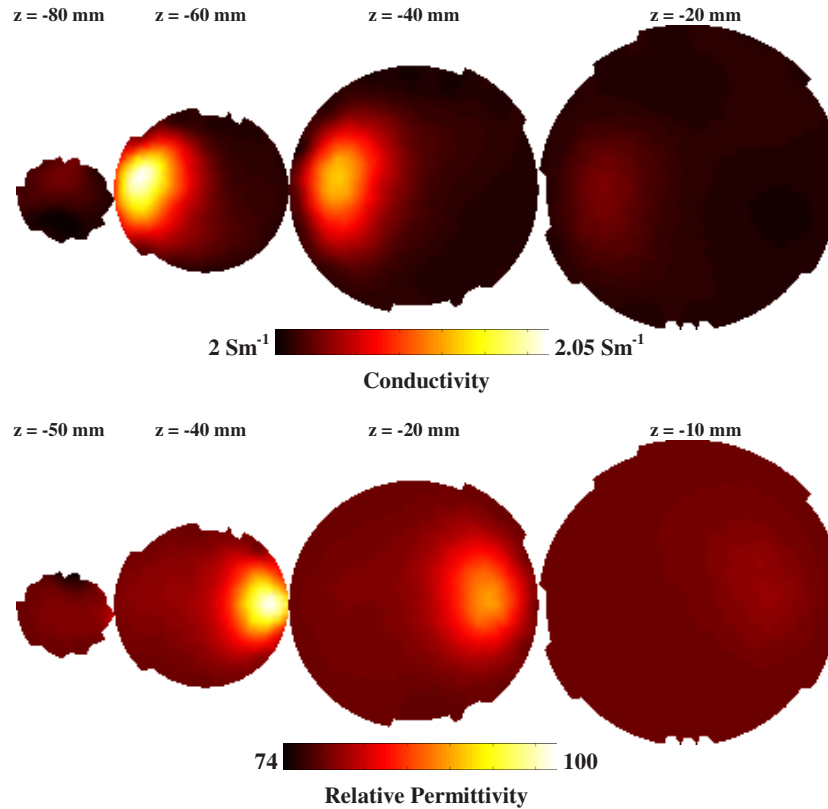
Figure 6. As in figure 4, but using the third drive pattern (90° out of phase).

at a cost of reduced sensitivity to these deeper regions. Therefore, since the out-of-phase driving patterns sample a larger area, the amount of information contained within them is increased. Finally it is very important to state that each of the 3 different current patterns does give rise to the same number of measurements, i.e. 15 current patterns (each plane in or out of phase with other planes) and 48 electrodes. Therefore the increase in the number of significant singular values is purely due to the amount of information contained and not to a change in the number of measurements.

In order to assess further these sensitivity results, actual images were reconstructed using simulated data, where two spherical anomalies (a single conductor and a single permittivity object) were modeled at the mid-plane of the breast mesh. Images were recovered using each drive pattern. All patterns generated good separation between the two anomalies. Although all of the images have recovered the anomalies in the correct position, results obtained using the first excitation pattern are more blurred. As evident in the results shown in the reconstructed images and table 1, although the peak value reached with the first excitation pattern is slightly higher, the spatial resolution from the second and third excitation patterns is superior. In all cases the third excitation pattern shows the best results, which is consistent with the SVD analysis. It should be noted that the quantitative accuracy of all images is relatively poor which is a common problem in 3D imaging and is sometimes referred to as a partial volume effect that has been reported (Gibson *et al* 2003). The quantitative accuracy can be improved
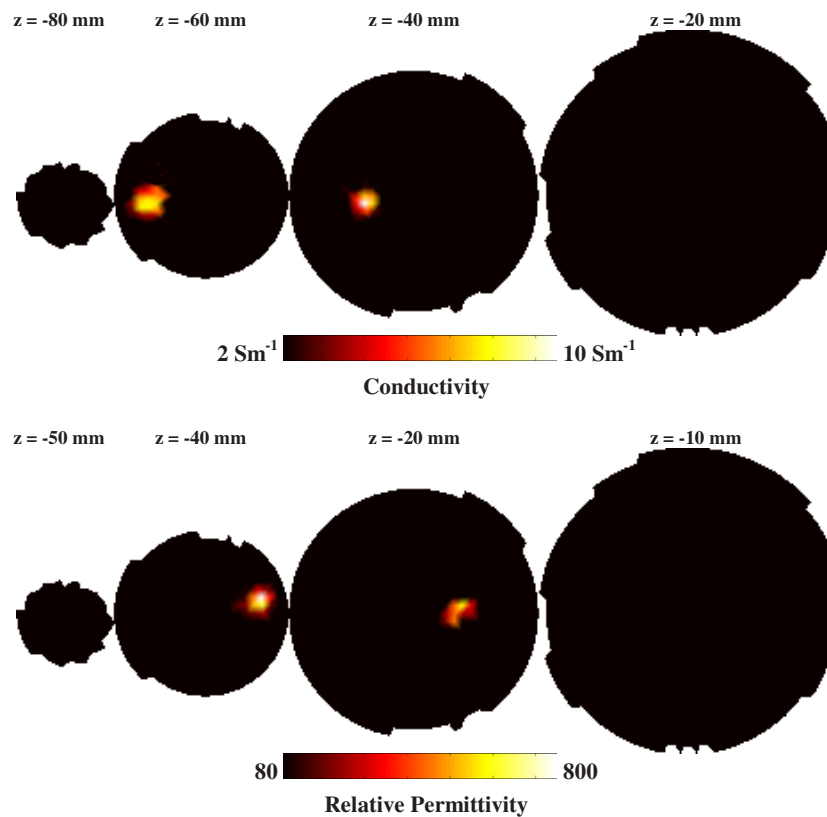
Figure 7. As in figure 4, but using *a priori* information for image reconstruction.

using other types of regularization, reconstruction bases and with the addition of constraints or *a priori* information, as shown in figure 7.

It may be argued that the convergence behavior of the nonlinear reconstruction algorithm is critically related to the choice of the regularization parameter. However, since in all of the results presented here, the initial choice of the regularization parameter and the Levenberg–Marquardt implementation within the nonlinear reconstruction algorithm have been identical regardless of the choice of excitation patterns, it is acceptable to conclude that the difference in the results presented is due to only the choice of the applied excitation patterns. However, it should be again stated that since different current patterns (i.e. in-phase planes versus out-of-phase) will cause the sampling of different volumes, different reconstruction results would be seen if the anomalies are nearer the boundary, but the general trend (that out-of-phase patterns have a higher amount of information) shown here will be expected. The in-phase pattern has shown a slightly better quantitative accuracy, simply because the anomalies are places such that the current flow through the medium is literally sweeping across the medium rather than in between planes of measurement.

6. Conclusions

In this work we have presented our 3D FEM implementation for EIT. We have used this model to assess the benefits of 3 different drive patterns for a female breast model having

4 planes of 16 electrodes. By using singular value decomposition of the Jacobian (sensitivity) matrix, it has been shown that the total amount of information about the domain is increased when phase shift in the z-direction is introduced between the driving patterns spanning the 4 layers of electrodes. Specifically, the best performance was observed when each plane is $90°$ out-of-phase as relative to the plane above or below it. In order to further investigate these findings, we have also shown reconstructed images from simulated data, which indicate that using out-of-phase driving patterns produces better images in terms of resolution. Furthermore, we have demonstrated 3D image reconstruction at relatively fast computation time and good conductivity/permittivity value separation. Although the quantitative accuracy of the reconstructed images is not yet satisfactory, methods exist for improvement including alternative regularizations, reconstruction bases and use of constraints and/or *a priori* information. An example of *a priori* information used as a parameter reduction technique for image reconstruction has been shown.

The SVD analysis is a powerful method for determining optimal system configurations, which yield the maximum amount of measurement information. For the purpose of the presented study, the three different applied excitation patterns were chosen since these are the obvious extension to the current patterns used for 2D imaging and they are a natural extension to the studies by other researchers in terms of distinguishability (Goble 1990). Further work is needed to assess how different pattern options actually perform in more complex models, for example, in a heterogeneous breast model using different electrode placements. However, regardless of the imaging domain, it has been shown that the SVD method can also be used to optimize a system to achieve the best possible data acquisition from different parts of the imaging domain.

Acknowledgments

References

Adler A *et al* 1997 Monitoring changes in lung air and liquid volumes with electrical impedance tomography *J. Appl. Physiol.* **83** 1762–7

Bagshaw A P L, Liston A D, Bayford R H, Tizzard A, Gibson A P, Tidswell A T, Sparkes M K, Dehghani H, Binnie C D and Holder D S 2003 Electrical impedance tomography of human brain function using reconstruction algorithms based on the finite element method *Neuroimage* **20** 752–64

Boone K, Barber D and Brown B 1997 Imaging with electricity: report of the European Concerted Action on Impedance Tomography *J. Med. Eng. Technol.* **21** 201–32

Borsic A 2002 Regularisation methods for imaging from electrical measurements *Thesis* Oxford Brookes University

Brown B H 2003 Electrical impedance tomography (EIT): a review *J. Med. Eng. Technol.* **27** 97–108

Brown B H *et al* 1992 Blood flow imaging using electrical impedance tomography *Clin. Phys. Physiol. Meas.* **13** 175–9

Brown B H *et al* 1994 Multi-frequency imaging and modelling of respiratory related electrical impedance changes *Physiol. Meas.* **15** A1–12

Cherepenin V *et al* 2001 A 3D electrical impedance tomography (EIT) system for breast cancer detection *Physiol. Meas.* **22** 9–18

Dehghani H, Pogue B W, Jiang S, Brooksby B and Paulsen K D 2003 Three dimensional optical tomography: resolution in small object imaging *Appl. Opt.* **42** 3117–28

Erol R A *et al* 1996 Can electrical impedance tomography be used to detect gastro-oesophageal reflux? *Physiol. Meas.* **17** A141–7

Frerichs I 2000 Electrical impedance tomography (EIT) in applications related to lung and ventilation: a review of experimental and clinical activities *Physiol. Meas.* **21** R1–21

Gibson A *et al* 2003 Optical tomography of a realistic neonatal head phantom *Appl. Opt.* **42** 3109–16

Goble J C 1990 The three-dimensional inverse problem in electric current computed tomography *Thesis* Rensselaer Polytechnic Institute

Hoetink A E, Faes Th J C, Marcus J T, Kerkkamp H J J and Heethaar R M 2001 Imaging of thoracic blood volume changes during the heart cycle with electrical impedance using a linear spot-electrode array *IEEE Trans. Med. Imaging* **21** 653–61

Holder D S 1992 Electrical impedance tomography (EIT) of brain function *Brain Topogr.* **5** 87–93

Isaacson D 1986 Distinguishability of conductivities by electric current computed tomography *IEEE Trans. Med. Imaging* **5** 91–5

Kerner T E, Paulsen K D, Hartov A, Soho S K and Poplack S P 2002 Electrical impedance spectroscopy of the breast: clinical results in 26 subjects *IEEE Trans. Med. Imaging* **21** 638–46

Lionheart W R 2004 EIT reconstruction algorithms: pitfalls, challenges and recent developments. *Physiol. Meas.* **25** 125–42

Metherall P *et al* 1996 Three-dimensional electrical impedance tomography *Nature* **380** 509–12

Molinari M *et al* 2002 Comparison of algorithms for non-linear inverse 3D electrical tomography reconstruction *Physiol. Meas.* **23** 95–104

Newell J C, Isaacson D, Saulnier G J, Cheney M and Gisser D G 1993 Acute pulmonary edema assessed by electrical impedance tomography *Proc. Annu. Int. Conf. IEEE Engineering in Medicine and Biology Soc.* 92–3

Noble T J *et al* 1999 Monitoring patients with left ventricular failure by electrical impedance tomography *Eur. J. Heart Failure* **1** 379–84

Polydorides N and Lionheart W R B 2002 A matlab toolkit for three-dimensional electrical impedance tomography: a contribution to the electrical impedance and diffuse optical reconstruction software project *Meas. Sci. Technol.* **13** 1871–83

Polydorides P and McCann M 2002 Electrode configuration for improved spatial resolution in electrical impedance tomography *Meas. Sci. Technol.* **13** 1862–70

Valente Barbas C S 2003 Lung recruitment maneuvers in acute respiratory distress syndrome and facilitating resolution. *Crit. Care Med.* **31** S265–71

van Genderingen H R, van Vught A J and Jansen J R 2003 Estimation of regional lung volume changes by electrical impedance pressures tomography during a pressure–volume maneuver *Intensive Care Med.* **29** 233–40

van Genderingen H R, van Vught A J and Jansen R 2004 Regional lung volume during high-frequency oscillatory ventilation by electrical impedance tomography *Crit. Care Med.* **32** 787–94

Vauhkonen M 1997 Electrical impedance tomography and prior information *Thesis* Univeristy of Kuopio

Vauhkonen P J *et al* 1999 Three-dimensional electrical impedance tomography based on the complete electrode model *IEEE Trans. Biomed. Eng.* **46** 1150–60

Vonk Noordegraaf A *et al* 1997 Noninvasive assessment of right ventricular diastolic function by electrical impedance tomography *Chest* **111** 1222–8

Wang W *et al* 2001 Preliminary results from an EIT breast imaging simulation system *Physiol. Meas.* **22** 39–48

Woo E J *et al* 1992 Measuring lung resistivity using electrical impedance tomography *IEEE Trans. Biomed. Eng.* **39** 756–60

Zou Y and Guo Z 2003 A review of electrical impedance techniques for breast cancer detection *Med. Eng. Phys.* **25** 79–90

Effects of refractive index on near-infrared tomography of the breast

Hamid Dehghani, Ben A. Brooksby, Brian W. Pogue, and Keith D. Paulsen

Near infrared (NIR) optical tomography is an imaging technique in which internal images of optical properties are reconstructed with the boundary measurements of light propagation through the medium. Recent advances in instrumentation and theory have led to the use of this method for the detection and characterization of tumors within the female breast tissue. Most image reconstruction approaches have used the diffusion approximation and have assumed that the refractive index of the breast is constant, with a bulk value of approximately 1.4. We have applied a previously reported modified diffusion approximation, in which the refractive index for different tissues can be modeled. The model was used to generate NIR data from a realistic breast geometry containing a localized anomaly. Using this simulated data, we have reconstructed optical images, both with and without correct knowledge of the refractive-index distribution to show that the modified diffusion approximation can accurately recover the anomaly given *a priori* knowledge of refractive index. But using a reconstruction algorithm without the use of correct *a priori* information regarding the refractive-index distribution is shown as recovering the anomaly but with a degraded quality, depending on the degree of refractive index mismatch. The results suggest that provided the refractive index of breast tissue is approximately 1.3–1.4, their exclusion will have minimal effect on the reconstructed images.   © 2005 Optical Society of America

OCIS codes: 170.3010, 170.3830, 170.6960.

1. Introduction

Near-infrared (NIR) optical tomography, is a noninvasive imaging modality in which images of internal optical properties are reconstructed by use of measured transmission data.[1–8] More specifically, a number of optical fibers are placed around the surface of the tissue to be imaged and light is transmitted from one fiber at a time, while all other fibers are used to measure the exiting light at discrete locations around the tissue. The recovery of the interior optical properties is treated as a nonlinear inverse problem based on measurements at the exterior of the domain to be imaged. The light source can be operated in continuous-wave (cw) pulsed or intensity-modulated modes, giving rise to output measurements of light intensity, temporal point-spread function, or phase and amplitude, depending on the strategy adopted.

Typically light sources are applied at a number of NIR wavelengths, each, in turn, giving rise to additional spectrally independent boundary measurements. The time-resolved or frequency-domain data allows for reconstruction of internal optical property distributions of absorption (μ_a) and/or reduced scatter (μ_s') for each wavelength, which can in turn be used to calculate images of the concentrations of the dominant chromophores, including oxyhemoglobin, deoxyhemoglobin and water, as well as scattering power and amplitude.[9] These images are the end results of NIR tomography, and they may complement other imaging modalities, potentially defining NIR tomography as a functional imaging technique.

For image reconstruction with the measured boundary data, several different algorithms can be used, depending on datatype, number of measurements, and domain under investigation.[10] Many imaging algorithms rely on a numerical model, whereby the process for iteratively updating the internal distribution of absorption and scatter is to match the measured data to model-based predictions. Assuming that the tissue scatter dominates absorption and that the imaging domain is large enough so that the smallest source–detector fiber distance is greater than a few mean scattering lengths, the diffusion approximation (DA) models the light propagation effectively.

The authors are with the Thayer School of Engineering, Dartmouth College, 8000 Cummings Hall, Hanover, New Hampshire 03755-8000. H. Dehghani's e-mail address is hamid.dehghani@dartmouth.edu.

Recently, advances have been made in representing bulk internal refractive-index (RI) variation in tissue within the numerical model.[11–13] Jiang and Xu[12] have used a higher-order DA that also takes into account the RI as a spatially varying property and have presented reconstructed images of internal absorption, reduced scatter, and refractive index using cw data. Our earlier study showed the implementation of RI spatial variation within the DA using a finite-element modeling approach.[11] Specifically, we defined an internal boundary condition that allows for discontinuous internal variations of RI between regions of contrast (or slowly varying) optical properties. This approach provided a good match between three-dimensional finite-element model results and Monte Carlo simulations, as well as controlled experimental measurements,[14] suggesting that the technique is a valid approximation.

The absolute values of RI for breast tissue types are still a subject under investigation. Estimates are difficult to obtain accurately *in vivo*, but some data have been reported for various tissue types.[14,15] Although adipose tissue (fatty layer) has been measured to be 1.455, to the best of our knowledge no results exist for fibroglandular tissue. Nonetheless, the RI of glandular tissue is believed to be lower than that of adipose (e.g., values of 1.4 have been assumed[15,16]). The rationale for a lower value is sound in that estimates of the composition of fibroglandular tissue place its water (typically greater than 60%) and blood content (greater than 1%) to be high, indicating that its bulk RI is likely close to that of water.[17,18]

In this paper, we have investigated at the effect of variation of RI within a realistic two-dimensional model of a female breast, by assuming distinct values for the adipose and glandular tissue compartments. Using our current dual modality magnetic resonance imaging (MRI)-NIR system, we can collect NIR and MRI data simultaneously[19] allowing accurate *a priori* information regarding the tissue structure under investigation. Specifically, we have generated NIR data from a two-dimensional model of the female breast, obtained from MRI, within which we have assumed RI variation for the two main types, namely, adipose and glandular tissue. Within the glandular layer, we have inserted an abnormality with absorption and scatter-only contrast. Using the modeled NIR data perturbed by noise, we have reconstructed images of internal absorption and reduced scatter and have shown the effect on RI variation within reconstructed images for the cases of either no *a priori* or exact information on the RI values.

2. Theory

A. Forward Model

It is generally accepted that if the magnitude of the isotropic fluence rate within tissue is significantly larger than the directional flux magnitude, the light field is diffuse, which occurs when the scattering interaction dominates over absorption in a region of interest. Mathematically, this assumption allows a simplification of the Boltzmann transport equation, by converting the description of an anisotropic light field into a diffusion equation approximation. The diffusion approximation in the frequency domain is given by

$$- \nabla \cdot \kappa(r) \nabla \Phi(r, \ \omega) + \left[\mu_a(r) + \frac{i\omega}{c_m(r)} \right] \times \Phi(r, \ \omega) = q_0(r, \ \omega), \quad (1)$$

where μ_a and μ_s' are absorption and reduced scattering, respectively; $q_0(r, \omega)$ is an isotropic source; $\Phi(r, \omega)$ is the photon fluence rate at position **r**;

$$\kappa = \frac{1}{3(\mu_a + \mu_s')}$$

is the diffusion coefficient; and $c_m(r)$ is the speed of light in the medium at any point, defined by $c/n(r)$, where $n(r)$ is the index of refraction at the same point and c is the speed of light in a vacuum.

The best description of the air–tissue boundary, is reported through an index-mismatched type III condition, in which the fluence at the edge of the tissue exits and does not return.[20] The flux leaving the external boundary is equal to the fluence rate at the boundary weighted by a factor that accounts for the internal reflection of light back into the tissue. This relation is described in

$$\Phi(\xi, \ \omega) + 2A\hat{\mathbf{n}} \cdot \kappa(\xi)\nabla \Phi(\xi, \ \omega) = 0, \quad (2)$$

where ξ is a point on the external boundary ($\partial\Omega_1$), and A depends on the relative RI mismatch between tissue Ω_1 and air. A can be derived from Fresnel's law,

$$A = \frac{2/(1 - R_0) - 1 + |\cos \theta_c|^3}{1 - |\cos \theta_c|^3}, \quad (3)$$

where $\theta_c = \arcsin(n_{\text{AIR}}/n_1)$, the angle at which total internal reflection occurs for photons moving from region Ω_1 with RI n_1 to air with RI n_{AIR}, and

$$R_0 = \frac{(n_1/n_{\text{AIR}} - 1)^2}{(n_1/n_{\text{AIR}} + 1)^2}. \quad (4)$$

At the external boundaries, $n_{\text{AIR}} = 1$, the RI of free space.

At interior nodes, which lie on an interface between two media with different indices of refraction, we apply the conditions used by Schmitt *et al.*,[21] Takatani and Graham,[22] and Faris[23]:

$$\hat{\mathbf{n}} \cdot D_1\nabla\Phi_1(\xi, \ \omega) = \hat{\mathbf{n}} \cdot D_2\nabla\Phi_2(\xi, \ \omega), \quad (5)$$

$$\frac{\Phi_1(\xi, \ \omega)}{\Phi_2(\xi, \ \omega)} = \left(\frac{n_1}{n_2}\right)^2. \quad (6)$$
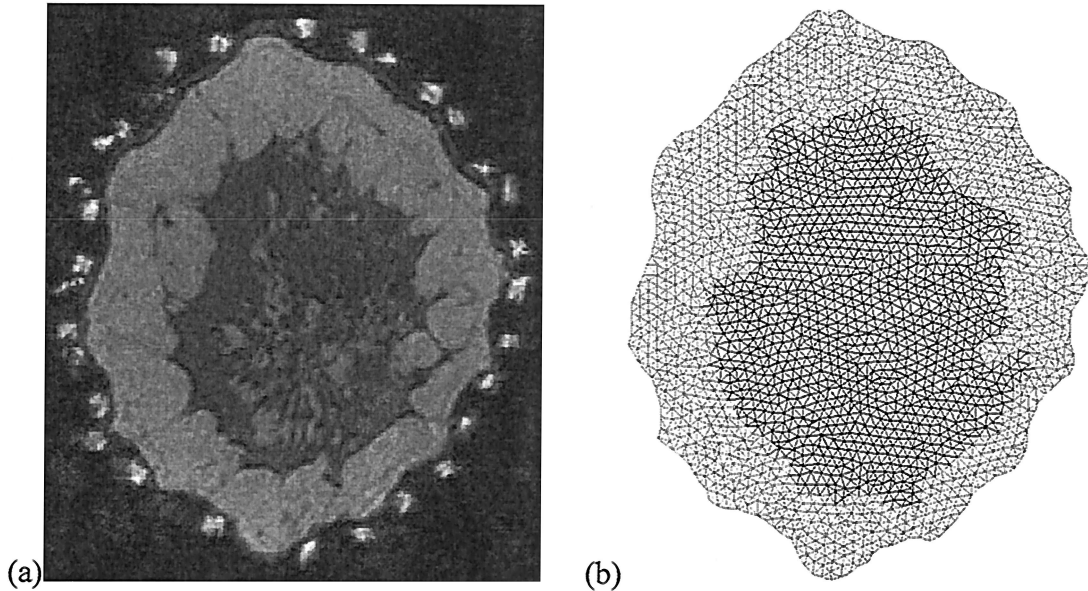
Fig. 1. (a) Coronal slice of an MRI of a female subject showing adipose and glandular tissue layers and (b) the finite-element model mesh created from segmenting the MRI.

These equations enforce continuity in the flux across a step change in RI (n), and establish a corresponding discontinuity in the fluence on the basis of the two RIs defining the regions separating the boundary.

B. Inverse Model

The data is represented by a nonlinear operator $\mathbf{y}^* = F[\mu_a, \kappa]$, where $\mathbf{y}^*$ is a complex vector having a real and imaginary components, which are mapped to log amplitude and phase in measurement. Then the image reconstruction method seeks a solution to

$$(\hat{\mu}_a, \hat{\kappa}) = \arg \min_{\mu_a, \kappa} \| [y^* - F(\mu_a, \kappa)] \|, \qquad (7)$$

where $\|.\|$ is the weighted L2-norm, representing the square root of the sum of the squared elements. The magnitude of this is sometimes referred to as the projection error and provides a value for determining the convergence of the iterative reconstruction algorithm.

The finite-element method is used as a general and flexible method for solving the forward problem in arbitrary geometries.[11,24,25] In the inverse problem, in which the aim is to recover internal optical property distributions from boundary measurements, we assume that $\mu_a(\mathbf{r})$ and $\kappa(\mathbf{r})$ are expressed in a basis with a limited number of dimensions (less than the dimension of the finite-element system matrices). A number of different strategies for defining reconstruction bases are possible; in this paper we use a linear pixel basis. To find $(\hat{\mu}_a, \hat{\kappa})$ in Eq. (7), we used a Levenberg–Marquardt algorithm in which is repeatedly solved

$$\mathbf{a} = J^T(JJ^T + \rho I)^{-1}\mathbf{b}, \qquad (8)$$

where $\mathbf{b}$ is the data vector, $\mathbf{b} = (\mathbf{y}^* - F[\mu_a, \kappa])^T$; $\mathbf{a}$ is

the solution update vector, $\mathbf{a} = [\delta\kappa; \delta\mu_a]$; ρ is the regularization factor; and J is the Jacobian (sensitivity or weight) matrix for the DA model that is calculated with the Adjoint method.[26]

3. Simulation Methods

An MRI of a female subject, Fig. 1(a), was used to create a two-dimensional mesh Fig. 1(b).[19] The mesh contained 2306 nodes corresponding to 4042 linear triangular elements and has a major and minor axis diameter of 101 and 82 mm, respectively. For this subject, experimental data was collected with an MRI-NIR system.[19] We combined the NIR measurements with *a priori* anatomical information from the MRI (assuming no RI variation) to estimate the optical absorption and reduced scatter for each tissue type. These procedures generated estimates of the adipose layer as having an absorption of 0.003 mm^{-1} and a reduced scatter of 0.95 mm^{-1}, whereas the glandular tissue resulted in an absorption of 0.006 mm^{-1} and a reduced scatter of 1.1 mm^{-1}. Alternatively, assuming a single tissue type within the breast, we calculated bulk properties for the breast as having an absorption of 0.0056 mm^{-1} and a reduced scatter of 1.125 mm^{-1}. Assuming an RI of 1.455 for the adipose tissue[15] and an RI of 1.2, 1.3, or 1.4 for glandular tissue, we calculated data with the presence of an anomaly within the breast, for two separate cases:

1. Assuming a homogenous distribution of absorption and reduced scatter of 0.0056 and 1.125 mm^{-1}, respectively, it was assumed that the RI varied between each layer with a value of 1.455 for the adipose tissue and 1.2, 1.3, or 1.4 for glandular tissue. The modeled anomaly, as shown in Fig. 2 (top row) had a contrast in absorption and reduced scatter only and
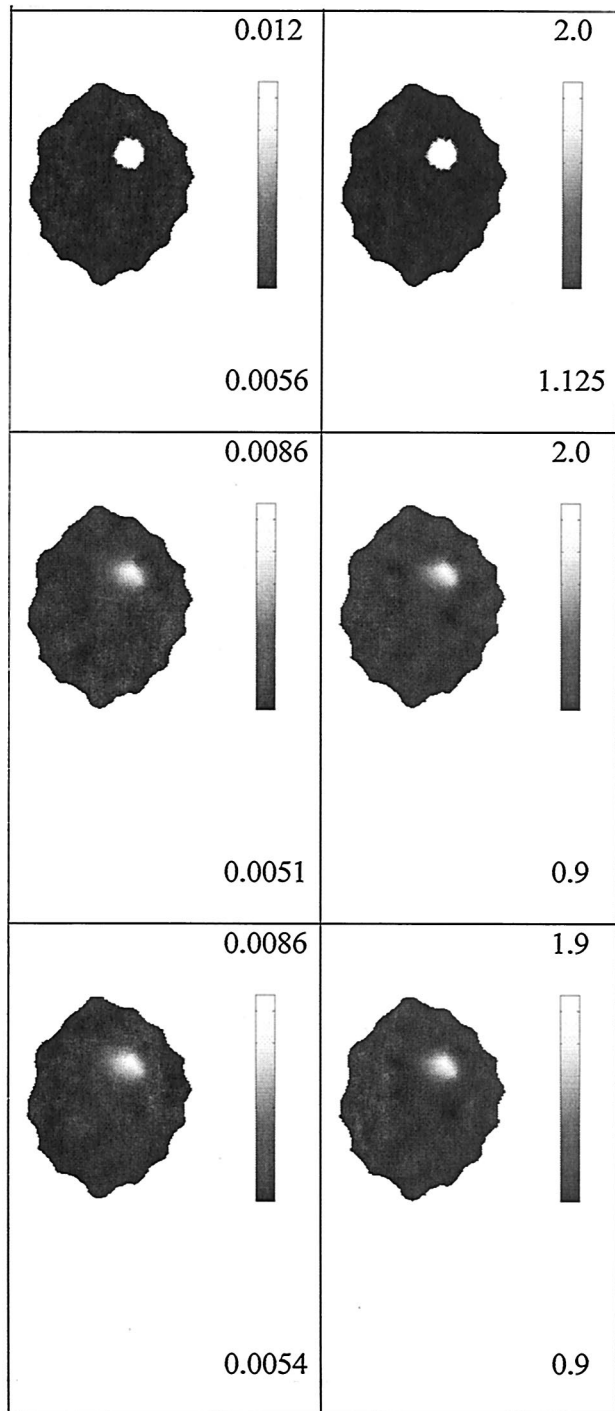
Fig. 2. Images [left column, absorption (mm^{-1}); right column, reduced scatter (mm^{-1})] reconstructed from synthetic data generated with a model with RI variation. Top row shows the exact optical properties; the adipose and glandular zones have the identical optical properties but different RI of 1.455 and 1.4, respectively. Middle row shows reconstructed images assuming the correct RI (same as in top row) distribution. Bottom row shows reconstructed images assuming a homogenous RI of 1.455.

was assumed to have the same RI as glandular tissue.

   2. The adipose layer had an absorption of 0.003 mm^{-1} and a reduced scatter of 0.95 mm^{-1}, whereas the glandular tissue had an absorption of 0.006 mm^{-1} and a reduced scatter of 1.1 mm^{-1}. The RI varied between each layer with a value of 1.455 for the adipose tissue and 1.2, 1.3, or 1.4 for glandular tissue. The modeled anomaly, as shown in Fig. 5 below, (top row) had a contrast in absorption and reduced scatter only and was assumed to have the same RI as glandular tissue.

Boundary data was modeled for 16 equally spaced sources and detectors arranged on the external periphery of the model, with added Gaussian noise of 1% in amplitude and 1° in phase. For each set of data, two types of reconstruction were investigated: (i) correct (*a priori*) information on RI variation and (ii) a constant RI of 1.455. In all cases images were reconstructed on a 20 × 20 uniform grid basis by use of an initial regularization [Eq. (8)] of ρ = 10, and the number of iterations was continued until the projection error [Eq. (7)] changed by less than 1% from the previous iteration.[1]

4. Results

In each of the cases described in Section 3, the simulated data were calibrated with methods described elsewhere[1,27,28] to provide an estimate of the bulk optical properties of absorption and reduced scatter for initiating the reconstruction algorithm.

   Figure 2 shows the exact (top row) and the reconstructed images for the model, which has a homogenous absorption and reduced scatter of 0.0056 and 1.125 mm^{-1}, respectively, except within the anomaly that was assigned values of 0.012 and 2 mm^{-1}. The RI is 1.455 for the adipose tissue and 1.4 for the glandular and the anomaly tissues. Images were reconstructed assuming either correct values of RI for each layer (middle row) or a constant RI distribution of 1.455 (bottom row). In each case, images of absorption and reduced scatter were recovered simultaneously by use of log amplitude and phase of the NIR data.

   Figures 3 and 4 present exact (top row) and reconstructed images in which the model is identical to that in Fig. 2, except for the RI of the glandular and the anomaly tissues, which was set to 1.3 and 1.2, respectively.

   Figure 5 shows exact (top row) and reconstructed images in which the adipose layer had an absorption of 0.003 mm^{-1} and a reduced scatter of 0.95 mm^{-1} whereas the glandular tissue had an absorption of 0.006 mm^{-1} and a reduced scatter of 1.1 mm^{-1}. The anomaly within the glandular tissue had an absorption of 0.012 mm^{-1} and a reduced scatter of 2 mm^{-1}. The RI was 1.455 for the adipose tissue and 1.4 for the glandular and the anomaly tissues. As in Fig. 2, images were produced assuming either the correct values for the RI in each layer (middle row) or a homogeneous RI distribution of 1.455 (bottom row). Figures 6 and 7 show analogous results to those in Figure 5, except for the RI of the glandular and the
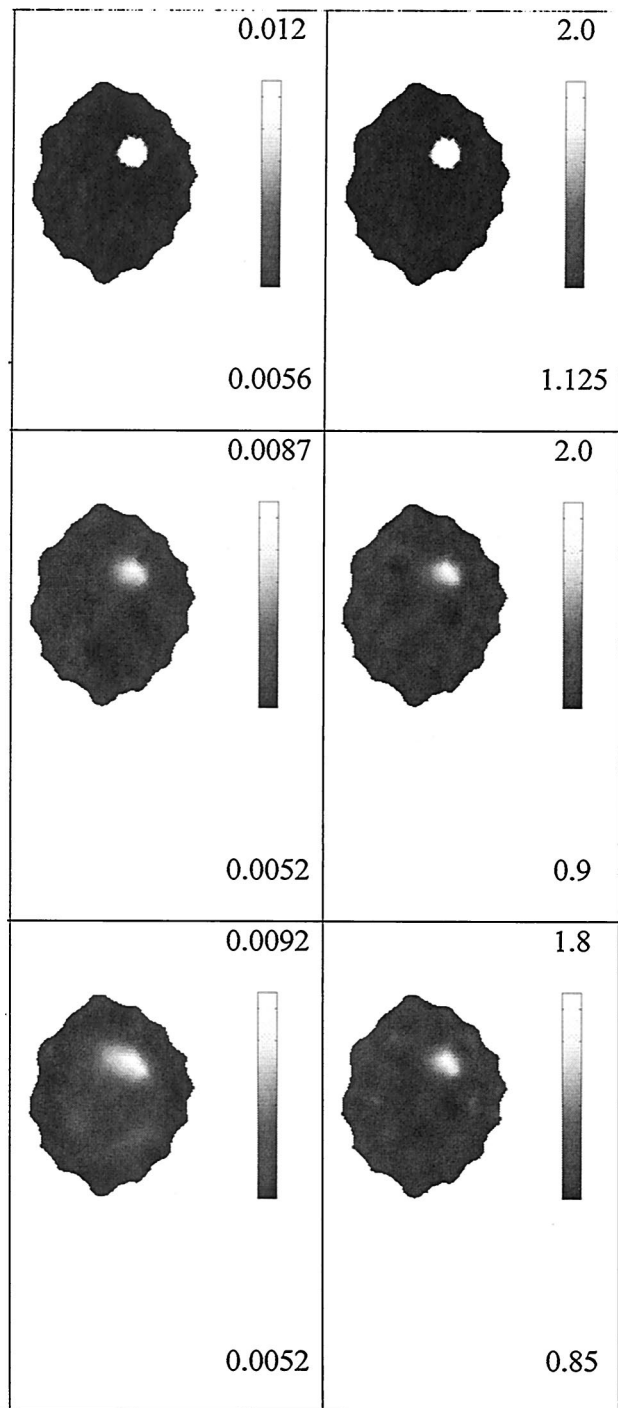
Fig. 3. Same as Fig. 2 except that the glandular tissue (and the anomaly) has an RI of 1.3.

Fig. 4. Same as Fig. 2 except that the glandular tissue (and the anomaly) has an RI of 1.2.

anomaly tissues, which was set to 1.3 and 1.2, respectively.

5. Discussion

In cases in which the tissue is optically (absorption and reduced scatter) homogenous (except for an anomaly) but has different RIs for different tissue types, the recovered optical properties are very similar to the expected values, yielding a peak value of
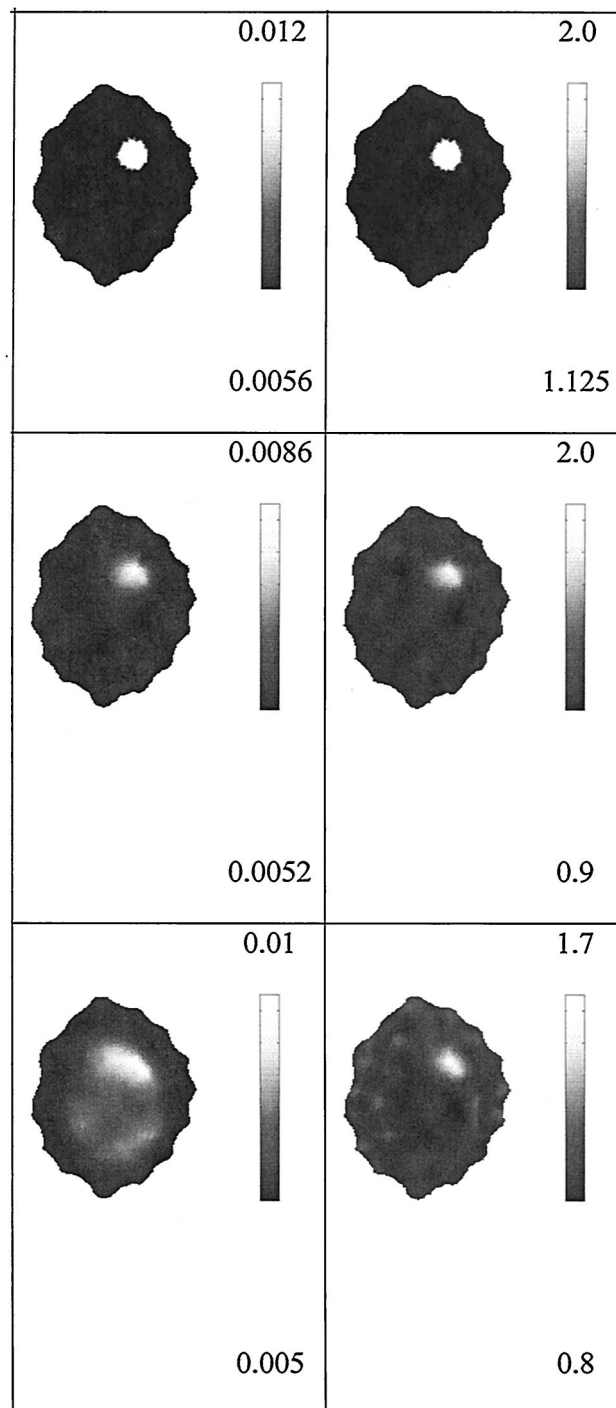
the anomaly for absorption and reduced scatter of approximately 0.0087 and 2.0 mm^{-1}, respectively, when correct *a priori* information on RI distribution is applied throughout the model. Assuming that the model is also uniform in RI, the quality of the reconstructed images varies, depending on the degree of deviation from the true values of RI as expected. For small deviations of RI, that is, when the glandular tissue has an RI of 1.455 but is assumed to be 1.4, the
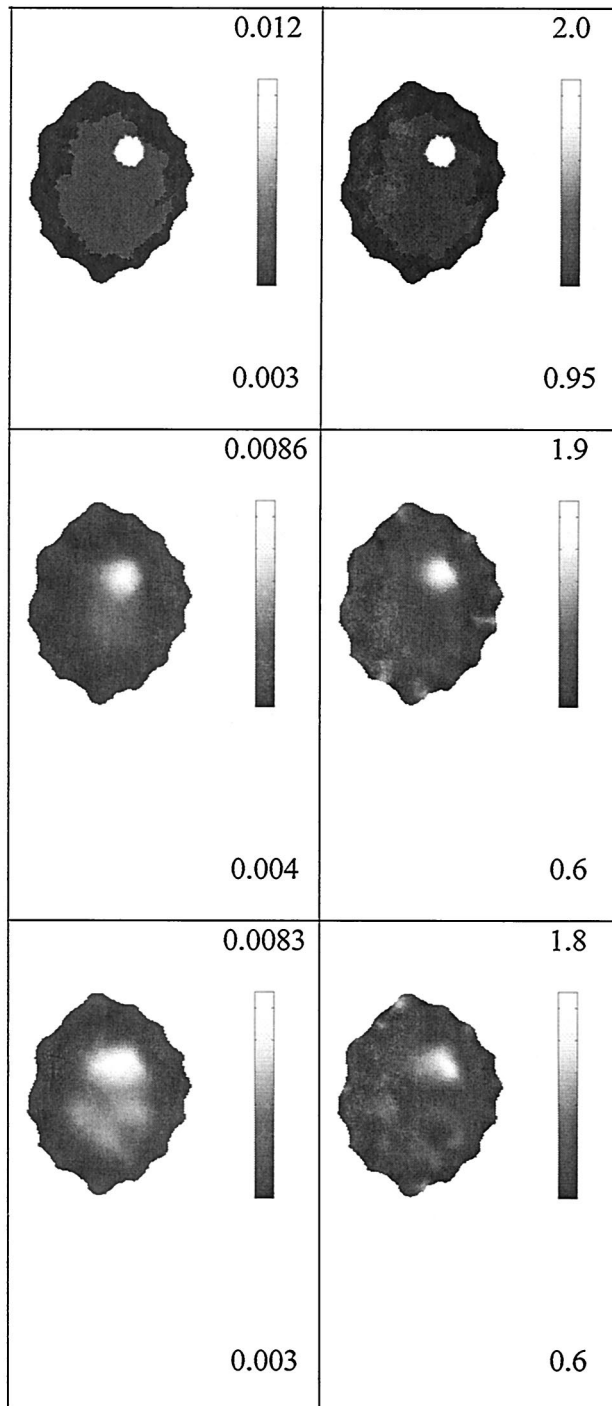
Fig. 5. Images [left column, absorption (mm^{-1}); right column, reduced scatter (mm^{-1})] reconstructed from synthetic data generated with a model with RI variation. Top row shows the exact optical properties; the adipose and glandular tissue have different optical properties and different RI of 1.455 and 1.4, respectively. Middle row shows reconstructed images assuming the correct RI distribution. Bottom row shows reconstructed images assuming a homogenous RI of 1.455.

Fig. 6. Same as Fig. 5 except that the glandular tissue (and the anomaly) has an RI of 1.3.

reconstructed images are very similar to the case in which correct RI is assumed, Fig. 2. As the deviation is increased (Figs. 3 and 4), the quality of the recon-

structed images is reduced. For example, in Fig. 4 (an assumed value of 1.2 for glandular tissue RI), the amount of background noise in absorption and scatter is increased, and the recovered anomaly is blurred and overly smoothed. Interestingly, the peak value of absorption has increased to $0.01\ mm^{-1}$.
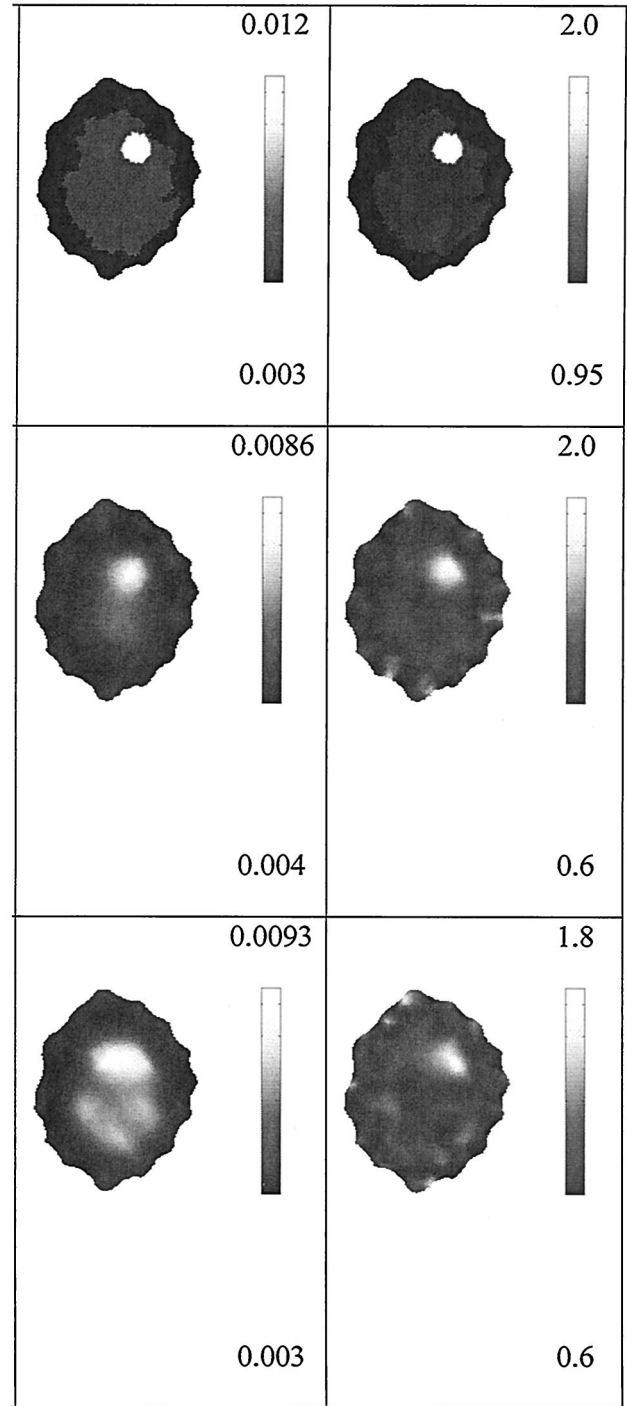
When the tissue is heterogeneous in both optical (absorption and reduced scatter) properties and RI, correct *a priori* information on the RI distribution
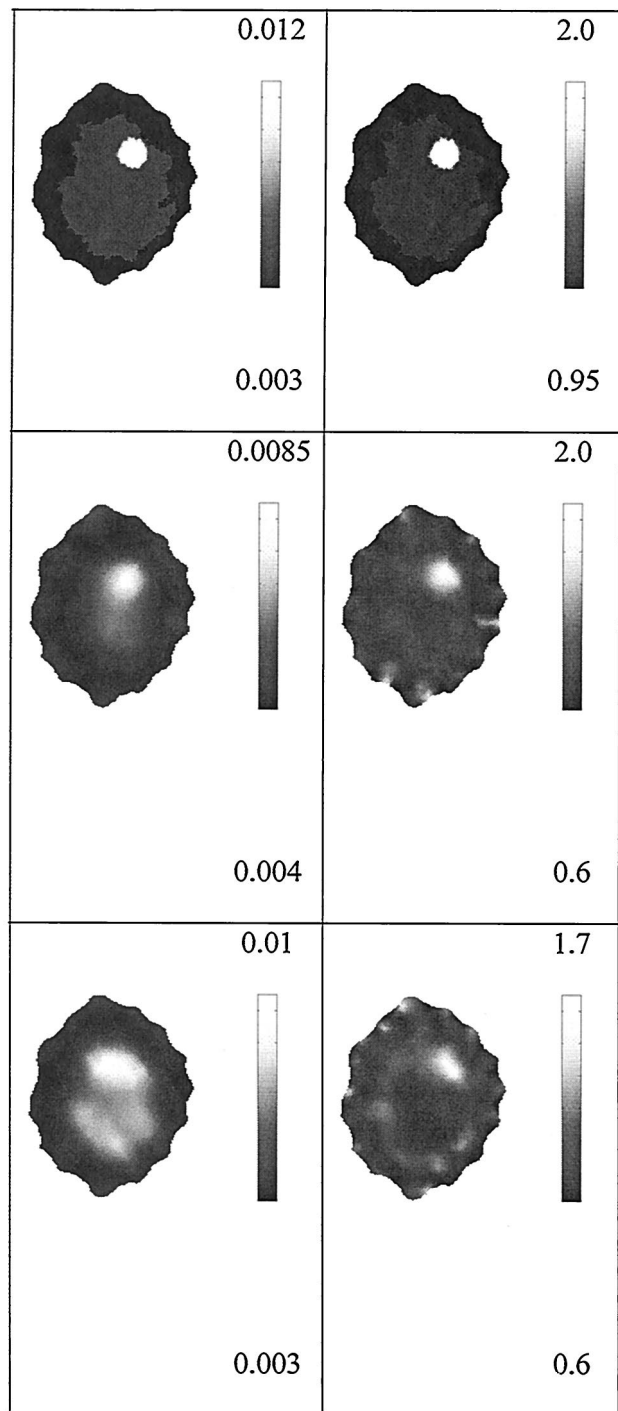
Fig. 7. Same as Fig. 5 except that the glandular tissue (and the anomaly) has an RI of 1.2.

throughout the model generates recovered optical properties that are very similar to the expected values, yielding a peak value in the anomaly for absorption and reduced scatter of approximately 0.0086 and 2.0 mm^{-1}, respectively. If the reconstruction assumes a uniform RI, the quality of the reconstructed images again varies, depending on the level of deviation from the true distribution of RI. For small deviations, the

reconstructed images are similar to the case in which correct RI is used (Fig. 5). As the deviation of the assumed RI increases (Figs. 6 and 7), the quality of the reconstructed images is reduced, but the peak value of recovered absorption increases. In Fig. 7, for example, the RI of the glandular tissue is 1.2, whereas the assumed value for the homogenous reconstruction is 1.455 (bottom row). As in the homogenous case, the amount of background noise in absorption and scatter is increased; however, the recovered anomaly is blurred and overly smoothed, and the peak value of absorption has increased to 0.01 mm^{-1}.

Figure 8 shows the sensitivity map (Jacobian matrix) of log amplitude and absorption for a single source and detector, where the RI distribution is assumed to be either homogeneous at 1.455 or heterogeneous with an adipose layer of RI = 1.455 and a glandular layer of RI = 1.2. From this figure, it evident that a decrease in RI of the glandular tissue reduces the sensitivity deep within the breast. This reduction in sensitivity may explain the increased errors observed when a homogenous assumption of RI is used for image reconstruction. A lower sensitivity within the glandular region will give rise to overly smoothed reconstructed images. However, note that an assumption for the glandular tissue RI of 1.2 is probably not realistic and is only included here for bracketing the effects on image reconstruction.

The recovery of the reduced scatter images seems to have been less affected by the variation of the RI. Although only the sensitivity maps of log amplitude and absorption are only shown, similar trend is seen for other available data types and optical properties (log amplitude or phase versus absorption and scatter). However, it is important to note that the magnitude of the reduced sensitivity for scatter and log amplitude or phase (not shown) is much smaller than that seen for log amplitude and absorption.

6. Conclusion

The effect of discrete RI changes within breast tissue upon NIR image reconstruction has been investigated. Previous studies[11] reported our results in modeling the effect of RI on the forward model. In our current results, the initiative was advanced to investigate the effect of RI variation on NIR image reconstruction, either by assumption of correct knowledge of the RI of each tissue or by application of a homogenous value throughout the model.

Synthetic measurement data have been generated from a realistic two-dimensional breast MRI, exhibiting two distinct layers of adipose and glandular tissue. Published values exist for the RI of adipose tissue but not for the glandular tissue. However, it is generally accepted that glandular tissue has a lower RI, and we have assumed a value of 1.4.[16] Nonetheless, to illustrate the effects of RI variation with NIR image reconstruction, we have generated data assuming an RI of glandular tissue of 1.4, 1.3, or 1.2. Furthermore, we have also modeled two distinct

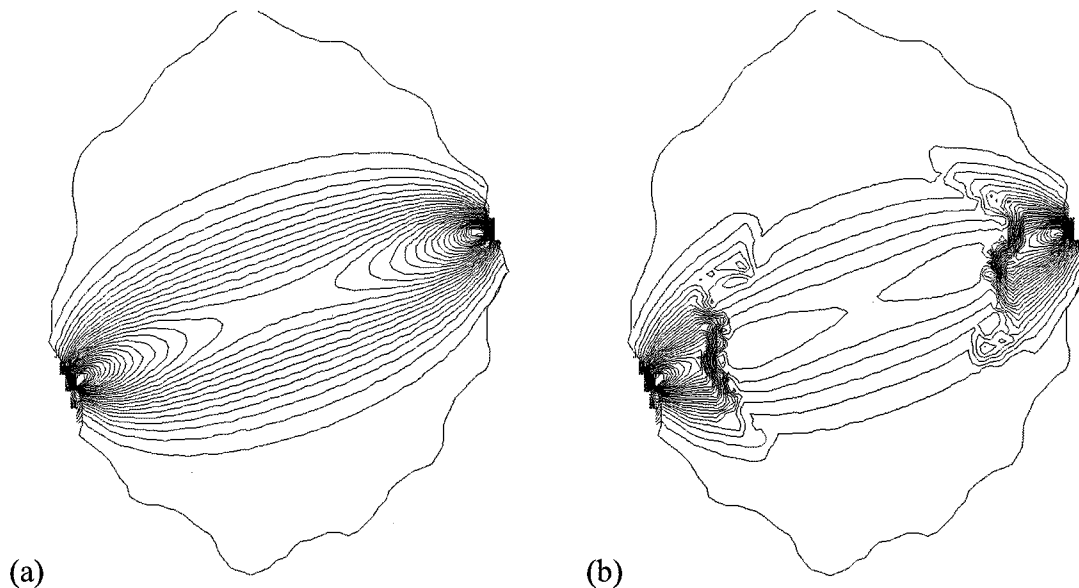(a)   (b)

Fig. 8. Sensitivity map (30 contour lines) of log amplitude to absorption changes for a single source and detector combination for (a) a model of homogenous RI of 1.455 having a maximum value of 1.4×10^{-10} and a minimum value of -1.72 and (b) a heterogeneous RI of adipose, 1.455, and glandular tissue, 1.2, having a maximum value of 1.3×10^{-10} and a minimum value of -1.78.

cases in which each layer had either the same or different absorption and reduced scatter properties, allowing us to separate the effects of absorption and reduced scatter from RI variation. In either case, we modeled an anomaly deep within the breast and reconstructed images assuming either correct information on the RI or simply assuming it to be homogenous.

The reconstructed images show that providing the RI of the glandular tissue, when it is not far from the value of adipose tissue, has little effect on the qualitative and quantitative accuracy of the results. For the layered model (Figs. 5–7) the difference in contrast of the reconstructed anomaly (between use of the correct RI or a homogenous value) is 3.5% when the actual glandular tissue RI is 1.4 (but assumed to be 1.455) and increases to 16% when the actual glandular tissue RI is 1.2. If the RI variation is not modeled, the background noise in the reconstructed images increases, and the reconstructed anomaly exhibits a more blurred character, which can be as large as 200% in the absorption images. This increase in noise and in blurriness can be understood by examination of the sensitivity functions in Fig. 8, which show that as the RI of the glandular tissue decreases with respect to adipose tissue, the sensitivity within the glandular tissue also decreases. Another interesting and very important point to note here is that when the RI distribution is not correctly modeled within the reconstruction algorithm, the effects of the data mismatched owing to the RI are exhibiting themselves within the reconstructed absorption images, clearly seen in Figs. 3 and 4. Also, images were reconstructed (not shown) assuming a homogeneous RI of 1.3 and 1.2 in all of the presented results (depending on the RI of the glandular tissue), and sim-

ilar results were found, as presented, when a homogeneous RI of 1.455 was assumed.

Our research has considered only the reconstruction of absorption and reduced scatter with data generated by a model with RI variation. Assuming the RI of the whole breast is similar, for example, the RI is 1.455 for adipose and 1.4 for glandular tissue, reconstructed images of absorption and scatter can be obtained that ignore the effect of RI with modest degradation in the recovery of information about an abnormality. However, it is also important to note that this analysis was completed under the assumption that the abnormality (i.e., tumor) has the same RI as its background tissue and is most typically located in the fibroglandular tissue. Although, a study by Jiang and Xu[12] has reported large variations in the RI of tumors relative to the background, little other pathologic or *in vivo* data exists on the RI of glandular tissue or the various types of tumor. Further studies are needed to establish the RI variation for different types of tumor and to investigate how such variations might alter NIR tomography.

References
1. H. Dehghani, B. W. Pogue, S. P. Poplack, and K. D. Paulsen, "Multiwavelength three-dimensional near-infrared tomography of the breast: initial simulation, phantom, and clinical results," Appl. Opt. **42,** 135–145 (2003).
2. S. Fantini, S. A. Walker, M. A. Franceschini, M. Kaschke, P. M. Schlag, and K. T. Moesta, "Assessment of the size, position, and optical properties of breast tumors *in vivo* by noninvasive optical methods," Appl. Opt. **37,** 1982–1989 (1998).

3. J. Hebden, A. Gibson, T. Austin, R. Yusof, N. Everdell, D. Delpy, S. Arridge, J. Meek, and J. Wyatt, "Imaging changes in blood volume and oxygenation in the newborn infant brain using three-dimensional optical tomography," Phys. Med. Biol. **49,** 1117–1130 (2004).

4. B. Chance, "Near-infrared (NIR) optical spectroscopy characterizes breast tissue hormonal and age status," Acad. Radiol. **8,** 209–210 (2001).

5. J. C. Hebden, F. M. Gonzalez, A. Gibson, E. M. C. Hillman, R. Yusof, N. Everdell, D. T. Delpy, G. Zaccanti, and F. Martelli, "Assessment of an *in situ* temporal calibration method for time-resolved optical tomography," J. Biomed. Opt. **8,** 87–92 (2003).

6. A. Y. Bluestone, G. Abdoulaev, C. Schmitz, R. L. Barbour, and A. H. Hielscher, "Three-dimensional optical-tomography of hemodynamics in the human head," Opt. Express **9,** 272–286 (2001), http://www.opticsexpress.org.

7. E. M. C. Hillman, J. C. Hebden, M. Schweiger, H. Dehghani, F. E. W. Schmidt, D. T. Delpy, and S. R. Arridge, "Time resolved optical tomography of the human forearm," Phys. Med. Biol. **46,** 1117–1130 (2001).

8. H. Xu, H. Dehghani, B. W. Pogue, R. Springett, K. D. Paulsen, and J. Dunn, "Near-infrared imaging in the small animal brain: optimization of fiber positions," J. Biomed. Opt. **8,** 102–110 (2003).

9. T. O. McBride, B. W. Pogue, S. Jiang, U. L. Osterberg, K. D. Paulsen, and S. P. Poplack, "Multi-spectral near-infrared tomography: a case study in compensating for water and lipid content in hemoglobin imaging of the breast," J. Biomed. Opt. **7,** 72–79 (2002).

10. S. R. Arridge, "Optical tomography in medical imaging," Inv. Probl. **15,** R41–R93 (1999).

11. H. Dehghani, B. Brooksby, K. Vishwanath, B. W. Pogue, and K. D. Paulsen, "The effects of internal refractive index variation in near-infrared optical tomography: a finite element modelling approach," Phys. Med. Biol. **48,** 2713–2727 (2003).

12. H. Jiang and Y. Xu, "Phase-contrast imaging of tissue using near-infrared diffusing light," Med. Phys. **30,** 1048–1051 (2003).

13. J. H. Lee, S. Kim, and Y. T. Kim, "Finite element method for diffusive light propagations in index-mismatched media," Opt. Express **12,** 1727–1740 (2004), http://www.opticsexpress.org.

14. B. Brooksby, H. Dehghani, K. Vishwanath, B. W. Pogue, and K. D. Paulsen, "Internal refractive index changes affect light transport in tissue," in *Optical Tomography and Spectroscopy of Tissue V*, B. Chance, R. R. Alfano, B. J. Tromberg, M. Tamura, and E. M. Sevick-Muraca, eds., Proc. SPIE **4955,** 296–304 (2003).

15. F. P. Bolin, L. E. Preuss, R. C. Taylor, and R. J. Ference, "Refractive index of some mammalian tissue using a fiber optic cladding method," Appl. Opt. **28,** 2297–2303 (1989).

16. B. J. Tromberg, O. Coquoz, J. B. Fishkin, T. Pham, E. R. Anderson, J. Butler, M. Cahn, J. D. Gross, V. Venugopalan, and D. Pham, "Non-invasive measurements of breast tissue optical properties using frequency-domain photon migration," Phil. Trans. R. Soc. Lond. B **352,** 661–668 (1997).

17. S. Srinivasan, B. W. Pogue, S. Jiang, H. Dehghani, C. Kogel, S. Soho, J. J. Gibson, T. D. Tosteson, S. P. Poplack, and K. D. Paulsen, "Interpreting hemoglobin and water concentration, oxygen saturation and scattering measured *in vivo* by near-infrared breast tomography," Proc. Natl. Acad. Sci. USA **100,** 12349–12354 (2003).

18. B. W. Pogue, S. Jiang, H. Dehghani, C. Kogel, S. Soho, S. Srinivasan, X. Song, S. P. Poplack, and K. D. Paulsen, "Characterization of hemoglobin, water and NIR scattering in breast tissue: analysis of inter-subject variability and menstrual cycle changes relative to lesions," J. Biomed. Opt. **9,** 541–552 (2004).

19. B. Brooksby, S. Jiang, C. Kogel, M. Doyley, H. Dehghani, J. B. Weaver, S. P. Poplack, B. W. Pogue, and K. D. Paulsen, "Magnetic resonance-guided near-infrared tomography of the breast," Rev. Sci. Instrum. **75,** 5262–5270 (2004).

20. M. Schweiger, S. R. Arridge, M. Hiroaka, and D. T. Delpy, "The finite element model for the propagation of light in scattering media: boundary and source conditions," Med. Phys. **22,** 1779–1792 (1995).

21. J. M. Schmitt, G. X. Zhou, E. C. Walker, and R. T. Wall, "Multilayer model of photon diffusion in skin," J. Opt. Soc. Am. A **7,** 2141–2153 (1990).

22. S. Takatani and M. Graham, "Theoretical analysis of diffuse reflectance from a two-layer tissue model," IEEE Trans. Biomed. Eng. **26,** 656–664 (1979).

23. G. W. Faris, "Diffusion equation boundary conditions for the interface between turbid media: a comment," J. Opt. Soc. Am. A **19,** 519–520 (2002).

24. H. Jiang, K. D. Paulsen, U. L. Osterberg, B. W. Pogue, and M. S. Patterson, "Optical image reconstruction using frequency-domain data: simulations and experiments," J. Opt. Soc. Am. A **13,** 253–266 (1996).

25. S. R. Arridge, M. Schweiger, M. Hiraoka, and D. T. Delpy, "A finite element approach for modeling photon transport in tissue," Med. Phys. **20,** 299–309 (1993).

26. S. R. Arridge and M. Schweiger, "Photon-measurement density functions. Part 2: Finite-element-method calculations," Appl. Opt. **34,** 8026–8037 (1995).

27. T. O. McBride, B. W. Pogue, U. L. Osterberg, and K. D. Paulsen, "Strategies for absolute calibration of near infrared tomographic tissue imaging," in *Oxygen Transport to Tissue XXIV*, J. F. Dunn and H. M. Schwartz, eds., Adv. Exp. Med. Biol. **531,** 85–99 (2003).

28. T. McBride, "Spectroscopic reconstructed near infrared tomographic imaging for breast cancer diagnosis," Ph.D. dissertation (Dartmouth College, Hanover, 2001).

Spectrally constrained chromophore and scattering near-infrared tomography provides quantitative and robust reconstruction

Subhadra Srinivasan, Brian W. Pogue, Shudong Jiang,
Hamid Dehghani, and Keith D. Paulsen

A multispectral direct chromophore and scattering reconstruction technique has been implemented for near-infrared frequency-domain tomography in recovering images of total hemoglobin, oxygen saturation, water, and scatter parameters. The method applies the spectral constraint of the chromophores and scattering spectra directly in the reconstruction algorithm, thereby reducing the parameter space of the inversion process. This new method was validated by use of simulated and experimental data, and results show better robustness and stability in the presence of higher levels of noise. The method suppresses artifacts, especially those significant in water and scatter power images, and reduces cross talk between chromophore and scatter parameters. Variation in scattering was followed by this spectral approach successfully in experimental data from 90-mm-diameter cylindrical phantoms, and results show linear variation in scatter amplitude and reduced scattering coefficient (μ_s'), with total hemoglobin, oxygen saturation, and water remaining constant and quantitatively accurate. Similar experiments were carried out for varying oxygen saturation and total hemoglobin. Accurate quantification was obtained with a mean error of 7.7% for oxygen saturation and 6.2% for total hemoglobin, with minimal cross talk between different parameters.   © 2005 Optical Society of America

OCIS codes: 170.3010, 170.6960.

1. Introduction

Near-infrared (NIR) tomography can be used to characterize malignant and normal tissue based on the high-contrast available from heme in the blood, leading to images that are related to intrinsic pathophysiologic processes such as angiogenesis and hypoxia. Absorption-based parameters can be recovered such as total hemoglobin in the tissue, hemoglobin oxygen saturation, and water fraction. It is also possible to estimate elastic scattering images that may provide information about the composition of the tissue. *In vivo* studies have demonstrated levels of hemoglobin in tumors over twice that in normal breast,[1,2] and lower levels of oxygen saturation have been found in malignancies[2,3]; however, one of the current chal-

lenges is to optimize the quantitative accuracy with which these parameters can be determined. The quantification of chromophores and scattering parameters relies upon the spectral decomposition of the images acquired at a sparse number of discrete wavelengths instead of a complete spectrum. This sparse spectral sampling coupled with an image reconstruction process that is ill posed, tends to amplify errors in quantifying the spatially resolved parameters of the tissue. In this study a spectrally constrained approach to image reconstruction is introduced, which follows the recent pioneering developments proposed by Corlu *et al.*[4] and Li *et al.*,[5] who showed that incorporation of spectral information into the reconstruction process improves the uniqueness of the image formation by using continuous-wave data. In this paper the addition of phase information and the improved accuracy in fitting water and scattering power are specifically examined by use of this spectrally constrained approach. The improvement in quantification of water and scattering has dramatic implications in terms of the value of these particular parameters in breast imaging. The potential to reduce cross talk between chromophores is also important.

In earlier research the absorption and scattering coefficients were recovered from boundary measurements of amplitude or phase or both on the object of interest, such as the breast or brain, by means of computational models in which both analytical and numerical approaches were used by different research groups.[6–8] After recovery of these optical coefficients, a spectral fitting to known absorption signatures of oxyhemoglobin, deoxyhemoglobin, and water is used to obtain the concentrations of these absorbing chromophores. Similarly, the reduced scattering coefficients at separate wavelengths were fit to yield the scatter amplitude (a) and scatter power (b), which are related to the structure of the tissue in terms of scatterer size and density. In this paper a modified reconstruction approach is used, which implements the possible spectral shapes of the chromophore and scattering models into the image formation process, thereby adding a spectral constraint into the reconstruction. The chromophore concentrations and scatter parameters are estimated directly by incorporating the known Beer's law attenuation relation and Mie scattering behavior as constraints. This type of parameter reduction has been applied in electrical impedance tomography in which Brandstatter *et al.*[9] showed that by using multifrequency data and by assuming a frequency dependence, one can reduce the ill-posed nature of the problem and make the reconstruction more robust to noise in data. A similar application in microwave image reconstruction[10] provides evidence of reduced artifacts in the images as a result of coupling measurements from different frequencies. Corlu *et al.*[4] implemented this approach by using continuous-wave (cw) measurements to find the optimal four wavelengths that reduce the cross talk between absorption and scatter parameters. Their results from simulations are encouraging and are based on the assumption that all change in scattering is due to the scatter amplitude with the scatter power kept constant. A similar approach to cw data has been implemented by Li *et al.*[5] used two of three wavelengths under the assumption that there is no scattering perturbation. They have applied this method to find chromophore concentrations directly and have shown in simulated and experimental data that their technique results in reduced image artifacts and parameter cross talk.

In the current study this overall approach is extended to the application of frequency-domain data, using six wavelengths. The method is evaluated with experimental data following individual variation of oxygen saturation, hemoglobin, and scattering parameters. A finite-element model of the diffusion equation is used, and the algorithm reconstructs images for five parameters: oxyhemoglobin, deoxyhemoglobin, water fraction, scatter amplitude, and scatter power, with no assumptions on the scatter amplitude or power. The results show that the new technique is more robust to noise in measurements than the conventional method. In addition, the spectral constraint reduces the noise in the recovered chromophore concentrations, especially in the water and scattering images, and the reconstructions from the experimental data show quantitatively accurate results.

2. Materials and Methods

A. Instrumentation

The NIR frequency-domain system for breast imaging has been described in detail in previous papers.[11] Briefly, it consists of optical fibers placed in three planes in a circular geometry. Each plane has 16 source–detector positions, and intensity light modulated at 100 MHz is used at six different wavelengths in the range 660–850 nm. The signals are detected by high-gain photomultiplier tubes, and the electrical signals are passed through rf mixer circuits to heterodyne down to a 500-Hz offset frequency. The signal amplitude and phase are calibrated to compensate for system offsets by matching measured data from homogeneous phantoms[12] to simulated results from the finite-element model. When optimized, the calibrated data have less than 1% offset from simulated values and provide a highly stable data set from which to reconstruct absorption and scattering coefficient images.

B. Reconstruction without Spectral Constraints

Under the assumption that breast tissue is a scatter-dominated medium, the diffusion approximation to the radiative transfer equation[8,13] was used to model the propagation of light at large distances from the source location. This is given by

$$-\nabla \cdot \kappa(r)\nabla\Phi(r,\ \omega) + \left(\mu_a(r) + \frac{i\omega}{c}\right)\Phi(r,\ \omega) = q_0(r,\ \omega),$$

(1)

where $\Phi(r, \omega)$ is the isotropic fluence at modulation frequency ω and position r, $\kappa(r)$ is the diffusion coefficient, $\mu_a(r)$ is the absorption coefficient, c is the speed of light in the medium, and $q_0(r, \omega)$ is an isotropic source. The diffusion coefficient can be written as

$$\kappa(r) = \frac{1}{3[\mu_a(r) + \mu_s'(r)]},$$

(2)

where μ_s' is the reduced scattering coefficient.

A finite-element-based-model solution to this equation was developed and was described and validated in Refs. 14 and 15. Briefly, the forward problem involves solving Eq. (1) for fluence, given an initial distribution of the optical properties, with the appropriate boundary conditions applied. The image reconstruction uses a Newton–Raphson minimization that iteratively updates the optical property parameters based on a least-squares-error norm given by

$$\chi^2 = \sum_i \left[\frac{(\phi_i^{\text{meas}} - \phi_i^{\text{cal}})^2}{\sigma_i^2}\right],$$

(3)

where ϕ_i^{meas} is the measured data and ϕ_i^{cal} is the data calculated for an initial distribution of the properties, using the forward solver. Here the measurements are assumed to be independent of each other. Using a Taylor's series approximation for the solution at some close distance from the boundary data (ϕ^{cal}) for the initial distribution and ignoring the higher-order terms, the update in the optical properties is related to the difference between the measured and the calculated data as

$$\partial\phi = \Im\,\partial\mu, \tag{4}$$

where $\partial\phi$ refers to the change in boundary data; $\Im$ is the Jacobian, the matrix containing the sensitivity of the boundary data to a change in optical properties, $\Im = [\Im_{\mu_a}; \Im_\kappa]$; and $\partial\mu$ is the update in the optical properties given by $\partial\mu = [\partial\mu_a; \partial\kappa]$.

The reconstruction is sensitive to the initial estimate of the parameters, which are given by a homogeneous prefitting algorithm based on the analytical solution for infinite medium.[12] The matrix $\Im$, being ill conditioned, requires that the inverse problem in Eq. (4) be solved with the application of a Levenberg–Marquardt regularization scheme[16,17] for stabilization. The stopping criterion for this reconstruction was chosen to be when the χ^2 error in Eq. (3), known as the projection error, changes by less than 2% between successive iterations.

Previously[18] the optical properties at each wavelength were obtained, and then the calculation of the chromophore concentrations was performed with a constrained least-squares fit to the Beer's law relation

$$\mu_a = [\varepsilon]c, \tag{5}$$

where ε is the molar absorption spectra of the absorbing chromophores and c is the concentration of these chromophores. Oxyhemoglobin (HbO$_2$), deoxyhemoglobin (Hb), and water are assumed to be the main absorbers, and their molar absorption spectra were obtained experimentally in our instrument. This approach of using values estimated by the system compensates for any offsets from the theoretical values, yet there was little difference between our experimental and theoretical estimates of molar absorption coefficients. By fitting for the concentrations, we calculate total hemoglobin as HbT = HbO$_2$ + Hb [in micromolar (μM)] and oxygen saturation as SO$_2$ = HbO$_2$/HbT $\times$ 100 (in percent); the contribution from other chromophores such as lipids has been found to be negligible, because the wavelengths used here were limited to less than 850 nm where lipid is a weak absorber. The constraints on the fitting process were for HbT to be below 100 μM, oxygen saturation to be nonnegative and with an upper bound of 100%, and water to be in the range [0%, 100%].

Similarly, the μ_s' spectrum of tissue has been shown to fit well to an empirical approximation to Mie scattering theory,[19,20] given by

$$\mu_s' = a\lambda^{-b}. \tag{6}$$

Equation (6) was used to derive the scatter amplitude (a) and the scatter power (b), with wavelength in micrometers. The coefficient μ_s' has units of inverse millimeters, and b is dimensionless so that a has units given by $10^{-3b}(\text{mm})^{b-1}$. Both the scattering power and the amplitude depend on the scattering center size and number density and may reflect variations in breast structural composition due to different cellular, organelle, and structural sizes and densities for fatty and glandular tissue. Typically, large scatterers have lower b and a values, whereas small scatterers have higher b and a coefficients.[19,20] Although scatterers in tissue are not necessarily homogeneous spheres, as assumed in Eq. (6), studies on red blood cells and yeast have shown this to be a reasonable approximation since measurements of μ_s' in these cells show trends similar to Mie theory.[21,22]

C. Spectrally Constrained Chromophore and Scattering Reconstruction

Instead of estimating the optical properties at each wavelength and then spectrally deconvolving the chromophore concentrations [Eqs. (5) and (6)], one can incorporate these constraints into the reconstruction to directly determine oxyhemoglobin, deoxyhemoglobin, water, scatter amplitude, and scatter power, thus reducing the parameter space from 12 images (μ_a and μ_s' at 6 wavelengths) to 5 parametric images. Assuming that we know $\Im_\mu = \partial\phi/\partial\mu$ and $\Im_\kappa = \partial\phi/\partial\kappa$, as calculated by the previous method (reconstruction without spectral priors), in the new approach the measurements at all wavelengths are coupled together, and the relations in Eqs. (5) and (6) are combined to create a new set of relations, which for each wavelength is represented by

$$\partial\phi_\lambda = \Im_{c,\lambda}\,\partial c + \Im_{a,\lambda}\,\partial a + \Im_{b,\lambda}\,\partial b, \tag{7}$$

where

$$\Im_{c,\lambda} = \left.\frac{\partial\phi}{\partial c}\right|_\lambda = \left.\frac{\partial\phi}{\partial\mu}\frac{\partial\mu}{\partial c}\right|_\lambda,$$

for each chromophore (c) in the model. From Eq. (5) we get $\partial\mu = \varepsilon\partial c$, so that, substituting for $\partial\mu/\partial c$,

$$\Im_{c,\lambda} = \left.\frac{\partial\phi}{\partial c}\right|_\lambda = \left.\frac{\partial\phi}{\partial\mu}\varepsilon\right|_\lambda$$

$$= \left(\frac{\partial\phi}{\partial\mu}\right)_\mu \otimes (\varepsilon_\lambda^{c1,c2,c3}) = \Im_{\mu,\lambda} \otimes (\varepsilon_\lambda^{c1,c2,c3}), \tag{8}$$

where $\otimes$ refers to the Kronecker tensor product.

Similarly,

$$\Im_{a,\lambda} = \left.\frac{\partial\phi}{\partial a}\right|_\lambda = \left.\frac{\partial\phi}{\partial\kappa}\frac{\partial\kappa}{\partial a}\right|_\lambda. \tag{9}$$

Rewriting

$$\frac{\partial \kappa}{\partial a} = \left(\frac{\partial \kappa}{\partial \mu_s'}\right)\left(\frac{\partial \mu_s'}{\partial a}\right)$$

and knowing that

$$\kappa = \frac{1}{3(\mu_a + \mu_s')},$$

we get

$$\frac{\partial \kappa}{\partial \mu_s'} = \frac{1}{3}\left[\frac{-1}{(\mu_a + \mu_s')^2}\right] = \frac{1}{3}(-9\kappa^2) = -3\kappa^2,$$

$$\frac{\partial \mu_s'}{\partial a} = \lambda^{-b}.$$

Substituting these expressions in Eq. (9) leads to

$$\Im_{a,\lambda} = \frac{\partial \phi}{\partial a} = \frac{\partial \phi}{\partial \kappa}\frac{\partial \kappa}{\partial a}\Big|_\lambda = \Im_\kappa(-3\kappa^2)(\lambda^{-b})|_\lambda. \quad (10)$$

Similarly, for the scatter power

$$\Im_{b,\lambda} = \frac{\partial \phi}{\partial b} = \frac{\partial \phi}{\partial \kappa}\frac{\partial \kappa}{\partial b}\Big|_\lambda$$

$$= \left(\frac{\partial \phi}{\partial \kappa}\right)\left(\frac{\partial \kappa}{\partial \mu_s'}\right)\left(\frac{\partial \mu_s'}{\partial \ln \mu_s'}\right)\left(\frac{\partial \ln \mu_s'}{\partial b}\right). \quad (11)$$

Knowing that $\partial \ln \mu_s' = (1/\mu_s')\partial \mu_s' \Rightarrow \partial \mu_s'/\partial \ln \mu_s' = \mu_s'$ and from Eq. (6), $\ln \mu_s' = \ln a - b \ln \lambda$, then it is found that $\partial \ln \mu_s'/\partial b = -\ln \lambda$. Substituting these relations produces

$$\Im_{b,\lambda} = \Im_\kappa(-3\kappa^2)(\mu_s')(-\ln \lambda)|_\lambda. \quad (12)$$

The overall system of equations is assembled by substituting the relations from Eqs. (8), (10), and (12) into Eq. (7):

$$\begin{pmatrix} \partial \phi_{\lambda 1} \\ \partial \phi_{\lambda 2} \\ \cdots \\ \partial \phi_{\lambda n} \end{pmatrix} = \begin{bmatrix} \Im_{c1,\lambda 1}\Im_{c2,\lambda 1}\Im_{c3,\lambda 1}\Im_{a,\lambda 1}\Im_{b,\lambda 1} \\ \Im_{c1,\lambda 2}\Im_{c2,\lambda 2}\Im_{c3,\lambda 2}\Im_{a,\lambda 2}\Im_{b,\lambda 2} \\ \cdots \\ \Im_{c1,\lambda n}\Im_{c2,\lambda n}\Im_{c3,\lambda n}\Im_{a,\lambda n}\Im_{b,\lambda n} \end{bmatrix}\begin{pmatrix} \partial c_1 \\ \partial c_2 \\ \partial c_3 \\ \partial a \\ \partial b \end{pmatrix}. \quad (13)$$

The size of the left-hand vector is equal to the number of wavelengths multiplied by the number of measurements per wavelength, and the size of the right-hand side vector is equal to the number of chromophores and scatter parameters multiplied by the number of nodes for updating each parameter in the mesh. The individual Jacobian matrices for each chromophore were computed with a dual-mesh technique,[23] on a 2000-node mesh for forward diffusion calculations and a 425-node mesh was used for image reconstruc-

tion. Equation (13) was implemented by building the new Jacobian (5 × 425 by 480 × 6), and the same Levenberg–Marquardt regularization scheme was applied. The computation time was approximately 25 min for typically 5–7 iterations, with the measure of convergence being when the projection error was less than 2% of the previous iteration value. Additional constraints based on the physiologically possible values for the parameters were applied at each iteration so that HbT does not exceed 100 μM (based on typical concentrations found in the breast), that oxygen saturation is in the range [0%, 100%], and that water is in the range [0%, 100%]. The scatter amplitude is bounded in the range [0.5, 2.0] in units of $10^{-3b}(\text{mm})^{b-1}$, and the scatter power is in the range [0, 2] based on previous studies,[24] so that together they cover the possible range for the reduced scattering coefficient. This range is [0.5,3.25] mm^{-1} for 785 nm. The approach can easily be extended to additional wavelengths without any computational expense in the inversion process since the size of the new Hessian from Eq. (13) depends on the number of nodes and not on the number of measurements, although the number of wavelengths will influence the calculation of individual Jacobian matrices. The algorithm typically converges after a lower number of iterations than the conventional method does, and no spatial filtering was necessary since the noise in the images is already damped by the spectral constraints.

3. Results

Subsections 3.A and 3.B show the improvement of the spectral technique over the conventional method by quantitative assessment of the mean and standard deviation from recovered images by use of simulated and experimental data. The results shown in Subsections 3.C, 3.D, and 3.E focus on validating the accuracy of the spectral technique in following the variation of scattering, oxygen saturation (Hill curve), and total hemoglobin individually by use of the appropriate experiments.

A. Effect of Noise in Amplitude and Phase Measurements

It is expected that the spectrally constrained nature of this new algorithm will make the reconstruction more immune to noise in measurements as compared with the conventional method, since all data are coupled. More noise in the data is typically observed at 661 nm for tissues containing lower oxygenation (due to high absorption of deoxyhemoglobin) and 849 nm (due to water absorption) and in higher-scattering cases. This behavior is taken into consideration in the algorithm by the *a priori* spectral information. To test the hypothesis of reduced noise sensitivity of the spectral method, we simulated amplitude and phase data at six wavelengths by using the finite-element model for a homogeneous phantom of diameter 86 mm with concentrations of 30 μM HbO$_2$, 30-μM Hb, 60% water, scatter amplitude of 1 [units of $10^{-3b}(\text{mm})^{b-1}$], and scatter power of 1. This yields
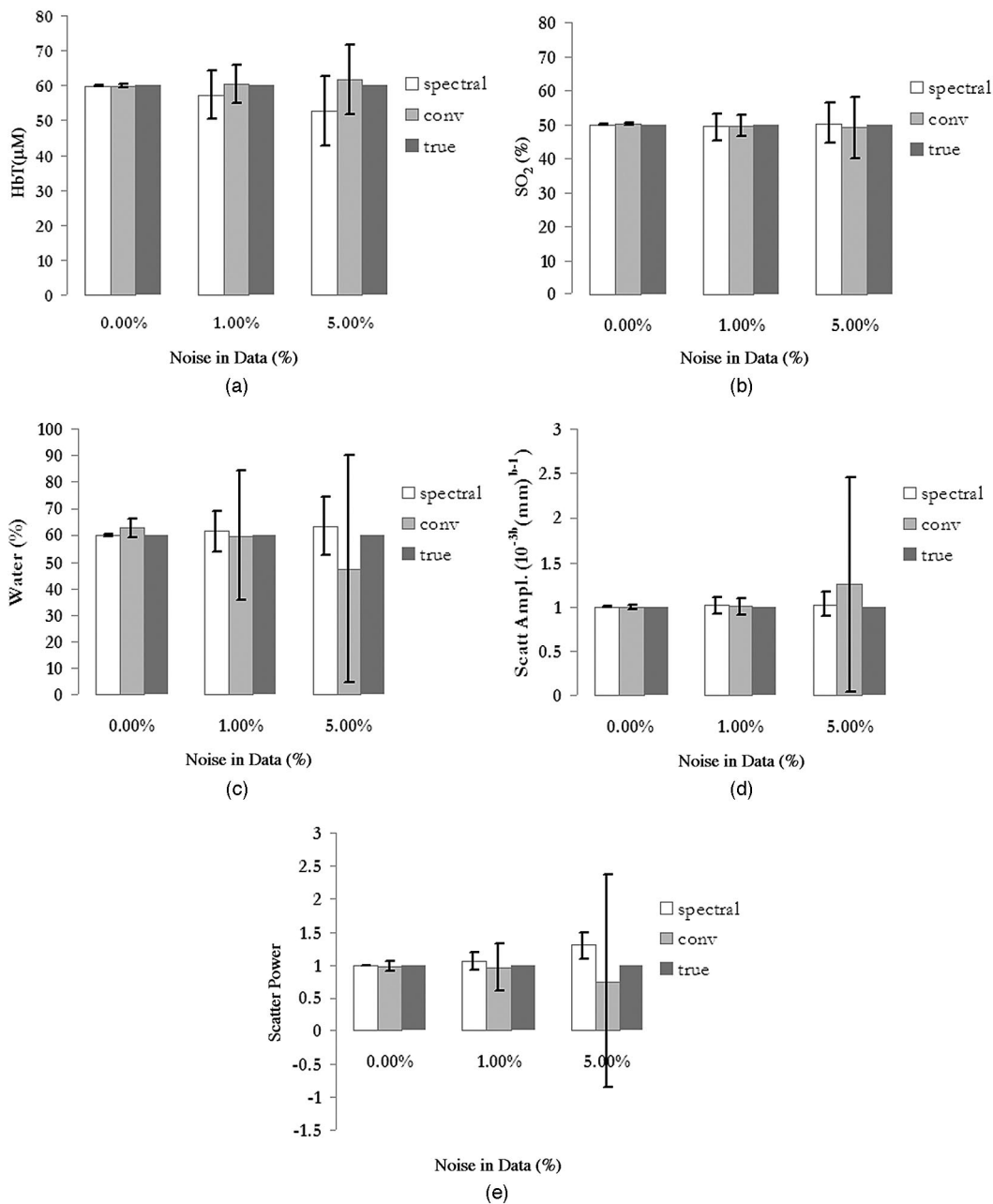
Fig. 1. Recovered mean values with standard deviation error bars are shown for (a) hemoglobin, (b) oxygen saturation (SO$_2$), (c) water (in percent), (d) scatter amplitude, and (e) scatter power. These were estimated from the interior of a homogeneous field reconstructed with different levels of noise in the original data. Values for the new spectrally constrained reconstruction are shown alongside results from the conventional approach.

total hemoglobin of 60 μM, SO$_2$ = 50%, and μ_s' at 785 nm = 1.27 mm^{-1}, which are concentrations typically found in the breast. Random Gaussian distributed noise was added to the amplitude and phase measurements in a systematic manner from 0.5% to 5%, and the spectrally constrained reconstruction was carried out on the data. The conventional technique of reconstructing each wavelength separately and then carrying out the spectral fit was also applied to these data for comparison. The mean and standard deviation for the reconstructed images from both techniques for each of the parameters are plotted in

Fig. 1; the results are shown for the cases with no noise, 1% noise, and 5% noise.

For the noiseless data reconstruction, both techniques show an accurate recovery of all five parameters (mean is within 3% of the true value), with an average standard deviation of 0.5% of the mean for the spectral method and 3.7% for the conventional technique. For the 1% and 5% noise cases, the standard deviation increases as expected; however, this increase is much more evident in the images from the conventional technique than from the spectral method. The results from the spectral method do not

differ significantly from the conventional technique for total hemoglobin and oxygen saturation images; however, the noise is significantly suppressed in the water and scatter images from the spectral method. For 1% noise in data, the mean is still within 5% of the true value for both methods, but the standard deviation in water has reduced from 40% in the conventional method to 12% of the mean for the spectral technique. Even in the 5% noise case, the spectral method shows a reasonable recovery of mean values for the parameters (accurate to within 10% on an average), with a 15.3% standard deviation (as percent of the mean). This shows a reduced sensitivity of the reconstruction to higher levels of noise compared with the conventional method.

B. Reduced Standard Deviation in Homogeneous Experimental Data

To assess the mean and standard deviation from homogeneous images in experimental data, we collected measurements on a liquid tissue-simulating phantom within a plastic circular container of 90-mm diameter, consisting of 9.3-μM pig blood in buffered saline and 1% Intralipid concentration. The blood hematocrit was measured before the experiment with a clinical co-oximeter that showed 1% of the pig blood contained 9.3 μM of hemoglobin for this sample. The expected values for the scatter amplitude and scatter power were derived from the work of van Staveren *et al.*[19] Using the expression given by van Staveren *et al.* with the units suitably modified produces the following equation: $\mu_s' = 0.928\lambda^{-1.4} - 0.16\lambda^{-2.4}$. Incorporating the higher-order term into the scatter amplitude factor (since the amplitude factor of the second term is much lower than that of the first term) by assuming that $\mu_s' = 1$ mm^{-1} at 800 nm, the scatter amplitude (a) = 0.73 and the scatter power (b) = 1.4. Water and oxygen saturation are expected to be close to 100%, since the phantom was an oxygenated liquid solution. Both the spectral and conventional techniques were applied to this data, and the mean and standard deviation from the reconstructed images are plotted in Fig. 2(a), along with the expected values. As described in Section 2, both reconstructions were terminated by use of the projection error criterion, and reconstructed parameters 15 mm from the edge have been removed from the calculation of mean and standard deviation to diminish contribution from any boundary artifacts.

Figure 2(a) shows the reduced standard deviation in the images obtained from the spectral method, compared with the conventional technique. The mean values for the parameters are accurate to within 6%, on average, for the spectral scheme and to within 11% for the conventional method. As with the simulations, no spatial filtering is applied to the spectral reconstruction, whereas the conventional method uses a mean filter. The stopping criterion for the spectral technique is a projection error change of less than 2% between iterations, and it converges in seven iterations. For the conventional method, the equivalent 7th iteration at every wavelength was used to obtain images based on earlier studies[25] that indicated 5–9 iterations are most suitable for experimental data. Both methods use the same initial regularization parameter (equal to 10 in this study[15]). The main improvement here was the suppression of noise in the water and scattering images by use of the spectral technique.

Figure 2(b) shows the reconstructed images from both methods along with a cross section of the middle plane. The spatial variation in the cross section is less in the spectral technique, and some of the boundary artifacts in the hemoglobin, water, and scatter power images are reduced. The scatter amplitude image shows some artifacts close to the boundary, which may indicate the need for higher regularization for the parameter. The hemoglobin and water images from the conventional technique show some cross talk between the images. A central artifact can be seen in the HbT image in which there is a decrease in its value, with saturation in the water image at this same region (=100%). The scatter parameter images, especially scatter power, show considerable noise that is possibly due to cross talk between the two scatter parameters and between deoxyhemoglobin and scatter.

C. Scattering Parameter Validation

Having shown that spectral reconstruction is superior to the conventional method of reconstructing each wavelength separately and then applying the spectral information in terms of reduced sensitivity to noise in the data and suppression of artifacts in the images, we now focus the following sections on validating the accuracy of the spectral reconstruction. One of the key advantages of the spectral method over the conventional technique is the reduction of noise in the water and scatter parameters. The implementation of this technique on frequency-domain measurements allows the separation of absorption and scatter, and this along with multiwavelength capability allows a modest separation of the scatter amplitude and scatter power. To test the cross talk and noise in the scatter parameters with experimental measurements and to follow their variation, the Intralipid concentration was varied in the liquid phantom solution containing 1% blood, from 0.75% to 1.5% in steps of 0.25% (the data from 1% Intralipid was also used for Fig. 2). The amplitude and phase measurements were taken for each concentration, and the spectrally constrained reconstruction was applied to the data. The total hemoglobin was constant through the varying concentrations of Intralipid, and the saturation for both water and oxygen was 100% for all data sets. The mean value along with standard deviation from the images are plotted for scatter amplitude and scatter power in Fig. 3(a), and Fig. 3(b) shows the average μ_s' at 661 and 785 nm. Figure 3(c) shows the total hemoglobin and Fig. 3(d) shows the oxygen saturation and water content. The scatter amplitude varies linearly with concentration and shows more variation (range 0.6–1.25) than the scatter power (range 1.3–1.53). Scatter power values are
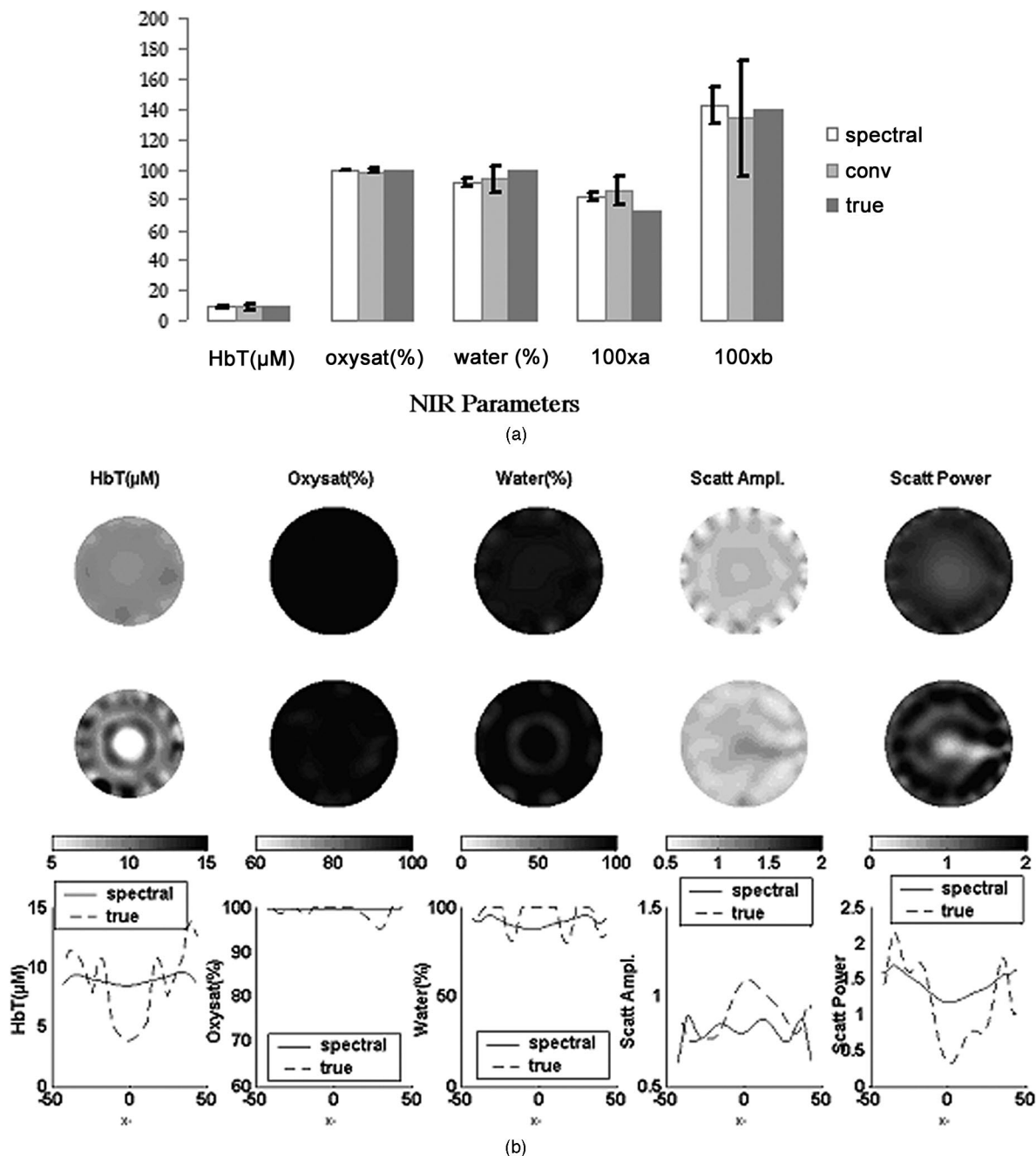
Fig. 2. Recovered mean values with standard deviation error bars are shown in (a) from reconstructed data with a 90-mm-diameter liquid phantom containing 1% Intralipid with 9.3-μM total hemoglobin. Values for the spectrally constrained reconstruction are shown alongside those obtained with the conventional reconstruction approach and the true theoretical values. (b) Images from this phantom are shown for comparison with the spectrally constrained reconstruction (top row), the conventional reconstruction (middle row), and the profile plots from the midplane of these images (bottom row).

comparable with the expected value of 1.4 from van Staveren *et al.*,[19] showing a mean of 1.4 ± 0.1 through the change in concentrations. The mean μ_s' at 785 nm varies linearly (slope of ≈1) with the change in percent Intralipid, and the value approximately doubles (0.89 versus 1.7 mm^{-1}) when the concentration doubles from 0.75% to 1.5% Intralipid, which is encouraging. The reduced scattering coefficient at 661 nm also shows a similar trend. The total hemoglobin stays constant with change in scattering

with a mean of 8.2 μM ± 0.8, and the oxygen saturation shows a mean value of 99.3% ± 1.2%, close to expected value of 100%. Water shows an average of 92.4% ± 4.2%, and some cross talk can be seen between hemoglobin and water at the higher Intralipid concentrations owing to the high-scattering medium.

D. Oxygen Saturation Validation

Malignant tumors typically have lower partial pressure values for oxygen (PO_2) owing to hypoxia,[26] and
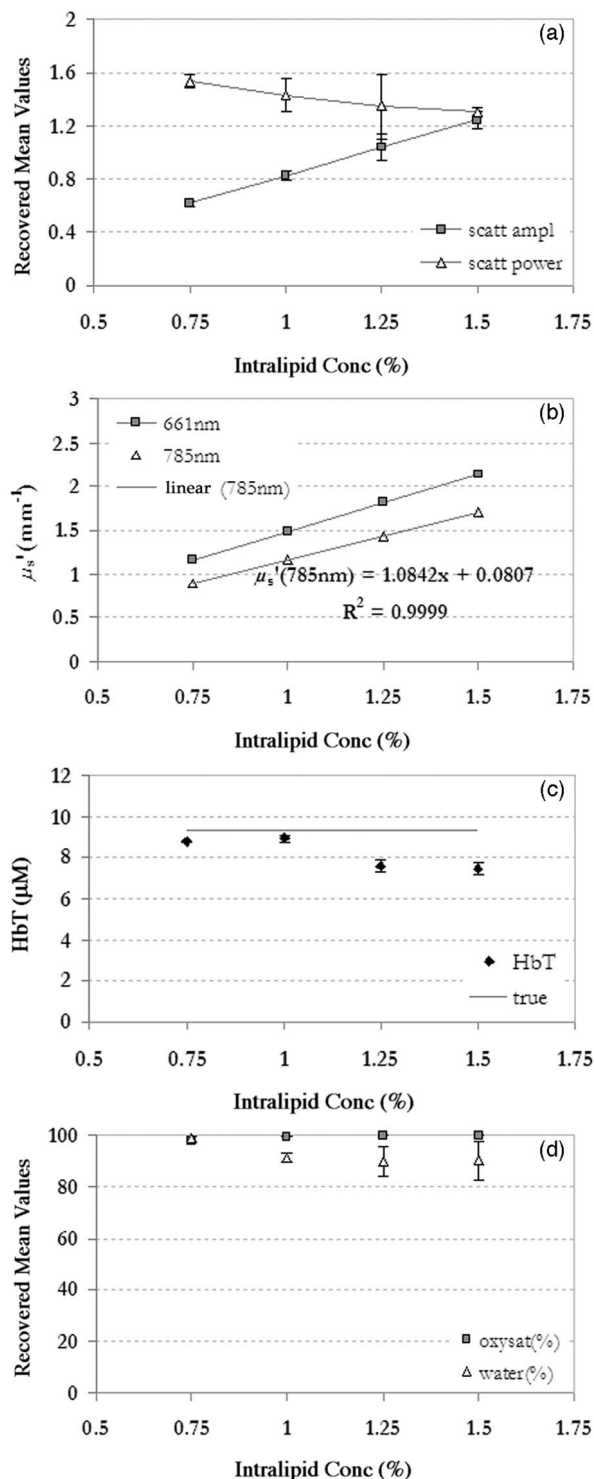
Fig. 3.   Recovered mean values are shown from a series of phantoms in which the scattering coefficient was systematically varied through concentrations (Conc) of Intralipid ranging between 0.75% and 1.5%. The estimated scattering power and amplitudes are shown in (a), and the reduced scattering coefficients at 661 and 785 nm are shown in (b). The total hemoglobin, which did not vary, is shown in (c), along with a line corresponding to the theoretical value. In (d) the oxygen saturation and water values are shown, which also did not vary. Both have theoretical estimates of 100%. Error bars represent the standard deviation of all pixels within the interior 60 mm of the region imaged.

it is useful to verify that the spectrally constrained reconstruction can follow these hypoxic conditions. The relation between oxygen saturation and the variation in partial pressure of oxygen has a well-characterized behavior given by the Hill curve. This curve was obtained previously for the conventional method and published in Ref. 27. Data were acquired by use of a phantom solution containing 1% whole blood and 1% Intralipid in saline, in a thin-walled plastic container, 70-mm in diameter. The whole blood (1%) was found to have 18-μM hemoglobin, and the oxygenation of the solution was reduced by varying the PO_2 values from 150 to 0 mm Hg by the addition of yeast. The PO_2 was independently measured by means of a chemical microelectrode after calibration of the electrode overnight in a saline solution. By varying the PO_2 gradually, using a small amount of yeast, and making measurements over this period of time, we eventually reduced the PO_2 to zero and obtained a complete set of data over the required range. The spectral reconstruction of this data gave HbT, SO$_2$, water, scatter amplitude, and scatter power images, from which the mean and standard deviation are plotted in Fig. 4. The oxygen saturation in Fig. 4(a) follows the theoretical Hill curve[28] reasonably well with a mean error of 7.7%, with the worst accuracy close to zero PO_2 and the higher accuracy when PO_2 is above 80% saturation. For PO_2 below 20-mm Hg, oxygen saturation is still accurate to within 15%, with a low standard deviation in the images.

With variation of PO_2, the total hemoglobin concentration stayed approximately constant [Fig. 4(b)], with a mean value of 17.5 $\pm$ 2.1 μM, which is within 97% of the true value given above, and water exhibited a mean value of 94.2% $\pm$ 8.3%. Both parameters show some cross talk at PO_2 values below 11-mm, which is possibly unavoidable owing to the limited number of wavelengths used in these data. Both scatter amplitude and scatter power stay approximately constant until a PO_2 of 11-mm Hg, beyond which both show some variation, which could be the result of cross talk between the two parameters. Above 11-mm Hg, the scatter amplitude has value of 0.92 $\pm$ 0.04 10^{-3b}(mm)$^{b-1}$, and the scatter power has values of 1.49 $\pm$ 0.14. The reduced scattering coefficient, however, stays constant throughout, as shown for 785 nm in Fig. 4(d), with a mean of 1.3 $\pm$ 0.03 mm^{-1}.

E.   Total Hemoglobin Validation

The final experimental homogeneous data set involved varying the total hemoglobin while keeping oxygen saturation, water, and scatter parameters constant. This was accomplished by use of a similar liquid phantom, with 1% Intralipid in saline, and by variation of the concentration of whole blood. The hematocrit level was measured by a clinical co-oximeter, yielding 1% blood, which is equivalent to 22-μM total hemoglobin. The blood concentration was varied from 0.2% to 1% in increments of 0.2%, and the amplitude and phase
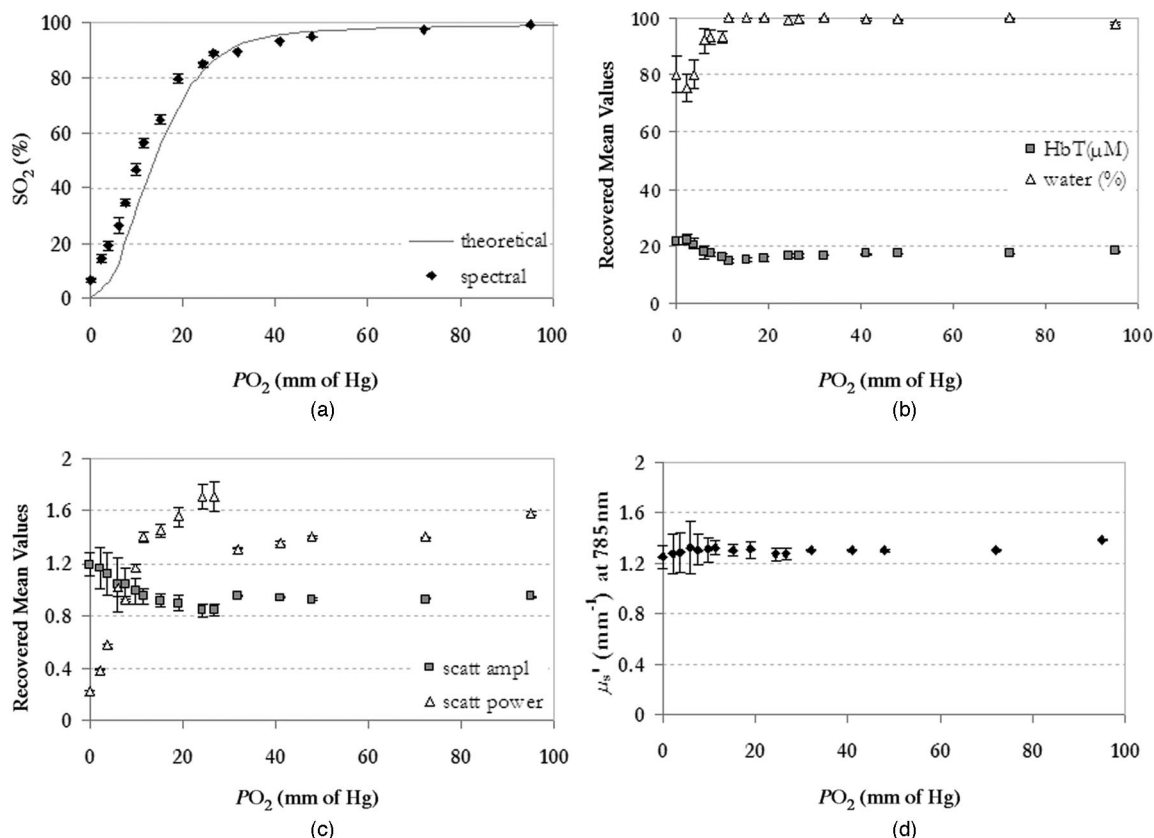
Fig. 4. Estimated mean values are shown from homogeneous reconstructions of a phantom with varying oxygen partial pressure (PO_2) of the solution induced by addition of yeast. The oxygen saturation is shown in (a), along with the theoretical estimate from the Hill curve. The total hemoglobin and percent water are shown in (b) with the theoretically estimated values of 18 mM and 100%, respectively, and should not vary with changes in oxygenation. The scatter power and amplitude are shown in (c) and should not vary. The reduced scattering coefficient at 785 nm is also shown in (d).

measurements were obtained for each level. After calibration, the spectrally constrained reconstruction was applied to the data, and the recovered mean and standard deviation from the NIR parameters are plotted in Fig. 5. The theoretical water and oxygen saturation values were 100%, as the phantom was a liquid oxygenated solution.

Figure 5(a) shows that the total hemoglobin followed the variation in blood (%) linearly and is quantitatively accurate, with a mean percent error of 6.2%. Oxygen saturation stayed constant with change in blood concentration [Fig. 5(b)], with a mean value of 98.9 ± 0.6%. The same trend was found in water, with a mean value of 98.2% ± 1.5%. The scatter amplitude and scatter power, shown in Fig. 5(b), are also independent of the variation in blood concentration, with a scatter amplitude of 0.65 ± 0.01. The scatter power had a mean value of 1.39 ± 0.08, and this agreed well with the estimated 1.4 derived from van Staveren et al.[19] The reconstruction converged in 4–6 iterations for the different concentrations, and no spatial filtering was applied in the reconstruction.

4. Discussion and Conclusions

The spectrally constrained direct chromophore and scattering reconstruction has been implemented and validated by use of simulated and experimental frequency-domain measurements. The results from Subsection 3.A show improved robustness of the reconstruction to increased amounts of noise in the data. The frequency-domain instrumentation in use typically has 0.5% noise in amplitude and 0.5 deg in phase,[11] and at this noise level. With simulated data from a homogeneous phantom, water images show a reduction in standard deviation from 32% to 10% (as percent of the mean) in going from the conventional to the spectral approach. Even at a 5% noise level, the spectral approach shows recovery of the parameters that is accurate within 10%, on average, with a significantly reduced standard deviation as compared with the conventional method. This insensitivity to noise is due to the use of multiwavelength data together with the spectral constraints, which results in a reduction in the number of unknowns, making the reconstruction problem less ill posed. The reduction in noise in the images is also observed in the homogeneous experimental data and is especially significant in water and scatter power. The NIR parameter images in Fig. 2 show the suppression of the artifacts in the images, particularly in water and scatter power, that is similar to the trend observed in the simulated data.
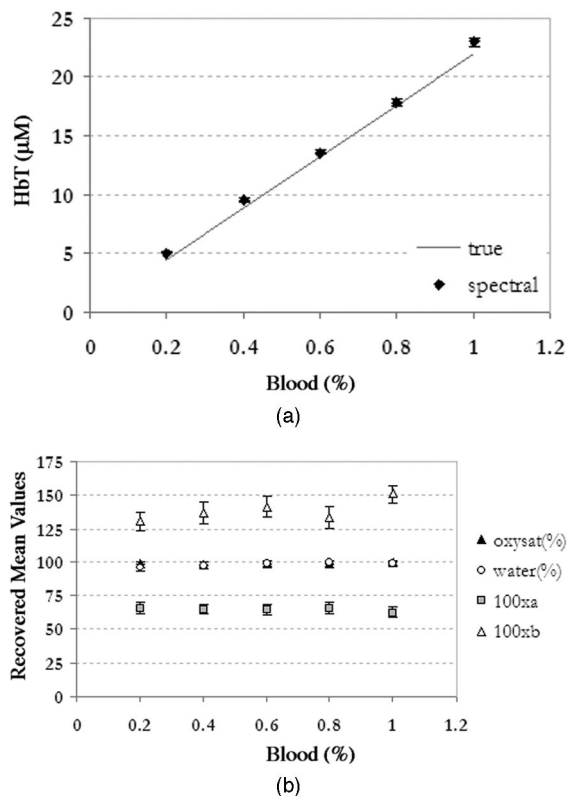
Fig. 5. Reconstructed mean and standard deviation values are shown from phantoms with varying concentrations of blood in which the total hemoglobin is graphed (a) alongside the theoretical value shown by a dotted line. The recovered values of oxygen saturation (%), water (%), scattering amplitude (a) and scattering power (b) are shown in (b), all of which are not expected to vary with changes in total blood (%). The scatter parameters are multiplied by 100 to allow them to be displayed on the same graph as the oxygen saturation and the water.

Water is an important measure of breast physiology; however, its quantitative accuracy from NIR tomography has yet to be validated. In the past several studies used a fixed water content in tissue (such as assuming 30%–31% fraction in tissue) to allow for spectral fitting of hemoglobin levels[29,30] or used radiological data[31] because sufficient wavelengths were unavailable and the cross talk between water and oxyhemoglobin prevented quantitatively accurate recovery of the water absorption. McBride et al.[32] and Cerussi et al.[33] have shown that using sparse spectral image data from a subject with assumptions about the bulk concentration for water and lipids could have up to 15% influence on HbT and oxygen saturation estimates. In recent studies water has been shown to have significant variation with breast size in normal subject studies,[24] with values between subjects varying significantly from 10% to 70%. This large range was observed in a 30-subject population, as shown by Cerussi et al.,[33] and values of 21% to 82% were observed in a 26-subject population studied by Srinivasan et al.[24] These large numbers suggest that water is a measure of the extravascular space, since the vascular space is clearly less than 2% in most

breast tissues. Thus water yields different information about the physiology of the breast than does hemoglobin, and spatial changes are expected in water owing to different content in the fatty and glandular tissues, which varies with the composition of the breast. The change in water content during the course of the menstrual cycle has been followed by Cubeddu et al., showing an increase in water in the second half of the cycle[34] for one patient. Shah et al.[35] have shown an increase of up to 28.1% in water in the luteal phase in a single volunteer, and Pogue et al.[36] have shown individual variations in seven subjects, with a mean value nearer to 2.5%. In a study following the effect of neoadjuvant chemotherapy[37] in a subject with a palpable adenocarcinoma, using optical white-light spectroscopy, water showed the most dramatic change, dropping 67% over the course of three treatment cycles. These studies have shown important trends in water content. However, to improve the clinical utility of the recovered values, it is important to show that they are quantitatively accurate estimates as well. The results shown here provide evidence of improvement in the quantification of water by use of the spectrally constrained approach compared with the conventional method of fitting for the chromophore and scattering parameters from optical property reconstructions. Water fraction values obtained by the new approach in data sets that follow variation in scattering, oxygen saturation, and total hemoglobin agree well with theoretical predictions and exhibit reduced noise and cross talk with oxyhemoglobin compared with the conventional technique.

Scattering is another area in which the constraints from Mie theory incorporated into the reconstruction significantly improve the quantification of the scatter amplitude and power. Recent studies have used scattering to study structural variations. For example, Poplack et al.[38] showed in a normal cohort of 23 women that there is a significant decrease in the reduced scattering coefficient (μ_s') at 785 nm with increasing body mass index and that adipose tissue was less scattering than glandular tissue, as expected. The same trend was observed by Durduran et al.[29] in a subject pool of 52 volunteers. Cerussi et al.[33] used the fit of μ_s' to the Mie theory approximation to show that scatter power decreases with increasing body mass index in a group of 30 healthy women. Pogue et al.[36] showed that scattering power and scatter amplitude could successfully separate categories of fatty and scattered breasts from extremely dense breasts ($p < 10^{-4}$) in a survey of 39 women with normal mammography. Since the risk of cancer is strongly correlated to the breast density,[39] this separation of breast densities in a noninvasive manner could prove very useful. Although these trends may prove to be promising in the future, their quantitative accuracy must be validated in phantom studies. Hence it is important to investigate the accuracy and standard deviation in these parameters to fully exploit the NIR information. Results in Subsection 3.A show the improved reconstruction of scatter power

images with robustness maintained at noise levels as high as 5% noise. In Fig. 2 the recovered mean for the scatter amplitude and scatter power agree well with predicted values from van Steveran *et al.*[19] for homogeneous experimental data (containing 1% blood and 1% Intralipid in saline). A change in scattering, obtained by varying the Intralipid concentration in a homogeneous phantom solution, was successfully followed (Fig. 3), in which the scatter amplitude varied linearly and the scatter power showed a mean of 1.4 ± 0.1 during the changes in concentration. The cross talk between scatter parameters and chromophore concentrations in minimal, with total hemoglobin, oxygen saturation, and water content staying constant through this change [Figs. 3(c) and 3(d)], except at the highest scattering concentration of Intralipid (1.5%). The mean of μ_s' also exhibits a linear increase, and μ_s' at 785 nm doubles as the Intralipid concentration changes from 0.75% ($\mu_s' = 0.89$ mm^{-1}) to 1.5% ($\mu_s' = 1.7$ mm^{-1}), shown in Fig. 3(b).

The Hill curve relation between oxygen saturation (SO$_2$) and PO$_2$ of oxygen was followed by the spectral method in the graphs of Fig. 4, which showed that SO$_2$ was accurate, with a mean error of 7.7%. Total hemoglobin estimates remained constant through this change in PO$_2$, producing a mean that is accurate to 97% of the expected value. Water content also showed this trend, with a mean of 94.2%, which compared well with the predicted value of 100%. Although some variation was found in the scatter amplitude and scatter power, μ_s' at 785 nm remained constant with change in oxygenation, with a mean of 1.3 ± 0.03 mm^{-1}. The standard deviations in the oxygen saturation images remain low, even at lower oxygenation. This translates into a successful recovery of SO$_2$ in malignancies without significant noise or cross talk between scatter parameters and deoxyhemoglobin. Total hemoglobin recovered by the spectral approach was separately validated by use of experimental data obtained by varying blood concentration from 0.2% to 1%. Quantitatively accurate results with a mean percent error of 6.2% were obtained. No cross talk between any of the parameters was observed during this variation, as shown in Fig. 5(b) in which oxygen saturation, water, scatter amplitude, and scatter power remained unchanged and close to predicted values.

The spectrally constrained approach is inherently robust owing to the addition of *a priori* spectral behavior. It requires less spatial filtering, whereas the conventional technique benefits from a mean filter to prevent excessive noise in the images. This new approach also converges faster and is readily extendable to three-dimensional models as well. Use of data at additional wavelengths can easily be implemented without much computational burden in the inversion process. A partial volume-type reconstruction may be an efficient means of processing a large number of measurements. There is certainly some cross talk found at PO$_2$ values of oxygen lower than 11-mm Hg or under extremely high scattering conditions, which can probably be resolved only by the addition of more wavelengths. Preliminary simulations have shown this to be true. The improved quantification of and robustness to noise of the reconstruction shown here for homogeneous measurements is currently also apparent in the heterogeneous data.

As the use of NIR tomography expands, spectrally constrained reconstruction should add considerable value to obtaining quantitatively accurate estimates of different parameters, particularly water and scatter power. The use of frequency-domain measurements allows a good separation of chromophore and scattering, and together with the spectral approach, we obtain reduced cross talk between the parameters, suppression of image artifacts, insensitivity to noise in the measurements, and, finally, accurate quantification of the NIR parameters.

References

1. B. W. Pogue, S. P. Poplack, T. O. McBride, W. A. Wells, O. K. S. Osterman, U. L. Osterberg, and K. D. Paulsen, "Quantitative hemoglobin tomography with diffuse near-infrared spectroscopy: pilot results in the breast," Radiology **218,** 261–266 (2001).
2. B. J. Tromberg, N. Shah, R. Lanning, A. Cerussi, J. Espinoza, T. Pham, L. Svaasand, and J. Butler, "Non-invasive *in vivo* characterization of breast tumors using photon migration spectroscopy," Neoplasia (New York) **2,** 26–40 (2000).
3. D. Grosenick, H. Wabnitz, K. T. Moesta, J. Mucke, M. Moller, C. Stroszczynski, J. Stossel, B. Wassermann, P. M. Schlag, and H. Rinneberg, "Concentration and oxygen saturation of hemoglobin of 50 breast tumors determined by time-domain optical mammography," Phys. Med. Biol. **49,** 1165–1181 (2004).
4. A. Corlu, T. Durduran, R. Choe, M. Schweiger, E. M. Hillman, S. R. Arridge, and A. G. Yodh, "Uniqueness and wavelength optimization in continuous-wave multispectral diffuse optical tomography," Opt. Lett. **28,** 2339–2341 (2003).
5. A. Li, Q. Zhang, J. P. Culver, E. L. Miller, and D. A. Boas, "Reconstructing chromosphere concentration images directly by continuous-wave diffuse optical tomography," Opt. Lett. **29,** 256–258 (2004).
6. S. R. Arridge and M. Schweiger, "Image reconstruction in optical tomography," Philos. Trans. R. Soc. London Ser. B **352,** 717–726 (1997).
7. K. D. Paulsen and H. Jiang, "Spatially varying optical property reconstruction using a finite element diffusion equation approximation," Med. Phys. **22,** 691–701 (1995).
8. M. S. Patterson, B. C. Wilson, and D. R. Wyman, "The propagation of optical radiation in tissue I. Models of radiation transport and their application," Lasers Med. Sci. **6,** 155–168 (1990).
9. B. Brandstatter, K. Hollaus, H. Hutten, M. Mayer, R. Merwa, and H. Scharfetter, "Direct estimation of Cole parameters in multifrequency EIT using a regularized Gauss–Newton method," Physiol. Meas. **24,** 437–448 (2003).
10. Q. Fang, P. M. Meaney, S. D. Geimer, A. V. Streltsov, and K. D. Paulsen, "Microwave image reconstruction from 3-D fields coupled to 2-D parameter estimation," IEEE Trans. Med. Imaging **23,** 475–484 (2004).
11. T. O. McBride, B. W. Pogue, S. Jiang, U. L. Osterberg, and K. D. Paulsen, "A parallel-detection frequency-domain near-

infrared tomography system for hemoglobin imaging of the breast *in vivo*," Rev. Sci. Instrum. **72,** 1817–1824 (2001).

12. T. O. McBride, B. W. Pogue, U. L. Österberg, and K. D. Paulsen, "Strategies for absolute calibration of near infrared tomographic tissue imaging," in *Oxygen Transport to Tissue XXI*, J. F. Dunn and H. M. Swartz, eds., (Pabst, Lengerich, Germany, 2001).

13. A. Ishimaru, *Wave Propagation and Scattering in Random Media*, Vol. 1 (Academic, New York, 1978).

14. H. Jiang, K. D. Paulsen, U. L. Osterberg, B. W. Pogue, and M. S. Patterson, "Optical image reconstruction using frequency-domain data: simulations and experiments," J. Opt. Soc. Am. A **13,** 253–266 (1996).

15. H. Dehghani, B. W. Pogue, J. Shudong, B. Brooksby, and K. D. Paulsen, "Three-dimensional optical-tomography: resolution in small-object imaging," Appl. Opt. **42,** 3117–3128 (2003).

16. D. W. Marquardt, "An algorithm for least squares estimation of nonlinear parameters," J. Soc. Ind. Appl. Math. **11,** 431–441 (1963).

17. W. H. Press, S. A. Teukolsky, W. J. Vetterling, and B. P. Flannery, *Numerical Recipes in Fortran: the Art of Scientific Computing*, 2nd ed. (Cambridge U. Press, Cambridge, UK, 1986).

18. T. O. McBride, B. W. Pogue, E. Gerety, S. Poplack, U. L. Osterberg, and K. D. Paulsen, "Spectroscopic diffuse optical tomography for quantitatively assessing hemoglobin concentration and oxygenation in tissue," Appl. Opt. **38,** 5480–5490 (1999).

19. H. J. van Staveren, C. J. M. Moes, J. van Marle, S. A. Prahl, and J. C. van Gemert, "Light scattering in Intralipid-10% in the wavelength range of 400–1100 nm," Appl. Opt. **30,** 4507–4514 (1991).

20. J. R. Mourant, T. Fuselier, J. Boyer, T. M. Johnson, and I. J. Bigio, "Predictions and measurements of scattering and absorption over broad wavelength ranges in tissue phantoms," Appl. Opt. **36,** 949–957 (1997).

21. J. M. Steinke and A. P. Shepherd, "Comparison of Mie theory and the light scattering of red blood cells," Appl. Opt. **27,** 4027–4033 (1988).

22. B. Beauvoit, H. Liu, K. Kang, P. D. Kaplan, M. Miwa, and B. Chance, "Characterization of absorption and scattering properties for various yeast strains by time-resolved spectroscopy," Cell Biophys. **23,** 91–109 (1993).

23. K. D. Paulsen, P. M. Meaney, M. J. Moskowitz, and J. M. Sullivan, "A dual mesh scheme for finite element based reconstruction algorithms," IEEE Trans. Med. Imaging **14,** 504–514 (1995).

24. S. Srinivasan, B. W. Pogue, S. Jiang, H. Dehghani, C. Kogel, S. Soho, J. J. Gibson, T. D. Tosteson, S. P. Poplack, and K. D. Paulsen, "Interpreting hemoglobin and water concentration, oxygen saturation and scattering measured *in vivo* by near-infrared breast tomography," Proc. Natl. Acad. Sci. USA **100,** 12349–12354 (2003).

25. X. Song, B. W. Pogue, T. D. Tosteson, T. O. McBride, S. Jiang, and K. D. Paulsen, "Statistical analysis of nonlinearly reconstructed near-infrared tomographic images: Part II—Experimental interpretation," IEEE Trans. Med. Imaging **21,** 764–772 (2002).

26. P. Vaupel, F. Kallinowski, and P. Okunieff, "Blood flow, oxygen and nutrient supply, and metabolic microenvironment of human tumors: a review," Cancer Res. **49,** 6449–6465 (1989).

27. S. Srinivasan, B. W. Pogue, S. Jiang, H. Dehghani, and K. D. Paulsen, "Validation of hemoglobin and water molar absorption spectra in near-infrared diffuse optical tomography," in *Optical Tomography and Spectroscopy of Tissue V*, B. Chance, R. R. Alfano, B. J. Tromberg, M. Tamura, and E. M. Sevick-Muraca, eds., Proc. SPIE **4955,** 407–415 (2003).

28. N. Varjavand, "The interactive oxyhemoglobin dissociation curve," http://www.ventworld.com/resources/oxydisso/dissochtml.2002.

29. T. Durduran, R. Choe, J. P. Culver, L. Zubkov, M. J. Holboke, J. Giammarco, B. Chance, and A. G. Yodh, "Bulk optical properties of healthy female breast tissue," Phys. Med. Biol. **47,** 2847–2861 (2002).

30. D. Grosenick, K. T. Moesta, H. Wabnitz, J. Mucke, C. Stroszczynski, R. Macdonald, P. M. Schlag, and H. Rinneberg, "Time-domain optical mammography: initial clinical results on detection and characterization of breast tumors," Appl. Opt. **42,** 3170–3186 (2003).

31. D. R. White and H. Q. Woodard, "Average soft-tissue and bone models for use in radiation dosimetry," Br. J. Radiol. **60,** 907–913 (1987).

32. T. O. McBride, B. W. Pogue, S. Jiang, U. L. Osterberg, K. D. Paulsen, and S. P. Poplack, "Multi-spectral near-infrared tomography: a case study in compensating for water and lipid content in hemoglobin imaging of the breast," J. Biomed. Opt. **7,** 72–79 (2002).

33. A. Cerussi, D. Jakubowski, N. Shah, F. Bevilacqua, R. Lanning, A. J. Berger, D. Hsiang, J. Butler, R. F. Holcombe, and B. J. Tromberg, "Spectroscopy enhances the information content of optical mammography," J. Biomed. Opt. **7,** 60–71 (2002).

34. R. Cubeddu, C. D'Andrea, A. Pifferi, P. Taroni, A. Torricelli, and G. Valentini, "Effects of the menstrual cycle on the red and near-infrared optical properties of the human breast," Photochem. Photobiol. **72,** 383–391 (2000).

35. N. Shah, A. Cerussi, C. Eker, J. Espinoza, J. Butler, J. Fishkin, R. Hornung, and B. Tromberg, "Noninvasive functional optical spectroscopy of human breast tissue," Proc. Natl. Acad. Sci. USA **98,** 4420–4425 (2001).

36. B. W. Pogue, S. Jiang, H. Dehghani, C. Kogel, S. Soho, S. Srinivasan, X. Song, S. P. Poplack, and K. D. Paulsen, "Characterization of hemoglobin, water and NIR scattering in breast tissue: analysis of inter-subject variability and menstrual cycle changes relative to lesions," J. Biomed. Opt. **9,** 541–552 (2004).

37. D. B. Jakubowski, A. E. Cerussi, F. Bevilacqua, N. Shah, D. Hsiang, J. Butler, and B. J. Tromberg, "Monitoring neoadjuvant chemotherapy in breast cancer using quantitative diffuse optical spectroscopy: a case study," J. Biomed. Opt. **9,** 230–238 (2004).

38. S. P. Poplack, K. D. Paulsen, A. Hartov, P. M. Meaney, B. W. Pogue, T. D. Tosteson, M. R. Grove, S. K. Soho, and W. A. Wells, "Electromagnetic breast imaging: average tissue property values in women with negative clinical findings," Radiology **231,** 571–580 (2004).

39. M. T. Mandelson, N. Oestreicher, P. L. Porter, D. White, C. A. Finder, S. H. Taplin, and E. White, "Breast density as a predictor of mammographic detection: comparison of interval- and screen-detected cancers," J. Natl. Cancer Inst. **92,** 1081–1087 (2000).

Combining near-infrared tomography and magnetic resonance imaging to study *in vivo* breast tissue: implementation of a Laplacian-type regularization to incorporate magnetic resonance structure

Ben Brooksby
Shudong Jiang
Hamid Dehghani
Brian W. Pogue
Keith D. Paulsen
Dartmouth College
Thayer School of Engineering
8000 Cummings Hall
Hanover, New Hampshire 03755

John Weaver
Christine Kogel
Steven P. Poplack
Dartmouth Hitchcock Medical Center
Department of Diagnostic Radiology
Lebanon, New Hampshire 03756

Abstract. An imaging system that simultaneously performs near infrared (NIR) tomography and magnetic resonance imaging (MRI) is used to study breast tissue phantoms and a healthy woman *in vivo*. An NIR image reconstruction that exploits the combined data set is presented that implements the MR structure as a soft-constraint in the NIR property estimation. The algorithm incorporates the MR spatially segmented regions into a regularization matrix that links locations with similar MR properties, and applies a Laplacian-type filter to minimize variation within each region. When prior knowledge of the structure of phantoms is used to guide NIR property estimation, root mean square (rms) image error decreases from 26 to 58%. For a representative *in vivo* case, images of hemoglobin concentration, oxygen saturation, water fraction, scattering power, and scattering amplitude are derived and the properties of adipose and fibroglandular breast tissue types, identified from MRI, are quantified. Fibroglandular tissue is observed to have more than four times as much water content as adipose tissue, almost twice as much blood volume, and slightly reduced oxygen saturation. This approach is expected to improve recovery of abnormalities within the breast, as the inclusion of structural information increases the accuracy of recovery of embedded heterogeneities, at least in phantom studies. © *2005 Society of Photo-Optical Instrumentation Engineers.* [DOI: 10.1117/1.2098627]

Keywords: cancer; breast; magnetic resonance; *a priori*; diffuse; adipose; glandular; near infrared.

Paper SS04250R received Dec. 16, 2004; revised manuscript received Mar. 4, 2005; accepted for publication Mar. 23, 2005; published online Oct. 10, 2005.

1 Introduction

Recently, near infrared (NIR) imaging and spectroscopy have demonstrated an ability to quantify intrinsic tissue chromophore concentrations and scattering properties, thereby providing valuable functional information.[1–8] Imaging systems that measure light transmission in the NIR wavelength range and utilize model-based computational methods can generate spatially resolved absolute images of oxyhemoglobin, deoxyhemoglobin, and water as well as scattering parameters affected by cellular and subcellular structural elements. This technology is well suited to the study of breast tissue, and spatial and temporal contrasts in these properties may be uniquely useful for diagnosing disease. The application of NIR tomography will likely be important, yet customized imaging systems which couple to ultrasound, magnetic resonance imaging (MRI), or x-ray methods must be developed to evaluate and exploit this potential. The clinical standards for breast cancer detection—ultrasound, contrast-enhanced MRI,

and x-ray mammography—provide high spatial resolution but comparatively little information about molecular-level changes in breast tissue.[9,10] X-ray mammography, the most common form of breast cancer screening, has high sensitivity in women with fatty breast composition,[11] but low sensitivity in radiographically dense breasts, and low positive predictive value. It also uses ionizing radiation, and requires uncomfortable breast compression. Biopsy is generally required to determine malignancy in most women with an abnormal mammogram. Adjunctive noninvasive imaging modalities are often required to characterize suspicious abnormalities, especially in women with radiographically dense tissue. There is considerable potential for functional NIR imaging to distinguish breast cancer noninvasively, yet this modality has consistently suffered from low spatial resolution.[12–14] This paper reports on the combination of NIR tomography with MRI for the investigation of breast tissue properties to provide fundamentally new information by exploiting the strengths of each modality. Such hybrid approaches could generate image data that achieves the intrinsically high optical contrast known to

---

Address all correspondence to Brian Pogue, Thayer School of Engineering, Dartmouth College, 8000 Cummings Hall, Hanover, NH 03755. Tel.: (603) 646-3861; Fax: (603) 646-3856; E-mail: pogue@dartmouth.edu

exist in tumors on the spatial scale of structural MRI. The potential benefits of this type of hybrid method can only be evaluated once prototype systems are developed and optimized in a clinical setting.

In both research and clinical applications, multimodality imaging is increasingly being used to interrogate tissue morphology and function simultaneously because of the inherently optimized coregistration. Structure and function of tissue afford different physical bases for contrast and combinations have proven beneficial in the diagnosis and management of disease.[15] With the advent of molecular medicine, a transition in diagnostic interpretation becomes possible based on biochemical perturbations that occur in disease, frequently in the absence of changes in anatomic structure. A prominent example is hybrid position emission tomography/computed tomography (PET/CT) systems, where coupling structure to functional images has been more informative when interpreting the metabolic data.[16] Hybrid imaging systems also avoid complications associated with tissue movement between separate exams, which reduce coregistration accuracy and thus degrade the diagnostic value of the image fusion.[17]

This paper explores the combination of structural and functional imaging into a single platform for the study of breast tissue. Functionally, NIR contrast mechanisms in tissue are dominated by elastic Mie-like scattering.[18] Measured signals are highly sensitive to tissue concentrations of oxyhemoglobin, deoxyhemoglobin, and water. Structurally, contrast in MRI derives from intrinsic tissue factors related to micromagnetic structural inhomogeneities. Relaxation times vary substantially for different tissues and are strongly dependent on their physical characteristics.

In addition to coregistration, data sets from combined NIR and MRI imaging offer other synergistic benefits, namely anatomical priors (from high-spatial-resolution MRI) enhance NIR (i.e., high-contrast-resolution) image reconstruction. NIR spectroscopy is biochemically rich, but spectroscopic imaging is hindered by the highly scattered photon paths that reduce resolution in tissue. The most widely adopted approach to this problem incorporates parameter estimation strategies based on models of light propagation in tissue. The estimation task is sensitive to small perturbations in the light measurements, not all of which are caused by the intrinsic changes in tissue optical properties. Experience has shown that significant improvement in the stability and accuracy of the reconstruction process can be obtained by including prior anatomical/optical information.[19–25]

Techniques for incorporating this information are relatively new, and are the subject of active research in a variety of disciplines, including medical imaging,[26–28] industrial process imaging,[29] and geophysical surveying,[30] yet there is no clear consensus on the optimal approach. Spatial resolution and quantitative image accuracy can be improved when the appropriate constraints, derived from *a priori* information, are applied. However, these priors and constraints can take a wide variety of forms, and currently there are few broadly adopted conventions even though it is commonly accepted that such constraints offer significant potential value. It is less well appreciated that misguided constraints can lead to gross solution errors that are detrimental to the image outcome. To date, NIR techniques have been combined with several high-spatial-

resolution, structure-bearing imaging modalities including x-ray tomosynthesis,[21] ultrasound,[31] and MRI (Refs. 27, 32, and 33) to study human tissues and small animals. Past experiences have contributed to a variety of imaging systems, imaging geometries, and numerical reconstruction techniques, but have not led to a consensus on the optimal way of applying *a priori* derived constraints.

This paper describes the clinical application of our breast imaging system—a highly sensitive multispectral frequency domain NIR tomography system that is compatible with the magnetic field environment inside a standard full-body MRI scanner. The combined data set offers measurements of light transmission through the full volume of the breast in a planar anatomically coronal geometry and a high-resolution MRI of that same volume. Algorithmic procedures for exploiting both NIR and MRI data to reconstruct first optical property (absorption and reduced scattering coefficient) distributions, and then tissue chromophores and scatter parameters are described and validated with phantom studies. The impact of including the MRI component of this imaging platform is shown for a human volunteer. The segmentation of adipose from fibroglandular tissue is examined and analyzed. The combined imaging system could become a valuable tool for characterizing the optical signatures of normal breast tissue, benign breast conditions, and breast cancer. Currently, NIR exams occur predominantly in laboratories that are developing the technology under National Institutes of Health (NIH) research funding. Considering that many women commonly undergo MRI breast exams, and that the system described here can be seamlessly integrated into these procedures, it provides an excellent opportunity to determine the optimal way to integrate prior spatial information into NIR tomography. This type of combined system may prove to be an important bridge that carries NIR imaging methods from the lab into accepted clinical application.

2 Methods

2.1 *Hardware*

The imaging system used records measurements of NIR light transmission through a pendant breast in a planar, tomographic geometry. The patient lies inside a 1.5-T whole-body MRI (GE Medical Systems) and the two data types (i.e., NIR and MRI) are acquired simultaneously. The system is shown in Fig. 1, and was described in detail by Brooksby et al.[34] Figure 1(a) shows the portable cart, which contains the light generation and detection hardware subsystems. Six laser diodes (660 to 850 nm) are amplitude modulated at 100 MHz. The bank of laser tubes is mounted on a linear translation stage, which sequentially couples the activated source into 16 bifurcated optical fiber bundles. The central seven fibers deliver the source light while the remaining fibers collect transmitted light and are coupled to photomultiplier tube (PMT) detectors located in the base of the cart. The fibers are positioned in a plane spanning the circumference of a pendant breast, and for each activated source, measurements of the amplitude and phase shift of the 100-MHz signal are acquired from 15 locations around the breast. Figure 1(b) shows a photograph of the MR-compatible fiber positioning system anchored inside an open architecture breast array coil (MRI De-
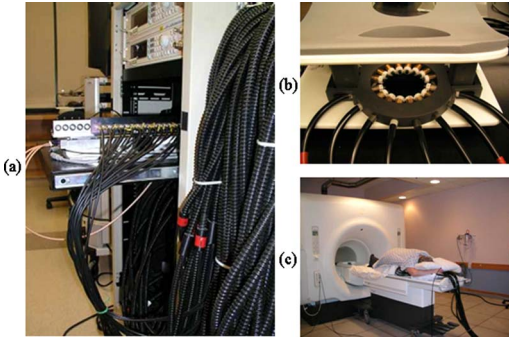
Fig. 1 (a) Photograph of the portable cart housing the NIR light generation and detection hardware. The cart remains outside of the rf-shielded MR chamber, and optical fibers extend 13 m to the MRI patient bed. On the retracted shelf, a linear translation stage sequentially couples one activated laser diode to each of the 16 optical fibers that contact the breast. (b) MR-compatible fiber-patient interface, made of polyvinyl chloride (PVC), is mounted inside a high-resolution MR breast coil. Compression springs ensure light contact between each fiber and the patient's skin. (c) A patient volunteer lying prone on the combined MRI-NIR bed prior to her exam.

vices). The vertical position of the imaging plane is manually adjusted, and contact with the breast is maintained automatically using bronze compression springs.

2.2 Image Formation

It is well established that in the interaction of NIR light with tissue, scattering dominates over absorption. Under these conditions, light transport can be effectively modeled using the diffusion equation over moderately large distances.[35,36] Analogous to the hardware approach, a frequency-domain diffusion model is used to simulate measured signals for any specified distribution of absorption and reduced scattering coefficients, μ_a and μ_s', within an imaged volume. This is given by

$$-\nabla \cdot D(r) \, \nabla \, \Phi(r,\omega) + \left[\mu_a(r) + \frac{i\omega}{c} \right] \Phi(r,\omega) = S(r,\omega),$$

(1)

where $S(r,\omega)$ is an isotropic light source at position r, $\Phi(r,\omega)$ is the photon density at r, c is the speed of light in tissue, ω is the frequency of light modulation, and $D = 1/[3(\mu_a + \mu_s')]$ is the diffusion coefficient. The reduced scattering coefficient is given by $\mu_s' = \mu_s(1-g)$, where g is the mean cosine of the single scatter function (the anisotropy factor), and μ_s is the scattering coefficient. A type III boundary condition is applied as

$$\Phi + \frac{D}{\alpha} \hat{n} \cdot \nabla \Phi = 0,$$

(2)

where α is a term that incorporates reflection as a result of refractive index mismatch at the boundary, and $\hat{n}$ is the outward-pointing normal to the boundary.

Equation (1) can be viewed as a nonlinear function of the optical properties. Its solution is represented as a complex-valued vector, $\mathbf{y}^* = F(\mu_a, D)$, having real and imaginary components that are transformed to logarithm of the amplitude and phase in the measurements. The phase shift of the signal

provides data that is dominated by the optical path length through tissue, while the amplitude of the transmitted light provides information about the overall attenuation of the signal. These measurements constitute the dataset necessary for successful estimation of both absorption and reduced scattering coefficients.

Data acquired by the detection system is processed with a finite element method (FEM)-based reconstruction algorithm to generate tomographic images of μ_a and μ_s'. In the image reconstruction, a Newton-minimization approach developed by Paulsen and Jiang[37] is used to seek a solution to

$$(\hat{\mu}_a, \hat{D}) = \min_{\mu_a, D} \{ \| \mathbf{y}^* - F(\mu_a, D) \| + \lambda \| (\hat{\mu}_a, \hat{D}) - (\mu_{a0}, D_0) \| \},$$

(3)

where $\|\cdot\|$ represents the square root of the sum of squared elements. This is the so-called Tikhonov approach,[38] and λ is a weighting factor of the difference between the current values of the optical properties and their initial estimates. The magnitude of this objective function is sometimes referred to as the projection error and provides a value for determining the convergence of the iterative solution. Its minimum is evaluated by setting first derivatives with respect to μ_a and D equal to zero. This leads to a set of equations that is solved iteratively, using the following matrix equation,[39] derived from Eq. (3):

$$\delta\mu = (\mathbf{J}^T \mathbf{J} + \lambda \mathbf{I})^{-1} \mathbf{J}^T [\mathbf{y}^* - F(\mu_a, D)] + \lambda(\mu - \mu_0). \quad (4)$$

At each iteration, the new set of μ_a and D values is updated by $\mu_a^{i+1} = \mu_a^i + \delta\mu_a^i$, and $D^{i+1} = D^i + \delta D^i$, where i is the index for the iteration number, $\mathbf{J}$ is the Jacobian matrix for the diffusion equation solution, and $\mathbf{J}^T\mathbf{J}$ is ill-conditioned and therefore regularized through the addition of $\lambda\mathbf{I}$, where $\mathbf{I}$ is an identity matrix. Regularization is implemented in a Levenberg-Marquardt algorithm where λ starts at a high value (typically 10 times the maximum value of the diagonal of $\mathbf{J}^T\mathbf{J}$) and is systematically reduced at each iteration. In Eq. (4), μ_0 is the initial estimate of optical properties input into the iterative estimation process, and is a form of prior information.[40] Here, the initial estimate is determined through a data calibration procedure which assumes a homogeneous property distribution.[41] In our experience, the last term in Eq. (4), $\lambda(\mu - \mu_0)$, has little effect on the solution due to the small size of both λ and $(\mu - \mu_0)$, especially at late iterations, and can be ignored. If this term were included, and λ were not reduced with each iteration, the current optical property estimate would not stray very far from the homogeneous initial estimate. This is not desirable when reconstructing heterogeneities. Efforts are currently being made toward the generation heterogeneous initial guesses, which could make the inclusion of this extra term beneficial.

2.3 Inclusion of Priors

Image reconstruction techniques which incorporate prior knowledge of tissue structure have been largely developed for nuclear imaging over the last decade.[26,42–45] Anatomical information is generally used to adjust image smoothness and reduce noise levels during reconstruction. Most of the approaches to this problem are based on Bayesian estimation
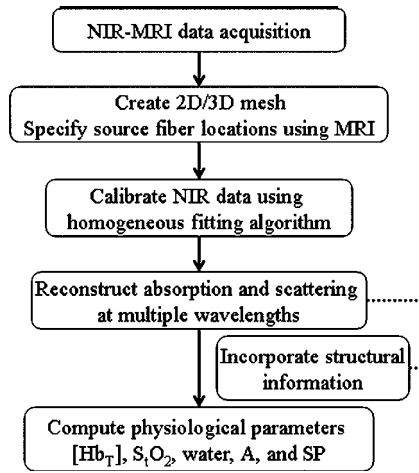
Fig. 2 Flow chart tracking the key steps associated with the use of the combined NIR-MRI imaging system.

techniques. Prior information consists of anatomical boundaries that are likely to correspond to discontinuities in an otherwise spatially smooth radionuclide distribution. In the reconstructed image, neighboring pixels within homogeneous regions should have similar intensity levels. In regions which exhibit distinctly different tissue characteristics, smoothing across their shared boundary should be limited. Improving NIR reconstructions by incorporating prior knowledge of tissue structure available from MRI data has been explored in previous work at Dartmouth[13,19,32,40,46] and by other authors.[20–22,27,31,33,47,48] Our early work involved using high-resolution MRI to construct an accurate rendering of the full volume of breast tissue probed by NIR light. Following the lead of Ntziachristos et al.[27] and Zhu et al.[31] it was further assumed that optical contrast correlated to MRI contrast, and the number of property estimates was dramatically reduced.[40] While generally effective in simulation studies, and for reconstructing simple phantom geometries containing a single discrete heterogeneity (i.e., inclusion), this method was vulnerable to overbiasing the inverse solutions toward the assumed distributions. Sensitivity to noise in the data and error in the region designation caused this "parameter reduction" algorithm to be unreliable when imaging complex and layered phantoms. Here, we describe an improved technique that guides the iterative evolution of reconstruction, but does not impose the rigid constraint of interregion homogeneity. This algorithm is still able to detect optical coefficient patterns that violate the prior information. Similar to the strategy outlined by Li et al.,[21] this is accomplished through regularization. The benefits of the implementation described here is that reconstruction is not a complex multistep process. For the first time, NIR measurements taken in a full tomographic geometry can be used to generate high-resolution functional images through a flexible procedure, regardless of arbitrary tissue structures.

A priori information can be incorporated directly through the objective function by formulating the minimization of a two term functional:[25]

$$(\hat{\mu}_a, \hat{D}) = \min_{\mu_a, D} \{\|\mathbf{y}^* - F(\mu_a, D)\| + \alpha \|\mathbf{L}[(\hat{\mu}_a, \hat{D})$$
$$- (\mu_{a0}, D_0)]\|\}. \quad (5)$$

The constant α balances the effect of the prior with the model-data mismatch. The filter matrix $\mathbf{L}$ is generated using MRI-derived priors and effectively relaxes the smoothness constraints at the interface between different tissues, in directions normal to their common boundary. The effect on image quality is similar to that achieved through total variation minimization schemes.[49] This procedure, however, is more robust and can easily encode internal boundary information from MR images. Each node in the FEM mesh is labeled according to the region, or tissue type, with which it is associated (in the MR image). For the i'th node of n in region $N, L_{i,l} = 1$. When nodes i and j are in the same region, $L_{i,j} = -1/n$, otherwise $L_{i,j} = 0$. The solution to Eq. (5) is again accomplished with a Newton-minimization approach, that produces the update equation

$$\delta\mu = (\mathbf{J}^T\mathbf{J} + \alpha\mathbf{L}^T\mathbf{L})^{-1}[\mathbf{J}^T[\mathbf{y}^* - F(\mu_a, D)] + \Lambda], \quad (6)$$

which is iteratively solved. Note $\mathbf{L}^T\mathbf{L}$ approximates a second-order Laplacian smoothing operator within each region separately. This construction of $\mathbf{L}$ has proved flexible and effective, as demonstrated in the phantom studies shown in Sec. 3, but other forms can easily be implemented and evaluated. Similarly to Eq. (4), the last term, $\Lambda = \alpha\mathbf{L}^T\mathbf{L}[(\mu_{ai}, D_i) - (\mu_{a0}, D_0)]$, has been ignored in the results presented here.

Simulation studies were performed to characterize the effect of $\mathbf{L}$ and α on the quality and quantitative accuracy of reconstructed images, and to establish a value of α that can be used routinely. Data was generated from numerical phantoms with a variety of heterogeneity patterns—ranging from a simple circular anomaly in a homogeneous background (similar to the physical phantom in Fig. 4 in Sec. 3.2) to irregular distributions of regions with two or three different properties (similar to the complexity of the breast in Fig. 5 in Sec. 3.3). Noise (1 to 2%) was added to simulated data to better replicate experimental conditions. Error was also added to the *a priori* region designation, to account for the small loss of resolution when spatial information is transferred from MR images to FEM meshes. Images were reconstructed from this data using a range of α from 1 to 100. A high α value increases the impact of the spatial prior, leading to images with sharper internal boundaries, but could negatively bias solutions if this prior is not correct. By accounting for the different sources of error that are present when data is acquired with the system presented here, simulation results indicate that setting α to 10 times the maximum value of the diagonal of $\mathbf{J}^T\mathbf{J}$ optimizes image quality and accuracy regardless of the level of geometric complexity present in the area under investigation. Unlike λ in Eq. (4), α does not decrease during the iterative solution process.

2.4 *Spectral Decomposition*

The absorption coefficient at any wavelength is assumed to be a linear combination of the absorption due to all relevant chromophores in the sample:
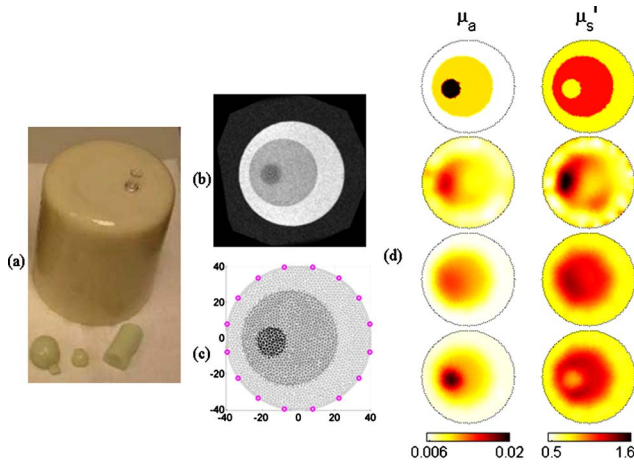
Fig. 3 (a) Photograph of a gelatin phantom and a variety of inclusions (small gelatin spheres and a cylinder with different optical properties); (b) MRI showing a cross section of the cylindrical phantom, visible in the MRI are three types of gel; and (c) finite element mesh segmented according to the MRI intensity. The optical fiber source/detectors marked around the circumference are specified with millimeter accuracy. The axes are in millimeters, showing the full diameter of the phantom to be 82 mm. (d) Reconstructed images of the absorption and reduced scattering coefficients for this phantom. The top pair of images shows the true distribution, the second pair shows the reconstructions that do not use *a priori* information, the third pair shows reconstruction in which two layers were assumed from the MRI (i.e., the inclusion was ignored), and the bottom pair shows reconstructions in which the full MRI is used. When the full compliment of prior information is used, root mean square image error decreases 43% for absorption and 55% for scattering.

$$\mu_a(\lambda) = \sum_{i=1}^{N} \varepsilon(i,\lambda)C_i, \qquad (7)$$

where λ is the molar absorption spectra, and C is the concentration of each chromophore.[18] In the presented analysis, the concentrations of three chromophores—oxyhemoglobin (HbO_2), deoxyhemoglobin (Hb), and water (H_2O)—are estimated. Hence, given μ_a at the k'th pixel for multiple wavelengths, a linear inversion of Eq. (7) determines the array of C values

$$C_k = \mathbf{E}^{-1}\mu_{a,k}, \qquad (8)$$

representing the concentrations of the three chromophores. In Eq. (8), $\mathbf{E}$ is the matrix of molar extinction coefficients having elements $\varepsilon(i,\lambda)$, for the i'th chromophore at different wavelengths.

The spectral character of the reduced scattering coefficient also provides information about the composition of the tissue. From an approximation to Mie scattering theory, it is possible to derive a relation between μ_s' and wavelength given by

$$\mu_s'(\lambda) = A\lambda^{-SP}, \qquad (9)$$

where SP is the scattering power and A is the scattering amplitude[50] (which depend on scatterer size and number density). Typically, large scatterers have lower SP and A values. These scattering parameters appear to reflect variations in
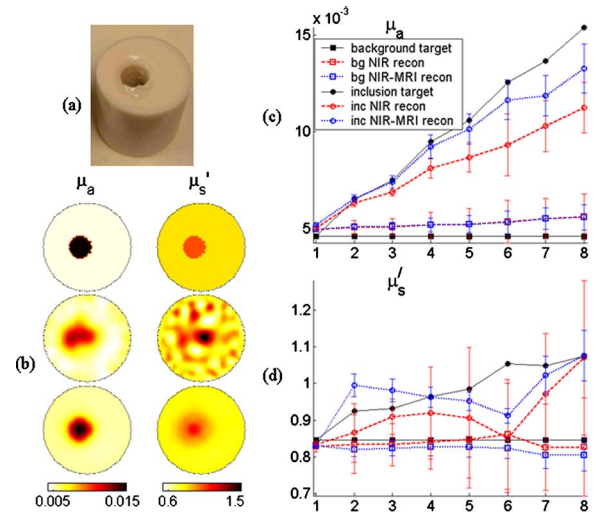

Fig. 4 (a) Photograph of the homogeneous gelatin phantom with a 22-mm cylindrical cavity slightly off-center and (b) reconstructed images of the absorption and reduced scattering coefficients for this phantom when an intralipid solution with 3:1 absorption contrast fills the opening. The top pair of images shows the true distribution, the middle pair shows the reconstructions which result when *a priori* information is not used, and the bottom pair results when prior information about the size and location of the anomaly is incorporated. When prior information is used, root mean square image error decreases 26% for absorption and 58% for scattering. Image artifacts appear in the form of artificial background heterogeneity when priors are not utilized. A more accurate estimate of the true optical properties, and shape of the inclusion, is obtained with the MR-guided iterative algorithm. (c) and (d) Absorption and reduced scattering coefficients respectively for both the background (bg) and the inclusion (inc), recovered using the two algorithms for eight intralipid solutions with different absorption coefficients. The images in (b) correspond to solution 8, on the far right of (c) and (d).

structural breast composition associated with age and radiographic density.[8,51]

2.5 Phantom Studies

Single- and multilayered phantoms were fabricated from gels with different optical properties using heated mixtures of water (80%), gelatin (20%) (G2625, Sigma Inc.), India ink or blood (for absorption), and titanium dioxide powder (for scatter) (TiO_2, Sigma Inc.) that are solidified by cooling to room temperature. Optically distinct layers were fabricated by successively hardening gel solutions containing different amounts of ink and TiO_2. True properties were estimated by measuring a large cylindrical sample of each material.[41] Because these phantoms are water-based, they are well suited for testing a combined NIR-MRI system. To increase MRI contrast between different gels in multilayered phantoms, 0.001 to 0.005 g/ml Omniscan™ (gadodiamide) was added.

Two studies with gelatin-based phantoms were performed. The first examined spatial resolution, while the second assessed quantitative accuracy as a function of inclusion contrast. The phantom imaging procedure is outlined in Fig. 2. Data acquisition is followed by automated MR image processing and FEM mesh generation. The MRI is segmented via automatic thresholding and edge detection, and pixels of similar intensity are assumed to represent the same material or
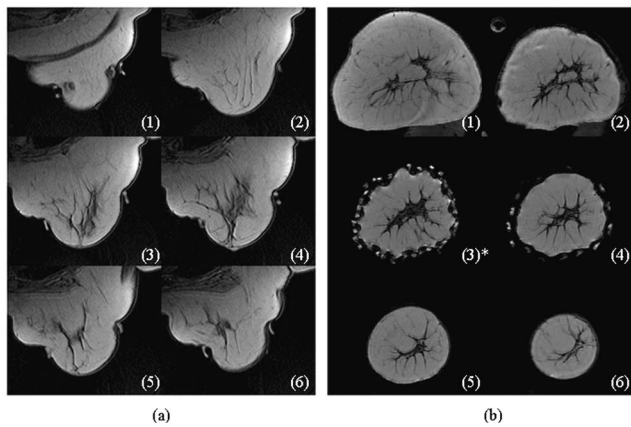
Fig. 5 MRI slices of a normal breast for a representative subject with scattered radiographic density, imaged with the NIR-MRI system. (a) Anatomically axial (cranial-caudal; slice 6 to slice 1) T_1-weighted MR images. Slice thickness is 5 mm and the space between slices is 10 mm. Toroidal fiducial markers surround the optical fibers approximately 1 cm from the tip, and appear as bright spots outside of the tissue. (b) Oblique coronal T_1-weighted MR images of the same breast. Slice (1) is toward the chest wall, and slice (6) is toward the nipple. Slice thickness is 2 mm and the space between slices is 10 mm. Coronal slice (3)* is the plane of the optical fibers. A region of glandular tissue (dark grey) appears surrounded by a layer of adipose (light gray). This slice was used to set construct the FEM mesh in order to reconstruct the optical property distributions (see Fig. 6).

tissue. This material information is transferred to the FEM mesh as a "region" label. NIR data are calibrated using a reference measurement of a homogeneous phantom to correct for variation between the 16 optical channels.[41,52] Optical property reconstruction is performed on the appropriate mesh, containing the same number of distinctly visible regions as the MRI. Appropriate labels are given to the mesh so that *a priori* guidance is automatic. If optical property images are obtained at multiple NIR wavelengths, spectral analysis is performed and chromophores/scatter parameters are calculated.

2.6 Human Subject Studies

All human studies are carried out under informed consent according to protocol approved by the Institutional Review Board at Dartmouth. Although we present a single case study here, several women participated in the study. Healthy volunteers were recruited from a pool of women having received a routine screening mammography at Dartmouth Hitchcock Medical Center. The subject lies prone on the scanner table with her breast pendant into the open architecture breast array coil, and a nurse or MRI technician operates the optical fiber positioning system to establish uniform tissue contact at sixteen points around the perimeter of the breast. Once inside the bore of the 1.5-T magnet, MRI and NIR data are acquired simultaneously. The MRI protocol typically involves two imaging sequences. First, scout images are acquired in three orthogonal planes to localize the orientation of the optical fiber array. Second, a T_1-weighted volume of the entire breast is obtained with each slice oriented parallel to the plane of the optical fibers. NIR data acquisition is automated via Labview software (National Instruments) executing on a separate com-

puter. Measurements are recorded serially at six wavelengths, and a typical exam lasts approximately 15 min. In the case study presented here, five wavelengths of NIR data were collected. Once the patient exits the magnet, the procedure outlined in Fig. 2, including MRI-guided NIR image reconstruction and spectral decomposition is performed. Images of physiological parameters, total hemoglobin concentration ($[Hb_T]$), percent blood oxygen saturation (S_tO_2), water fraction (H_2O), scattering amplitude (A), and scattering power (SP) can be generated approximately 15 min after data acquisition.

3 Results

3.1 Phantom Imaging: Spatial Resolution

A two-layer gelatin phantom with a cylindrical inclusion embedded inside the inner layer was used to evaluate the ability of the NIR-MRI system to resolve this type of structure. A photograph of the phantom is shown in Fig. 3(a). Figure 3(b) shows an MRI slice through the phantom at the height of the inclusion, and Fig. 3(c) shows the FEM mesh, and optical fiber locations. Each gel layer possessed a different absorption (outer layer, 0.0055 mm^{-1}; inner layer, 0.01 mm^{-1}; inclusion, 0.02 mm^{-1}) and reduced scattering coefficient (outer layer, 0.75 mm^{-1}; inner layer, 1.2 mm^{-1}; inclusion, 0.75 mm^{-1}). The outer and inner layers extended the full height of the phantom (10 cm) while the inclusion (height, 2.5 cm; diameter, 1.5 cm) was embedded half-way from top to bottom.

Figure 3(d) contains reconstructed images of the optical properties at a 785-nm wavelength. The top pair of images shows the true distribution of absorption and reduced scattering coefficients. The second pair of images indicates the reconstructions that result from the solution of Eq. (3), which is the standard Newton-minimization and does not use *a priori* information. Although not presented here, a parameter reduction algorithm that reconstructs a single absorption and reduced scattering coefficient for each region was also used. The estimated properties do not match the true phantom properties. The maximum absorption was localized to the inner layer rather than the inclusion, and the maximum scatter was localized to the inclusion rather than the inner layer. The third pair of images results from the solution of Eq. (5), where the layered MRI data was used to form the regularization matrix. In this case, to illustrate the performance of the algorithm when prior information is incomplete or incorrect, the presence of the inclusion was not specified. The bottom pair of images results from the solution of Eq. (5), where the full MRI data, including the presence of the inclusion, was used to form the regularization matrix. Clearly these images more accurately represent the true property distributions. The iterative reconstruction process is terminated automatically when the projection error reaches its minimum. For both algorithms this occurred at iteration 11.

3.2 Phantom Imaging: Contrast Resolution

To characterize the performance of the system and the quality of the defined algorithm, a phantom with inclusions of different contrast was imaged. A gelatin solution (μ_a = 0.005 mm^{-1}, μ_s' = 0.85 mm^{-1}) was hardened inside an 82-mm cup, with a 22-cm-diam cylindrical rod included in
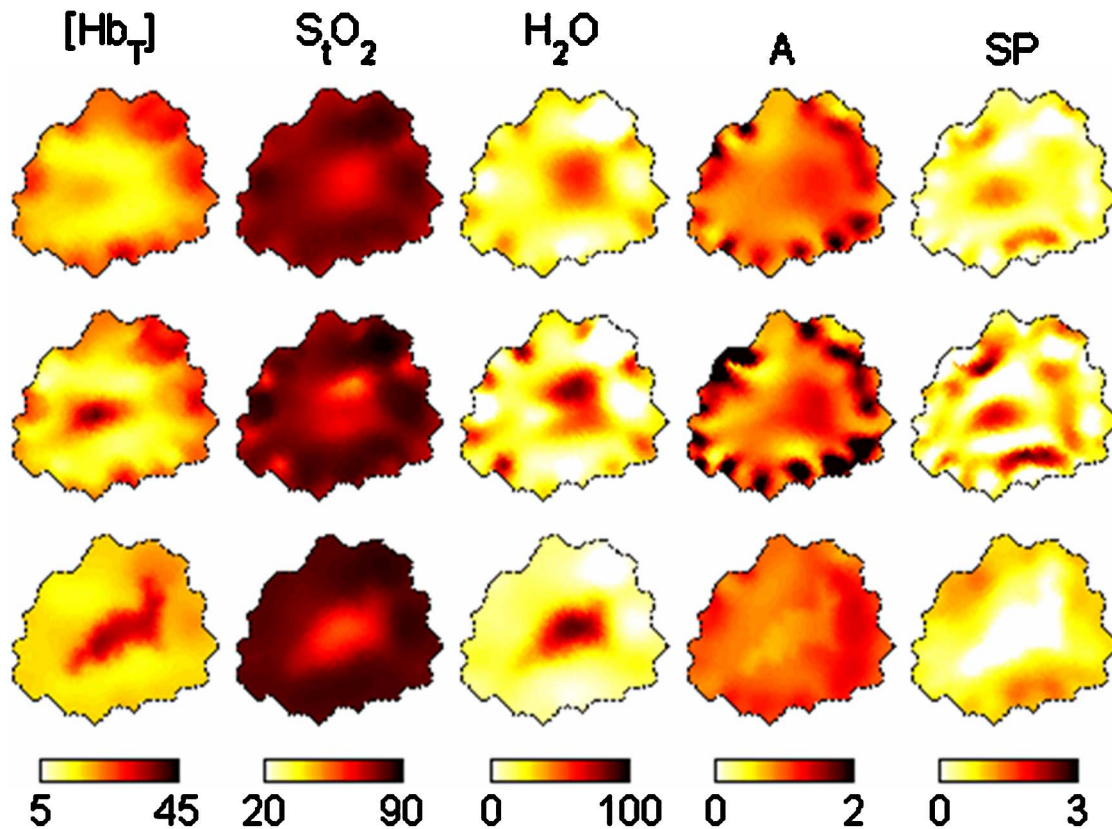
Fig. 6 NIR-MRI results for a representative subject. These tomographic NIR images correspond to MRI slice (3)* in Fig. 5(b). NIR chromophore concentrations and scattering parameters were derived from spectral analysis and Mie theory. Three sets of images are shown. Two sets were derived from absorption and reduced scattering coefficients that were reconstructed with a standard Newton-minimization algorithm, unconstrained by priors obtained from MRI. The first (top) used the fifth iteration while the second (middle) used the projection error minimum as a stopping criteria (iterations 9 to 11). The third set (bottom) incorporated regional structure visible in the MRI to guide optical property estimation and projection error minimum stopping criteria. When the algorithm is unconstrained by MR, intertissue contrast appears to develop at later iterations, but noise also increases (especially in scatter). Using MRI constraints, artifacts are suppressed and images exhibit high contrast and good resolution.

the interior. After the gelatin hardened, the rod was removed and the empty column was filled with intralipid solutions having absorption coefficients ranging from 0.005 to 0.015 mm^{-1}. A photograph of the phantom is shown in Fig. 4(a). Another photograph (not shown) taken of the phantom in the imaging array was used as a surrogate MRI. This was used to define *a priori* information of the phantom's structure, and provided the necessary detail to carry out region of interest analysis to assess reconstruction accuracy. Figure 4(b) presents target values of absorption and reduced scattering coefficients (top) for a phantom with 3:1 absorption contrast, along with the corresponding reconstructions based on Eq. (3) (middle) and Eq. (5) (bottom). Figures 4(c) and 4(d) report the absorption and reduced scattering coefficient averages for both the background and the inclusion when recovered with the two algorithms. In general, the inclusion absorption coefficient is more accurately estimated when the MRI information is utilized in the reconstruction algorithm. Additionally, the spatial variation in both properties is reduced.

3.3 Representative Breast Results

Here we present in detail the study of a healthy volunteer whom we examined with the combined NIR-MRI imaging system. Anatomically axial and oblique coronal T_1-weighted gradient echo MR images are shown in Figs. 5(a) and 5(b), respectively. The woman had breasts with scattered radiographic density (i.e., fatty tissue containing scattered fibroglandular densities). The MR slices reveal an area of blood vessels and vascularized glandular tissue near the center of the breast (dark in the MR image), surrounded by a subsurface layer of adipose tissue (light gray in the MR image). Fiducial markers, attached to each fiber are visible just outside the breast surface. In Fig. 5(b), image slice (3)* corresponds to the optical measurement plane. An FEM mesh for image reconstruction was generated by segmenting adipose and glandular tissue in this image slice, based on image intensity. The mesh accurately describes the convoluted outer breast boundary, the size and shape of the glandular region, and the location of the 16 NIR measurement sites. Along with the MRI, NIR transmission data (amplitude and phase) was measured at five wavelengths (661, 785, 808, 826, and 849 nm). Spectral deconvolution was performed from images of μ_a and μ_s' reconstructed at these wavelengths. The images of NIR chromophore concentrations and scattering properties are shown in Fig. 6. The three sets of images correspond to spectral analysis using different μ_a or μ_s' reconstructions. The
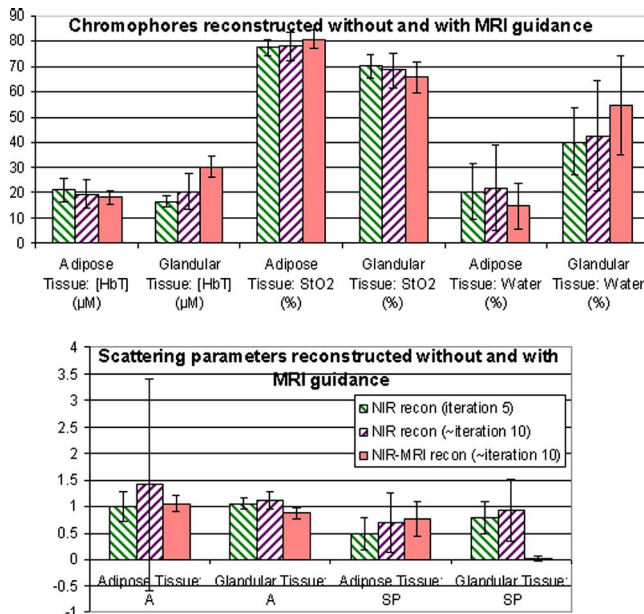
Fig. 7 Graphs of reconstructed tissue properties from Fig. 6. Total hemoglobin concentration ([Hb$_T$]), oxygen saturation (S_tO_2), water, scattering amplitude (A), and scattering power (SP) are reported separately for adipose and fibroglandular tissue, again as defined from the spatial pattern of gray-scale intensity from the simultaneously acquired MRI. Error bars represent the standard deviation of property values within a particular tissue. For each chromophore, MR-guided NIR reconstruction decreases intratissue variation and increases intertissue contrast. For scattering parameters, MR-guidance primarily reduces the size of the error bars.

images presented estimate total hemoglobin concentration [Hb$_T$], blood oxygen saturation S_tO_2, water H$_2$O, scattering amplitude A, and scattering power SP. The first set of images (top row) results when the solution of Eq. (3) is stopped prior to convergence at iteration 5, which is the approach we have utilized in our previous NIR breast studies. The second set of images (in the middle row) results when the algorithm continues to the projection error minimum (iterations 9 to 11). The third set of images (bottom row) is obtained from the convergent solution of Eq. (5). In this case the full knowledge of tissue structure, provided by MRI, is brought to bear in the NIR image reconstruction. When the algorithm is unconstrained by MR, intertissue contrast appears to develop at later iterations, but noise also increases. The estimates that rely on constraints from MRI data suppress artifacts and produce images that exhibit high contrast and resolution. Average values of each of these parameters are tabulated in Fig. 7, for both the adipose and the glandular tissue regions, and for all three reconstruction approaches.

4 Discussion

NIR tomography is potentially an important adjunct to anatomical imaging because of the possibility of adding unique information to the characterization of diseased tissue. This paper explored the implementation of simultaneous NIR-MRI imaging methods that were used to study breast tissue *in vivo*. There is little debate that knowledge of tissue structure can constrain/guide NIR image reconstruction to improve spatial

resolution and quantitative accuracy of recovered physiological parameters. However, there is considerably less certainty about how best to incorporate the information. In this paper, we developed a full regularization matrix where locations are linked within the same tissue type. The validation of the approach was demonstrated through phantom experiments designed to mimic the layered geometry apparent in many breasts.

The first phantom study, described in Sec. 3.1, evaluated spatial resolution of the combined NIR-MRI imaging system. The results shown in Fig. 3(d) indicate that the MR-guided iterative algorithm performed much better than the standard reconstruction approach in terms of the ability to resolve layer location and interior heterogeneities. In particular, it produced absorption and reduced scattering coefficient images which accurately represented the layered optical contrast (μ_a, 4:2:1; μ_s', 1:1.6:1). When the MRI data was neglected, and amplitude and phase data were reconstructed with a standard Newton type reconstruction, the calculated images only slightly resembled the true spatial structure. Additionally, quantitative accuracy suffered. The scattering of the inclusion appeared to increase relative to the inner layer while in actuality it decreased. The root mean square (rms) error of the recovered distributions of the absorption and reduced scattering coefficients were estimated to be 0.0023 and 0.230, respectively. When a subset of the prior knowledge of the phantoms structure provided by the MRI was used in image reconstruction, the images that result indicate the presence of three material types, but quantitative accuracy is not optimal. When the full data set was utilized, and MR-derived priors guided the reconstruction, distinct boundaries separating each of the phantom layers were recovered. In this case, the rms error of the absorption and reduced scattering coefficient images decreased 43% to 0.0014, and 55% to 0.104, respectively. The ability to quantify deeply embedded regions was also greatly improved. The mean value of the absorption coefficient estimated in the region of the inclusion was accurate within 10% (0.018 mm^{-1} compared to the expected 0.02 mm^{-1}). Estimation of the reduced scattering coefficient improved to within 20% (0.9 mm^{-1} compared to the expected 0.75 mm^{-1}). This experiment indicated that resolution and accuracy were both improved with the added information about the layer, when implemented through a full regularization matrix. The algorithm responded to MRI-derived information about the structure of the imaged volume, and the spatial image patterns that it produced resembled that of the MRI. Note, however, that when a prior is specified, but no absorption or scattering contrast exists, the algorithm does not introduce artificial contrast within the image space matching the prior.

The second phantom study was completed to assess contrast-resolution. For the images shown in Fig. 4(b), when prior information is used in image reconstruction the rms error of the absorption and reduced scattering coefficient images decreased from 0.0019 to 0.0014 (26%) and from 0.1444 to 0.0613 (58%), respectively. The data plotted in Figs. 4(c) and 4(d) indicated that linearity exists between the estimated and the true contrast for the two reconstruction methods discussed here. A collection of intralipid solutions (primarily with different absorption coefficients) was imaged inside a homogeneous background of gelatin. MRI-guided reconstructions re-

covered more accurate property values over the entire range of contrast. Figure 4(b) showed that with MRI-guidance, image artifacts were suppressed (especially in μ_s' images). The error bars in Figs. 4(c) and 4(d) representing the NIR image pixel standard deviation indicated that the variation in the background and inclusion were reduced by using MRI priors.

An initial study of the breasts of normal volunteers has been conducted to assess the feasibility and comfort of the NIR array in the MR breast coil. Subject feedback indicated that the examination table is comfortable. As developed, the data acquisition system has proved feasible as well. We presented a single case study from the cohort of women imaged with our NIR-MRI system. MR images can distinguish adipose from glandular tissue with excellent contrast. This tissue discrimination was used as a prior and the two tissue types were treated separately in NIR image reconstruction. Figure 6 showed the detailed results from a typical volunteer exam. The same amplitude and phase data was processed three different ways, and Fig. 7 presented a quantitative summary of the results. Tissue parameters derived from spectral analysis ([Hb$_T$], S$_t$O$_2$, water, A, and SP) were reported separately for adipose and glandular tissue. Error bars represented the standard deviation of property values within a particular tissue. For each chromophore, MR-guided NIR reconstruction decreased intratissue variation and increased intertissue contrast. For scattering parameters, MR guidance primarily reduced the size of the error bars. Adipose tissue in this subject appeared to be composed of 18-μM hemoglobin (approximately 0.75% blood volume, assuming an average 15.6 dL/L hematocrit), 80% oxygen saturation of the blood, and 15% water fraction. In the glandular tissue it appeared to be composed of 30-μM hemoglobin (approx. 1.25% blood volume), with 66% blood oxygen saturation, and 55% water fraction.

5 Conclusions

Phantom studies indicated that MRI can be used to improve the spatial resolution and quantitative accuracy of NIR parameter image reconstruction. In particular, by using an MR-guided iterative algorithm, layered structures can be recognized in diffuse media, and the properties of embedded objects can be studied with higher quantitative accuracy. Studies with a stand-alone NIR imaging system have shown that reconstructed tissue properties ([Hb$_T$], A, and SP) correlate with tissue radiographic density.[8,18] Based on phantom studies presented here, which show that MRI-guided NIR characterization is more accurate, it is reasonable to conclude that the tissue characterization offered by the NIR-MRI system is preferred over stand-alone systems when available. The true values of these parameters in adipose and glandular tissue of individual subjects are not known, however, the trends observed in Fig. 6 and 7 are reasonable physiologically, when the MR information is encoded within the NIR reconstruction approach. Without the MRI, the potential to estimate NIR parameters for different tissues within the breast is not as accurate. The combined imaging approach may be particularly useful for breast lesion diagnosis or management, which will be the subject of future studies.

References

1. D. T. Delpy and M. Cope, "Quantification in tissue near-infrared spectroscopy," *Philos. Trans. R. Soc. London, Ser. B* **352**, 649 (1997).
2. B. Chance, Q. Luo, S. Nioka, D. C. Alsop, and J. A. Detre, "Optical investigations of physiology: a study of intrinsic and extrinsic biomedical contrast," *Philos. Trans. R. Soc. London, Ser. B* **352**, 707 (1997).
3. S. Fantini, S. A. Walker, M. A. Franceschini, M. Kaschke, P. M. Schlag, and K. T. Moesta, "Assessment of the size, position, and optical properties of breast tumors *in vivo* by noninvasive optical methods," *Appl. Opt.* **37**, 1982–1989 (1998).
4. B. J. Tromberg, N. Shah, R. Lanning, A. Cerussi, J. Espinoza, T. Pham, L. Svaasand, and J. Butler, "Non-invasive *in vivo* characterization of breast tumors using photon migration spectroscopy," *Neoplasia* **2**, 26 (2000).
5. V. Ntziachristos and B. Chance, "Probing physiology and molecular function using optical imaging: applications to breast cancer," *Breast Cancer Res.* **3**, 41 (2001).
6. D. A. Boas, D. H. Brooks, E. L. Miller, C. A. DiMarzio, M. Kilmer, R. J. Gaudette, and Q. Zhang, "Imaging the body with diffuse optical tomography," *IEEE Signal Process. Mag.* **13**, 57–75 (2001).
7. B. W. Pogue, S. Geimer, T. O. McBride, S. Jiang, U. L. Osterberg, and K. D. Paulsen, "Three-dimensional simulation of near-infrared diffusion in tissue: boundary condition and geometry analysis for finite-element image reconstruction," *Appl. Opt.* **40**, 588 (2001).
8. S. Srinivasan, B. W. Pogue, S. Jiang, H. Dehghani, C. Kogel, S. Soho, J. J. Gibson, T. D. Tosteson, S. P. Poplack, and K. D. Paulsen, "Interpreting hemoglobin and water concentration, oxygen saturation, and scattering measured in vivo by near-infrared breast tomography," *Proc. Natl. Acad. Sci. U.S.A.* **100**, 12349 (2003).
9. M. F. Ernst and J. A. Roukema, "Diagnosis of non-palpable breast cancer: a review," *The Breast* **11**, 13 (2002).
10. T. Hata, H. Takahashi, K. Watanabe, M. Takahashi, K. Taguchi, T. Itoh, and S. Todo, "Magnetic resonance imaging for preoperative evaluation of breast cancer: a comparative study with mammography and ultrasonography," *J. Am. Coll. Surg.* **198**, 190 (2004).
11. P. A. Carney, C. J. Kasales, A. N. A. Tosteson, J. E. Weiss, M. E. Goodrich, S. P. Poplack, W. S. Wells, and L. Titus-Ernstoff, "Likelihood of additional work-up among women undergoing routine screening mammography: the impact of age, breast density, and hormone therapy use," *Prev. Med.* **39**, 48 (2004).
12. V. Chernomordik, A. H. Gandjbakhche, M. Lepore, R. Esposito, and I. Delfino, "Depth dependence of the analytic expression for the width of the point spread function (spatial resolution) in time-resolved transillumination," *J. Biomed. Opt.* **6**, 441 (2001).
13. H. Dehghani, B. W. Pogue, S. Jiang, B. A. Brooksby, and K. D. Paulsen, "Three-dimensional optical tomography: resolution in small-object imaging," *Appl. Opt.* **42**, 3117 (2003).
14. D. A. Boas, K. Chen, D. Grebert, and M. A. Francheschini, "Improving the diffuse optical imaging spatial resolution of the cerebral hemodynamic response to brain activation in humans," *Opt. Lett.* **29**, 1506 (2004).
15. P. S. Conti, D. L. Lilien, K. Hawley, J. Keppler, S. T. Grafton, and J. R. Bading, "PET and [18F]-FDG in oncology: a clinical update," *Nucl. Med. Biol.* **23**, 717 (1996).
16. M. Tatsumi, C. Cohade, Y. Nakamoto, and R. L. Wahl, "Fluorodeoxyglucose uptake in the aortic wall at PET/CT: possible finding for active atherosclerosis," *Radiology* **229**, 831 (2003).
17. A. L. Goertzen, A. K. Meadors, R. W. Silverman, and S. R. Cherry, "Simultaneous molecular and anatomical imaging of the mouse *in vivo*," *Phys. Med. Biol.* **47**, 4315 (2002).
18. B. W. Pogue, S. Jiang, H. Dehghani, C. Kogel, S. Soho, S. Srinivasan, X. Song, T. D. Tosteson, S. P. Poplack, and K. D. Paulsen, "Characterization of hemoglobin, water, and NIR scattering in breast tissue: analysis of intersubject variability and menstrual cycle changes," *J. Biomed. Opt.* **9**, 541 (2004).
19. B. W. Pogue and K. D. Paulsen, "High-resolution near-infrared to-

mographic imaging simulations of the rat cranium by use of *a priori* magnetic resonance imaging structural information," *Opt. Lett.* **23**, 1716 (1998).

20. R. L. Barbour, H. L. Graber, J. Chang, S. S. Barbour, P. C. Koo, and R. Aronson, "MRI-guided optical tomography: prospects and computation for a new imaging method," *IEEE Comput. Sci. Eng.* **2**, 63 (1995).

21. A. Li, E. L. Miller, M. E. Kilmer, T. J. Brukilaccio, T. Chaves, J. Stott, Q. Zhang, T. Wu, M. Choriton, R. H. Moore, D. B. Kopans, and D. A. Boas, "Tomographic optical breast imaging guided by three-dimensional mammography," *Appl. Opt.* **42**, 5181 (2003).

22. M. Schweiger and S. R. Arridge, "Optical tomographic reconstruction in a complex head model using *a priori* region boundary information," *Phys. Med. Biol.* **44**, 2703 (1999).

23. J. P. Kaipio, V. Kolehmainen, M. Vauhkonen, and E. Somersalo, "Construction of nonstandard smoothness priors," *Inverse Probl.* **15**, 713 (1999).

24. M. Vauhkonen, D. Vadasz, J. P. Kaipio, E. Somersalo, and P. A. Karjalainen, "Tikhonov regularization and prior information in electrical impedance tomography," *IEEE Trans. Med. Imaging* **17**, 285 (1998).

25. A. Borsic, W. R. B. Lionheart, and C. N. McLeod, "Generation of anisotropic-smoothness regularization filters for EIT," *IEEE Trans. Med. Imaging* **21**, 579 (2002).

26. X. Ouyang, W. H. Wong, V. E. Johnson, X. Hu, and C. Chen, "Incorporation of correlated structural images in PET image reconstruction," *IEEE Trans. Med. Imaging* **13**, 627 (1994).

27. V. Ntziachristos, A. G. Yodh, M. D. Schnall, and B. Chance, "MRI-guided diffuse optical spectroscopy of malignant and benign breast lesions," *Neoplasia* **4**, 347 (2002).

28. M. Glidewell and K. T. Ng, "Anatomically constrained electrical impedance tomography for anisotropic bodies via a twostep approach," *IEEE Trans. Med. Imaging* **14**, 498 (1995).

29. F. Dickin and M. Wang, "Electrical resistance tomography for process tomography," *Meas. Sci. Technol.* **7**, 247 (1996).

30. M. H. Loke, *Electrical Imaging Surveys for Environmental and Engineering Studies*, (1997). www.geo.mtu.edu/~ctyoung/LOKENOT.pdf

31. Q. Zhu, N. G. Chen, and S. H. Kurtzman, "Imaging tumor angiogenesis by use of combined near-infrared diffusive light and ultrasound," *Opt. Lett.* **28**, 337 (2003).

32. B. W. Pogue, H. Zhu, C. Nwaigwe, T. O. McBride, U. L. Osterberg, K. D. Paulsen, and J. F. Dunn, "Hemoglobin imaging with hybrid MR and diffuse optical tomography" in *Advanced Experiments in Medical Biology*, Ch. 21, pp. 215–224 (2003).

33. G. Gulsen, H. Yu, J. Wang, O. Nalcioglu, S. Merritt, F. Bevilacqua, A. J. Durkin, D. J. Cuccia, R. Lanning, and B. J. Tromberg, "Congruent MRI and near-infrared spectroscopy for functional and structural imaging of tumors," *Technol. Cancer Res. Treat.* **1**, 1 (2002).

34. B. A. Brooksby, S. Jiang, H. Dehghani, C. Kogel, M. Doyley, J. B. Weaver, S. P. Poplack, B. W. Pogue, and K. D. Paulsen, "Magnetic resonance-guided near-infrared tomography of the breast," *Rev. Sci. Instrum.* **75**, 5262–5270 (2004).

35. M. S. Patterson, B. C. Wilson, and D. R. Wyman, "The propagation of optical radiation in tissue II. Optical properties of tissues and resulting fluence distributions," *Lasers Med. Sci.* **6**, 379 (1991).

36. M. S. Patterson, B. C. Wilson, and D. R. Wyman, "The propagation of optical radiation in tissue I. Models of radiation transport and their application," *Lasers Med. Sci.* **6**, 155 (1991).

37. K. D. Paulsen and H. Jiang, "Spatially varying optical property reconstruction using a finite element diffusion equation approximation," *Med. Phys.* **22**, 691 (1995).

38. A. N. Tikhonov, "Regularization of mathematically incorrectly posed problems," *Sov. Math.* **4**, 1624 (1963).

39. H. Jiang, K. D. Paulsen, U. L. Osterberg, B. W. Pogue, and M. S. Patterson, "Optical image reconstruction using frequency-domain data: simulations and experiments," *J. Opt. Soc. Am. A* **13**, 253 (1996).

40. B. A. Brooksby, H. Dehghani, B. W. Pogue, and K. D. Paulsen, "Near-infrared tomography breast image reconstruction with a priori structural information from MRI: algorithm development for reconstructing heterogeneities," *IEEE J. Sel. Top. Quantum Electron.* **9**, 199 (2003).

41. T. O. McBride, B. W. Pogue, U. L. Osterberg, and K. D. Paulsen, *Oxygen Transport to Tissue XXIV*, p. 85 (2002).

42. G. Gindi, M. Lee, A. Rangarajan, and I. G. Zubal, "Bayesian reconstruction of functional images using anatomical information as priors," *IEEE Trans. Med. Imaging* **12**, 670 (1993).

43. B. A. Ardekani, M. Braun, B. F. Hutton, I. Kanno, and H. Iida, "Minimum cross-entropy reconstruction of PET images using prior anatomical information," *Phys. Med. Biol.* **41**, 2497 (1996).

44. J. E. Bowsher, V. E. Johnson, T. G. Turkington, R. J. Jaszczak, C. E. Floyd, and R. E. Coleman, "Bayesian reconstruction and use of anatomical a priori information for emission tomography," *IEEE Trans. Med. Imaging* **15**, 673 (1996).

45. C. Comtat, P. E. Kinahan, J. A. Fessler, T. Beyer, D. W. Townsend, M. Defrise, and C. Michel, "Clinically feasible reconstruction of 3D whole-body PET/CT data using blurred anatomical labels," *Phys. Med. Biol.* **37**, 1 (2002).

46. H. Xu, H. Dehghani, B. W. Pogue, R. Springett, K. D. Paulsen, and J. F. Dunn, "Near-infrared imaging in the small animal brain: optimization of fiber positions," *J. Biomed. Opt.* **8**, 102 (2003).

47. M. Torregrossa, C. V. Zint, and P. Poulet, "Effects of prior MRI information on image reconstruction in diffuse optical tomography," *Proc. SPIE* **5143**, 29–40 (2003).

48. X. Intes, C. Maloux, M. Guven, T. Yazici, and B. Chance, "Diffuse optical tomography with physiological and spatial *a priori* constraints," *Phys. Med. Biol.* **49**, N155 (2004).

49. K. D. Paulsen and H. Jiang, "Enhanced frequency-domain optical image reconstruction in tissues through total-variation minimization," *Appl. Opt.* **35**, 3447 (1996).

50. H. J. van Staveren, C. J. M. Moes, J. van Marle, S. A. Prahl, and M. J. C. van Gemert, "Light scattering in intralipid-10% in the wavelength range of 400–1100 nm," *Appl. Opt.* **30**, 4507 (1991).

51. A. E. Cerussi, A. J. Berger, F. Bevilacqua, N. Shah, D. Jakubowski, J. Butler, R. F. Holcombe, and B. J. Tromberg, "Sources of absorption and scattering contrast for near-infrared optical mammography," *Acad. Radiol.* **8**, 211 (2001).

52. S. Jiang, B. W. Pogue, T. O. McBride, M. M. Doyley, S. P. Poplack, and K. D. Paulsen, "Near-infrared breast tomography calibration with optoelastic tissue simulating phantoms," *J. Electron. Imaging* **12**, 613 (2003).

Spectral priors improve near-infrared diffuse tomography more than spatial priors

**Ben Brooksby, Subhadra Srinivasan, Shudong Jiang, Hamid Dehghani,
Brian W. Pogue, and Keith D. Paulsen**

Thayer School of Engineering, Dartmouth College, 8000 Cummings Hall, Hanover, New Hampshire 03755

John Weaver, Christine Kogel, and Steven P. Poplack

Department of Diagnostic Radiology, Dartmouth Hitchcock Medical Center, Lebanon, New Hampshire 03756

We compare the benefits of spatial and spectral priors in near-infrared diffuse tomography image reconstruction. Although previous studies that incorporated anatomical spatial priors have shown improvement in algorithm convergence and resolution, our results indicate that functional parameter quantification by this approach can be suboptimal. The incorporation of *a priori* spectral information significantly improves the accuracy observed in recovered images. Specifically, phantom results show that the maximum total hemoglobin concentration ($[Hb_T]$) in a region of heterogeneity reached 91% of the true value compared to 63% using spatial priors. The combination of both priors produced results accurate to 98% of the true $[Hb_T]$. When both spatial and spectral priors were applied in a healthy volunteer, glandular tissue showed a higher $[Hb_T]$, water fraction, and scattering power compared to adipose tissue. © 2005 Optical Society of America

OCIS codes: 110.3080, 110.6960, 170.3010, 170.3880.

In near-infrared (NIR) tomography, measurements of light remitted and transmitted through tissue, along with suitable mathematical models of light propagation, are used to obtain images of tissue constituents—total hemoglobin concentration ($[Hb_T]$), oxygen saturation (S_tO_2), water, and scatter. Qualitative, moderate-resolution images may be used to diagnose tumors based on their metabolic and functional status, but improvements in quantitative accuracy and resolution are still needed. Simulation studies and some phantom experiments have shown that anatomical information from other modalities such as magnetic resonance imaging (MRI), ultrasound, or x-ray tomosynthesis, when used in reconstruction procedures, can improve the stability of the estimation process and speed convergence to higher-resolution images.[1,2] However, priors corrupted by systematic errors and noise may bias property estimates. Brooksby *et al.*[3] encoded MRI priors into a regularization scheme, thereby relaxing the requirement that spatial constraints be error free. Phantom data at a single wavelength were used to show that quantitative accuracy and spatial resolution of optical property images could be improved without increasing the vulnerability to systematic errors. The net effect of such anatomical priors on quantitative spectroscopic accuracy is less clear.

Another type of prior incorporates the known spectral behavior of tissue chromophores and Mie scattering theory as constraints. This type of reconstruction uses multiwavelength measurements simultaneously to compute images of constituent parameters without intermediate recovery of optical properties. Corlu *et al.*[4] and Li *et al.*[5] applied the technique to continuous-wave data and showed images with improved parameter independence in simulations. Srinivasan *et al.*[6] extended the approach to the frequency domain and showed experimental evidence of

improved quantification. In this Letter, we compare this latter approach of spectral priors to spatial priors when applied to experimental and clinical data. Results show that (i) spatial priors improve image resolution but can underestimate the $[Hb_T]$ of a heterogeneity, (ii) spectral priors generate superior quantification of all estimated NIR parameters, and (iii) the use of the two together produces images that are quantitatively accurate and spatially superior.

Having obtained measurements at the periphery of the phantom or breast, image reconstruction is carried out by repeated solution of the diffusion equation using the finite-element method to estimate optical properties.[7] A Newton–Raphson method is used to minimize the least-squares functional $\chi^2 = \sum_{j=1}^{M}(\phi_j^m - \phi_j^c)^2$ for M measurements, where ϕ_j^m and ϕ_j^c are the measured and calculated fluence at the boundary, respectively. The optical property update, $\partial\mu$, is governed by the matrix equation $(\mathcal{J}^T\mathcal{J}+\alpha I)\partial\mu = \mathcal{J}^T\partial\phi$, where $\partial\phi=(\phi^m-\phi^c)$ and $\mathcal{J}=[\mathcal{J}_{\mu_a}, \mathcal{J}_\kappa]$ is the Jacobian containing the derivatives of ϕ^c with respect to the optical properties $\mu=(\mu_a, \kappa)$. Here, μ_a is the absorption coefficient, $\kappa=1/[3(\mu_a+\mu_s')]$ is the diffusion coefficient, and μ_s' is the reduced scattering coefficient. α, which is initially set to ten times the maximum value of $\mathcal{J}^T\mathcal{J}$ and reduced with each iteration, controls the regularization or smoothness applied. The linear system $\mu_a=[\varepsilon]c$ is then solved for the concentrations c of oxyhemoglobin, deoxyhemoglobin, and water, where ε is the molar absorption spectra of these chromophores. The Mie theory approximation, $\mu_s'=A\lambda^{-b}$, is used to derive images of scatter amplitude A and scatter power b, where λ is the wavelength in micrometers.

Incorporating spectral relationships into the reconstruction directly, the least-squares functional includes measurements at all (n) wave-
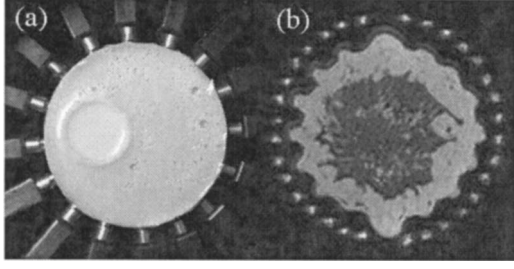
Fig. 1.   (a) Cylindrical breast phantom inside our NIR system. (b) Anatomically coronal MRI of a healthy breast imaged with our simultaneous NIR–MRI system. Two tissue types are visible: fibroglandular (dark gray) and adipose tissue (light gray).

lengths. The Newton method produces the relationship $\partial\phi_\lambda = \mathcal{J}_{c,\lambda}\mathrm{d}c + \mathcal{J}_{A,\lambda}\mathrm{d}A + \mathcal{J}_{b,\lambda}\mathrm{d}b$, where $\mathcal{J}_{c,\lambda}$, $\mathcal{J}_{A,\lambda}$, and $\mathcal{J}_{b,\lambda}$ represent the Jacobians for each of the chromophore and scattering parameters. With $(\widetilde{\mathcal{J}}^T\widetilde{\mathcal{J}} + \alpha I)\partial c = \widetilde{\mathcal{J}}^T\partial\phi$, where $\partial\phi = (\phi^{m,\lambda} - \phi^{c,\lambda})_{\lambda=1:n}$ and $\widetilde{\mathcal{J}} = [\mathcal{J}_{c,\lambda}, \mathcal{J}_{A,\lambda}, \mathcal{J}_{b,\lambda}]_{\lambda=1:n}$, the update occurs in terms of c, A, and b, directly.[6]

To introduce spatial constraints, the minimization functional is modified to include a penalty term, becoming $\hat{\chi}^2 = \Sigma_{j=1}^{Mn}(\phi_j^m - \phi_j^c)^2 + \beta\Sigma_{j=1}^{NN}L(\mu_j - \mu_{o,j})^2$, where β is the regularizing factor for the spatial prior, NN is the number of unknowns sought, and L is a matrix generated from MRI-derived spatial data acting on the solution μ. The L constructed here applies a second-derivative filter to all locations (nodes) in a particular tissue type (glandular or fatty), but not across internal boundaries, preserving sharp edges.[3] Setting the first derivatives of $\hat{\chi}^2$ with respect to each of the parameters sought equal to zero, the final matrix equation that is solved iteratively becomes $(\widetilde{\mathcal{J}}^T\widetilde{\mathcal{J}} + \beta L^T L)\partial c = \widetilde{\mathcal{J}}^T\partial\phi$. The effects of L and β on reconstructed μ_a and μ_s' images were characterized in simulation and phantom studies, accounting for measurement noise and error in the spatial prior.[3] Results indicate that setting β to ten times the maximum value of $\widetilde{\mathcal{J}}^T\widetilde{\mathcal{J}}$ optimizes image quality and accuracy regardless of the level of geometric complexity present.

A phantom and a clinical case study are presented here to evaluate these spectral and spatial constraints. Figure 1(a) shows a gelatin phantom placed inside our NIR imaging array. The gelatin properties include [Hb_T] = 23 μM, S_tO_2 = 72%, H_2O = 57%, A = 0.65, and b = 1.35. Near the edge is a 25 mm cylindrical cavity that was filled with Intralipid solutions with varying [Hb_T]. Figure 1(b) shows an anatomically coronal T1-weighted MRI of an asymptomatic volunteer imaged with our combined NIR–MRI system.[8] NIR measurements were acquired at six wavelengths (661, 761, 785, 808, 829, and 849 nm) for both the phantom and the clinical case.

Figure 2 (top row) shows the true properties of the phantom with an inclusion, along with images reconstructed with four algorithms. The first uses no priors—absorption and reduced scattering coefficients are reconstructed at each wavelength, then spectrally decomposed to produce images of the [Hb_T], S_tO_2, the water fraction, A, and b (second row). The second, third, and fourth algorithms incorporate spatial, spectral, and both spatial and spectral priors, respectively, and their images appear in the third, fourth, and fifth rows of Fig. 2. Spatial priors are derived from Fig. 1. The conventional method (no priors) yields images with considerable artifacts. Spatial priors remove these, so that the inclusion is clearly visible and matches the expected size and shape. However, the [Hb_T] contrast is significantly underestimated. The recovered mean in the region of the anomaly reaches only 57% of the true value (the maximum reaches 63% of the true value). Spectral priors show substantial improvement in the quantification with the mean [Hb_T] at 78% of the true value (maximum at 91%). Finally, the application of both constraints results in images with further reduction in artifacts close to the boundary, and the mean [Hb_T] reaches 88% of the expected value (maximum at 98%).

The experiment was carried further using four different blood concentrations in Intralipid solution as inclusions (22–43 μM [Hb_T], S_tO_2 = 100%, water = 100%, A = 0.65, b = 1.35). Figure 3 shows the mean property values recovered in the region of interest for each change in [Hb_T] by applying the four methods of reconstruction. As suggested in Fig. 2, although the standard deviation in the region of interest is reduced using spatial constraints (leading to smoother images), the values are underestimated and may even be degraded relative to the reconstruction without any priors. The spectrally constrained technique improves [Hb_T] accuracy, and including both priors gives the best results: accurate quantification along with reduced standard deviation.
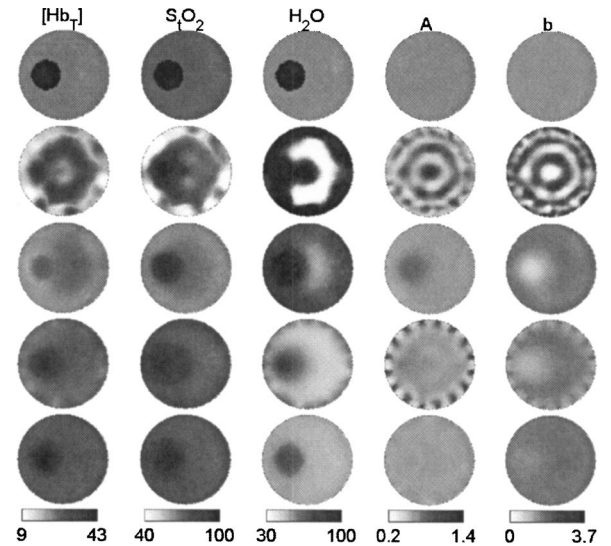

Fig. 2.   Images of total hemoglobin concentration (μM), oxygen saturation (%), water (%), scattering amplitude, and scattering power for the phantom. The top row shows the true values, the second shows the reconstruction that uses no priors, the third uses spatial constraints, the fourth uses spectral constraints, and the bottom uses both spectral and spatial priors.
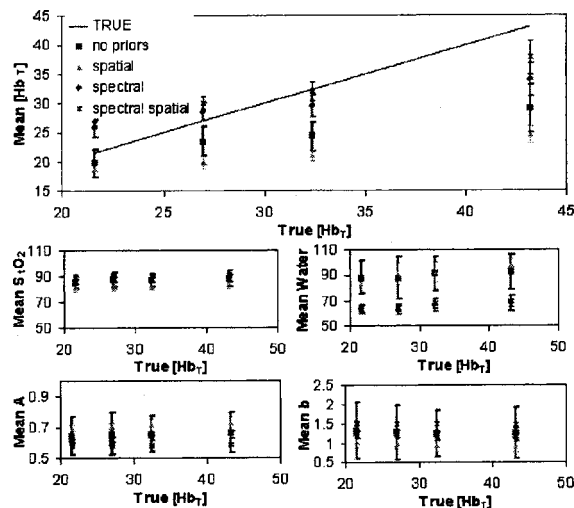
Fig. 3.   Mean reconstructed values of $[Hb_T](\mu M)$, S_tO_2 (%), water (%), A, and b, in the region of the inclusion using four algorithms. When the blood concentration is high, the best results are achieved by combining spectral and spatial priors. As expected, S_tO_2, water, A, and b within the cavity remain constant.
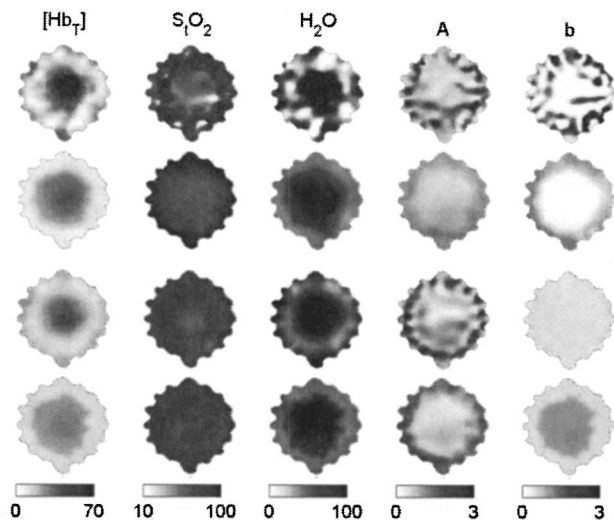

Fig. 4.   Breast property images for a healthy volunteer. First (top), only the outer boundary of the tissue and optical fiber positions are specified. Second, the algorithm used spatial constraints derived from the MRI [Fig. 1(b)] related to the internal distribution of adipose and glandular tissue. Third, spectral constraints were applied and chromophore concentrations and scattering parameters were reconstructed directly. Fourth (bottom), spatial and spectral constraints were combined.

Our combined NIR–MRI imaging system was used in a case study to estimate the properties of normal breast tissue. A finite-element method mesh generated from the MRI in Fig. 1(b) was used in the reconstruction. Using the MRI gray scale, each mesh point was associated with glandular or adipose tissue. Figure 4 shows the tissue properties estimated by the four procedures used in the phantom study. The images obtained using an unconstrained reconstruction exhibit boundary artifacts. The spatial priors make these images smoother but preserve the trends in chromophore and scattering quantification. Previous

studies suggest that glandular tissue has a higher number density of scatterers and may therefore have a greater scatter power than fat. Hence, the results from the spatially constrained reconstruction, although appearing smoother, may be misleading. The scatter power image obtained by the spectrally constrained method (row 3) is more quantitatively acceptable. Including the spatial priors within this spectral method (row 4) produces the most intuitively appealing image for this parameter by also showing the layered structure of the breast. We observed elevated $[Hb_T]$ (25:13 μM), water (91:49%), and scattering power (1.0:0.5) in glandular relative to adipose tissue by using the combined priors, which matches the higher degree of vascularization expected.

Intes *et al.*[9] and Li[10] showed in simulation studies that the combination of spatial and spectral priors improves the accuracy and quality of NIR images, but this Letter provides the first analysis, to our knowledge, of their individual benefits with experimental measurements. With our implementation, anatomical information improves image quality by reducing artifacts but does not significantly improve functional parameter quantification. The spectral prior obtained by including the intrinsic behavior of tissue chromophores and scattering plays a more important role in preserving quantitative functional parameter estimates. A synergy between these two priors yields the most accurate characterization of breast tissue properties currently available.

References

1. M. Schweiger and S. R. Arridge, Phys. Med. Biol. **44**, 2703 (1999).
2. V. Ntziachristos, A. G. Yodh, M. D. Schnall, and B. Chance, Neoplasia **4**, 347 (2002).
3. B. Brooksby, S. Jiang, H. Dehghani, B. W. Pogue, K. D. Paulsen, J. Weaver, C. Kogel, and S. P. Poplack, "Combining near infrared tomography and magnetic resonance imaging to study *in vivo* breast tissue: implementation of a Laplacian-type regularization to incorporate MR structure," J. Biomed. Opt. (to be published).
4. A. Corlu, T. Durduran, R. Choe, M. Schweiger, E. M. Hillman, S. R. Arridge, and A. G. Yodh, Opt. Lett. **28**, 2339 (2003).
5. A. Li, Q. Zhang, J. P. Culver, E. L. Miller, and D. A. Boas, Opt. Lett. **29**, 256 (2004).
6. S. Srinivasan, B. W. Pogue, S. Jiang, H. Dehghani, and K. D. Paulsen, Appl. Opt. **44**, 1858 (2005).
7. K. D. Paulsen and H. Jiang, Appl. Opt. **35**, 3447 (1996).
8. B. A. Brooksby, S. Jiang, H. Dehghani, C. Kogel, M. Doyley, J. B. Weaver, S. P. Poplack, B. W. Pogue, and K. D. Paulsen, Rev. Sci. Instrum. **75**, 5262 (2004).
9. X. Intes, C. Maloux, M. Guven, T. Yazici, and B. Chance, Phys. Med. Biol. **49**, N155 (2004).
10. A. Li, "Diffuse optical tomography with multiple priors," Ph.D. dissertation (Tufts University, 2005).

Near-Infrared Characterization of Breast Tumors *In Vivo* using Spectrally-Constrained Reconstruction

www.tcrt.org

Subhadra Srinivasan, Ph.D.[1,*]
Brian W. Pogue, Ph.D.[1,*]
Ben Brooksby, Ph.D.[1]
Shudong Jiang, Ph.D.[1]
Hamid Dehghani, Ph.D.[1]
Christine Kogel, R.N.[2]
Wendy A. Wells, M.D.[3]
Steven P. Poplack, M.D.[4]
Keith D. Paulsen, Ph.D.[1]

[1]Dartmouth College
Thayer School of Engineering
Hanover, New Hampshire 03755, USA
[2]Dartmouth Hitchcock Medical Center
Norris Cotton Cancer Center
Lebanon, New Hampshire 03756, USA
[3]Department of Pathology
Dartmouth Hitchcock Medical Center
Norris Cotton Cancer Center
Lebanon, New Hampshire 03756, USA
[4]Department of Radiology
Dartmouth Hitchcock Medical Center
Norris Cotton Cancer Center
Lebanon, New Hampshire 03756, USA

Multi-wavelength Near-Infrared (NIR) Tomography was utilized in this study to non-invasively quantify physiological parameters of breast tumors using direct spectral reconstruction. Frequency domain NIR measurements were incorporated with a new spectrally constrained direct chromophore and scattering image reconstruction algorithm, which was validated in simulations and experimental phantoms. Images of total hemoglobin, oxygen saturation, water, and scatter parameters were obtained with higher accuracy than previously reported. Using this spectral approach, *in vivo* NIR images are presented and interpreted through a series of case studies (n=6 subjects) having differing abnormalities. The corresponding mammograms and ultrasound images are also evaluated. Three of six cases were malignant (infiltrating ductal carcinomas) and showed higher hemoglobin (34-86% increase), a reduction in oxygen saturation, an increase in water content as well as scatter changes relative to surrounding normal tissue. Three of six cases were benign, two of which were diagnosed with fibrocystic disease and showed a dominant contrast in water, consistent with fluid filled cysts. Scatter amplitude was the main source of contrast in the volunteer with the benign condition fibrosis, which typically contains denser collagen tissue. The changes monitored correspond to physiological changes associated with angiogenesis, hypoxia and cell proliferation anticipated in cancers. These changes represent potential diagnostic indicators, which can be assessed to characterize breast tumors.

Introduction

Near-Infrared (NIR) imaging of tissue can potentially provide quantitatively accurate estimates of physiologically important parameters such as hemoglobin, oxygen saturation, water fraction, lipid fraction, and scattering indices (1-6). However, past approaches to NIR tomography have suffered from using too few wavelengths, and simplistic strategies for spectral deconvolution. More recently there have been significant breakthroughs in the development of algorithms which incorporate the underlying multispectral constraints available from chromophore extinction spectra within the image reconstruction process (7-10). In this paper, an optimized direct spectral reconstruction technique is implemented and evaluated in phantoms and initial patient studies to demonstrate the potential benefits of this algorithmic approach. The major benefits of direct spectral reconstruction are well established (9, 10) and have shown to lead to improvements in the accuracy of quantification of oxygen saturation, water fraction, and scattering parameters. The importance of improved accuracy in these parameters is significant, because they provide fundamental metabolic information about tissue which is not currently being obtained with any other imaging modalities.

The value of oxygen saturation in particular could be significant, if sufficient accuracy can be achieved in estimating this parameter with an imaging method.

* Corresponding Authors:
Subhadra Srinivasan, Ph.D.
Email: subha@dartmouth.edu
Brian W. Pogue, Ph.D.
Email: pogue@dartmouth.edu

Tissue hypoxia is found in breast cancers due to metabolic imbalance between oxygen supply and consumption (11), which has significant potential in diagnosis as well as prognosis for radiation treatment. On average, the mean partial pressure of oxygen (pO_2) is lower in malignancies than in surrounding tissues (typically $\leq$ 20mm Hg) (11). This presents a difficult situation for radiotherapy which is ineffective when pO_2 is less than 5mm Hg (12). Tumor oxygenation may serve to predict its response to radiation treatment as suggested by its critical role in modifying the dose response curve (13) and may also be related to the likelihood of occurrence of distant metastases as well (14). Vaupel *et al*. (15) have shown that although hypoxia did not correlate with tumor size, tumor location, grade or stage, it did depend critically on whole blood hemoglobin levels; even mild anemia in breast cancer subjects causes the development of hypoxia. Pretreatment hemoglobin levels (16) can also aid in predicting tumor response to primary chemotherapy. While the hemoglobin levels referred to here were baseline values, those measured by NIR imaging for the normal tissue surrounding the tumor may also be representative of the oxygen carrying capacity of the blood in the breast.

Conover *et al*. (17) used NIR spectroscopic measurements *in vivo* on subcutaneous rat mammary adenocarcinomas to show correlation with cryospectrophotometry estimates of oxygen saturation on rapidly frozen sections of the same tumors. These studies suggested that NIR may be able to detect hypoxic regions even when their distribution occurs on a spatial scale that is beyond the resolution limit of NIR. Tromberg *et al*. (18) observed a decrease in oxygen saturation in spectroscopic studies on a palpable mass diagnosed as ductal carcinoma *in situ* (DCIS). In a related study which monitored neoadjuvant chemotherapy using spectroscopy (19), they found an initial tissue oxygen saturation decrease in the lesion with respect to the surrounding tissue followed by a slight peak, when tracked over a ten week course of treatment. Spectroscopic methods, however suffer from over-sampling of the superficial bulk tissue, which while suitable for palpable tumors, may misrepresent spatial changes in deeper lesions. Tomographic imaging methods sample more broadly and provide a better representation of the whole breast volume. In a study (20) using time domain instrumentation with two wavelengths and a water contribution fixed at 30%, lower oxygen saturation was observed in images of two carcinomas. Heffer *et al*. (21) used an 'oxygenation index', generated from frequency domain measurements, to show a decrease in carcinomas. In previous work at Dartmouth, McBride *et al*. (22) used an NIR tomography system to image a subject with a 2.5 cm infiltrating ductal carcinoma, and although an increase in hemoglobin was observed, reduction in oxygen saturation was not found. Dehghani *et al*. (23) used three-dimensional modeling to obtain tomographic images from a patient with a infil-

trating ductal carcinoma and reported an increase in blood oxygen saturation level, contrary to expectation. Grosenick *et al*. (24) surveyed results from 50 carcinomas using a dual wavelength time domain instrument and showed good separation of tumors from healthy tissue based on total hemoglobin. However, in their study oxygen saturation both increased and decreased at the location of tumors such that no clear hypoxic trend was evident.

Thus, it appears that without direct spectral reconstruction, the accuracy of predicting oxygen saturation values may be diminished. In this paper, the spectrally constrained direct chromophore and scattering reconstruction which has been shown to be quantitatively superior and stable to measurement and image noise in homogeneous phantom measurements (9) and simulations (25), is validated further in experiments and is applied to the study of breast lesions.

Another NIR parameter of significant interest is scattering. Optical scattering has been correlated to mammographic density (26), which is a major risk factor in the development of cancer (27). A recent study (28) to assess NIR transillumination spectroscopy as related to mammographic density and cancer risk, showed that optical spectroscopy predicted the radiological assessment of density with a principal components analysis (PCA) model in the range of 90% with an odds ratio comparable to mammography. In breast cancer locations, scattering is certainly expected to increase because the tumor cells stimulate endothelial cell proliferation (29), which increases the cellular density. In addition, the tortuous tumor vessel network is held together by dense fibrotic connective tissue (30), which may be optically dense, owing to the presence of different sized scatterers relative to the surrounding tissue. Spectroscopic studies have shown this increase in scattering in a palpable carcinoma (31). In this paper, scattering is analyzed from the region of the tumor, as detected in the tomographic images obtained through spectrally constrained direct reconstruction.

Methods and Materials

Imaging System

All patients were imaged with a multi-wavelength frequency domain instrumentation system [documented earlier (32)] which collects amplitude and phase measurements of light reflectance, after passing signals through the pendant breast at five or six wavelengths in the near infra-red range. The wavelengths were specifically, 661, 761, 785, 808, 826, and 849 nm and the use of five wavelengths excluded the availability of 849 nm. The imager is designed for a non-compressive, cross-sectional breast exam (using data from three planes spaced 1 cm apart) involving 240 measurement points in each slice at each wavelength acquired with a configura-

tion of 16 sources and 15 detectors. The measurements are calibrated to compensate for system offsets and an initial estimate close to the bulk background tissue properties is obtained from a homogeneous calculation of the diffusion equation for the relevant breast size.

A finite-element model to the diffusion approximation for the radiative transfer equation, is used for image reconstruction to simulate the way that photons diffuse through tissue due to the multiple scattering processes that occur as they travel (33, 34). Studies have shown that this model allows reasonable separation of the absorption and scattering processes of light within tissue (35) and has been utilized in reconstruction algorithms to produce images of absorption and reduced scattering coefficients (μ_a, μ_s', respectively). A Newton-Raphson iterative scheme for minimization of measured and model-calculated data, along with Levenberg Marquardt regularization have been utilized to obtain these images. This followed by spectral fitting has been termed as the "conventional" method of image recovery, in this work. This model for image reconstruction was recently extended to incorporate spectral *a priori* information related to the behavior of the absorbers and scatterers as a function of wavelength (9). Assuming the main absorbers in the tissue are oxy-hemoglobin (HbO$_2$), de-oxyhemoglobin (Hb) and water (within this wavelength band) and knowing their molar absorption spectra (absorption per unit concentration) at the six wavelengths, it is possible to calculate each of their contributions to the absorption using Beer's law:

$$\mu_a(\lambda) = \sum_{i=1}^{3} \varepsilon_i(\lambda) c_i \qquad [1]$$

where ε_i is the molar absorption spectra of the ith chromophore at wavelength λ and c_i is the chromophore's concentration. In this way, images of these chromophores as well as extended indices given by Hb$_T$ = HbO$_2$ + Hb (in μM), and oxygen saturation as S$_t$O$_2$ = HbO$_2$/ Hb$_T$ × 100 (in %) can be obtained from the absorption images.

An empirical approximation to scattering behavior predicted by Mie theory for particles approaching sizes larger than the wavelength was introduced by Van Steveran (36) and Mourant *et al.* (37) and has been in several studies to derive associated parameters. The relationship is given by:

$$\mu'_s(\lambda) = a\lambda^{-b} \qquad [2]$$

This fit can be used to estimate scatter amplitude (*a*) and power (*b*) images with wavelength in μm, based on μ'_s images at the six wavelengths obtained from the image reconstruction. The coefficient μ'_s has units mm^{-1} and *b* is dimensionless so that *a* has units given by 10^{-3b}(mm)$^{b-1}$. Scattering power is governed by the shape or slope of scat-

tering which is predominantly affected by the size distribution of membrane bound scatterers within tissue (38, 39); the amplitude relates to the number density of these scatterers. Together, these two parameters may reflect variations in breast structural composition due to different sub-cellular organelle and ultra-structural sizes/densities within the fatty, fibroglandular, collagen, and epithelial tissue compartments.

Relationships from Equations [1] and [2] form the basis of the "spectral approach" to image reconstruction: this involves direct recovery of images of the concentrations of HbO$_2$, Hb, water, scatter amplitude, and power by coupling multi-wavelength measurements together. This approach also uses the Newton's method along with the Levenberg-Marquardt regularization, but now the minimization includes all wavelengths' measurements. The technique reduces the total number of unknown parameters in the image reconstruction (from number of wavelengths times optical properties to overall five parameters) and makes the inverse problem better posed by increasing the stability to noise in the measured data. The initial guesses for the functional parameters are set using a constrained least squares fit on the initial optical properties; the optical properties were in turn obtained using a homogeneous fitting algorithm where data was averaged over all source positions and the assumption of a homogeneous medium was used on the circular mesh. Details can be found elsewhere (23). Optimized in terms of obtaining initial estimates of the parameters, regularization, convergence criteria, filtering, and to allow for best calibration procedure for data; and validated in homogeneous imaging fields and simulations (9, 25), this method is further evaluated here in experimental phantom measurements where the results indicate that higher qualitative and quantitative accuracy as well as reduced cross-talk between the functional parameters is achieved.

Human Subjects

As part of a clinical trial to investigate alternate imaging modalities for diagnosis of breast cancer, NIR imaging was carried out on women with mammographically-detected abnormalities. All clinical work was approved by the institutional committee for the protection of human subjects at Dartmouth, and informed consent was obtained from all participants. The women were imaged in the prototype NIR tomography system at the Dartmouth Hitchcock Medical Center (DHMC). The mammograms were interpreted by a radiologist specializing in breast imaging (S.P.P.). The clinical information utilized in the study included the radiographic density, the location of the tumor and its size, in addition to architectural features. The breast radio-density was categorized according to the BI-RADS system (40) as classifications of (i) almost entirely fat, (ii) scattered fibroglandular tissue, (iii) heterogeneously dense, or (iv) extreme-

ly dense. Pathologic studies were completed following biopsy (WAW) to provide tumor histologic type, grade, and size. In addition, using reproducible, computer-assisted image processing methodology described elsewhere (41), the mean vessel density of the tumor and the ratio of malignant epithelium to surrounding stroma (epithelial to stroma ratio) were also assessed. The results from six women with breast tumors, three of which were diagnosed as infiltrating ductal carcinomas, one with fibrosis, and two with fibrocystic disease; were analyzed here using the spectrally constrained direct chromophore and scattering reconstruction. The contrast between the tumor and background was documented along with interpretation of the images and their correlation to mammography, pathology, and the physiology of the different types of cancers.

Results

Application to Heterogeneous Experimental Measurements: Phantom Study

In order to test the spectrally-constrained image reconstruction approach on experimental measurements in a heterogeneous geometry, a cylindrical phantom consisting of gelatin with whole blood added for absorption and Titanium dioxide for scatter was made. Two such gelatin phantoms with a diameter of 8.2 cm were obtained from the same mixture, one of which was maintained in its homogeneous state, and the other had a 2.5 cm cylindrical hole drilled to have its boundary 1 cm from the external boundary. This hole was filled with a saline solution containing 4% pig blood (the hematocrit level of the blood was measured by a clinical co-oximeter so that 4% blood = 43.2 μM total hemoglobin) with 0.75% Intralipid for scattering. The background chromophore concentrations and scatter for the gel were determined by imaging the phantom in its homogeneous state and using the mean from the reconstructed NIR images, ignoring contributions close to the boundary (taken empirically to be

12% of the total diameter); earlier experiments have shown that concentrations obtained this way are quantitatively accurate (9). The inclusion had a contrast of nearly 2:1 in total hemoglobin and was expected to have 100% oxygen saturation and water content. The scattering images were expected to be almost homogeneous because 0.75% Intralipid was measured to be similar in scattering quantitatively to the background gelatin in the phantom. Amplitude and phase data were collected on this heterogeneous phantom at the six wavelengths and image reconstruction was carried out using both the conventional technique of separate wavelength reconstruction as well as the spectrally-constrained procedure. The top row in Figure 1 shows true images for the five NIR parameters, followed by the images generated with the spectrally-constrained reconstruction and the images from the conventional technique (in the bottom-most row).

The images obtained with the spectrally constrained reconstruction are qualitatively much smoother and more accurate than their conventional counterparts. The simultaneous use of six wavelengths of data along with the spectral priors makes the inverse problem better posed and this along with the parameter reduction procedure provides the smoothness in the spectral images. Images from the conventional technique have more spatial artifacts, including higher cross-talk between oxy-hemoglobin and water, which have similar spectral behavior, resulting in under-estimation of total hemoglobin in the anomaly and saturation of water. In order to obtain the mean, peak, and standard deviation in the anomaly, a FWHM regionization was performed on the images, using the total hemoglobin image for the spectral method and the oxygen saturation image for the conventional technique. While the peak in total hemoglobin still reaches 98% of the true value, the mean in the anomaly is lower (80.6%) with significant standard deviation (~ 10% of the mean). The scatter images from the conventional method suffer from a ring-type artifact, which arises from the difficulty in separating the two scatter parameters. This results in
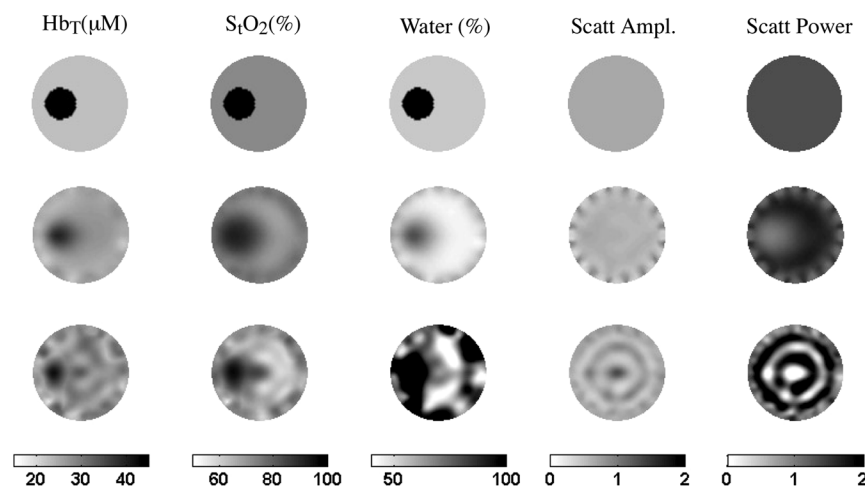

Figure 1: Comparison of images obtained with the spectrally constrained direct chromophore reconstruction and the conventional technique of independent optical property at separate wavelengths recovery on measurements from a gelatin phantom (8.2 cm total size) with a 2.5 cm inclusion. The gelatin phantom contained whole blood and TiO_2 for scattering and the inclusion was filled with 4% pig blood and 0.75% Intralipid in buffered saline. The expected images are shown in the top row for Hb_T (μM), oxygen saturation (%), water (%), scatter amplitude, and scatter power. The spectral method images appear in the second row while conventional technique images are located in the bottom-most row.

high standard deviation in the images, close to 25% of the mean for scatter amplitude and 82% of the mean for scatter power in the anomaly region. This has been circumvented in the spectrally constrained reconstruction through prior information related to scattering, providing well-defined limits for scatter amplitude and power. The standard deviation is now reduced to 2.3% of the mean for scatter amplitude and 7% for scatter power. The mean of the scatter amplitude in the anomaly region is quantitatively accurate with a mean error of 3.3% (reduced from 7% for the conventional method); and similarly for scatter power, the mean error is reduced to 19% from 32.4% for the conventional technique.

The spectral shapes of oxy-hemoglobin and water embedded into this reconstruction minimizes the crosstalk between these parameters and provides accuracy in total hemoglobin in the anomaly within 91.6% of expected value for the peak and within 84% for the average and standard deviation reduced by almost half, to 4.83% of the mean. Water content has been underestimated by 20.3% using the spectral method. This may be due to the steep difference in background and anomaly water content (typically not observed in a patient), making it difficult to recover the high contrast in the anomaly. A possible solution to improving the accuracy of water content is the use of data in the longer wavelength range (850-1000 nm). This strategy has been examined in simulations (not shown here), which will incorporate stronger features of water.

Variation of Hemoglobin and Scattering

In order to investigate the response of the spectrally-constrained algorithm to changes in total hemoglobin, the inclusion's blood concentration was varied systematically from 20 to 44 μM and measurements at six wavelengths were taken. The resulting images for total hemoglobin recovered using the spectral priors are shown in Figure 2, along with a comparison to the images obtained from the conventional technique and the expected images.

The images presented in Figure 2 are consistent with those reported from previous experiments and simulations. Specifically, the spectral reconstructions now not only appear smoother but also follow the variation in Hb_T more accurately than the conventional method without the use of priors. The mean and standard deviation for all NIR parameters in the region of the inclusion were obtained using a FWHM segmentation procedure on the total hemoglobin image. In this calculation, the anomaly was defined as the region containing hemoglobin values above a threshold (midway between the maximum and average of the values for the image). The mean in the anomaly recovered from the spectral method tracked the change in blood concentration with an average error of 12.3%. The other parameters remained constant through this change with a lower standard deviation for the spectral method (<5% overall compared to 23.5% for the conventional method, as percent of the mean).

Imaging the effect of scattering was similarly examined by varying the Intralipid concentration in the 25 mm inclusion in the gelatin phantom from 0.75% to 1.75% in steps of 0.25%; while keeping the total hemoglobin concentration fixed. This change results in an increase in the number density of scatterers while their size remains the same. The Mie theory approximation to scattering behavior in the regime where scatterer size is comparable to the wavelength, predicts that the number density only changes the magnitude of the scattering coefficients, but not the spectral shape or scatter power parmeter (38). This means that an increase in Intralipid concentration translates to a change in scatter amplitude with scatter power remaining the same. The images for scatter amplitude following the change in Intralipid percentage are shown in Figure 3 for the spectrally constrained procedure. Images obtained from the conventional method and the
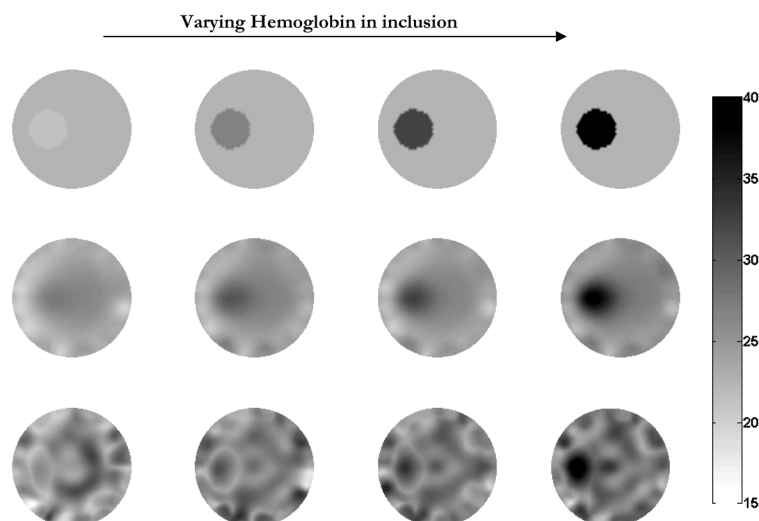
Varying Hemoglobin in inclusion

Figure 2: Images of a gelatin phantom whose inclusion Hb_T concentration was varied from 20-44 μM. Top row shows true images for Hb_T. Images obtained by application of spectral priors appear in second row while the bottom row contains the images resulting from the conventional technique. The images for all other parameters (oxygen saturation, water and scatter) remained nearly constant with the Hb_T change.
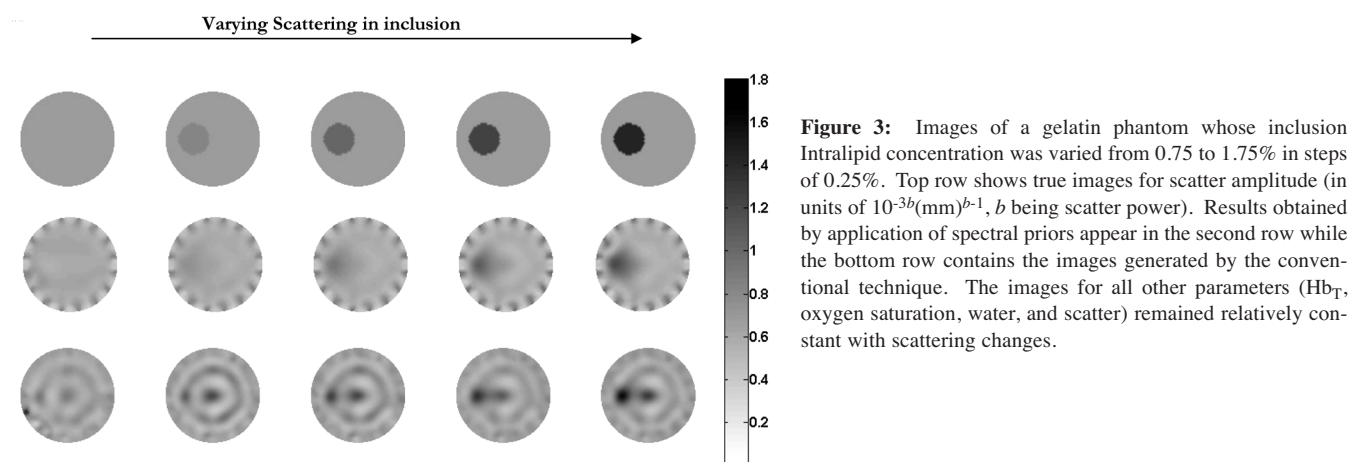
Varying Scattering in inclusion

Figure 3: Images of a gelatin phantom whose inclusion Intralipid concentration was varied from 0.75 to 1.75% in steps of 0.25%. Top row shows true images for scatter amplitude (in units of $10^{-3b}(mm)^{b-1}$, b being scatter power). Results obtained by application of spectral priors appear in the second row while the bottom row contains the images generated by the conventional technique. The images for all other parameters (Hb$_T$, oxygen saturation, water, and scatter) remained relatively constant with scattering changes.

expected images are also included. The expected values were obtained from the homogeneous experimental results.

While the images for both the spectral and conventional methods in Figure 3 reveal a localized increase in scatter amplitude in the region of the anomaly, the conventional method generates a ring type artifact found in Figure 1, potentially due to coupling with scatter power. This makes it difficult to discern the inclusion in the conventional images for the first three contrast changes in the experiment. The effect is eliminated in the spectrally reconstructed images, which exhibit a smoother variation with change in scattering. Artifacts close to the boundary exist in the spectral scattering images and this may illustrate the need for increased regularization compared to the other parameters in the direct reconstruction. Scatter amplitude reconstructed using the direct spectrally constrained procedure was found to follow the variation in Intralipid percentage successfully with a mean error of 17.6%. Here, the error increased from 3% at the lower Intralipid percent to 27.5% at higher Intralipid concentrations due to scattering. Scatter power stayed constant as expected, with a mean value of 1.19±0.16 for the conventional reconstruction procedure and 1.23±0.03 from the spectral method, both of which are comparable to the expected value of 1.4 from van Staveren *et al*. (36). The total hemoglobin, oxygen saturation and water content remained approximately constant with scattering variation, as expected.

Imaging of Infiltrating Ductal Carcinomas (IDCs) (Case Studies 1-3)

Case Study 1: NIR tomographic images were obtained from a 73-year-old female volunteer (patient ID #1035) with breast cancer. The left craniocaudal and magnified close-up mediolateral views (22) of the mammogram are shown in Figures 4(a) and (b). They revealed a peripherally located spiculated mass of size 2.5 cm (maximum focal diameter) at 2:30 in clock face position with architectural distortion occurring

over a much larger area (up to 6 cm). The patient also went through ultrasonography which confirmed the existence of a hypoechoic irregular mass in the same location. Multiple simple cysts were also evident. Following a 1.1 cm core needle biopsy, the tumor was diagnosed as infiltrating ductal carcinoma with lobular features. The subject underwent the NIR clinical exam two weeks after the biopsy; the images obtained by applying spectrally constrained reconstruction, along with the conventional method of recovering the optical properties at separate wavelengths, are shown in Figure 4(c). The mid-plane (marked to contain the tumor) measurements at five wavelengths, excluding 849 nm, were used and the breast diameter was 10.4 cm corresponding to this plane. The breast density was categorized as heterogeneously dense (category 3) and pathological examination of the tumor through the biopsy sample revealed a vessel density of 0.9%.

The total hemoglobin image obtained from the spectral reconstruction shows a localized increase at the site of the tumor along with a reduction in oxygen saturation. The oxygenation decrease, an indication of an hypoxic situation in the tissue, is not observable in the images from the conventional method. This finding is consistent with results generated from simulated data (with 1% random Gaussian noise) (25) and other experiments which showed that the spectral method is quantitatively and qualitatively superior when tracking a change in oxygenation. Imaging of the tumor oxygenation response is a strong indicator of the potential of NIR tomography to study hypoxic fractions in malignancies. The increase in hemoglobin is consistent with earlier studies (2) and the theory that angiogenic activity results in increased vascularity (29, 30). The conventional method shows higher values for total hemoglobin in the tumor, compared to the spectral method, with the water content saturating in most of the image, at 100%. Corlu *et al*. (9, 10) have also reported this trend in a carcinoma, indicating a false-increase in hemoglobin with the conventional technique, possibly due to a cross-talk between oxy-hemoglobin and water. The water image using the conventional method

shows significant artifacts; however, the artifacts are removed in the spectral method in which case water shows a clear increase at the location of the tumor. This is consistent with the expected physiological changes in a tumor which include a leaky vasculature formed in the process of angiogenesis that is responsible for creating an interstitium containing inflammatory cells, fibroblasts, and other enzymes facilitating cell growth (29).

The scatter images from the conventional method are more artifacts-ridden with abnormally high values for amplitude at certain locations as well as negative values for power, that do not correspond to the scattering model predictions. However, with the spectral approach, both scatter amplitude and power show a localized increase at the site of the tumor. Scatter amplitude from the Mie theory approximation, is found to be more sensitive to the number density of the scatterers whereas their size is usually governed by the slope of scattering or the scatter power (38). Hence, we expect the change in scatter amplitude due to cell proliferation to be more localized than scatter power. The contrast in scatter power is possibly due to fibrosis occurring in malignancies which explains the increased optical density.
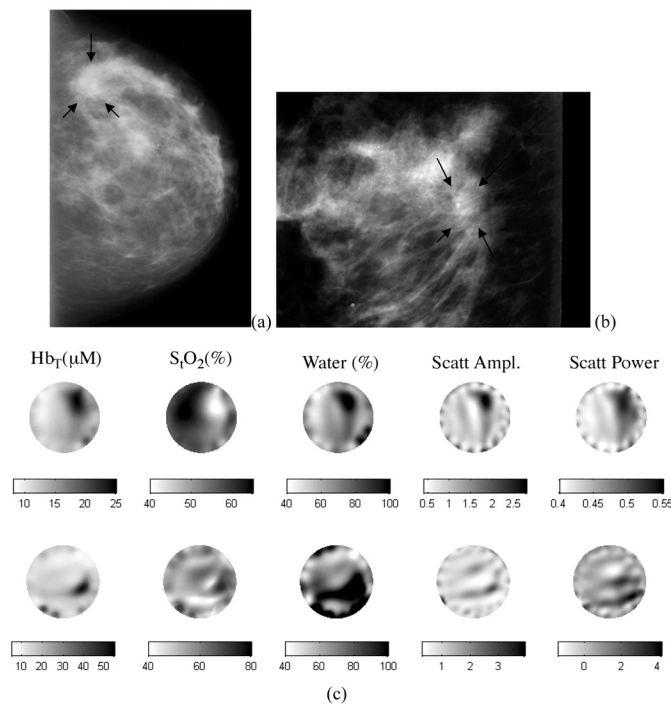
It is evident that the images from the spectrally constrained reconstruction show physiological changes more clearly, with undeniable improvement in image quality. The accuracy of the method has already been validated and henceforth only the spectral method is used to analyze breast cancer images presented. Based on the five NIR parameter images from the top row in Figure 4(c), the average in the tumor and the background were obtained from a FWHM criterion applied to the total hemoglobin image. This ensures that the tumor size, while close to the true size, is specific to the NIR imaging modality and defined accordingly. The criteria has been applied successfully in earlier studies (42). Figure 5 shows the results when the approach is applied to the images above from the spectrally constrained reconstruction. The total hemoglobin increased to a maximum of 24.5 μM in the tumor, while the background had a mean of 13.2 μM, resulting in an increase by 86% in tumor versus surrounding tissue. A decrease in oxygen saturation was observed at the location of the tumor reducing by nearly 13% from an average of 56.4% in the background to 43.6% in the tumor. Water showed an average increase of up to 89% in the cancer relative to 65% in the background, which may also be due to the existence of the cysts found in the sonogram. The tumor also showed a contrast of nearly twice that of scatter amplitude (mean of 0.98 in the background to 2.0 in the tumor). The contrast in scatter power was less pronounced, though an increase in tissue density at the cancer location could still be observed.
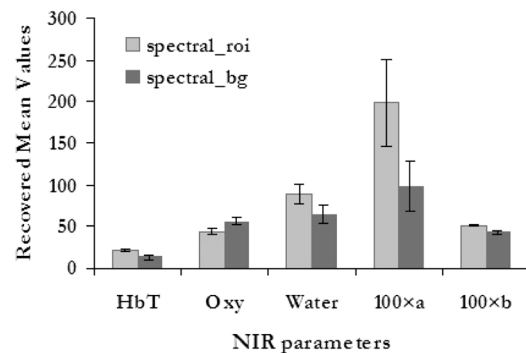

Figure 4: (**a**) left craniocaudal mammogram and (**b**) magnified close-up mediolateral mammogram (22) from the left breast of a 73-yr-old woman with a 2.5 cm spiculated mass (marked with black arrows) diagnosed as infiltrating ductal carcinoma by core-needle biopsy. (**c**) top row shows images for Hb_T(μM), S_tO_2 (%), water (%), scatter amplitude, and scatter power obtained using the spectrally constrained direct chromophore reconstruction; bottom row shows the images of the same using the conventional separate wavelength approach. Images in top row correspond well with tumor location (given as 2:30 clock face position, close to the periphery) from the mammogram.

Figure 5: The average for the five NIR parameters along with standard deviation in the region of the tumor and the background (for the patient corresponding to Figure 4). The tumor was defined by segmentation of the images obtained from the spectrally constrained direct chromophore reconstruction using the FWHM criterion. The tumor exhibits increases in total hemoglobin (Hb_T), water, and scatter with decreases in oxygenation, compared to the surrounding tissue.

Case Study 2: In the second case, the NIR clinical examination was carried out on a 37-year-old female volunteer (patient ID# 1077) to image a palpable mass. Mammography revealed a 3 cm irregular lesion centrally located at the 6:30 clock face position, with ill-defined margins in both the left craniocaudal and left mediolateral oblique mammograms [left craniocaudal mammogram and magnified view are shown in Figures 6(a) and (b)]. The tumor was 5 cm from

the chest wall. The patient underwent ultrasonography which showed a solid mass larger than 5 cm in size [Figure 6(c)]. The tumor was confirmed by a biopsy to be an infiltrating ductal carcinoma. Pathology studies on the resected specimen indicated a vessel density of 0.74%. The radiographic classification of the breast was heterogeneously dense. The amplitude and phase data were obtained from the periphery of both breasts and the measurements at five wavelengths (excluding 849 nm) from the tumor-bearing left breast were used by the spectral reconstruction to provide the tomographic images shown in Figure 6(d) for the lowest plane closest to the nipple, where the breast diameter was 8.5 cm.

(a)

(b)

(c)

Hb$_T$(μM)   S$_t$O$_2$(%)   Water (%)   Scatt Ampl.   Scatt Power

25 30 35 40   50 60 70   80 90 100   0.5 1 1.5   0.35 0.4 0.45

(d)
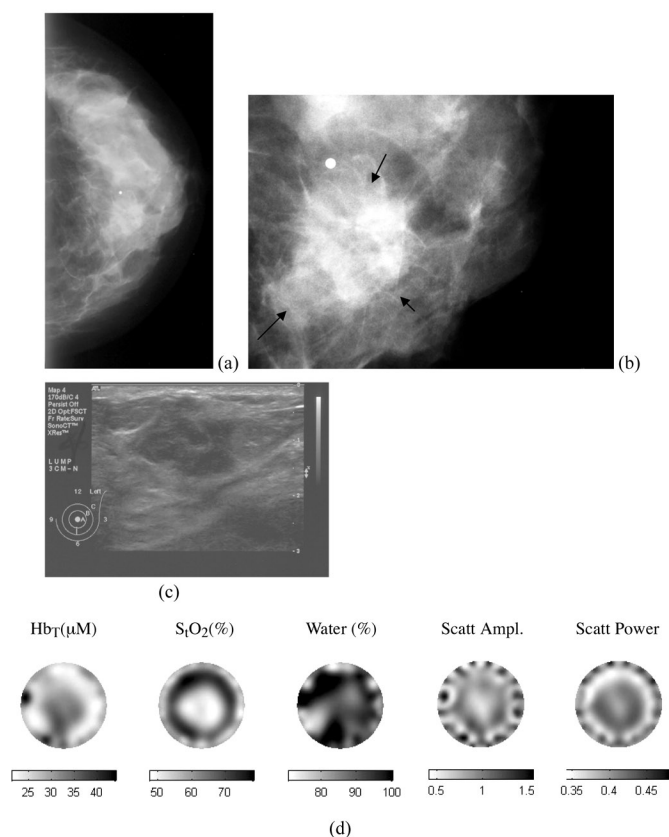
Figure 6: (**a**) left craniocaudal mammogram, (**b**) magnified view of mammogram, and (**c**) ultrasound images from the left breast of a 37-yr-old woman with a 3 cm irregular mass (indicated with black arrows) centrally located at 6:30 on the clock face; diagnosed as infiltrating ductal carcinoma through biopsy. (**d**) images for Hb$_T$(μM), S$_t$O$_2$ (%), water (%), scatter amplitude, and scatter power obtained using the spectrally constrained direct chromophore reconstruction. The tumor is most clearly visible in the Hb$_T$ image.

A localized increase in total hemoglobin was found in the location given by the mammogram, increasing to a peak of 37 μM in the tumor. Oxygen saturation showed a decrease with respect to the breast background reducing to a minimum of 47.4%, consistent with the prediction of hypoxia in malignancies. A contrast in water was also observed, increasing at the site of the cancer. Scattering did not change appreciably at the cancer site, though the cross-section

reveals a mild peak (increasing to 1.1 with respect to a background minimum of 0.5). The lack of a higher contrast in scatter may be due to the fact that the subject was younger in age and had a radiographically dense breast (category 3) so that scattering in general is high.

Figure 7 shows the mean and standard deviation for all five reconstructed parameters in the cancer and surrounding tissue following the same FWHM segmentation procedures. Total hemoglobin increased from an average of 27.7 μM in the normal tissue to a peak of 37 μM (equivalent to an increase by 34%) and an average of 34.4 μM in the tumor. The oxygen saturation reduced by 6.4% in the cancer, from an average of 61.7% in the surrounding tissue. Water increase in the location of the cancer was not as predominant as in the previous case; it changed by less than 5%. This may be due to the large size of the tumor, averaging out the change between the tumor and the surrounding tissue. Scatter amplitude and power remained nearly unchanged in their averages between tumor and the background.
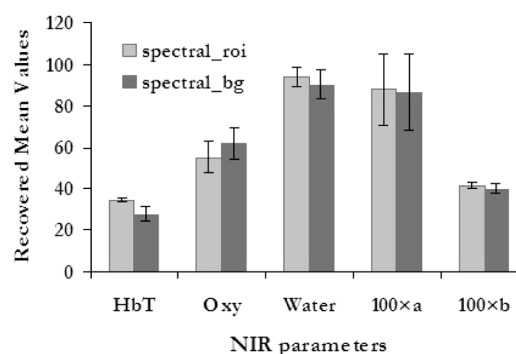

Figure 7: The average and standard deviation for the five NIR parameters in the region of the tumor and the background (for patient corresponding to Figure 6). The tumor was defined by segmentation of the images obtained using the spectrally constrained direct chromophore reconstruction and FWHM criterion. The tumor exhibits an increase in total hemoglobin (Hb$_T$) and water, with decreases in oxygenation, compared to the surrounding tissue.

Case Study 3: In the final cancer case presented here, the subject was a 73-yr-old female volunteer (patient id # 2034) whose mammogram [see Figure 8(a) and (b)] revealed an approximately 2 cm focal density with subtle associated architectural distortions in the lower outer left breast at the 4:30 clock position. Just below this was an approximately 1 cm focal asymmetric density with ill-defined margins, also in the lower, outer left breast. The first abnormality was 6 cm in depth from the nipple and the second adjacent abnormality was 8 cm in depth from the nipple. Ultrasound directed to the lower, outer left breast at 4:30, approximately 4.5 cm from the nipple, demonstrated the two adjacent abnormalities with a questionable hypoechoic bridge between them. The two abnormalities collectively measured 2.5 cm in greatest diameter. The radio-density of the breast belonged to category 2, the scattered type. Excisional biop-
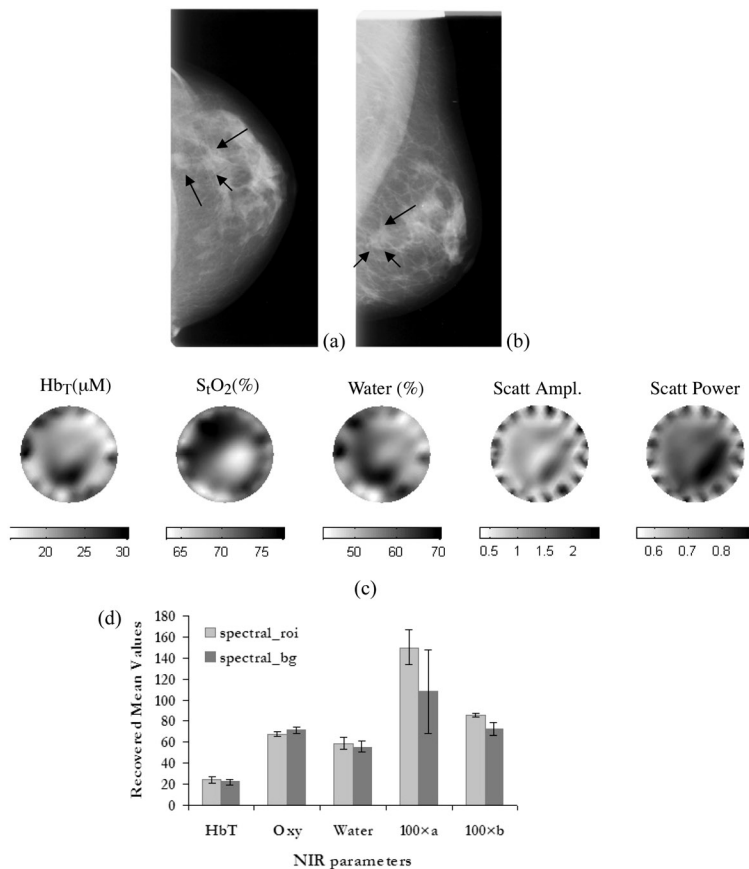
Figure 8: (**a**) Left craniocaudal mammogram, (**b**) left mediolateral oblique mammogram for a 73-yr-old subject, revealed two abnormalities close to each other in the lower outer left breast, diagnosed by excision biopsy as infiltrating ductal carcinoma and 2.5 cm in size. The mass is indicated with black arrows. (**c**) NIR tomographic images obtained using amplitude and phase measurements at the periphery of the breast and the spectrally constrained reconstruction approach. The tumor is visible in total hemoglobin, water, and scatter as a localized increase and in oxygen saturation, as a decrease. (**d**) The average and standard deviation for total hemoglobin, oxygen saturation, water, and scatter amplitude (*a*) and power (*b*) (multiplied by 100 to fit in the same figure) obtained from the images in (**c**) The tumor was segmented using a FWHM criterion from the scatter power image, which shows the cancer most clearly, corresponding to location from mammogram.

sy confirmed the tumor as an infiltrating ductal carcinoma with a vessel density of 0.71. On excision, there was a single lesion with a fatty interface and the pathology size of the tumor was 2.5 cm. The NIR exam used six wavelengths and the images obtained, are shown in Figure 8(c) for total hemoglobin, oxygen saturation, water, and scatter.

Total hemoglobin showed an increase at the 6:00 clock position, slightly different from the location of 4:30 given by the Radiologist. Oxygen saturation and scatter show the tumor at the right location, with a reduction in oxygen saturation observed at the cancer site to a minimum of 64%. The water content in the tumor showed an increase with respect to the background with a maximum value of 68%. Both scatter amplitude and power also showed a contrast discerning the cancer from the surrounding tissue.

The cancer observed in the images in Figure 8(c) was regionized using the FWHM approach to zone into the tumor which placed it in the correct location (corresponding to the mammograms). The average and standard deviation was obtained in the lesion and plotted alongside the mean in the surrounding normal tissue in Figure 8(d). The maximum in total hemoglobin in the tumor increased by 36% relative to the background. Oxygenation and water content did not change substantially but scatter amplitude

increased at the location of the cancer by 39%. Scatter power showed a contrast with a value of 0.85 compared to 0.72 in the background.

Human Imaging of a Fibrosis Lesion (Case Study 4)

Case Study 4: Also studied here are subjects with benign conditions, specifically, fibrosis (a benign, localized lesion comprising an abundance of scar-like, dense stromal collagen in proportion to a reduced epithelial component); and fibrocystic disease. The mammogram of a 49-yr-old female volunteer (patient id #2135) showed a peripheral tumor in a scattered type breast. The left craniocaudal and mediolateral oblique mammograms (see Figure 9) revealed an approximately 5 cm area of asymmetric density in the upper outer quadrant of the left breast; the cone compression views of the mammograms gave it the appearance of normal glandular tissue. Ultrasound of the majority of this area showed dense fibroglandular tissue; however, at the 2:30 clock position, 10 cm from the nipple, was an approximately $2.7 \times 1.7 \times 1.2$ cm ill-defined hypoechoic area with dense posterior acoustic shadowing, giving the suspicion of local fibrosis. There were several tiny cysts in the same area. The patient's symptoms and concerning ultrasound lead to a core biopsy which confirmed the lesion as fibrosis, a benign condition, with a vessel density of 0.33.
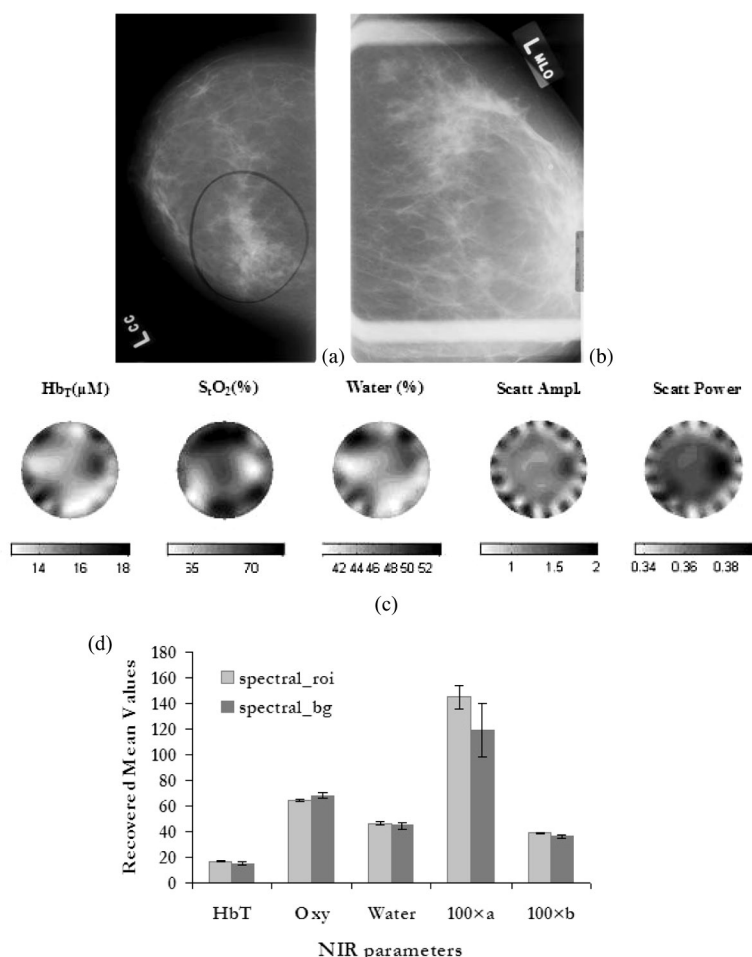
(a)   (b)

(c)

(d)

Figure 9: (**a**) Left craniocaudal mammogram, (**b**) left medi-olateral oblique mammogram magnified for a 49-yr-old subject showing a 2.7 cm mass in the 2:30 clock position, diagnosed by core biopsy as the benign condition, fibrosis. (**c**) NIR tomographic images obtained by applying the spectral reconstruction on the frequency domain data from the plane closest to the chest wall containing the tumor. The tumor is most clearly discernible in total hemoglobin and scatter in the 3:00 clock position with oxygen saturation and water having almost homogeneous images. (**d**) The average for the five NIR parameters along with the standard deviation in the region of the tumor and the background for a subject with fibrosis The tumor exhibits a small increase in total hemoglobin (10%) and a larger increase in scatter amplitude (22%) with respect to the surrounding tissue; other NIR parameters do not show much change.

The NIR clinical examination was carried out two days prior to the biopsy. It consisted of collecting three planes of frequency domain data where the measurements from plane 0 (which contained the tumor), closest to the chest wall (at six wavelengths), was used to reconstruct for the NIR parameters. The spectral approach was used and the images are shown in Figure 9(c). The tumor is most clearly visible in total hemoglobin and scatter amplitude and power. Total hemoglobin showed a slight increase whereas the contrast in scatter is more pronounced. Since the vessel density is much lower compared to the malignancies documented here, the contrast in total hemoglobin is also expected to be low. Fibrosis contains a higher density of tissue which explains the increases observed in the scattering parameters. Scatter amplitude increased to a maximum of 1.6 and a lower contrast is observed in scatter power. Water content exhibited a contrast but overall, has a small range from 42 to 52% overall. Oxygenation varied by less than 5% between tumor and background. The tumor and background averages are shown along with standard deviations in Figure 9(d) using the regionization scheme employed in all of the earlier cases. The same trend is visible, with a contrast in the tumor of less than 10% of the surrounding

tissue in total hemoglobin and scatter amplitude showing the most dominant change, increasing by 22% in the tumor, from a background value of 1.2.
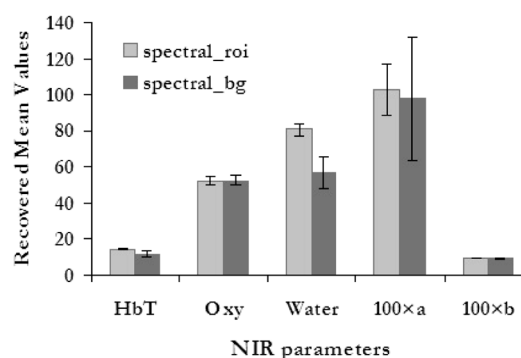

Figure 10: Mean values and standard deviation in the tumor (segmented using FWHM criterion as in previous cases) and surrounding tissue obtained from the NIR images reconstructed with the spectral approach using frequency domain data from the periphery of the breast. The volunteer was a 49-yr-old subject, presenting with an 0.7 × 0.5 cm ill-defined mass, diagnosed by stereotactic guided biopsy as the benign condition, FCD. Contrast was observed at the location of the lesion in total hemoglobin and water, but no decrease in oxygen saturation was observed in the images (17). The dominant contrast was found to be in water.

Human Imaging of fibrocystic disease (FCD) (Case Study 5)

Case Study 5: Frequency domain measurements were obtained from a 50-year-old female volunteer whose mammogram revealed a 0.7×0.5 cm ill defined mass in the upper-inner left breast, approximately 9 cm deep to the nipple. Although portions of the margins were fairly well-circumscribed, at least half was ill-defined or obscured. The lesion was non-calcified and non-palpable and the ultrasound exam of this region showed no sonographic abnormality. A stereotactic guided biopsy revealed the lesion as the benign condition of Fibrocystic Disease (FCD). The NIR parameter images using the spectrally constrained technique applied to frequency domain data at six wavelengths, were discussed in Srinivasan *et al.* (25). The comparison of the mean in the lesion versus the background is plotted in Figure 10. The dominant contrast was in water, which increased by nearly 24% from a background content of 57%.

Another female volunteer with FCD imaged with the NIR modality was a 61-yr-old woman (patient id #1059) with multiple cysts, whose mammogram did not reveal any

abnormality [see Figure 11 (a) and (b)]. Ultrasound showed the lesion, 1.1 cm in size, centrally located at 9.30 on the clock face in the right breast and core biopsy confirmed FCD. The subject had a breast density belonging to category 3 (heterogeneously dense), which probably explains why it was difficult to find the cysts, in both the craniocaudal and mediolateral oblique mammograms. The volunteer was taken through the NIR clinical exam and all six wavelengths were used for the tissue interrogation.

The images are shown in Figure 11(c); the lesion is clearly distinguishable in hemoglobin and scatter as a localized increase in the expected position. There is also a centralized decrease in oxygenation which may confound the diagnosis of this lesion; however, examination of the contralateral breast images [shown in Figure 11(c), bottom row] revealed a similar trend which leads to the conclusion that this change in oxygen saturation is more likely due to the metabolic activity of glandular relative to adipose tissue. Water showed an increase consistent with the previous FCD case study analyzed suggesting that water content is a likely indicator of cysts containing fluids. Scatter amplitude also
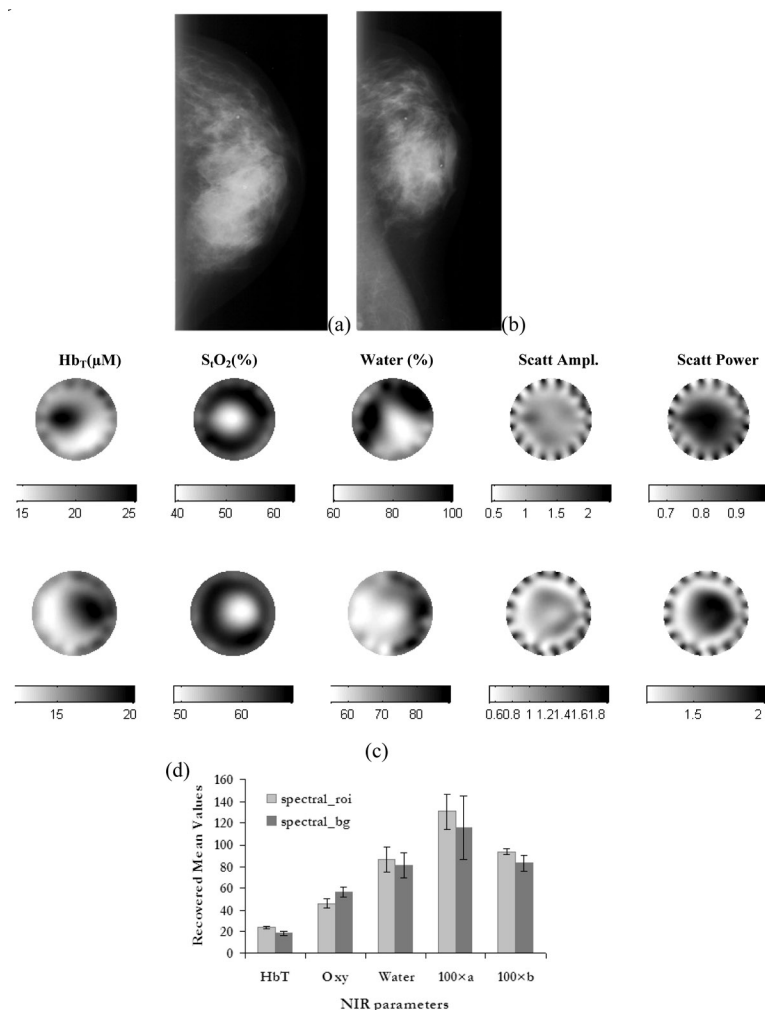

Figure 11: (**a**) Right craniocaudal and (**b**) right mediolateral oblique mammograms for a 61-yr-old subject. The mammograms showed no abnormality. Ultrasound revealed a 1.1 cm lesion at the 9:30 clock position diagnosed as FCD. (**c**) top row shows the images obtained using the spectral reconstruction for the right breast; bottom row shows the images for the contralateral normal breast. Both show a trend of decreasing oxygenation corresponding to an increasing hemoglobin; likely occurring as a result of fibroglandular tissue rather than tumor location. (**d**) Average and standard deviation in the benign lesion and the surrounding tissue. Water and scatter show a contrast over the background.

showed a contrast and this maybe an indicator of denser tissue enveloping the cysts. This is also the primary change not visible in the contralateral breast.

Discussion and Conclusions

Studies have indicated that measurements of neovasculature, hypoxia and cellular microenvironment could have a role in tumor detection and treatment planning (13, 29), as they are all indicators of tissue function, which are important features of solid cancers. NIR tomography is an imaging method which can directly quantify some of these functional processes with non-invasive imaging. Hemoglobin should be a measure of the vascularization of tissue; oxygen saturation offers an indirect measure of tissue oxygenation which relates to partial pressure of oxygen in tissue, and hence to a direct measure of hypoxic fractions in tumors. Water is a measure of the microenvironment and cellular compartments (26) and scattering is related to subcellular organelle density. These together provide noninvasive measures through which to study changes in the breast from malignanices and benign lesions.

While correlation plots of NIR cancer and benign clinical data are useful to identify overall trends separating malignant from benign disease, [an example is the hemoglobin-oxygen saturation plot shown in Grosenick *et al.* (24)] the reality may be that separating the two is more complicated. Certain features of benign conditions, such as fibrocystic disease, present difficulties in diagnosing it from cancer, when based only upon mammographic image features (30). NIR tomography is undergoing several clinical trials evaluating its role in aiding breast lesion diagnosis (2, 18); however, defining the particular NIR characteristics expected in different types of tumors is not yet well defined. While NIR gives estimates of oxygenation in the tumor and surrounding tissue, hypoxia is not a sole indicator in tumor diagnosis, as Okunieff *et al.* (13) showed that some malignancies may not have pO_2 values less than 5 mm Hg. In the three case studies presented here for infiltrating ductal carcinomas each had reduction in oxygen saturation. However, the change varied from a decrease of 4% to 13% from the surrounding oxygenation, indicating that if this decrease is accurate, the contrast available is likely subtle. A similar decrease was also observed in the FCD case study (patient id #1059), where the reduction was more likely due to the higher metabolism of fibroglandular tissue; this was verified by a similar trend of a central lower oxygenation in the normal contralateral breast, corresponding to both a more vascularized tissue region as well as an increase in scatter power indicative of higher radio-density. While more clinical cases will be required to validate the trend shown here, it may be that oxygen saturation alone is not sufficient to separate cancer from FCD. Hence, it is likely more useful to examine the charac-

teristics of different tumors in the NIR images along with the comprehensive data sets which are available from mammograms, ultrasound and potentially MR images.

The NIR images presented here appear to be the most accurate representation of these functional quantities possible, due to the use of the direct spectral reconstruction algorithm. The spectrally-constrained image reconstruction process was validated in phantom experiments and showed a superior ability to follow changes related to total hemoglobin and scattering as well as oxygen saturation [shown before (9)]. The images for the case studies presented here are consistent with the physiological changes that would be expected based upon conventional understanding of larger solid tumors. Total hemoglobin showed a localized increase in the malignancies with a higher contrast (34-86% increase in the lesion with respect to the surrounding tissue) compared to the benign lesions (10-28% increase in lesion compared to background). Hemoglobin also seemed to correlate with vessel density, obtained through biopsy of tumor tissue, where higher vessel density has been associated with higher hemoglobin content. Using the six cases studied here along with other tumors imaged (n=12, seven cancers and five benign lesions, size > 8mm), Figure 12 shows this trend. The data does not include the patient with FCD (patient id #1059), whose mammogram did not show a lesion; and whose NIR images show an increase in hemoglobin, more likely indicating glandular tissue. The figure supports an interesting observation: typically 1% human blood in its normal state contains ~20-25 μM blood; and 1% vessel density from the graph shows a correspondence of 1% blood = 26 μM. This trend has to be validated in a larger number of clinical cases.
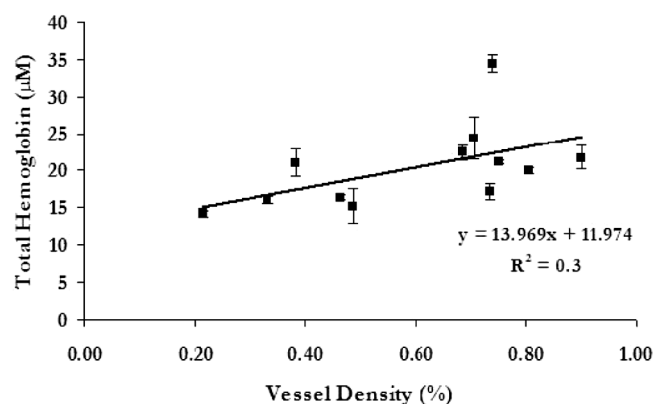

Figure 12: The average total hemoglobin and standard deviation in the location of the lesions from 12 tumors imaged *in vivo* (seven cancers and five benign lesions) including the case-studies reported in this paper, plotted against vessel density in the tumor obtained from pathology, indicates a possible correlation.

All three carcinomas studied here showed a localized change in all five NIR images; the same was not true in the benign conditions. In the subject with fibrosis, the dominant change

was in scatter amplitude, consistent with the densely packed fibrous tissue. In cancers, the contrast in scatter amplitude agreed with an expectation of cell proliferation resulting in higher number density of scatterers in the cancers. This yields the encouraging conclusion that scatter amplitude could be an emerging indicator of the density of localized tissues, which when interpreted along with total hemoglobin, oxygenation and water, may enable separation of malignant and benign disease. Scatter power, on the other hand, may be more indicative of bulk radiodensity of the breast (26, 43, 44). Scattering was found to correlate inversely with E/S ratio in preliminary studies and this will be investigated with the spectral approach in future work.

Water content in the images studied here, obtained using the spectrally constrained direct reconstruction, has yielded increased information, compared to the conventional approach of separate wavelength recovery. In all three malignancies, water showed an increase with respect to the surrounding tissue coinciding with the physiological expectation of a leaky endothelium. Water was the dominant mechanism of contrast in the FCDs (see images in Figure 10 and 11) along with scatter change for one of the cases (patient #1059).

Overall, using the spectrally constrained direct reconstruction approach, the NIR images studied here offer an example of qualitative ways of characterizing different types of lesions. The analysis when performed on a larger number of clinical cases will present distinctive features of tumors useful in diagnosis. The physiological changes observable here can be extended to monitoring response to therapy, predicting risk of malignancy or aggressiveness of tumors. At this stage of development, the role of NIR imaging in diagnosis is still uncertain; however, through algorithm improvement and case study analysis, the potential value of the NIR parameters becomes clearer. It is likely that this system can be used to measure physiological changes which are not observable in other imaging modalities, and further patient imaging sessions will help determine those parameters and indications where the system will have its most important impact.

Acknowledgements

References

1. B. Chance, Q. Luo, S. Nioka, D. C. Alsop, and J. A. Detre. Optical Investigations of Physiology: A Study of Intrinsic and Extrinsic Biomedical Contrast. *Phil. Trans. R. Soc. Lond. B 352*, 707-716 (1997).
2. B. W. Pogue, S. P. Poplack, T. O. McBride, W. A. Wells, O. K. S., U. L. Osterberg, and K. D. Paulsen. Quantitative Hemoglobin Tomography with Diffuse Near-Infrared Spectroscopy: Pilot Results in the Breast. *Radiology 218*, 261-266 (2001).
3. B. J. Tromberg, O. Coquoz, J. B. Fishkin, T. Pham, E. R. Anderson, J. Butler, M. Cahn, J. D. Gross, V. Venugopalan, D. Pham. Non-invasive Measurements of Breast Tissue Optical Properties Using Frequency-domain Photon Migration. *Phil. Trans. R. Soc. Lond. B 352*, 661-668 (1997).
4. X. Intes, J. Ripoll, Y. Chen, S. Nioka, A. G. Yodh, and B. Chance. *In Vivo* Continuous-wave Optical Breast Imaging Enhanced with Indocynanine Green. *Med. Phys. 30*, 1039-1047 (2003).
5. M. A. Franceschini, K. T. Moesta, S. Fantini, G. Gaida, E. Gratton, H. Jess, W. W. Mantulin, M. Seeber, P. M. Schlag, and M. Kaschke. Frequency-domain Techniques Enhance Optical Mammography: Initial Clinical Results. *Proc. Nat. Acad. Sci USA 94*, 6468-6473 (1997).
6. X. Gu, Q. Zhang, M. Bartlett, L. Schutz, L. L. Fajardo, and H. Jiang. Differentiation of Cysts from Solid Tumors in the Breast with Diffuse Optical Tomography. *Acad. Radiology 11*, 53-60 (2004).
7. A. Corlu, T. Durduran, R. Choe, M. Schweiger, E. M. Hillman, S. R. Arridge, and A. G. Yodh. Uniqueness and Wavelength Optimization in Continuous-wave Multispectral Diffuse Optical Tomography. *Opt. Lett. 28*, 2339-2341 (2003).
8. A. Li, Q. Zhang, J. P. Culver, E. L. Miller, and D. A. Boas. Reconstructing Chromosphere Concentration Images Directly by Continuous-wave Diffuse Optical Tomography. Opt. Lett. *29*, 256-258 (2004).
9. S. Srinivasan, B. W. Pogue, S. Jiang, H. Dehghani, and K. D. Paulsen. Spectrally Constrained Chromophore and Scattering NIR Tomography Provides Quantitative and Robust Reconstruction. *Appl. Opt. 44*, 1858-1869 (2005).
10. A. Corlu, R. Choe, T. Durduran, K. Lee, M. Schweiger, S. R. Arridge, E. M. Hillman, and A. G. Yodh. Diffuse Optical Tomography with Spectral Constraints and Wavelength Optimization. *Appl. Opt. 44*, 2082-2093 (2005).
11. P. Vaupel, K. F., and O. P. Blood Flow, Oxygen and Nutrient Supply, and Metabolic Microenvironment of Human Tumors: A Review. *Cancer Research 49*, 6449-6465 (1989).
12. M. Hockel and P. Vaupel. Tumor Hypoxia: Definitions and Current Clinical, Biologic, and Molecular Aspects. *J. Natl. Cancer Inst. 93*, 266-276 (2001).
13. P. Okunieff, M. Hoeckel, E. P. Dunphy, K. Schlenger, C. Knoop, and P. Vaupel. Oxygen Tension Distributions are Sufficient to Explain the Local Response of Human Breast Tumors Treated with Radiation alone. *Int. J. Radiation Oncology Biol. Phys. 26*, 631-636 (1993).
14. D. M. Brizel, S. P. Scully, J. M. Harrelson, L. J. Layfield, J. M. Bean, L. R. Prosnitz, and M. W. Dewhirst. Tumor Oxygenation Predicts for the Likelihood of Distant Metastases in Human Soft Tissue Sarcoma. *Cancer Research 56*, 941-943 (1996).
15. P. Vaupel, A. Mayer, S. Briest, and M. Hockel. Oxygenation Gain Factor: A Novel Parameter Characterizing the Association Between Hemoglobin Level and the Oxygenation Status of Breast Cancers. *Cancer Research 63*, 7634-7637 (2003).
16. A. Bottini, A. Berruti, M. P. Brizzi, A. Bersiga, D. Generali, G. Allevi, S. Aguggini, G. Bolsi, S. Bonardi, G. Bertoli, P. Alquati, and L. Dogliotti. Pretreatment Haemoglobin Levels Significantly Predict the Tumour Response to Primary Chemotherapy in Human Breast Cancer. *Br. J. Cancer 89*, 977-982 (2003).
17. D. L. Conover, B. M. Fenton, T. H. Foster, and E. L. Hull. An Evaluation of Near Infrared Spectroscopy and Cryospectrophotometry Estimates of Haemoglobin Oxygen Saturation in a Rodent Mammary Tumour Model. *Physics in Medicine & Biology 45*, 2685-2700 (2000).
18. B. J. Tromberg, N. Shah, R. Lanning, A. Cerussi, J. Espinoza, T. Pham, L. Svaasand, and J. Butler. Non-invasive *In Vivo* Characterization of Breast Tumors Using Photon Migration Spectroscopy. *Neoplasia (New York) 2*, 26-40 (2000).

19. D. B. Jakubowski, A. E. Cerussi, F. Bevilacqua, N. Shah, D. Hsiang, J. Butler, and B. J. Tromberg. Monitoring Neoadjuvant Chemotherapy in Breast Cancer using Quantitative Diffuse Optical Spectroscopy: A Case Study. *J. Biomed. Opt. 9*, 230-238 (2004).

20. V. Chernomordik, D. W. Hattery, D. Grosenick, H. Wabnitz, H. Rinneberg, K. T. Moesta, P. M. Schlag, and A. Gandjbakhche. Quantification of Optical Properties of a Breast Tumor Using Random Walk Theory. *Journal of Biomed. Opt. 7*, 80-87 (2002).

21. E. Heffer, V. Pera, O. Schutz, H. Siebold, and S. Fantini. Near-infrared Imaging of the Human Breast: Complementing Hemoglobin Concentration Maps with Oxygenation Images. *Journal of Biomed. Opt. 9*, 1152-1160 (2004).

22. T. O. McBride, B. W. Pogue, S. Jiang, U. L. Osterberg, K. D. Paulsen, and S. P. Poplack. Multi-spectral Near-infrared Tomography: A Case Study in Compensating for Water and Lipid Content in Hemoglobin Imaging of the Breast. *J. Biomed. Opt. 7*, 72-79 (2002).

23. H. Dehghani, B. W. Pogue, S. P. Poplack, and K. D. Paulsen. Multiwavelength Three-dimensional Near-infrared Tomography of the Breast: Initial Simulation, Phantom, and Clinical Results. *Applied Optics 42*, 135-145 (2003).

24. D. Grosenick, H. Wabnitz, K. T. Moesta, J. Mucke, M. Moller, C. Stroszczynski, J. Stossel, B. Wassermann, P. M. Schlag, and H. Rinneberg. Concentration and Oxygen Saturation of Haemoglobin of 50 Breast Tumours Determined by Time-domain Optical Mammography. *Phys. Med. Biol. 49*, 1165-1181 (2004).

25. S. Srinivasan, B. W. Pogue, S. Jiang, H. Dehghani, and K. D. Paulsen. Spectrally Constrained NIR Tomography for Breast Imaging: Simulations and Clinical Results. *Proc. SPIE 2005* (2005).

26. S. Srinivasan, B. W. Pogue, S. Jiang, H. Dehghani, C. Kogel, S. Soho, J. J. Gibson, T. D. Tosteson, S. P. Poplack, and K. D. Paulsen. Interpreting Hemoglobin and Water Concentration, Oxygen Saturation and Scattering Measured *In Vivo* by Near-infrared Breast Tomography. *PNAS 100*, 12349-12354 (2003).

27. M. T. Mandelson, N. Oestreicher, P. L. Porter, D. White, C. A. Finder, S. H. Taplin, and E. White. Breast Density as a Predictor of Mammographic Detection: Comparison of Interval- and Screen-detected Cancers. *J. Natl. Cancer Inst. 92*, 1081-1087 (2000).

28. M. K. Simick, R. Jong, B. Wilson, and L. Lilge. Non-ionizing Near-infrared Radiation Transillumination Spectroscopy for Breast Tissue Density and Assessment of Breast Cancer Risk. *Journal of Biomed. Opt. 9*, 794-803 (2004).

29. B. S. Kuszyk, F. M. Corl, F. N. Franano, D. A. Bluemke, L. V. Hofmann, B. J. Fortman, and E. K. Fishman. Tumor Transport Physiology: Implications for Imaging and Image-guided Therapy. *AJR 177*, 747-753 (2001).

30. S. Thomsen and D. Tatman. Physiological and Pathological Factors of Human Breast Disease that can Influence Optical Diagnosis. *Ann. N.Y. Acad. Sci. 838*, 171-193 (1998).

31. N. Shah, A. Cerussi, D. Jakubowski, D. Hsiang, J. Butler, and B. Tromberg. The Role of Diffuse Optical Spectroscopy in the Clinical Management of Breast Cancer. *Disease Markers 19*, 95-105 (2003-2004).

32. T. O. Mcbride, B. W. Pogue, S. Jiang, U. L. Osterberg, and K. D. Paulsen. A Parallel-detection Frequency-domain Near-infrared Tomography System for Hemoglobin Imaging of the Breast *In Vivo*. *Review of Scientific Instruments 72*, 1817-1824 (2001).

33. K. D. Paulsen and Jiang, H. Spatially Varying Optical Property Reconstruction Using a Finite Element Diffusion Equation Approximation. *Med. Phys. 22*, 691-701 (1995).

34. S. R. Arridge, M. Schweiger, M. Hiraoka, D. T. Delpy. A Finite Element Approach for Modeling Photon Transport in Tissue. *Med. Phys. 20*, 299-309 (1993).

35. T. O. McBride, B. W. Pogue, S. Jiang, U. L. Osterberg, K. D. Paulsen, and S. P. Poplack. Initial Studies of *In Vivo* Absorbing and Scattering Heterogeneity in Near-infrared Tomographic Breast Imaging. *Opt. Lett. 26*, 822-824 (2001).

36. H. J. van Staveren, C. J. M. Moes, J. van Marle, S. A. Prahl, and J. C. van Gemert. Light Scattering in Intralipid – 10% in the Wavelength Range of 400-1100nm. *Applied Optics 30*, 4507-4514 (1991).

37. J. R. Mourant, T. Fuselier, J. Boyer, T. M. Johnson, and I. J. Bigio. Predictions and Measurements of Scattering and Absorption Over Broad Wavelength Ranges in Tissue Phantoms. *Applied Optics 36*, 949 (1997).

38. X. Wang, B. W. Pogue, S. Jiang, X. Song, K. D. Paulsen, C. Kogel, S. P. Poplack, and W. A. Wells. Approximation of Mie Scattering Parameters in Near-infrared Tomography of Normal Breast Tissue *In Vivo*. *Journal of Biomed Opt* (in press) (2005).

39. J. R. Mourant, A. H. Hielscher, A. A. Eick, T. M. Johnson, and J. P. Freyer. Evidence of Intrinsic Differences in the Light Scattering Properties of Tumorigenic and Nontumorigenic Cells. *Cancer Cytopathology 84*, 366-374 (1998).

40. *Breast Imaging Reporting and Data System (BIRADSTM)*. Reston[VA]: American College of Radiology (1998).

41. W. A. Wells, C. P. Daghlian, T. D. Tosteson, M. R. Grove, S. P. Poplack, S. Soho, and K. D. Paulsen. Analysis of the Microvasculature and Tissue Type Ratios in Benign and Malignant Breast Tissue. *Analytical and Quantitative Cytology and Histology 26*, 166-174 (2004).

42. S. Srinivasan, B. W. Pogue, H. Dehghani, S. Jiang, X. Song, and K. D. Paulsen. Improved Quantification of Small Objects in Near-infrared Diffuse Optical Tomography. *Journal of Biomed Opt. 9*, 1161-1171 (2004).

43. B. W. Pogue, S. Jiang, H. Dehghani, C. Kogel, S. Soho, S. Srinivasan, X. Song, S. P. Poplack, and K. D. Paulsen. Characterization of Hemoglobin, Water and NIR Scattering in Breast Tissue: Analysis of Inter-subject Variability and Menstrual Cycle Changes Relative to Lesions. *J. Biomed. Opt. 9*, 541-552 (2004).

44. S. P. Poplack, K. D. Paulsen, A. Hartov, P. M. Meaney, B. W. Pogue, T. D. Tosteson, M. R. Grove, S. K. Soho, and W. A. Wells. Electromagnetic Breast Imaging: Average Tissue Property Values in Women with Negative Clinical Findings. *Radiology 231*, 571-580 (2004).

Contrast-detail analysis characterizing diffuse optical fluorescence tomography image reconstruction

Scott C. Davis*
Brian W. Pogue
Hamid Dehghani
Keith D. Paulsen
Dartmouth College
Thayer School of Engineering
Hanover New Hampshire 03755

Abstract. Contrast-detail analysis is used to evaluate the imaging performance of diffuse optical fluorescence tomography (DOFT), characterizing spatial resolution limits, signal-to-noise limits, and the trade-off between object contrast and size. Reconstructed images of fluorescence yield from simulated noisy data were used to determine the contrast-to-noise ratio (CNR). A threshold of CNR=3 was used to approximate a lowest acceptable noise level in the image, as a surrogate measure for human detection of objects. For objects 0.5 cm inside the edge of a simulated tissue region, the smallest diameter that met this criteria was approximately 1.7 mm, regardless of contrast level, and test field diameter had little impact on this limit. Object depth had substantial impact on object CNR, leading to a limit of 4 mm for objects near the center of a 51-mm test field and 8.5 mm for an 86-mm test field. Similarly, large objects near the edge of both test fields required a minimum contrast of 50% to achieve acceptable image CNR. The minimum contrast for large, centered objects ranged between 50% and 100%. Contrast-detail analysis using human detection of lower contrast limits provides fundamentally important information about the performance of reconstruction algorithms, and can be used to compare imaging performance of different systems. © *2005 Society of Photo-Optical Instrumentation Engineers.* [DOI: 10.1117/1.2114727]

Diffuse optical fluorescence tomography (DOFT) is an emerging technology to image fluorophore spatial distributions in deep tissues or other structures that are dominated by elastic scattering. The modality involves both a complex theoretical framework[1–4] as well as advanced experimental systems.[5–7] Several studies have shown evidence of successful fluorescence tomography in both phantom and animal models.[8] Case examples have been presented to illustrate the accuracy and precision of select images, but few studies have addressed the limits of imaging performance in a systematic manner, following the conventions of standard medical imaging practice. Graves et al. examined the limits of detectable contrast for a particular sized object and the spatial resolution limits for a particular contrast level for their system configuration.[8] The natural extension of this work is to fully consider the known trade-off between an object's size and contrast, in terms of detectability. Contrast-detail analysis can be used to systematically define three imaging performance regimes; a spatial-resolution-limited regime, a signal-to-noise (SNR)-limited regime, and a transitional regime that describes the trade-off between object size and contrast. In this letter, an optimized DOFT reconstruction algorithm is evaluated in the context of size-contrast analysis, and the expected limits of image recovery are discussed.

Contrast-detail analysis is commonly used to determine the performance of a medical imaging system[9–11] and has been previously adapted to near-infrared (NIR) diffuse tomography.[12,13] Such performance measurements seek to determine the contrast thresholds for an imaging system, providing quality assurance, optimization, and intersystem comparisons. Determining the detection threshold for a given range of object diameters can generate limits on minimum detectable object size and contrast.

The diffuse nature of NIR photon propagation in biological tissue is the foundation of the model system used. In this regime, the initial excitation source and the fluorescence emission photon field can be described by a system of coupled diffusion equations, as presented in Ref. 1. The imaging algorithm used here incorporates a finite element solution of these coupled equations, and the inverse problem is solved iteratively for the spatial distribution of fluorescence yield, $\eta\mu_{af}$, where η is the fluorescence quantum yield and μ_{af} is the fluorophores absorption at the excitation wavelength.

Simulated data was generated by solving the model system using typical tissue optical property parameters of μ_a $=0.01$ mm^{-1} and $\mu_s'=1.0$ mm^{-1}, and extracting the boundary data at each simulated detector position. To compare the influence of domain size on contrast-detail characteristics, two circular test fields were used; one 51 mm in diameter and the other 86 mm in diameter. The smaller test field approximates a domain expected to be encountered in small animal imaging and the 86-mm test field mimics larger imaging fields such as a human breast. Each test field was simulated as a 10,000-node circular mesh circumscribed by 16 source/detector fiber positions and used to generate 240 data points, matching our experimental fluorescence tomography design. The system is similar to our automated tomography system currently in clinical trials.[14] Random noise was added to each transmission data point with 1% mean error.

Image reconstruction was performed with a nonlinear Newton-Raphson type algorithm, which was stopped when the projection error changed by less than 2% between iterations. Intrinsic optical properties μ_{ax}, μ_{am}, μ_{sx}', and μ_{sm}' were held constant, as were the fluorophore lifetime τ and quantum yield η. The algorithm recovered the fluorescence yield only, $\eta\mu_{af}$, as a best-case scenario for how accurately the images can be formed. The homogeneous background fluorescence yield, $\eta\mu_{af}=0.0001$ mm^{-1}, was used as an initial estimate for the iterative algorithm. Figure 1 shows an example of a reconstructed image and compares the estimated property val-

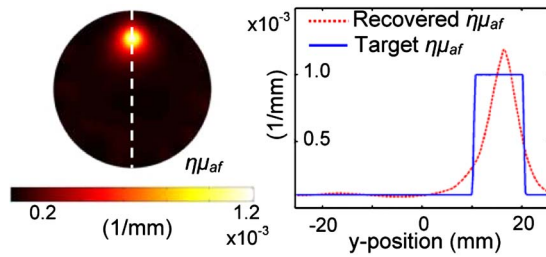*Tel: 603-646-2230; E-mail: scott.c.davis@dartmouth.edu

Fig. 1 Typical reconstructed image (a) in the 51-mm test field showing the value of $\eta\mu_{af}$ for simulated data with 1% random noise and η set to 0.1. Reconstructed and actual values are compared (b) along the vertical transect through the object superimposed on the image.

ues with the true values for an object near the edge of the 51-mm phantom. The regularization parameter was selected empirically and weighted at each iteration by the maximum of the diagonal of $\mathbf{JJ}^t$, where $\mathbf{J}$ is the Jacobian matrix (240 $\times$ 900). The algorithm in this example converged after 12 iterations.

The contrast parameter, fluorophore absorption μ_{af}, was varied for a single object, or region of interest (ROI), while the background fluorophore absorption was held constant at 0.001 mm^{-1}. Contrast was calculated as

$$\text{contrast} = (\mu_{af}^{\text{true\_ROI}} - \mu_{af}^{\text{true\_background}})/\mu_{af}^{\text{true\_background}}, \quad (1)$$

where the absorption coefficient values were the true values used to simulate the data. Images were recovered for each contrast and test object diameter combination. For both test fields, 51 mm and 86 mm, these calculations were repeated for two different object positions, one near the edge of the phantom (object edge 5 mm from the boundary), and one near the center (object center 2 mm from the test field center). At least 2,000 images (similar to the image shown in Fig. 1) for each of the four test cases were used in the analysis.

Contrast-detail studies for clinical systems often use trained readers to determine the threshold for detectable contrast and size. In the current study, CNR is specified as a surrogate parameter of detectability, which provides an objective threshold measure. CNR was calculated directly from the reconstructed images following the approach outlined in Song et al.[13]

$$\text{CNR} = \frac{\mu_{af}^{\text{ROI}} - \mu_{af}^{\text{background}}}{(w_{\text{ROI}}\sigma_{\text{ROI}}^2 - w_{\text{background}}\sigma_{\text{background}}^2)^{1/2}}, \quad (2)$$

where w_{ROI} and $w_{\text{background}}$ are weighting factors compensating for the relative area of the ROI and the background, as a fraction of the total test field area. The values σ_{ROI} and $\sigma_{\text{background}}$ are the standard deviations in the ROI and background regions of the reconstructed image, respectively. The ROI size and location are assumed known, which is common for contrast-detail analyses where the objective is to determine system performance for a known test field.

CNR is plotted as a function of both ROI diameter and true contrast for an object just off-center in the 51-mm test field edge (Fig. 2). Similar plots were generated for the other three cases examined. By specifying a minimum CNR value required to "detect" an object, the contrast threshold for visibility is determined for each object diameter. The choice of a
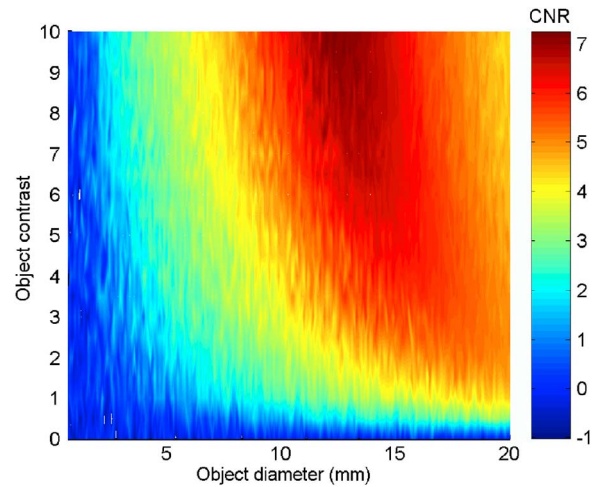

Fig. 2 Calculated CNR ratio for a range of object diameters and contrast levels. In this case, the object is near the test field center (2 mm from the center of a 51-mm phantom). In this analysis, objects that are reconstructed with a CNR value below 3.0 are thought to be undetectable by human perception, illustrating that there are regions of size and contrast that are not feasible to image with the algorithm.

minimum CNR value is somewhat arbitrary since it represents the threshold of object detection in the images. Evaluating human detection of objects is more complicated than CNR analysis and intra- and interhuman observer variability can result in a range of CNR threshold values. However, empirical observations indicate human detection thresholds are reasonably well approximated with CNR=3, which is the value used in the current analysis.[15]

The contrast-detail results for a threshold limit of CNR =3 are plotted in Fig. 3 for the two test fields and object positions. Objects that are recovered with greater than CNR =3 have contrast-detail characteristics that are above and to the right of the line shown in Fig. 3, while those below and to the left are too small or have too little contrast to be recovered with CNR >3 in the image. Accordingly, the limiting diameter for an object near the edge of the field is approximately
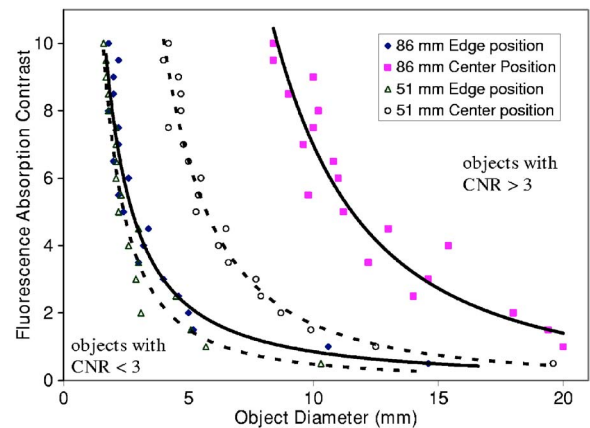

Fig. 3 Contrast-detail curve showing the CNR of 3 to approximate limits of detectable contrast and diameter for two anomaly positions in 51-mm (dashed lines) and 86-mm (solid lines) diameter test fields. In this analysis, objects above and to the right of each line are in the region where CNR≥3 and "detection" is considered possible.

1.7 mm for both test field diameters. There seems to be little influence of test field diameter on CNR limits for high-contrast objects near the edge. Above an object contrast of about 8, the continued decrease in the minimum size for CNR=3 is very small with increasing contrast, indicating that this size is a fundamental limit of the imaging algorithm for this geometry. It does not appear that the fundamental limits have been reached for objects near the center of either test field for the contrast range studied and expected to be encountered experimentally. Furthermore, CNR value of objects near the center is strongly influenced by the test field size. For a 51-mm test object, the limiting diameter is approximately 4 mm, for the maximum object contrast (10). This increases to approximately 8.5 mm for the larger test field. These results indicate the dramatic decrease in sensitivity for objects deeper in the test field.

The horizontal asymptotes of these lines represent the SNR limitations of the imaging system. These correspond to the low-contrast large-detail portion of the curve where small changes in contrast result in large changes in the diameter for the CNR=3 threshold. For objects near the phantom edge, the minimum contrast for CNR=3 is less than 0.5, though this limit is reached for smaller object sizes in the 51-mm test field, indicating slightly better imaging performance. This same contrast limit applies to objects near the center of the smaller test field, though again, it is not reached until the object diameter is larger than on the edge. Due to the poor sensitivity to objects in the center of the 86-mm test field, SNR limits are outside of the test range. The SNR limits determined in this study will likely vary with the noise level in the system.

In addition to fundamental limits of the imaging system, the contrast-detail curve provides information on the trade-off between object size and contrast. This "transition" zone lies between the vertical (spatial-resolution-limited) and horizontal (SNR-limited) asymptotes and defines system imaging performance for objects mostly likely to be encountered experimentally.

Algorithms based on the photon migration equation are considered to be more sensitive closer to the source/detectors and this nonlinear sensitivity is manifested as a nonuniform image response across the field of view. The contrast-detail curves shown in Fig. 3 demonstrate the significance of this effect. For the smaller test field, the minimum object diameter for the best-case high-contrast regime differs by 150% between an object at the edge and one centered in the test field. In a larger field, that difference increases to 360%. Thus, objects closer to the center will need to be larger in order to be detected. Further contrast-detail studies may be used to investigate image reconstruction parameters in addition to object position, such as adaptive meshing techniques[16] and the effect of intrinsic optical properties.

The results provide a best-case analysis for imaging tissue containing fluorophore *in vivo* with this algorithm. A number of factors will increase the contrast and size required to detect an anomaly in an experimental or clinical setting, thus shifting the contrast-detail curves up and to the right, including:

1. reconstruction of unknown intrinsic optical properties;
2. heterogeneity of optical properties and fluorophore distribution;
3. excitation cross-talk in the fluorescence signal;
4. higher experimental noise or model-mismatch; and
5. increased phantom size and/or intrinsic absorption.

Contrast-detail analyses may also be used to track imaging performance as system improvements/adjustments are implemented. Future work will explore some of the factors expected to degrade performance in practice, especially cases where the intrinsic optical parameters are unknown. These analyses may also be used to compare reconstruction techniques now beginning to emerge within the research community, thus offering an efficient and systematic approach to intersystem comparison.

References

1. D. Y. Paithankar, A. U. Chen, B. W. Pogue, M. S. Patterson, and E. M. Sevick-Muraca, "Imaging of fluorescent yeild and lifetime from multiply scattered light reemitted from random media," *Appl. Opt.* **36**(10), 2260–2272 (1997).
2. M. J. Eppstein, D. J. Hawrysz, A. Godavarty, and E. M. Sevick-Muraca, "Three-dimensional, Bayesian image reconstruction from sparse and noisy data sets: near-infrared fluorescence tomography," *Proc. Natl. Acad. Sci. U.S.A.* **99**(15), 9619–9624 (2002).
3. J. Ripoll, V. Ntziachristos, J. P. Culver, D. N. Pattanayak, A. G. Yodh, and M. Nieto-Vesperinas, "Recovery of optical parameters in multiple-layered diffusive media: theory and experiments," *J. Opt. Soc. Am. A Opt. Image Sci. Vis* **18**(4), 821–830 (2001).
4. A. B. Milstein, O. Seungseok, K. J. Webb, C. A. Bouman, Q. Zhang, D. A. Boas, and R. P. Millane, "Fluorescence optical diffusion tomograhy," *Appl. Opt.* **42**(16), 3081–3094 (2003).
5. D. J. Hawrysz and E. M. Sevick-Muraca, "Developments toward diagnostic breast cancer imaging using near-infrared optical measurements and fluorescent contrast agents," *Neoplasia* **2**(5), 388–417 (2000).
6. V. Ntziachristos and R. Weissleder, "Experimental three-dimensional fluorescence reconstruction of diffuse media by use of a normalized Born approximation," *Opt. Lett.* **26**(12), 893–895 (2001).
7. V. Ntziachristos and R. Weissleder, "Charge-coupled-device based scanner for tomography of fluorescent near-infrared probes in turbid media," *Med. Phys.* **29**(5), 803–809 (2002).
8. E. Graves, J. Ripoll, R. Weissleder, and V. Ntziachristos, "A submillimeter resolution fluorescence molecular imaging system for small animal imaging," *Med. Phys.* **30**(5), 901–911 (2003).
9. R. Hendrick and E. Berns, "Optimizing mammographic techniques," in *RSNA Categorical Course in Breast Imaging*, edited by A. Haus and M. Yaffe (Rad. Soc. North Am. Inc., Oak Brook, IL, 1999).
10. G. Cohen, "Contrast-detail-dose analysis of six different computed tomographic scanners," *J. Comput. Assist. Tomogr.* **3**(2), 197–203 (1979).
11. K. J. Robson, C. J. Kotre, and K. Faulkner, "The use of a contrast-detail test object in the optimization of optical density in mammography," *Br. J. Radiol.* **68**(807), 277–282 (1995).
12. B. W. Pogue, C. Willscher, T. O. McBride, U. L. Osterberg, and K. D. Paulsen, "Contrast-detail analysis for detection and characterization with near-infrared diffuse tomography," *Med. Phys.* **27**(12), 2693–2700 (2000).
13. X. Song, B. W. Pogue, S. Jiang, M. M. Doyley, H. Dehghani, T. D. Tosteson, and K. D. Paulsen, "Automated region detection based on the contrast-to-noise ratio in near-infrared tomography," *Appl. Opt.* **43**(5), 1053–1062 (2004).
14. T. O. McBride, B. W. Pogue, S. Jiang, U. L. Osterberg, and K. D. Paulsen, "A parallel-detection frequency-domain near-infrared tomograhy system for hemoglobin imaging of the breast in vivo," *Rev. Sci. Instrum.* **72**(3), 1817–1824 (2001).
15. X. Song, "Statistical analysis and evaluation of near infrared tomographic imaging system," PhD thesis, Dartmouth College (2005).
16. A. Joshi, B. Wolfgang, and E. M. Sevick-Muraca, "Adaptive finiter element based tomography for fluorescence optical imaging in tissue," *Opt. Express* **12**(22), 5402–5417 (2004).

Incorporation of MR Structural Information in Diffuse Optical Tomography using Helmholtz Type Regularization

Phaneendra K. Yalavarthy, Colin M. Carpenter, Shudong Jiang,
Hamid Dehghani, Brian W. Pogue, and Keith D. Paulsen
Thayer School of Engineering, Dartmouth College, Hanover NH 03755
(Email: phani@dartmouth.edu, Tel:(603) 646-2685, Fax:(603) 646-3856)

Astract: A framework to incorporate analytical forms of structural MRI information is presented. This type of information gives superior quantitative results compared to standard NIR tomography and the covariance forms preserve the structural shape function expected.
©2005 Optical Society of America
OCIS codes: (170.3830) Mammography; (170.6960) Tomography; (100.3010) Image reconstruction techniques

1. Introduction

Near Infrared (NIR) optical tomography is used to image brain function and breast physiology using NIR light as the signal[1, 2]. Typically, NIR light is delivered and collected on the boundary of interrogating tissue volume using optical fibers in contact with the tissue. Using these boundary measurements, recovery of spatial distribution of optical absorption and reduced scattering properties (μ_a and $\mu_s^/$) is done using a model based non-linear iterative procedure. These optical parameters can be used in determining the tissue hemoglobin and water contents using the spectral signature of the NIR light in tissue [2]. NIR imaging has the advantage of getting these functional parameters using a non-invasive and non-ionizing mechanism. Due to diffusive nature of NIR light, the spatial resolution of NIR imaging is quite poor (about 5 mm), whereas MRI has high spatial resolution (~ 1 mm), but lacks to provide the functional information. To take advantage of both imaging modalities, a dual imaging system, combining both NIR with MRI has been developed at Dartmouth [3] and is being used in an ongoing clinical trial for breast cancer imaging. In this work, a technique which uses the spatial *a priori* structural information available from MRI with NIR image reconstruction procedure is quantitatively assessed. In this work a Helmholtz-type of regularization is used where the imaging problem is penalized with possible variations within the regions of same property and region (termed as *soft-priors*). This is in parallel with Laplacian-type of regularization developed by Brooksby et. al[4] allowing the intra-region variability which can work well even if the confidence in structural *a priori* information is low.

2. Methods
2.1 Image Reconstruction
Light transport in breast tissue can be described accurately by the Diffusion Equation (DE), which is an approximation to the Radiative Transport Equation (RTE). In frequency-domain, the DE is given by:

$$- \nabla . \kappa(r) \nabla \Phi(r,\omega) + \left(\mu_a(r) + \frac{i\omega}{c} \right) \Phi(r,\omega) = q_0(r,\omega) \tag{1}$$

Where $\Phi(r,\omega)$ is the photon density at position r and modulation frequency ω (in this work, ω = 100 MHz), and κ = $1/[3(\mu_a + \mu_s^/)]$ is the diffusion coefficient, and $q(r,\omega)$ is an isotropic source term. In this work, a Robin (Type III) boundary condition is used. The boundary data for a frequency domain system are the measured amplitude and phase of the measured signal, which is often used with Finite Element Method (FEM) based reconstruction procedure to get the internal spatial distributions of μ_a and μ_s'.

2.2 Inclusion of a priori information
Based on a Newton-minimization approach [5], the objective function with inclusion of *a priori* information is given as

$$[\bar{\mu}_a, \bar{k}] = \min_{\mu_a, k} \left\{ \| y - F(\mu_a, k) \| + \alpha \left\| L \left[(\bar{\mu}_a, \bar{k}) - (\mu_{a0}, k_0) \right] \right\| \right\} \tag{2}$$

Where, 'F' is the forward operator to generate the forward data and 'y' is the experimental measured data. ||.|| represents the square root of the sum of the squared elements. This is known as Tikhonov approach, where α (chosen to be 10 in this case) balances the effect of the prior with model-data mismatch. *L* is the penalty matrix

which can be derived from MRI structural priors. Note that for a general case, i.e. without the *a priori* information L becomes identity matrix (I). The update equation resulting from this procedure then becomes:

$$(J^T J + \alpha L^T L)(\delta\mu_a, \delta k) = \{ J^T [y - F(\mu_a, k)] \} \tag{3}$$

Each node in the FEM mesh is labeled according the region (typically fatty, glandular, tumor) obtained from MRI T1-weighted images[4]. Note that, it is also assumed that there is no covariance between the nodes belonging to different regions of the imagine domain. The L-matrix is calculated once initially before the reconstruction procedure starts and it is used throughout the reconstruction procedure to penalize the solution. Helmholtz forms for the L-matrix, used in this work are discussed individually in the subsections below.

2.2.a Helmholtz-1D
In this approach, the co-variance of nodes within a region becomes the basis by which the constraint is applied. As discussed by Lynch and McGillicuddy[6, 7], the basic idea is to represent the estimated parameter variability over the distance as the outcome of stochastic process. The result of a stochastically forced one dimensional Helmholtz equation, without applying any boundary conditions, so the process noise has the analytical form $(1 + kr)e^{-kr}$, where k has the dimensions of inverse of length, which is the length scale over which the covariance is expected (i.e. The diameter of volume being imaged) and r is the distance between the nodes in a given region. More explicitly,

$$C(i,j) = \begin{cases} 0 & \text{if i \& j are not in the same region} \\ (1+kr)\,e^{-kr} & \text{if i \& j are in the same region} \\ 1 & \text{if i=j} \end{cases} \tag{4}$$

Note that the length scale for covariance is considered as the diameter of the domain since it is assumed that there is no covariance between different regions. The Penalty matrix should be the inverse of covariance matrix (for the generalized least-square approach [7], so $L = C^{-1}$

2.2.b Helmholtz-2D
In a two-dimensional covariance matrix, a similar form can be found [7], having

$$C(i,j) = \begin{cases} 0 & \text{if i \& j are not in the same region} \\ kr\,K_1(kr) & \text{if i \& j are in the same region} \\ 1 & \text{if i=j} \end{cases} \tag{5}$$

where K_1 is the Bessel function of second kind and k and r are same as defined in Helmholtz-1D case. Note that this is an analytical covariance form (i.e. $kr\,K_1(kr)$) obtained when the two-dimensional Helmholtz equation is driven with a present and expected process noise (i.e. a disturbance with no spatial correlation in both the dimensions).

2.3 Phantom studies
A multi-layered gelatin phantom was fabricated with different optical properties using heated mixtures of water (80%), gelatin (20%) (G2625, Sigma Inc.), India Ink for absorption and TiO_2 (titanium dioxide powder, Sigma Inc.) for scattering, that are solidified by cooling at room temperature[4]. The phantom had a diameter of 86 mm and a height of 25 mm. A two-dimensional cross section of this phantom is shown in Fig. 1. Data is acquired using a stand-alone clinical NIR system[8] where the fibers were appropriately marked and photographed to extract region information (to mimic MRI images). This regional information is used to label the corresponding regions in the FEM mesh. NIR data is calibrated using a reference homogenous phantom to get initial guess and minimize the variation between the 16 optical channels, as is standard practice in human imaging studies.

3. Results

A photograph of the phantom used is shown in Fig. 1, and it is used to collect data at 785nm using 16 fibers (giving 240 measurements) in a single plane geometry[8]. The data is calibrated to give an initial homogeneous starting guess for the iterative reconstruction procedure. Fig. 2 gives the reconstructed images of μ_a and μ_s'. The legend of the Fig. 2 gives the mean and standard values for different regions obtained from the reconstructed images.

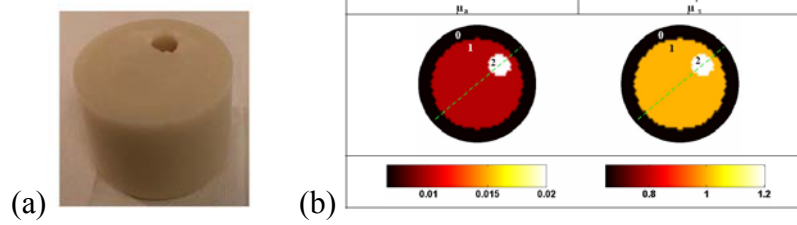(a)   (b)

Figure 1. (a) The gelatin phantom fabricated is shown (b). A 2-D cross-section of this gelatin phantom, Optical properties for the region labeled '0' are: $\mu_a = 0.0065$ mm^{-1}and $\mu'_s = 0.65$ mm^{-1}. Region '1' values are: $\mu_a = 0.01$ mm^{-1}and $\mu'_s = 1.0$ mm^{-1}. Region '2' values are: $\mu_a = 0.02$ mm^{-1}and $\mu'_s = 1.2$ mm^{-1}.

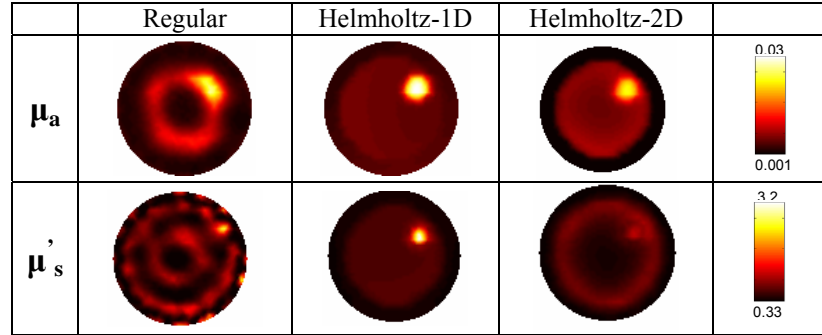|	Regular	Helmholtz-1D	Helmholtz-2D	
μ_a				
μ'_s				

Figure 2. Reconstructed μ_a and μ_s' images using the methods describted in Sec. 2. Reconstructed optical properties using regular, Helmholtz-1D and Helmholtz-2D for the region labeled '0' (in the original Fig. 1) are: $\mu_a = 0.0022\pm0.0005$, 0.0032 ± 0.0008, 0.0005 ± 0.0007 mm^{-1}and $\mu'_s = 0.64\pm0.40$, 0.38 ± 0.03, 0.42 ± 0.12mm^{-1}. Region '1' values are: $\mu_a = 0.0061\pm0.0032$, 0.0051 ± 0.0011, 0.0060 ± 0.0014 mm^{-1}and $\mu'_s = 0.66\pm0.27$, 0.63 ± 0.06, 0.64 ± 0.15 mm^{-1}. Region '2' values are: $\mu_a = 0.0192\pm0.0044$, 0.0227 ± 0.0051, 0.0181 ± 0.0032 mm^{-1}and $\mu'_s = 0.76\pm0.16$, 1.60 ± 0.80, 0.87 ± 0.15 mm^{-1} respectively.

4. Discussion

The reconstructed results (Fig. 2) show that the structural *a priori* information improves the reconstructed image quality dramatically as compared to the regular NIR reconstructions. The penalized problem (Helmholtz type of regularizations) gives smoother images resulting in smaller standard deviations from the mean values (see Fig. 2) as compared to the generalized problem which does not use *a priori* information. From reconstructed images (Fig. 2), it is apparent that Helmholtz-1D and Helmholtz-2D techniques are preserving the structure since the covariance of the optical properties is over the whole length scale of the imaging domain. Quantitatively Helmholtz-1D results are close to the expected results.

6. Acknowledgements

7. References

[1] D. A. Boas, D. H. Brooks, E. L. Miller, C. A. DiMarzio, M. Kilmer, R. J. Gaudette, and Q. Zhang, "Imaging the body with diffuse optical tomography," *IEEE Signal Processing Magazine*, vol. 18, pp. 57-75, 2001.

[2] S. Srinivasan, Pogue, B. W., Jiang, S., Dehghani, H., Kogel, C., Soho, S., Gibson, J. J., Tosteson, T. D., Poplack, S. P., and Paulsen, K. D., "Interpreting Hemoglobin and Water Concentration, Oxygen Saturation and Scattering Measured In Vivo by Near-Infrared Breast Tomography," *PNAS*, vol. 100, pp. 12349-12354, 2003.

[3] B. Brooksby, Jiang, S., Kogel, C., Doyley, M., Dehghani, H., Weaver, J. B., Poplack, S. P., Pogue, B. W., Paulsen, K. D., "Magnetic resonance-guided near-infrared tomography of the breast," *Rev. Sci. Instrum.*, vol. 75, pp. 5262-5270, 2004.

[4] B. Brooksby, Jiang, S., Dehghani, H., Pogue, B. W., Paulsen, K. D., Weaver, J. B., Kogel, C., Poplack, S. P.,, "Combining near infrared tomography and magnetic resonance imaging to study in vivo breast tissue: implementation of a Laplacian-type regularization to incorporate MR structure," *J Biomed. Opt.*, vol. 10, pp. 0515041, 2005.

[5] A. H. Hielscher and S. Bartel, "Use of penalty terms in gradient-based iterative reconstruction schemes for optical tomography," *J. Biomed. Opt.*, vol. 6, pp. 183-192, 2001.

[6] D. R. Lynch and D. J. McGillicuddy, "Objective analysis for coastal regimes," *Contin. Shelf Res.*, vol. 21, pp. 1299-1315, 2001.

[7] D. R. Lynch, *numerical partial differential equations for environmental scientists and engineers - A first practical course*, 1 ed: Springer, 2005.

[8] T. O. McBride, B. W. Pogue, S. Jiang, U. L. Osterberg, and K. D. Paulsen, "Development and Calibration of a Parallel Modulated Near-Infrared Tomography System for Hemoglobin Imaging In Vivo," *Rev. Sci. Instr.*, vol. 72, pp. 1817-1824, 2001.